UNIVERSITY OF OKLAHOMA

GRADUATE COLLEGE

UNIFIED FIBER-REINFORCED POLYMER COMPOSITE SOLUTIONS FOR ENHANCING THE STRUCTURAL DURABILITY OF AGING CIVIL INFRASTRUCTURE

A DISSERTATION

SUBMITTED TO THE GRADUATE FACULTY

in partial fulfillment of the requirements for the

Degree of

DOCTOR OF PHILOSOPHY

By

ALI AKBARPOUR

Norman, Oklahoma

2025

Downloaded from SHAREOK. Persistent Handle URL: https://hdl.handle.net/11244/341795

UNIFIED FIBER-REINFORCED POLYMER COMPOSITE SOLUTIONS FOR ENHANCING THE STRUCTURAL DURABILITY OF AGING CIVIL INFRASTRUCTURE

A DISSERTATION APPROVED FOR THE

SCHOOL OF CIVIL ENGINEERING AND ENVIRONMENTAL SCIENCE

BY THE COMMITTEE CONSISTING OF

Dr. Shreya Vemuganti, Chair

Dr. Jeffery S. Volz

Dr. Royce W. Floyd

Dr. Vivek K. Bajpai

©Copyright by ALI AKBARPOUR 2025

All Rights Reserved.

Dedication

To my mother, Akram Shahsavari, and my father, Mahmoud Akbarpour,

whose sacrifices, quiet worries, and unspoken prayers carried me farther than any plane ticket.

When I told my mother that I wanted to leave home and travel to another country to study for my Ph.D., she did not try to hold me back with fear. The next day, she placed a copy of Golestan-e Saadi in my hands so I could take it with me wherever I go. Golestan is a book of stories and poems about life, kindness, patience, and the weight of our choices; in its pages, she was sending me her faith, our culture, and a reminder to stay human, no matter how hard the road becomes.

There were many nights when this journey felt too heavy. In those moments, I would remember my mother's eyes when she gave me that book, and my father's lifetime of steady work and quiet strength. Their belief in me made it clear: I do not have the right to give up. Every new step forward is a way to honor the life they built and the dreams they had for their son.

To my sister, Rahil Akbarpour, whose love has always felt like home even across distance, and whose messages, laughter, and quiet support reminded me that I was always remembered and truly cared for, even from far away.

To my partner, Sana, who stood beside me through all the hard years of my Ph.D.; your kindness and love for people and the world, along with your quiet strength, kept me connected to life and gave me the courage to keep moving forward.

Acknowledgments

The completion of this dissertation would not have been possible without the support and guidance of many people. I am deeply grateful to my advisor, Dr. Shreya Vemuganti, for her mentorship, patience, and constant encouragement throughout my doctoral studies. I also thank Dr. Royce Floyd, Dr. Jeffery Volz, and Dr. Vivek Bajpai for thoughtful feedback and constructive suggestions that improved the quality of this work.

I would like to thank the faculty and staff of the School of Civil Engineering and Environmental Science and the Fears Structural Engineering Laboratory for providing an excellent environment for research and learning, especially Mr. John Bullock and Dr. Tommy Bounds. I am also thankful to my lab mates, collaborators, and project partners for their help with experiments, discussions, and data collection.

Portions of this dissertation are adapted from co-authored publications and reports. In these works, I led the experimental design, specimen preparation, testing, and data analysis, while my co-authors contributed to project conception, supervision, and manuscript review.

Looking back, I know that I did not walk this path alone. From my earliest teachers who helped me take the first steps in science and mathematics, to the many professors, mentors, classmates, and staff who supported me at different stages of my education, each of you has left a lasting impact on my life. Your guidance, kindness, and belief in me, whether in the classroom, the laboratory, or in everyday conversations, made it possible for me to reach this point. For all of these contributions, I am sincerely and deeply grateful.

Abstract

U.S. transportation assets continue to operate at or beyond design life under corrosion, chemical attack, and cyclic environmental loading, driving strength and serviceability deficiencies that demand constructible, design-checkable rehabilitation. This dissertation advances the structural use of fiber-reinforced polymer (FRP) and polymer-based systems through five coordinated studies that span material, interface, member, and system scales with direct relevance to design, detailing, and quality assurance.

Project 1 quantifies the flexural behavior and failure mechanisms of RC beams strengthened with combined CFRP systems. Across five configurations—control, U-wrap only, NSM-CFRP bars only, NSM+full U-wrap, and NSM+shear U-wrap—the strengthened beams achieved substantial capacity gains: +19% (U-only), +83% (NSM), +99% (NSM+full U-wrap), and +105% (NSM+shear U-wrap). The combined systems promoted bar strain development, mitigated debonding, and shifted failures toward CFRP rupture when confinement was effective.

Project 2 evaluates polymer-concrete (PC) overlays modified with multi-walled carbon nanotubes (MWCNTs) using direct tensile pull-off (ASTM C1583). On normal substrates, neat PC provided the most reliable adhesion; on sulfate-deteriorated substrates, a 0.5 wt.% COOH-functionalized MWCNT mix increased interface tensile capacity by ~15%, establishing substrate-conditioned material selection and dispersion guidance for bonded overlay design.

Project 3 establishes grout-dependent composite action in GFRP slip-lined corrugated metal pipe (CMP) culverts via circumferential ring testing. Polymeric annular grout produced stiffness factors ≈7× those of cementitious grout for uncorroded rings (≈6.8× for corroded), elevating

grout modulus and bond to first-order design variables for circumferential stiffness, load rating, and service-load deformation in trenchless rehabilitation.

Project 4 isolates matrix/interface durability of CFRP under 0–250 freeze–thaw cycles using off-axis tensile coupons (ASTM D3039). Neat laminates lost strength, modulus, and ultimate strain; on the other hand, CNT-modified laminates largely retained their strength, stiffness, and strain capacity after 250 freeze–thaw cycles. The mix with 1.0 wt.% COOH-functionalized CNTs showed the smallest change in properties.

Project 5 investigates 3D-printed thermoplastic CFRP lattices (cage/flat) as internal reinforcement in PCC, UHPC, and PC beams. Four-point bending benchmarks demonstrate displacement-ductility enhancement with matrix-dependent differences between observed and predicted nominal moments; performance is sensitive to lattice placement (cover, floating/tilt) and junction quality, motivating installation checks and matrix-appropriate stress-block adjustments.

Collectively, the dissertation contributes: (i) validated strength and failure data for combined NSM-and-wrap CFRP schemes enabling more ductile design checks; (ii) a chemically informed route to preserve overlay bond on sulfate-damaged substrates with functionalized CNTs; (iii) quantitative stiffness factors that elevate grout selection to a codifiable parameter for GFRP slip-lining; (iv) durability evidence that CNT nanomodification can stabilize off-axis CFRP properties under long-term freeze–thaw; and (v) structural-scale benchmarks for thermoplastic CFRP lattice reinforcement across cementitious and polymer matrices. Together, these results guide the design of durable composite rehabilitation systems against the key deterioration mechanisms.

Table of Contents

1. CHAPTER 1: Introduction 1

1.1. Overview 1

2. CHAPTER 2: Literature Review 5

2.1. CFRP Strengthening of RC Beams using NSM and U-Wraps 5

2.1.1. Overview 5

2.1.2. Fiber-Reinforced Polymers (FRP) – historical background 6

2.1.2.1. Reinforcing Fibers: The Load-Bearing Element 7

2.1.2.2. Polymer Matrix (Resins): The Binding Agent 9

2.1.3. FRPs in Construction: Properties and Applications 10

2.1.4. Flexural Strengthening of RC Beams using the Near-Surface-Mounted (NSM) Method 12

2.1.5. Shear Strengthening of RC Beams using the FRP U-Wrap Method 13

2.1.6. Research Gap and Proposed Investigation 14

2.2. CNT-Enhanced Polymer Concrete Overlays 15

2.2.1. Polymer Concrete Overlays 15

2.2.2. Polymer Concrete Formulation and Binders 16

2.2.3. Polymer Concrete Properties and Interfacial Bonding 17

2.2.4. Limitations of Conventional Microfiber Reinforcement in PC 19

2.2.5. Carbon Nanotubes (CNTs) as Potential Additives for PC 19

2.2.6. Dispersion and Reinforcement Mechanisms of CNTs in Polymers 21

2.2.7. Impact of Substrate Deterioration on Overlay Bonding 22

2.2.8. Influence of CNTs on Durability and Bonding 23

2.2.9. Research Gap and Proposed Investigation 24

2.3. GFRP Slip-Lined Culverts 25

2.3.1. The Challenge of CMP Deterioration 25

2.3.2. Slip Lining as a Rehabilitation Solution 26

2.3.3. Liner Materials: HDPE and the Emergence of GFRP 26

2.3.4. The Critical Role of Grout 28

2.3.5. Structural Behavior and Design Considerations 29

2.3.6. Performance Evaluation: Experimental Findings and Hydraulics 29

2.3.7. Research Gap and Proposed Investigation 30

2.4. Freeze–Thaw Durability of FRP Systems 31

2.4.1. Freeze-Thaw Mechanism 31

2.4.2. Bonding Importance 32

2.4.3. Effects of freeze-thaw cycles on fiber reinforced polymers 33

2.4.4. Overview of Carbon nanotubes in fiber reinforced polymers 35

2.4.5. Research Gap and Proposed Investigation 36

2.5. 3D-Printed CFRP Lattice as Internal Reinforcement 37

2.5.1. Infrastructure Resilience Imperatives and the Case for FRP Composites 37

2.5.2. FRP Manufacturing Methods and Woven Architectures..... 37

2.5.3. Thermoplastic Woven/Lattice CFRP for Construction: Geometric Flexibility and Process Sensitivities..... 38

2.5.4. Thermoplastic vs. Thermoset FRP..... 38

2.5.5. Research Gap and Proposed Investigation..... 39

3. CHAPTER 3: Motivation, Objectives, and Goals 40

3.1. Motivation..... 40

3.1.1. Rehabilitation Drivers and Required Outcomes 40

3.1.1.1. Corrosion..... 40

3.1.1.2. Chemical Attack..... 40

3.1.1.3. Freeze-Thaw Cycles..... 41

3.2. Limitations and Gaps in Current Rehabilitation Practices:..... 41

3.2.1. Combined Flexural and Shear Strengthening of RC Beams using FRPs: 41

3.2.2. Polymer Concrete Overlays: 41

3.2.3. GFRP Slip-Lining: 42

3.2.4. Freeze–Thaw Durability of FRP Systems..... 42

3.2.5. 3D-Printed CFRP Lattice as Internal Reinforcement 42

3.3. Need for Validated Advanced Solutions 43

3.4. Goals 45

3.5. Objectives 46

3.5.1.1. CFRP-Strengthened RC Beams: 46

3.5.1.2. CNT-Enhanced Polymer Concrete Overlays: 47

3.5.1.3. GFRP Slip-Lined Culverts: 48

3.5.1.4. Freeze–Thaw Durability of Nanomodified CFRP (Off-Axis): 49

3.5.1.5. 3D-Printed CFRP Lattice as Internal Reinforcement: 49

4. CHAPTER 4: Methods, Approach, and Scope of Work 51

4.1. Project 1: CFRP Strengthening of RC Beams using NSM and U-Wraps 51

4.1.1. Scope of Work: 51

4.1.2. Tasks Grouped by Method: 52

4.1.2.1. Specimen Fabrication and Strengthening: 52

4.1.2.2. Material Characterization: 52

4.1.2.3. Structural Testing and Data Acquisition: 53

4.1.2.4. Analysis and Reporting: 53

4.1.3. End Products: 54

4.2. Project 2: Nanomodification of Polymer Concrete for Enhanced Bonding 54

4.2.1. Scope of Work: 54

4.2.2. Tasks Grouped by Method: 54

4.2.2.1. Material Preparation and Characterization: 54

4.2.2.2. Bond Strength Testing:..... 55

4.2.2.3. Microscopic Analysis:..... 56

4.2.2.4. Analysis and Reporting:..... 56

4.2.3. End Products:..... 56

4.3. Project 3: Role of Grout and GFRP Slip Liner on Circumferential Behavior of Retrofitted Corroded Metal Culverts..... 57

4.3.1. Scope of Work:..... 57

4.3.2. Tasks Grouped by Method:..... 57

4.3.2.1. Material Procurement and Preparation:..... 57

4.3.2.2. Grout Characterization:..... 58

4.3.2.3. Specimen Fabrication:..... 58

4.3.2.4. Structural Testing and Data Acquisition:..... 58

4.3.2.5. Analysis and Reporting:..... 59

4.3.3. End Products:..... 59

4.4. Project 4: Freeze–Thaw Durability of Nanomodified CFRP (Off-Axis Tensile)..... 60

4.4.1. Scope of Work:..... 60

4.4.2. Tasks Grouped by Method:..... 60

4.4.2.1. Materials and Dispersion..... 60

4.4.2.2. Laminate Fabrication using Vacuum-Assisted Hand Lay-up Technique (VAHT)61

4.4.2.3. Specimen Preparation & Conditioning..... 61

4.4.2.4. Mechanical Testing and Data Collection 61
4.4.2.5. Microscopy and Interpretation 61
4.4.3. End Products: 62
4.5. Project 5: 3D-Printed CFRP Lattice as Internal Reinforcement 62
4.5.1. Scope of Work: 62
4.5.2. Tasks Grouped by Method: 63
4.5.2.1. Materials & Documentation 63
4.5.2.2. Concrete Mix 63
4.5.2.3. Beam Fabrication and Reinforcement Placement 63
4.5.2.4. Mechanical Characterization and Testing 63
4.5.2.5. Microscopy and Analytical Comparisons 63
4.5.3. End Products: 64
5. CHAPTER 5: An Experimental Study Incorporating Carbon Fiber Composite Bars and Wraps for Concrete Performance and Failure Insight 65
5.1. Literature Review 65
5.1.1. Overview 65
5.1.2. Fiber-Reinforced Polymers (FRP) – historical background 66
5.1.2.1. Reinforcing Fibers: The Load-Bearing Element 67
5.1.2.2. Polymer Matrix (Resins): The Binding Agent 69
5.1.3. FRPs in Construction: Properties and Applications 71

5.1.4. Flexural Strengthening of RC Beams using the Near-Surface-Mounted (NSM) Method 72

5.1.5. Shear Strengthening of RC Beams using the FRP U-Wrap Method 73

5.1.6. Research Gap and Proposed Investigation 74

5.2. Materials and Methods 75

5.2.1. Materials 75

5.2.2. Methods 77

5.2.2.1. U-Wrap Shear Strengthening (U Type) 81

5.2.2.2. NSM Flexural Strengthening (N Type) 84

5.2.2.3. Combination of Shear and Flexural Strengthening Methods (NU and NSU Type) 86

5.3. Results and Discussion 87

5.4. Key Discussion 96

5.5. Conclusions 97

6. CHAPTER 6: The Influence of Multi-Walled Carbon Nanotubes on the Pull-off Strength of Polymer Concrete Overlays on Concrete Substrates with Sulfate Exposure 100

6.1. Literature Review 100

6.1.1. Polymer Concrete Overlays 100

6.1.2. Polymer Concrete Formulation and Binders 101

6.1.3. Polymer Concrete Properties and Interfacial Bonding 102

6.1.4. Limitations of Conventional Microfiber Reinforcement in PC 104

6.1.5. Carbon Nanotubes (CNTs) as Potential Additives for PC 104

6.1.6. Dispersion and Reinforcement Mechanisms of CNTs in Polymers..... 106

6.1.7. Impact of Substrate Deterioration on Overlay Bonding 107

6.1.8. Influence of CNTs on Durability and Bonding..... 108

6.1.9. Research Gap and Proposed Investigation..... 109

6.2. Materials and Methods.....110

6.2.1. Mix Design Properties 110

6.2.2. Preparation of Nanomodified Polymer Concrete.....111

6.2.3. Preparation of Sulfate Exposure Environment 113

6.2.4. Preparation of Specimens for ASTM C1583 Test.....114

6.2.5. Microscopic Analysis.....117

6.3. Results and Discussion 118

6.3.1. Normal Condition 118

6.3.2. Sulfate Conditions..... 123

6.3.3. Microscopic Analysis..... 128

6.4. Discussion..... 129

6.5. Conclusions..... 131

7. CHAPTER 7: Role of Grout and GFRP Slip Liner on the Circumferential Behavior of Retrofitted Corroded Metal Culverts 133

7.1. Literature Review 133
7.1.1. The Challenge of CMP Deterioration 133
7.1.2. Slip Lining as a Rehabilitation Solution 134
7.1.3. Liner Materials: HDPE and the Emergence of GFRP 135
7.1.4. The Critical Role of Grout 136
7.1.5. Structural Behavior and Design Considerations 137
7.1.6. Performance Evaluation: Experimental Findings and Hydraulics 137
7.1.7. Research Gap and Proposed Investigation 138
7.2. Materials and Methods 139
7.2.1. Accelerated Corrosion Procedure 141
7.2.2. Mix design and compressive testing of grouts: 143
7.2.2.1. Cementitious Grout (Hi-Flow Grout): 143
7.2.2.2. Polymeric Grout (E3-Flowable): 144
7.2.2.3. Compressive Testing: 144
7.2.3. Fabrication of test specimens: 147
7.2.3.1. Initial Preparation: 147
7.2.3.2. Positioning Pipes: 147
7.2.3.3. Sealing Procedure: 149
7.2.3.4. Grout Casting: 150

7.2.3.5. Curing Procedure: 153

7.2.3.6. Post-corrosion Specimen Fabrication: 153

7.2.4. Preparation of the test setup: 154

7.3. Results and Discussion: 160

7.3.1. Load-Displacement of LVDTs: 160

7.3.1.1. Polymeric Grout 160

7.3.1.2. Cementitious grout: 165

7.3.2. Load-Displacement Results of the Machine 169

7.3.3. Stiffness Factor: 173

7.4. Conclusions: 174

8. CHAPTER 8: Effects of Freeze-Thaw Environments on Nanomodified Carbon Fiber Reinforced Polymer Composites 177

8.1. Literature Review 177

8.1.1. Freeze-Thaw Mechanism 177

8.1.2. Bonding Importance 178

8.1.3. Effects of freeze-thaw cycles on fiber reinforced polymers 179

8.1.4. Overview of Carbon nanotubes in fiber reinforced polymers 180

8.1.5. Research Gap and Proposed Investigation 182

8.2. Materials and Methods 182

8.2.1. CNT Dispersion in Epoxy Resin 183

8.2.2. Vacuum-Assisted Hand Lay-up Technique (VAHT) 184
8.2.3. Testing Overview 185
8.2.4. Freeze-Thaw Cycling 186
8.2.5. Static Tensile Testing of CFRP 187
8.2.6. Scanning Electron Microscopy (SEM) Imaging 190
8.3. Results and Discussion 190
8.3.1. Mechanical properties 190
8.3.2. CNT Dispersion Quality and SEM 197
8.4. Conclusions 198
9. CHAPTER 9: Thermoplastic Carbon Fiber Reinforced Polymer Tapes in Cementitious and Polymer Concretes 201
9.1. Literature Review 201
9.1.1. Infrastructure Resilience Imperatives and the Case for FRP Composites 201
9.1.2. FRP Manufacturing Methods and Woven Architectures 202
9.1.3. Thermoplastic Woven/Lattice CFRP for Construction: Geometric Flexibility and Process Sensitivities 202
9.1.4. Thermoplastic vs. Thermoset FRP 203
9.1.5. Research Gap and Proposed Investigation 203
9.2. Materials and Methods 204
9.2.1. Woven thermoplastic CFRP composite 204

9.2.2. Concrete mix designs and process 206
9.2.3. Compressive Strength Test 208
9.2.4. Fabrication of Test Beams 209
9.2.5. Flexural Test 210
9.2.6. Microscopic analysis 211
9.2.7. Theoretical calculations 211
9.3. Results and Discussion 212
9.4. Conclusions 218
10. CHAPTER 10: Conclusions and Recommendations for Future Work 221
10.1. Conclusions: 221
10.1.1. Project 1: CFRP-Strengthened RC Beams (NSM Bars + U-Wraps) 221
10.1.2. Project 2: CNT-Enhanced Polymer Concrete Overlays (Bond on Healthy vs. Sulfate-Damaged Substrates) 222
10.1.3. Project 3 — GFRP Slip-Lined CMP Culverts (Role of Annular Grout) 223
10.1.4. Project 4 — Freeze–Thaw Durability of Nanomodified CFRP (Off-Axis Tensile) 223
10.1.5. Project 5 — 3D-Printed Thermoplastic CFRP Lattice as Internal Reinforcement (PCC, UHPC, PC) 224
10.2. Recommendations for Future Work 225
11. References 227
12. Appendix: Publications 250

List of Tables

Table 1: Load and deflection results upon test completion..... 88

Table 2: Portland cement, concrete, and polymer concrete mix designs. 110

Table 3: Unconfined compression and modulus of rupture test results of PCC and PC. 118

Table 4: Mix design of cementitious grout 143

Table 5: Mix design of polymeric grout 144

Table 6: Uniaxial compression test results for cementitious grout specimens 145

Table 7: Uniaxial compression test results for polymeric grout specimens..... 146

Table 8: Peak load and displacement at peak load of tested specimens 170

Table 9: VAHT Layer Dimensions and Quantities 184

Table 10: Results of CFRP specimens 193

Table 11: Data Sheet for CFRP Tape (provided by WEAV3D Inc) 206

Table 12: Mix Design constituents for PCC, UHPC and PolC..... 207

List of Figures

Figure 1: Schematic overview illustrating the integrated research approach 44

Figure 2: Testing of concrete cylinder for (a) Modulus of Elasticity ASTM C469 (b) Split tensile strength ASTM C496 and (c) compressive strength ASTM C39. 6 cylinders tests per batch of concrete mixed. 76

Figure 3: (a) Tyfo unidirectional CFRP fabric (b) No. 3 RenewWrap CFRP bar. 77

Figure 4: (a) Schematic of RC beam dimensions (b) NSM bar included for types N, NU and NSU not included for C and U types. 78

Figure 5: Cross section of RC beams for (c) C (d) U (e) N and (f) NU and NSU. Groove for NSM and U-Wrap dimensions indicated. 79

Figure 6: Materials used for Strain Gauge Application 80

Figure 7: Beam molds and strain gauges attached steel cages prepared for fabrication..... 80

Figure 8: Steel reinforcement cages prepared with strain gauge application (a) Surface grinding (b) Strain gauge adhered to steel (c) Completed strain gauge application on tension and compression surfaces. 80

Figure 9: Strain gauge application (a) on concrete compression (b) compression and tension (indicated in red) steel (c) NSM FRP. 81

Figure 10: Surface preparation steps for U-wrap to ensure adequate bond. (a) surface grinding, (b) edge grinding, (c) mixing Part A and Part B of epoxy, and (d) applying prime coat on the beam 82

Figure 11: (a) Carbon fiber fabric wetting process for U-wrap. (b) Rolling wet fabric onto plastic pipe for layup on beam. 83

Figure 12: Rolling wet fabric onto pre-marked beam covering three sides for U-wrap. 83

Figure 13: Wet layup process (a) Layup with soft roller, (b) Layup with hard roller, and (c) Finished beam after U-wrap. 84

Figure 14: Grinding process for the NSM groove to ensure adequate bond between resin and concrete. (a) Use of a wire brush for grinding inside the groove, (b) Closer look at grind surface. 85

Figure 15: Steps of NSM-CFRP strengthening: (a) plastic form used at the bottom of the beam to create a groove before casting, (b) beam after fabrication and hardening, (c) beam after removing plastic form, (d) dispensing NSM gel in the groove, and (e) beam after performing surface preparation and NSM-CFRP flexural strengthening. 85

Figure 16: Combination strengthening NSM + complete U-wrap. (a) Wetting process of carbon fiber fabric, (b,c) wet-layup on NSM strengthened beams, (d) completed U-wrap strengthening on NSM-strengthened beam. 86

Figure 17: Combination strengthening NSM + shear only U-wrap (a) prime coat on NSM-strengthened beams for wet layup, (b) wet layup in shear only zones, (c) finished wet layup for U-wrap strengthening in shear-only zones for NSM-strengthened beams. 87

Figure 18: Load-displacement behavior of the median of all tested beams. 89

Figure 19: Mean flexural load capacity of tested beams. The percentage increase compared to control beams is shown on each bar. 91

Figure 20: Different failure modes of the tested beams. (a) Control beam before performing the test, (b) control beam after performing the test, (c) only U-wrap beam, (d) NSM only beam, (e) NSM + full U-wrap beam, (f) NSM + shear U-wrap beam. 93

Figure 21: Strain distribution diagrams at various loads for type (a) N, (b) NU, (c) NSU beams. 95

Figure 22: Various failure modes of RC beams strengthened with NSM-CFRP, (a) type NU beams, failed by the CFRP bar rupture, (b) type NSU beams, failed by the CFRP bar rupture, (c) type NSU beams, failed by sudden spilling of the epoxy cover. 96

Figure 23: Schematic flowchart illustrating the preparation process of nanomodified polymer concrete. 113

Figure 24: Carbon nanotube dispersion stages in resin: (a) weight of resin and MWCNTs, (b) magnetic stirring, (c) ultrasonication, (d) mixing of PC liquid component incorporating MWCNTs and powder component. 113

Figure 25: Specimens being in contact with sulfate ions after (a) 28 days, (b) 140 days, and (c) 210 days, and (d) shows the production of ettringite after 210 days. 114

Figure 26: The PCC specimens after performing the surface preparation. (a) cured in normal conditions and (b) cured in the presence of sulfate ions. 115

Figure 27: Preparation of the test specimens for the pull-off method (left–right), drilling cores, and the attachment of tensile loading devices. 116

Figure 28: Pull-off test setup. 116

Figure 29: Dispersion stabilization of MWCNT-modified resin after 48 h. 119

Figure 30: Microscopic images of the neat and nanomodified PC specimens: (a) PC-FC50, (b) PC-Neat. 120

Figure 31: Pull-off strength results of specimens which were cured in normal conditions. 122

Figure 32: Specimens which were cured in normal conditions after performing the pull-off test: (a) PC-Neat, (b) PC-P25, (c) PC-P50, (d) PC-FC25, (e) PC-FC50, (f) PC-FN25, (g) PC-FN50. ... 122

Figure 33: Specimens which were cured in sulfate conditions after performing the pull-off test: (a) PC-Neat, (b) PC-FC25, (c) PC-FC50, (d) PC-FN25, (e) PC-FN50. ... 124

Figure 34: Comparison between PC-Neat and PC-FC50 in healthy and sulfate conditions, considering one or two of the assumptions. ... 125

Figure 35: The chemical structures of (a) gypsum and (b) ettringite. ... 126

Figure 36: A schematic overview of the chemical reactions between nanomodified polymer concrete and concrete after sulfate exposure. ... 127

Figure 37: Microscopic images of the surface of the interface of PCC and PC after performing the pull-off test: (top) healthy conditions and (bottom) after sulfate attack. ... 129

Figure 38: Corrugated steel pipes used in this study ... 140

Figure 39: GFRP pipes used in this study. ... 140

Figure 40: Schematic view of composite pipe dimensions ... 141

Figure 41: CMP specimens before and after three months of accelerated corrosion, showing the initial uncorroded sections in the tank, the corrosion setup with anode and cathode connections, and the resulting heavy rust concentrated at the crown region. ... 142

Figure 42: Cementitious grout specimens before and after failure. ... 145

Figure 43: Polymeric grout specimens before and after failure. ... 147

Figure 44: Placement of the pipe on a plate covered by release film ... 148

Figure 45: Connecting wood pieces outside the steel pipe and inside the GFRP pipe to hold them in place during casting 149

Figure 46: Using GE advanced silicone to seal the inside of the GFRP pipe and outside of the steel pipe..... 150

Figure 47: Uncorroded CMP with cementitious grout..... 151

Figure 48: Polymer grout mixing and curing setup, showing prepared grout batches in buckets with the mixer (top) and the slip-lined specimens immediately after polymer grout placement while curing on the support plates (bottom). 152

Figure 49: Curing cementitious specimens after casting 153

Figure 50: Corroded CMP with polymeric grout..... 154

Figure 51: Hydrostone capping and instrumentation: (a) Hydrostone cast on the top of the specimen to fill the corrugations, (b) Hydrostone layer on the bottom surface after demolding, providing a flat bearing surface, and (c) string potentiometer (wire pods) used to record machine displacement during testing. 155

Figure 52: LVDT support system..... 156

Figure 53: Two-point loading test setup used in this study..... 157

Figure 54: Pipes before testing. (a) Uncorroded pipe with cementitious grout, (b) Corroded pipe with cementitious grout, (c) Uncorroded pipe with polymeric grout, (d) Corroded pipe with polymeric grout..... 159

Figure 55: Load-displacement behavior of uncorroded CMP with polymeric grout..... 161

Figure 56: Load-displacement behavior of corroded CMP with polymeric grout..... 162

Figure 57: Uncorroded CMP with polymeric grout; (a) at the beginning of the test, (b) after failure; (c) and (d) symmetry of failure which happened in the pipes 164

Figure 58: Bridging between GFRP pipe and polymeric grout 165

Figure 59: Load-displacement behavior of uncorroded CMP with cementitious grout 166

Figure 60: Load-displacement behavior of corroded CMP with cementitious grout 166

Figure 61: Uncorroded CMP with cementitious grout; (a) at the beginning of the test, (b) after failure 167

Figure 62: Pipes with cementitious grout after failure; (a) and (b) no bridging was observed between cementitious grout and GFRP pipe, (c) symmetry of failure..... 168

Figure 63: Load-displacement of uncorroded CMP with polymeric grout..... 171

Figure 64: Load-displacement of corroded CMP with polymeric grout..... 171

Figure 65: Load-displacement of uncorroded CMP with cementitious grout 172

Figure 66: Load-displacement of corroded CMP with cementitious grout 172

Figure 67: Matrix of CFRP types manufactured for freeze-thaw cycling. 183

Figure 68: CNT Dispersion Equipment. 184

Figure 69: Freeze-thaw cycling in environmental chamber..... 187

Figure 70: Tensile testing setup (a) Instron 5967 Universal Testing Frame tensile grips with specimen loaded; (b) Instron AVE 2 Non-Contacting Video Extensometer with tensile test setup; (c) CFRP tabbed tensile specimen. 188

Figure 71: Schematic of off-axis versus on-axis loading: (a) Off-axis fiber orientation; (b) On-axis Fiber Orientation (c) Off-axis failure mode in tension, loaded at 0°; (d) On-axis failure mode in tension, loaded at 0°. 189

Figure 72: Evolution of (a) strength, (b) strain, and (c) modulus of elasticity of CFRP tensile specimens over 250 freeze-thaw cycles. 191

Figure 73: Stress-strain relationship for CFRP after (a) 0 freeze-thaw cycles and (b) 250 freeze-thaw cycles. 196

Figure 74: SEM images of (a) neat 25K X, (b) neat 50K X, (c) pristine CNT 5K X, (d) pristine CNT 25K X, (e) pristine CNT 25K X, (f) functionalized-COOH CNT 25K X, (g) functionalized-COOH CNT 25K X, (h) functionalized-COOH CNT 50K X epoxy cured at room temperature. 198

Figure 75: Woven thermoplastic CFRP cage (top) and flat lattices (bottom) composite acquired from WEAV 3D Inc. 205

Figure 76: Fabrication of (a) PCC beams and (b) UHPC beams 209

Figure 77: Flexural Bending Setup for (a) flat lattice, (b) cage lattice (not to scale), and (c) concrete beams loaded in the test frame. 210

Figure 78: Microscopic images indicating defects in the material (a) long defect (b) small defects 211

Figure 79: Load vs displacement graphs of (a) PCC, (b) PolC and (c) UHPC beams 213

Figure 80: Failure Pattern of PCC beams with (a) Flat lattice, (b) no WEAV3D Reinforcement, and (c) Cage lattice. 214

Figure 81: Failure Pattern of UHPC beams with (a) Flat lattice, (b) No WEAV3D reinforcement, and (c) Cage lattice. 215

Figure 82: Failure Pattern of PolC beams with (a) Flat lattice, (b) No WEAV3D reinforcement, (c) Cage Lattice 215

Figure 83: Bar Plot showing theoretical capacity vs observed capacity of PCC, UHPC, and PolC beams with cage and flat lattices 218

1. CHAPTER 1: Introduction

1.1. Overview

U.S. civil infrastructure, which has been regarded as the backbone of national prosperity, is now facing huge distress after decades of underinvestment and deferred maintenance. The American Society of Civil Engineers (ASCE) assigned an overall grade of 'C' to the U.S. infrastructure in 2025, which is an improvement compared to 'C-' in 2021, but still indicative of systems requiring significant attention (Infrastructure Report CARD 2025). Based on the Failure to Act study by ASCE, postponing critical rehabilitation is going to cost the U.S. economy more than $10 trillion in GDP. This will eventually eradicate roughly 3 million jobs by 2039, which translates into an average $3300 loss in annual disposable income per household. Bridges alone show the immense risk: one-third of the 623,000 spans need work, and 45% have already exceeded their 50-year design life, leaving a ten-year gap of $373 billion. Addressing this important challenge and mitigating this infrastructure crisis necessitates the exploration of more innovative and cost-effective approaches for the rehabilitation of the U.S. infrastructure.

Aging of the structures beyond their service life and degradation due to environmental exposure are the main reasons for the deterioration of civil infrastructure. In reinforced concrete (RC) structures like bridges, the corrosion of conventional steel reinforcement is the prime concern, which can lead to reduced load-carrying capacity and structural failure. Similarly, metallic infrastructure elements, such as corrugated metal pipe (CMP) culverts, are hugely susceptible to corrosion. On the other hand, chemical attacks pose a considerable threat as well. Sulfate attack, which originates from external sources such as groundwater and soil or internal sources within concrete, causes destructive reactions with cement hydration products. These reactions will lead

to expansion, cracking, and strength loss of the structure. The aforementioned degradation mechanisms necessitate rehabilitation strategies that can address specific failure modes and enhance or restore the structural performance of the infrastructure.

One of the materials that can be used as a promising alternative for civil infrastructure rehabilitation is fiber-reinforced polymer (FRP) composites. FRPs are comprised of high-strength fibers (such as glass, aramid, or carbon) that have been embedded in a polymer matrix. This composition will lead to a material that has high tensile strength, excellent durability, a high strength-to-weight ratio, and, most importantly, corrosion resistance, which makes it advantageous for rehabilitation purposes. Carbon fiber reinforced polymer (CFRP) offers high stiffness and tensile strength, which makes it more effective in flexural and shear strengthening of RC beams. On the other hand, glass fiber-reinforced polymer (GFRP) provides a cost-effective, corrosion-resistant solution that is suitable for applications such as culvert liners. In addition to externally bonded and lining applications, emerging thermoplastic CFRP lattice reinforcements offer lightweight, 3D-printable internal reinforcement for cementitious and polymer concretes, enabling enhanced ductility and recyclable, rapidly manufactured reinforcement architectures.

Alongside FRPs, polymer concrete (PC) represents another advanced material class utilized for infrastructure repair and overlay applications (Zhang et al. 2020). PC replaces the traditional portland cement binder with a polymer resin, typically mixed with fine and coarse aggregates (Dikeou 2003). This formulation yields a material known for its rapid curing, high compressive and flexural strength, wear resistance, impermeability, and excellent adhesion to concrete substrates (Pratap 2002). These properties make PC particularly suitable for thin bonded overlays on bridge decks and pavements, where minimizing traffic disruption and providing a durable, protective layer are crucial (Dang et al. 2024). Ensuring a strong and long-lasting bond between

the PC overlay and the concrete substrate, especially when the substrate has suffered deterioration, is paramount for the long-term performance of the repair system (Manawadu et al. 2023). Beyond overlays, polymer concrete can serve as a structural matrix; benchmarking its flexural response with thermoplastic CFRP lattice reinforcement alongside PCC and UHPC helps clarify material–reinforcement interactions for ductility and capacity.

Despite the advantages of FRP and PC, challenges remain in optimizing their application and performance for long-term infrastructure rehabilitation. For FRP-strengthened RC beams, understanding the interaction between different strengthening configurations and their influence on failure modes is crucial for developing reliable design guidelines and preventing premature, brittle failures (Chennareddy and Taha 2017). In the realm of PC overlays, enhancing bond strength, particularly to substrates weakened by chemical attack (like sulfates), is a critical research need; exploring nanomodification, such as the incorporation of functionalized carbon nanotubes (CNTs), offers a potential pathway to improve interfacial properties without compromising workability (Byron et al. 2021). Furthermore, for trenchless rehabilitation methods like GFRP slip-lining for corroded culverts, the role of the grout material in achieving composite action and contributing to the overall circumferential stiffness and load-carrying capacity requires thorough investigation, as current design approaches often lack specific guidance for these systems. In cold regions, an additional durability challenge is the effect of repeated freeze–thaw cycling on CFRP matrix and interface properties; evaluating whether CNT nanomodification can sustain or improve off-axis tensile behavior after prolonged cycling is essential to guide FRP selection for harsh environments. In parallel, the structural role of thermoplastic CFRP lattice reinforcement must be benchmarked across PCC, UHPC, and polymer concrete, including how lattice geometry and placement influence ductility and how PCC-based stress-block assumptions should be adapted for

nontraditional matrices such as polymer concrete. This dissertation addresses these specific challenges by investigating advanced FRP and polymer-based systems – specifically CFRP strengthening of RC beams, CNT-enhanced PC overlays, and GFRP slip-lined culverts – to provide critical insights and data necessary for improving the rehabilitation and resilience of vital civil infrastructure components. Additionally, it evaluates the freeze–thaw durability of nanomodified CFRP laminates and the flexural behavior of concrete beams reinforced with thermoplastic CFRP lattices, completing a materials-to-structural-scale assessment across five integrated projects.

2. CHAPTER 2: Literature Review

2.1. CFRP Strengthening of RC Beams using NSM and U-Wraps

2.1.1. Overview

The rehabilitation and strengthening of existing reinforced concrete (RC) structures have become increasingly vital in civil infrastructure management. Reinforced and prestressed concrete infrastructure built in the 60s and 70s is now experiencing severe deterioration, and action is needed to ensure the structural performance is adequate for the demands imposed. Bridges built between 1955 and 1975 are now past their nominal 50-year design life. Corrosion of conventional steel reinforcement is a primary driver of this deterioration and is responsible for numerous structurally deficient bridges, a multi-billion-dollar challenge creating a cycle of maintenance, repair, and replacement. Corrosion undermines structural integrity by degrading the reinforcing steel's physical and mechanical characteristics (e.g., diminishing its cross-sectional area), weakening the crucial bond between steel and concrete, and inducing concrete cover cracking due to expanding rust products (Rodrigues et al. 2021).

For instance, analysis of the 2023 FHWA National Bridge Inventory reveals that 58% of bridges built between 1955 and 1975 now require major rehabilitation or load posting, primarily because corrosion has reduced reinforcing steel cross-sections and induced concrete cover cracking. This deterioration presents a high risk for future closures or weight restrictions and requires substantial investment. Furthermore, a recent life-cycle assessment demonstrated that failing to intervene early can raise total agency costs by approximately 12% over a 75-year horizon (Lee et al. 2025).

While conventional methods exist to mitigate corrosion (e.g., cathodic protection, inhibitors, coatings, stainless steel rebar (Yan et al. 2016)) or repair compromised structures (e.g., section enlargement, external post-tensioning, epoxy injection, externally bonded steel plates (Al-Mahaidi and Kalfat 2018), these can have limitations in terms of cost, durability, or installation disruption. Therefore, cost-effective and durable repair and strengthening techniques are essential to extend the service lives of structures like bridges safely and efficiently, especially to accommodate rising traffic volumes and comply with contemporary design standards (Sharaky et al. 2018; Wang et al. 2021). Given these challenges, advanced materials like Fiber-Reinforced Polymers (FRPs) have emerged as a promising alternative for structural strengthening, the background and properties of which are discussed next.

2.1.2. Fiber-Reinforced Polymers (FRP) – historical background

The emergence of FRP composites dates back to the 1930s, when Owens Glass Company, having partnered with the Corning company, manufactured the initial patented version of fiberglass (Marsh 2006). Following this, the FRP sector achieved substantial development during World War II, a growth trend that carried on for the subsequent two decades, with implementations mainly found in the aerospace and military sectors (Lubin 1982). Recognizing the potential demonstrated in demanding aerospace applications (Van Den Einde et al. 2003), significant research has since explored FRP composites for the structural engineering field. FRPs have become a major focus for the engineering community, leading to widespread adoption by the construction industry for the repair and strengthening of infrastructure (Vedernikov et al. 2021). Their use spans diverse geographic regions and climates, highlighting their versatility (Bakis et al. 2003). Economically, while initial material costs can be higher than traditional materials, FRPs offer potential long-term

benefits through reduced maintenance needs and extended service life, contributing to their cost-effectiveness in many scenarios (Bakis et al. 2003).

For concrete structures, these FRP applications generally fall into two classifications: internal applications using components like tendons, bars, or rods, and external applications that employ plates, fabrics, or wraps. Typically, internal applications relate to new construction projects (like concrete structures reinforced or prestressed with FRP), whereas external techniques are connected with the rehabilitation, upgrading, and mending of already existing structures, which are usually steel-reinforced concrete, though FRP-reinforced concrete structures themselves might require future strengthening (Ortiz et al. 2023). FRP composites fundamentally consist of reinforcing fibers embedded within a polymer matrix. Understanding the properties of these constituents is key to selecting and designing effective strengthening systems.

2.1.2.1. Reinforcing Fibers: The Load-Bearing Element

Fibers act as the primary load-bearing constituent in FRP composites, necessitating properties like considerable strength, significant stiffness (high elastic modulus), and adequate elongation before fracture. They also need suitable durability for the specific environmental conditions where the structure will be utilized. A fiber's effectiveness is influenced by its length, chemical structure, and cross-sectional geometry, with fibers being available in multiple shapes and sizes. Depending on the specific fiber, diameters typically range from 5 to 25 microns (Budelmann and Rostasy 1993). Carbon, Glass, and Aramid represent the most frequent fiber types for FRPs, yielding the corresponding composite materials commonly known as CFRP, GFRP, and AFRP. Understanding their distinct properties is crucial for material selection:

1. **Carbon Fibers:** Carbon fibers possess desirable qualities such as significant stiffness (elastic modulus between 200-800 GPa), advantageous ratios of strength and stiffness relative to weight, minimal susceptibility to fatigue damage, and exceptional durability against moisture and chemical exposure. However, their limited ultimate strain results in lower resistance to impacts and limited ductility. Carbon fibers also feature high thermal and electrical conductivity, which presents either an asset or a liability depending on the specific design context. According to (Malik and Foster 2010), these fibers are classified into four categories using their elastic modulus: low modulus (230-250 GPa), intermediate modulus (290-300 GPa), high modulus (350-380 GPa), and ultrahigh modulus types (480-760 GPa). Typically, the low-modulus carbon fibers exhibit lower density, reduced cost, greater strength in tension and compression, and higher ultimate tensile strain compared to their high-modulus counterparts.
2. **Glass Fibers:** As the most widely utilized reinforcement type within FRP composites, glass fibers offer affordability combined with high tensile strength and excellent insulation characteristics. Their disadvantages include limited stiffness (low tensile modulus), high density, and vulnerability to abrasion damage and alkaline conditions; they also exhibit comparatively weaker performance when exposed to moisture, sustained loading (creep), or cyclic stresses (fatigue). Glass fibers are generally classified into three varieties: C-glass, S-glass, and E-glass. C-glass is noted for its high chemical durability, making it suitable for diverse applications. E-glass represents a low-cost, versatile fiber providing good strength, electrical resistivity, and acid resistance. While S-glass fibers deliver superior strength, stiffness, and ultimate elongation compared to E-glass, they carry a higher price tag and show greater susceptibility to degradation from environmental factors.

3. **Aramid Fibers:** Aramid fibers are synthetic fibers made from aromatic polyamides. Most structural aramids used in FRP composites are para-aramid fibers with straight-chain aromatic rings, which provide high strength along the fiber length but relatively low transverse bond strength. Common para-aramid fibers used in FRP fabrication include Kevlar 149, Kevlar 49, and Kevlar 29 (Kevlar is a commercial para-aramid fiber), with elastic moduli of about 179 GPa, 131 GPa, and 82 GPa, respectively. Key advantages of aramid fibers include outstanding impact toughness, considerable stiffness, high thermal stability, and lower density relative to other fibers. Conversely, aramids are susceptible to degradation from ultraviolet light, and exposure to moisture can induce creep. In terms of cost, aramid fibers are priced higher than glass fibers but lower than carbon fibers (Ishtiaq et al. 2024; Jambhulkar and Sahu 2024; Nanni 1993).

2.1.2.2. Polymer Matrix (Resins): The Binding Agent

The polymer matrix, or resin, plays several critical roles within the composite: it encases the fibers to shield them from physical abrasion, enables the transfer of shear stresses both between layers (inter-laminar) and within a layer (in-plane), and provides lateral bracing to fibers resisting buckling under compressive forces. Resins are typically rigid or semi-rigid polymers at room temperature. Additionally, the resin's own physical and thermal characteristics substantially impact the final mechanical performance achieved by the composite product. Thermosetting and thermoplastic materials represent the two principal polymer types employed in FRP composites.

1. **Thermosetting Resins:** These are more commonly used in structural FRPs. They begin as low-viscosity liquids composed of small molecules. Upon curing, these molecules chemically cross-link to establish a rigid three-dimensional network; this

transformation is permanent, meaning the material cannot be subsequently reformed using heat or pressure. Common examples utilized in composites include polyesters, vinyl esters, and epoxies. Generally, these thermosets demonstrate good resistance to heat and chemicals, along with minimal creep and stress relaxation tendencies. Their primary disadvantages typically include limited strain capacity before failure (brittleness), constrained storage durations prior to use (shelf life), and relatively lengthy manufacturing cycles (Bank 2006).

2. **Thermoplastic Resins:** Polymers used in thermoplastic matrices are composed of molecules arranged in linear chains. These chains are connected by comparatively weak secondary forces (intermolecular bonds), which thermal energy or pressure can disrupt. Consequently, the material softens or melts upon heating and resolidifies when cooled. This behavior allows thermoplastic polymers to be repeatedly softened and reshaped through heating, though doing so might diminish their mechanical performance over time. Their use in externally bonded structural strengthening is less common than thermosets (Bank 2006).

Following the examination of constituent materials, the discussion proceeds to the practical applications and principal properties of the FRP systems most widely employed for structural strengthening.

2.1.3. FRPs in Construction: Properties and Applications

Building on the properties of these constituent materials, specific FRP composites, particularly carbon-fiber-reinforced polymers (CFRP) and glass-fiber-reinforced polymers (GFRP), have

found significant application in construction strengthening due to their advantageous characteristics (M. A. Kadhim et al. 2023; Sokairge et al. 2022).

Material Comparison (CFRP vs. GFRP): CFRP and GFRP differ significantly in mechanical properties. CFRP typically exhibits tensile strengths of 3.5–6 GPa and an elastic modulus of 230–250 GPa (for standard modulus fibers), while GFRP offers tensile strengths of 1.5–2.5 GPa and an elastic modulus of 70–90 GPa (Kabashi et al. 2020). This approximately three-fold stiffness advantage means CFRP is highly effective in controlling deflections; for instance, in flexure-critical members, a CFRP retrofit can potentially halve the mid-span deflection compared to an equivalent GFRP retrofit (Qureshi and Sheikh 2023). CFRP's superior tensile strength and stiffness make it particularly effective for enhancing the shear and flexural capacity of RC beams (Zhang et al. 2017).

Material Comparison (CFRP vs. Steel): Compared to traditional steel reinforcement, CFRP exhibits a significantly higher tensile strength-to-weight ratio, potentially offering several times the strength for the same weight. This lighter weight facilitates handling and installation and reduces the dead load added to the structure. Although CFRP's initial material costs are typically higher than steel, its excellent corrosion resistance eliminates a primary deterioration mechanism seen in steel-RC structures, leading to reduced long-term maintenance and potentially lower life-cycle costs, making it a valuable alternative depending on project needs (Bakis et al. 2003).

Corrosion Resistance: FRP's inherent resistance to electrochemical corrosion is a major advantage, significantly contributing to enhanced durability, especially in aggressive environments (Tharmarajah et al. 2015). This property is critical for prolonging the life of structures affected by steel corrosion, making FRP invaluable in rehabilitating aging infrastructure (Liu et al. 2018).

Limitations: A key limitation, particularly for building applications, is the vulnerability of the polymer matrix (especially epoxy) to degradation at elevated temperatures and long-term exposure to ultraviolet (UV) radiation and moisture, potentially reducing the effectiveness of FRP strengthening unless appropriate protection measures are implemented (Nanni 1993). For this reason, externally bonded FRP systems are often protected with coatings, paints, or wraps to limit UV exposure and weathering.

2.1.4. Flexural Strengthening of RC Beams using the Near-Surface-Mounted (NSM) Method

In the flexural strengthening of RC beams with the usage of FRP, two approaches are suggested by the American Concrete Institute (ACI) 440-2R: near-surface-mounted (NSM) FRP and externally bonded (EB) FRP (Nanni, A., Alkhrdaji, T., Chen, G., Barker, M., Xinbao, Y., and Mayo 1999; Toufigh et al. 2013). EB-FRP involves attaching an FRP laminate to the beam's tension side using epoxy, allowing the laminate to serve as extra reinforcement and boost the beam's flexural strength (Saadatmanesh and Ehsani 1990). NSM-FRP entails creating a groove on the beam's tension side, partially filling it with epoxy, inserting an FRP bar or strips, and then completely sealing it with epoxy (Nanni, A., Alkhrdaji, T., Chen, G., Barker, M., Xinbao, Y., and Mayo 1999). The primary benefit of the NSM-FRP method is its bonding efficiency with the concrete (De Lorenzis and Teng 2007).

For NSM flexural strengthening, CFRP is often preferred over GFRP due to its superior axial stiffness and tensile strength (Van Cao and Pham 2019). The high stiffness allows CFRP to effectively contribute to the beam's capacity at small strains, and its high strength provides significant reinforcement potential. This efficiency can also allow for optimization of groove sizes

(Zhang et al. 2013). Common failure modes observed in tests of NSM-FRP strengthened beams include concrete crushing, yielding of internal steel reinforcement followed by FRP rupture or debonding, or premature debonding of the NSM FRP element (Aljidda et al. 2023; ChennaReddy 2016; M. A. Kadhim et al. 2023). Debonding failure often initiates near cracks or at the end of the NSM strip/bar, potentially due to high interfacial stress concentrations, and is frequently the governing failure mode, especially if the FRP is not sufficiently anchored. Research suggests that with adequate anchorage length, FRP rupture might be less common, as the FRP may only reach 60–70% of its ultimate tensile capacity before other failure modes occur (Hassan and Rizkalla 2003).

2.1.5. Shear Strengthening of RC Beams using the FRP U-Wrap Method

RC beams requiring flexural strengthening (e.g., with NSM FRP) often also need shear strengthening to accommodate increased loads or address existing shear deficiencies. Externally bonded FRP wraps are commonly used for this purpose. The U-wrapping method (wrapping the sides and bottom soffit of the beam) using a wet layup process is frequent. This involves saturating FRP fabric (often CFRP or GFRP) with epoxy resin and applying it to the prepared concrete surfaces, typically with fibers oriented perpendicular to the beam axis or vertically to effectively resist shear cracks (Chennareddy and Taha 2017). Variations include fully wrapping the section (if possible), three-sided U-wraps, or applying discrete strips on the two sides only (Murad and Abu-AlHaj 2021). Extensive research has examined the effectiveness of different wrapping schemes and configurations (Chajes et al. 1995; Kachlakev and McCurry 2000; Taerwe 2020).

Typical failure modes for FRP shear strengthening include debonding of the FRP (often initiating at corners or free edges) or rupture of the FRP fibers. While epoxy-based FRP systems are

common, it is worth noting that alternative systems using inorganic matrices, such as fabric-reinforced cementitious matrix (FRCM) composites, are also being investigated, offering potential advantages like better performance at elevated temperatures (Ombres and Mazzuca 2024).

2.1.6. Research Gap and Proposed Investigation

The preceding review establishes the effectiveness of Near-Surface Mounted (NSM) CFRP bars for flexural strengthening and externally bonded CFRP U-wraps for shear strengthening of RC beams. Previous research indicated that combining these techniques could significantly enhance load capacity compared to using NSM reinforcement alone. However, while the strength benefits were recognized, a detailed understanding of the interaction between the NSM bar and the U-wrap confinement, particularly concerning the resulting failure mechanisms and overall structural behavior, remained less explored. NSM-only strengthened beams often exhibit failure due to debonding of the FRP bar from the concrete substrate before the bar's full tensile capacity is utilized. Adding U-wrap confinement was expected to improve this bond, but the precise manner in which this confinement alters the governing failure mode (from debonding to potentially more brittle modes like bar rupture) and influences the overall ductility of the system required further experimental clarification. Specifically, there was a need to investigate how different U-wrap configurations (e.g., full vs. partial span) interact with NSM bars, observe the resulting failure modes directly, and assess the trade-offs between increased capacity and potential changes in failure abruptness.

This research is aimed at addressing this gap by experimentally investigating the flexural behavior and failure modes of RC beams strengthened with NSM-CFRP bars, CFRP U-wraps, and, critically, combinations of both (full-span U-wrap and shear-span-only U-wrap).

2.2. CNT-Enhanced Polymer Concrete Overlays

2.2.1. Polymer Concrete Overlays

The deterioration of civil infrastructure, particularly concrete bridge decks, necessitates rapid and durable repair solutions. Overlays are a common strategy, and Polymer Concrete (PC) represents a class of composite materials where the traditional cementitious binder found in portland cement concrete (PCC) is entirely replaced by a synthetic organic polymer, making it a viable selection for infrastructure maintenance, rehabilitation, and preservation (Dikeou 2003; Pratap 2002). This fundamental difference distinguishes PC, sometimes known as synthetic resin or resin concrete, from polymer-modified concrete (PMC) or polymer-impregnated concrete (PIC). PC is generally lightweight, offers high wear and skid resistance, is relatively impermeable to water and chlorides, and cures rapidly (often within hours) – characteristics highly suitable for accelerated construction (Dang et al. 2024; Laredo Dos Reis 2005; Wheat et al. 1993).

Polymer concrete overlays are frequently employed for bridge decks, typically applied in thin layers ranging from 1/2 to 3/4 inch (12.7 to 19 mm). Their primary functions include extending service life, providing a durable/impermeable wearing surface, protecting the underlying substrate and reinforcement from water and chlorides, and restoring friction. The rapid curing nature allows for quick application and return to service, significantly minimizing traffic disruption – often enabling overnight installation and reopening the bridge the following day, making PC overlays highly suitable for accelerated bridge construction (ABC) projects (Dang et al. 2024; Laredo Dos Reis 2005; Wheat et al. 1993). Different types exist, including Thin Polymer Overlays (TPOs) and Slurry Overlays. While general performance is favorable, success hinges critically on proper

installation, especially substrate preparation, as localized failures are often linked to inadequate preparation or mixing.

Similar to the use of advanced FRP composites for strengthening deteriorated beams, PC overlays represent another application of polymer-based materials aimed at restoring or enhancing the performance and durability of existing concrete infrastructure, addressing challenges like rapid repair needs and protection against environmental degradation.

2.2.2. Polymer Concrete Formulation and Binders

Typically, a polymer concrete is comprised of fine and coarse aggregates, a catalyst, and a binder. The defining characteristic of PC is this polymer binder system, usually involving a thermosetting resin (monomer or prepolymer) combined with a catalyst or hardener to initiate polymerization, creating a cross-linked polymer network that binds the aggregates. PC formulations do not contain portland cement or water as part of the binder system (Stansbury and Idacavage 2016). The selection and proportioning of aggregates and fillers (like fly ash, silica fume, slag) are crucial for performance and economy, often used to reduce expensive resin volume and potentially enhance properties. For instance, specific fillers can improve strength, while others might enhance insulation but reduce strength, requiring careful selection (Hong et al. 2017).

The choice of binder for bridge deck overlays is an important factor in achieving several characteristics. The most commonly used binder systems are based on methyl methacrylate (MMA), unsaturated polyester resins, epoxy resins, and vinyl ester resins (Nodehi 2022). Each offers distinct advantages and disadvantages. Epoxies generally provide excellent adhesion, low shrinkage, and superior chemical resistance, but are relatively expensive and have slower curing. Unsaturated Polyesters are the lowest cost option but suffer from high shrinkage and potentially

higher water absorption. MMAs offer very rapid curing even at low temperatures, require less surface preparation, and exhibit good weathering and friction retention, making them ideal for rapid construction, but the monomer is flammable with a strong odor. Vinyl esters present a compromise with low cost, low viscosity (aiding penetration), and good chemical resistance, but also have high shrinkage and potential exothermic reaction issues during cure (Nodehi 2022). The selection involves balancing project needs like speed, budget, environmental exposure, and desired performance. The binder's chemical nature also critically influences interaction with nanomaterials like CNTs.

The suggested ratio of binder to aggregate (filler and coarse) for the design of the PC mix is usually around 1:3.7 by weight (Hong et al. 2017). Studies have also shown that maintaining a weight ratio between filler and coarse aggregate of around 7:3 can enhance the performance of PC. Optimal resin content often falls between 10-20 wt.%, varying with binder and aggregate characteristics. Optimization is key, as resin is the most expensive component (Hong et al. 2017; Manawadu et al. 2023).

2.2.3. Polymer Concrete Properties and Interfacial Bonding

PC has great crack resistance and durability. It generally possesses significantly higher compressive, flexural, and tensile strength than conventional concrete, with rapid strength development being a key advantage (Byron et al. 2021). Its low permeability provides waterproofing and excellent resistance to freeze-thaw cycles and chemical attack (Toufigh et al. 2017). PC overlays offer good abrasion/wear resistance and skid resistance. Also, in order to decrease galvanic corrosion, it acts as an effective barrier between different substances (Sun and

Lee 2023; Yeon et al. 2014). However, properties like shrinkage vary significantly with binder type, and workability depends on resin viscosity and fillers.

A solid adhesion to the concrete substrate is necessary when considering bridge deck overlays. The bond between the overlay and substrate is frequently identified as the main factor concerning serviceability and durability. A strong bond ensures monolithic action for stress transfer and is crucial for the overlay to function effectively and protect the substrate. The interface is often the weakest link, and bond failure (delamination) compromises performance. The ability of the bonded joint to withstand all anticipated in-service loads (traffic, fatigue) and internal stresses from differential volume changes (shrinkage, thermal cycles) is crucial (Manawadu et al. 2023). Given the thinness of overlays, their reliance on the substrate makes bond integrity paramount.

Adhesion relies on a combination of mechanical interlocking and chemical/physical adhesion (Ganguli et al. 2006). Mechanical interlocking occurs as the liquid binder penetrates substrate pores and roughness, forming physical anchors upon hardening. Its effectiveness depends heavily on substrate roughness, often described by the concrete surface profile (CSP). Physical adhesion involves intermolecular forces (van der Waals, hydrogen bonding) requiring intimate molecular contact. Chemical bonding involves primary bonds forming between reactive groups in the binder and on the concrete surface, potentially enhanced by coupling agents like silanes (Gorninski et al. 2004).

Achieving a strong bond is influenced by many factors. Substrate preparation is consistently highlighted as most critical, requiring removal of all unsound material and contaminants to achieve a clean, sound surface with adequate roughness (Wang et al. 2019). Substrate condition (moisture content, strength) also plays a role. PC properties like binder type, shrinkage, and viscosity affect bond development. Application conditions (temperature, humidity) influence curing and bonding.

Environmental factors (temperature cycles, moisture, loading) challenge the bond long-term (Wang et al. 2019). Enhancing the bond strength of PC with the concrete substrate is therefore of great importance and needs to be explored.

2.2.4. Limitations of Conventional Microfiber Reinforcement in PC

Previous studies added carbon fibers and synthetic chopped glass to PC in weight-based amounts ranging from 0.3% to 7.5% to improve toughness, but the mechanical characteristics of PC were often only slightly improved (Shokrieh et al. 2011). Nevertheless, the fiber addition limits the use of PC and decreases its workability (Toufigh et al. 2017). This problem stems from the fact that using chopped fibers makes it harder to achieve an ideal finish, in addition to the lower flowability. While PC generally exhibits high strength, some binders can be inherently brittle with low fracture toughness. Although ductility can be improved by raising the ratio of resin to filler, compressive strength can be reduced by up to 26% and flexural strength by up to 70% (Byron et al. 2021). This suggests a scale mismatch where microfibers struggle to effectively modify matrix behavior without causing processing issues. These limitations highlight the need for innovative approaches, such as nanomaterial incorporation, to improve PC performance, particularly toughness and bond strength, without sacrificing its benefits.

2.2.5. Carbon Nanotubes (CNTs) as Potential Additives for PC

Within the last decade, research studies have evaluated the potential of using nanomaterials to change the performance of materials. The motivation stems from the limitations of micro-scale additives. Whereas the much greater surface area of nanomaterials, relative to microfibers, enables interactions at multiple levels (molecular, nano/meso-structural) and therefore promotes a more significant impact on the mesoscale, often at very low loading fractions (Ganguli et al. 2006). The

role of the PC binder's chemical composition is critical for the efficiency of nano-materials (Theodore et al. 2011). Nanomaterials are more efficient in performance when they are in close contact with the host matrix and a chemical binder because they enhance chemical interactions throughout the polymerization process (Chuah et al. 2014a; David et al. 2014a).

One of the nanomaterials that has been widely utilized is carbon nanotubes (CNTs). Since CNTs were first discovered (Iijima 1991), their unique structural, chemical, and physical characteristics have drawn considerable interest. Structurally visualized as rolled graphene sheets, CNTs feature a high aspect ratio, with diameters on the nanometer scale and lengths on the micrometer scale, coupled with low densities (Yu et al. 2008). They possess remarkable properties due to strong sp^2 bonds: extreme stiffness (Young's Modulus ~1 TPa for SWCNTs), high strength (>100 GPa possible), high thermal conductivity, and metallic or semiconducting electrical behavior (Popov et al. 2016). These exceptional characteristics make CNTs a highly regarded potential filler material for polymeric nanocomposites (Yu et al. 2016). Researchers have aimed to harness these remarkable traits for various types of applications, such as field emission displays, electronic devices, hydrogen storage, and polymer composites (Avouris 2002).

CNTs are broadly divided into multi-walled carbon nanotubes (MWCNTs) and single-walled carbon nanotubes (SWCNTs). SWCNTs consist of a single graphene cylinder (1-2 nm diameter), while MWCNTs comprise multiple concentric cylinders (5-100+ nm diameter). SWCNTs generally have higher aspect ratios, superior intrinsic mechanical properties (strength, stiffness), are more flexible, and have fewer defects compared to MWCNTs (Thakre et al. 2011). By rolling concentric graphene sheets, MWCNTs can be conceptually derived from SWCNTs. However, SWCNTs are exponentially more expensive to produce. Consequently, MWCNTs are more commonly used in practical research for composites like PC due to their affordability and

availability, despite potentially lower intrinsic properties and higher defect density. The choice depends on balancing performance and cost. Regarding mechanical properties, a single-walled carbon nanotube (SWCNT) is significantly stiffer than steel (Park et al. 2003). For multi-walled nano-tubes (MWCNT), the modulus can range from 200 to 4,000 GPa. MWCNTs offer outstanding mechanical characteristics and have been linked to enhancements in polymer durability, fatigue resistance, glass transition temperature, strength, fracture toughness, and controlled viscoelastic properties (Tang et al. 2013; Yu et al. 2008).

2.2.6. Dispersion and Reinforcement Mechanisms of CNTs in Polymers

The effectiveness of CNTs hinges on overcoming their strong tendency to agglomerate due to van der Waals forces, particularly for high aspect ratio MWCNTs (Chuah et al. 2014a). Achieving uniform dispersion is crucial but challenging. The most widely used dispersion methods include stirring, shear mixing, ball milling, ultrasonication, chemical functionalization, and extrusion (Chuah et al. 2014a). Mechanical methods like high-shear mixing or three-roll milling (calendering) apply physical forces to break agglomerates, with milling being effective for viscous systems and generally non-damaging. Functionalization (chemically modifying the CNT surface) is often critical to improve compatibility, reduce attraction, and enhance interfacial bonding. Covalent functionalization (e.g., acid oxidation creating -COOH groups) forms strong bonds but can alter CNT structure and properties. Non-covalent functionalization uses weaker interactions (e.g., surfactants, polymer wrapping) to preserve CNT structure but may yield weaker adhesion (Hirsch and Vostrowsky 2005). Often, a combination of functionalization and mechanical mixing is needed.

Well-dispersed CNTs reinforce polymers via several nanoscale mechanisms: 1) Load Transfer: Transferring stress from the matrix to the stiff CNTs via the interface, crucial for strength/stiffness improvements and dependent on interfacial adhesion. 2) Crack Bridging: CNTs spanning nano/microcracks resist their opening and propagation, enhancing fracture toughness. 3) Crack Deflection: Forcing cracks along more tortuous paths increases fracture energy. Other mechanisms include energy dissipation through nanotube pull-out or fracture. The success of these mechanisms relies entirely on good dispersion and a strong interface.

2.2.7. Impact of Substrate Deterioration on Overlay Bonding

In addition to bonding with regular concrete, bonds that PC can develop with concrete exposed to extreme, harsh climatic conditions need to be strong. Such conditions cause degradation and negatively impact the performance of concrete infrastructure (Al-samawi et al. 2023; Tang et al. 2013). One of the main negative influences on concrete performance, particularly in unfavorable climatic environments, is sulfate attack (Al-samawi and Zhu 2022; Ikumi et al. 2018).

Sulfate attack is a major concern in sulfate-rich soils, groundwater, or seawater. It involves chemical reactions between sulfate ions and cement hydrates (like $Ca(OH)_2$ and C_3A), forming expansive products like gypsum and ettringite (Akbarpour et al. 2022b; a). The significant volume increase associated with ettringite formation generates internal stresses leading to expansion, cracking, and spalling (Neville 2004). Physical salt crystallization within pores under wet-dry cycles can also exert damaging pressure. Magnesium sulfate attack is particularly aggressive as it can also decompose the C-S-H binder (Rodriguez-Camacho and Uribe-Afif 2002). The sources of sulfate attack can be external or internal; external sources include soil, groundwater, seawater, and

acid rain (Ikumi et al. 2019; Ouyang et al. 1988). This degradation results in reduced strength and integrity, particularly at the concrete surface.

2.2.8. Influence of CNTs on Durability and Bonding

Studies on cementitious materials suggest CNTs can enhance durability. (Han et al. 2013) discovered that MWCNTs can reduce gas and water permeability. (Li et al. 2015a) found that CNTs refine the pore structure. Bheel et al. (2023) reported improved compressive strength, reduced expansion due to sulfate attack, minimized acid attack effects, and lower chloride permeability with 0.05% CNTs. However, Camacho et al. (2014) observed increased porosity and accelerated deterioration under carbonation/chloride ingress with CNTs, highlighting the critical importance of dispersion and potential variability.

While previous studies highlighted potential durability benefits of CNTs against chemical attacks, the specific impact of sulfate-induced deterioration on the bond strength of polymer concrete overlays remains underexplored. As noted earlier, the interaction mechanisms of CNTs differ significantly between cement and polymer matrices. Therefore, direct investigation within the PC system is required to understand CNT effects on PC bond performance, especially on deteriorated substrates.

Evidence from related systems suggests CNTs can enhance polymer adhesion. Studies on CNT-modified epoxy adhesives bonding FRP to concrete consistently show improved bond performance, increased load capacity, mitigation of debonding, and enhanced adhesion, often attributed to matrix toughening near the interface and interfacial crack bridging (Li et al. 2021). Enhanced fatigue resistance and fracture toughness reported for CNT-PC (Douba et al. 2019) are highly relevant, as bond failure often involves crack propagation near the interface. Functionalized

CNTs also offer potential for direct chemical bonding across the interface. It is hypothesized that these mechanisms could be particularly beneficial when bonding to flawed, deteriorated substrates where crack initiation resistance is critical.

2.2.9. Research Gap and Proposed Investigation

The main goal of this research is to investigate the effect of incorporating carbon nanotubes on the pull-off strength of polymer concrete with healthy and unhealthy (sulfate-deteriorated) concrete substrates. While the potential benefits are suggested by related literature, direct experimental data quantifying the influence of CNTs on the bond between PC overlays and sulfate-damaged concrete are lacking. Understanding this interaction is crucial for developing materials suitable for harsh environmental conditions and reliable rehabilitation measures.

In order to ascertain these objectives, a wide range of tests is proposed, ranging from the preparation and characterization of polymer concrete with various MWCNT concentrations (using functionalized and pristine MWCNTs) to mechanical property tests such as modulus of rupture (ASTM C580/C78) and compressive strength (ASTM C579). Concrete specimens will be subjected to controlled sulfate-exposed environments to induce deterioration. Polymer concrete with and without nanomodification will be used to bond with both healthy and deteriorated concrete substrates. The bond strength will be evaluated using ASTM C1583 pull-off tests. Microscopy analysis will be performed to evaluate the dispersion of MWCNTs in PC and the failure surfaces of specimens after the pull-off test to understand failure mechanisms. The findings of these tests aim to provide insight into the effect of nanomaterials on polymer concrete bonds with unhealthy and deteriorated concrete, thus enabling the realization of more long-lasting and efficient rehabilitation measures for degraded bridge decks.

2.3. GFRP Slip-Lined Culverts

2.3.1. The Challenge of CMP Deterioration

Corrugated metal pipes (CMPs) are fundamental components of transportation and drainage infrastructures, prominently adopted for their low initial costs, ease of fabrication, and straightforward installation (Hoult et al. 2013). These pipes represent a cornerstone, widely utilized due to these initial advantages. Despite these advantages, CMPs face substantial deterioration primarily due to corrosion (Moore 2001). Corrosion involves the electrochemical degradation of the metal (typically galvanized or aluminized steel), leading to material thinning, reduced structural capacity, and eventual perforation. Environmental elements such as water chemistry (pH, dissolved oxygen, aggressive ions like chlorides and sulfates), aggressive soil characteristics (resistivity, pH, moisture, organics), abrasion from sediment load, and galvanic corrosion interactions significantly accelerate their degradation, posing challenges to infrastructure longevity and public safety (Smith et al. 2015). Low pH and low soil resistivity are particularly aggressive factors. This corrosion, particularly in culverts beneath roads, necessitates frequent maintenance and costly rehabilitation or replacement, significantly impacting transportation budgets and public inconvenience. The typical design lifespan of 50 years is often not achieved, with service life potentially reduced to less than 30 years in aggressive environments, highlighting the need for condition-based assessment rather than relying solely on age (Moore 2001). Common defects stemming from deterioration include shape distortion, joint misalignment or separation, and perforations, which can lead to infiltration of surrounding soil, formation of voids, and potential roadway subsidence (Moore 2001).

Similar to the corrosion issues affecting steel reinforcement in concrete beams (Project 1) and the general degradation impacting concrete substrates needing overlays (Project 2), the corrosion of CMPs represents a major infrastructure durability challenge, motivating the search for advanced, corrosion-resistant rehabilitation materials and techniques.

2.3.2. Slip Lining as a Rehabilitation Solution

In response to deteriorating culverts, trenchless rehabilitation techniques have gained prominence for minimizing surface disruption and costs (McKim 1997). Among available rehabilitation techniques, slip lining emerges prominently as a widely adopted trenchless method that offers cost-effective and minimally disruptive solutions for rehabilitating deteriorated culverts (Moore and Hu 1996; Zhao and Daigle 2001). Slip lining involves inserting a smaller diameter liner pipe within an existing host pipe and typically filling the annular gap between the liner and host with grout (McAlpine 2006). The trenchless nature reduces traffic delays, environmental disturbance, and enhances safety compared to open-cut replacement. Installation can involve discrete pipe segments joined inside or pulling/pushing a continuous liner pipe (Syachrani et al. 2010). It is important to note that the specific liner material, installation method, and the intended role of the grout significantly influence the design and performance, requiring a tailored approach rather than a generalized one. While excavation along the alignment is minimized, preparatory work like cleaning, obstruction removal, flow bypass, and potential insertion/reception pits can still be substantial (Moore and Hu 1996).

2.3.3. Liner Materials: HDPE and the Emergence of GFRP

Various materials are used for slip liners, including thermoplastics (HDPE, PVC), thermosetting composites (GFRP), and traditional materials (steel, concrete). High-density polyethylene

(HDPE), noted for corrosion resistance, flexibility, and superior hydraulic properties, is frequently employed for this application (Haghani et al. 2021). Its flexibility aids installation, and smooth surfaces (Manning's n ~0.009-0.012) enhance hydraulics (Haghani et al. 2021). However, HDPE has relatively low stiffness and strength and is susceptible to long-term creep deformation under sustained load, often necessitating reliance on the grout for structural capacity (Moore and Hu 1996). Standards like ASTM F585 and AASHTO M326 govern its use.

Recognizing the limitations of traditional materials such as steel (corrosion susceptibility) and HDPE (lower structural capacity, creep), (Abdellatef et al. 2021) advocated for glass fiber-reinforced polymer (GFRP) slip liners. GFRP is a composite of high-strength glass fibers (providing strength/stiffness) embedded in a polymer resin matrix (polyester, vinyl ester, or epoxy, which binds fibers and provides protection). These liners, characterized by corrosion resistance, reduced weight (high strength-to-weight ratio), and superior hydraulic performance, represent a promising alternative (Liu et al. 2005). GFRP's key advantage is its excellent corrosion resistance, making it highly durable in aggressive environments where CMPs degrade rapidly, leading to projected service lives of 75-100 years. Its hydraulic smoothness (Manning's n ~0.009-0.011) is comparable to HDPE (Yan et al. 2016).

Haghani et al. (2021) provided an extensive evaluation of fiber-reinforced polymer (FRP) composites, especially glass FRP (GFRP), highlighting their suitability as alternative materials for culvert construction and rehabilitation. Their research emphasized improved lifecycle costs, exceptional durability, and reduced maintenance demands compared to traditional steel culverts. FRP composites, with their intrinsic corrosion resistance, lightweight properties, and ease of installation, emerged as sustainable and economically viable solutions for new construction and rehabilitation projects alike. Compared directly to HDPE, GFRP offers substantially higher short-

term strength (tensile ~550-1380+ MPa) and stiffness (flexural modulus ~20-40+ GPa), potentially allowing thinner liners or greater structural enhancement. However, GFRP is anisotropic, meaning its properties depend on fiber orientation, which must be considered in design (Bank 2007). While expected to have better long-term strength retention than HDPE, GFRP is not immune to time-dependent effects (creep rupture), and determining appropriate long-term reduction factors requires careful consideration and validated data, as standard creep tests can be challenging to apply.

2.3.4. The Critical Role of Grout

The grout filling the annular space is crucial, serving multiple functions: void filling (preventing liner movement/buckling), load transfer between host/liner/soil, structural support, host pipe stabilization (filling cracks/voids), and sealing against infiltration/exfiltration (Das 2021).

Several grout types are used:

Cementitious Grouts: Traditional portland cement-based grouts, often including fly ash or admixtures. Controlled Low Strength Material (CLSM or flowable fill), with high sand content and low specified strength, is common due to flowability and cost, but field issues with incomplete fill exist. Shrinkage must be controlled (Das 2021).

Cellular Grouts: Lightweight cementitious grouts with high air content (30-90%) introduced via foaming agents. Their low density minimizes hydrostatic pressure on the liner during placement, reducing flotation/collapse risk, especially for large/flexible liners. They are very flowable but typically have lower strength than denser grouts. The trade-off between installability (low density) and structural performance (strength/stiffness) is a key consideration (Alzlfawi 2023).

Polymer and Geopolymer Grouts: Newer options include rapid-setting, high-strength, high-bond polymer grouts (polyurethane, epoxy) and geopolymers. Geopolymers, based on alkali-activated industrial byproducts (fly ash, slag), offer rapid cure, high early strength, excellent bond, superior chemical/sulfate resistance, low shrinkage, and environmental benefits. They appear highly promising for culvert rehabilitation but require more long-term field validation and specialized expertise (Kohankar Kouchesfehani et al. 2021).

Grout selection depends on structural needs (strength/stiffness), flowability, setting time, shrinkage control, density (to manage pressure), durability requirements, cost, and availability.

2.3.5. Structural Behavior and Design Considerations

The effectiveness of the rehabilitation relies heavily on the interaction between the liner, grout, host pipe, and surrounding soil, aiming for composite action where components share load effectively (Smith et al. 2015). This depends critically on the bond at the grout-liner and grout-host interfaces, achieved via mechanical interlock and chemical adhesion. Bond strength is influenced by grout properties (especially shrinkage), liner surface characteristics (roughness, material type), host pipe condition, and installation quality (Smith et al. 2015).

2.3.6. Performance Evaluation: Experimental Findings and Hydraulics

Experimental studies provide crucial insights. (Simpson et al. 2016) investigated HDPE slip liners with high-density grout, showing significant stiffness improvements and >90% deflection reductions compared to unlined culverts, attributing stiffness mainly to the grout. Investigations by Tetreault et al. (2020) compared grout types under severe loading: high-density grout resulted in a rigid, fully composite system with minimal deformation, while low-density grout allowed greater liner flexibility, significant deformation, and grout failure, highlighting grout quality's

critical role. Complementary laboratory studies (Tetreault et al. 2020) reinforced this, showing ~10x load capacity and ~50x stiffness increases with high-strength grout compared to unrehabilitated pipes, with modest gains from low-strength grout. These studies collectively underscore the substantial impact of grout selection on rehabilitation efficacy and the importance of achieving composite action.

Advocating for GFRP, Abdellatef et al. (2021) used FE modeling to show GFRP liners effectively withstand traffic stresses, enhancing structural reliability. Furthermore, ChennaReddy (2016) identified critical design factors for GFRP liners (wall thrust, bending, buckling, deflection) and used FEA to confirm their stress resistance under traffic loads, validating their suitability. Tetreault et al. (2020) emphasized the mechanics of liner-grout interaction, clarifying that fully bonded composite behavior enhances performance, while compromised bonding reduces effectiveness.

Hydraulic performance is another key consideration. While slip lining reduces diameter, the smoother surfaces of HDPE and GFRP liners (Manning's n ~0.009-0.012) compared to deteriorated CMPs (n ~0.022+) often maintain or even improve flow capacity. This hydraulic efficiency is essential for effective drainage and flood management.

2.3.7. Research Gap and Proposed Investigation

While the potential of Glass Fiber-Reinforced Polymer (GFRP) slip liners for rehabilitating corroded corrugated metal pipes (CMPs) is recognized, and some longitudinal testing data exists, a critical knowledge gap persists regarding their circumferential structural behavior under realistic loading conditions. Specifically, there is a lack of experimental data quantifying how different grout types (e.g., cementitious vs. polymeric) interact with the GFRP liner and influence the composite ring stiffness and load capacity, particularly when rehabilitating CMPs that have

undergone corrosion. This deficiency is compounded by the absence of standardized testing protocols specifically for GFRP slip-lined CMPs, hindering the development of reliable design parameters, such as the stiffness factor, needed for safe and efficient field implementation. This research directly addresses this gap by undertaking circumferential two-point bending tests on both uncorroded and corroded CMP specimens rehabilitated with GFRP liners using different grout systems, aiming to provide the necessary experimental data to characterize circumferential performance and derive key design parameters.

2.4. Freeze–Thaw Durability of FRP Systems

2.4.1. Freeze-Thaw Mechanism

Freeze-thaw (F–T) durability of concrete is highly important in cold areas. Pore structure has close relations to F-T durability (Kong et al. 2005). The amount of ice formed in pores and the freezing point of pore solution are decided by the size, radius, and volume of the pores (Cai and Liu 1998). In general, in a specific range of temperature intervals, a bigger internal hydraulic pressure will be caused by frozen concrete pore solution, and as a result, more destructive frost damage will happen (Pinandita Faiz 1998). F–T can generate surface spalling, which will lead to mass loss of concrete; also, the developed internal cracking will cause strength deterioration of the concrete (Guo et al. 2018). Under F–T cycles, the coefficient of thermal expansion and thermal conductivity will increase, while the specific heat capacity of concrete will decrease. Because of the coarsening effect, the porosity of concrete will increase, which is one of the outcomes of F–T cycles (Luo et al. 2022). The F-T deterioration is a complicated chemical and physical phenomenon, which starts at the internal microstructure of concrete. For instance, the permeability of concrete increases when F-T happens because the pore structure of concrete deteriorates, and the F-T damage accelerates

the entry of erosion medium and external water (Qiu et al. 2020). After the cracks form in concrete due to the F-T, it facilitates the penetration of carbon dioxide, salt, moisture, and other agents into the concrete pore structure. This penetration will cause deterioration of the reinforcement materials. For instance, steel reinforcement corrosion (SRC) will happen inside the concrete as a result of an increase in permeability (Kim and Kim 2013).

2.4.2. Bonding Importance

The basis of the capacity of concrete and steel to coordinate deformation and work together is their sufficient bonding force (Zhang et al. 2022). This bonding force is hugely important when using fiber-reinforced polymers (FRPs) as a reinforcement material in concrete structures as well. This bonding force can be affected by harsh environments since the coefficients of expansion and contraction in these two materials are different. Hugely effective alternatives to steel are fiber-reinforced polymer sheets and plates, which are being used as internal and external reinforcement materials for strengthening and rehabilitation (Zaman et al. 2013). FRPs are comprised of a polymer matrix, which has been strengthened using different types of fibers, such as carbon fibers or glass fibers (Barkoula et al. 2008). A wide range of materials that have a good resistance against corrosion and adverse environments, possess good mechanical properties, and are lightweight can be produced by combining these two types of fibers with a polymer-based matrix. The fiber fraction that is being mostly used is between 30 to 60 percent and primarily rests on the type of composite that is being used. Among the most common materials that are being used for reinforcement of polymer matrix, glass is the most used one, which comprises 90% of manufacturing exercises (Vaidya 2015). There are three types of glass fibers: C-glass, S-glass, and E-glass. E-glass is the most used one, and S-glass is the strongest. The number of different oxides such as iron, aluminum, calcium, boron, and sodium, along with silica oxide, defines the type of

glass (Hwang and Han 1986). Polyacrylonitrile is the main component of 90% of carbon fibers; others are made of rayon and petroleum pitch. Compared to glass fibers, these fibers possess a low coefficient of thermal expansion, high thermal conductivity, dimensional accuracy at higher temperatures, and excellent strength and modulus (Hosford 2013).

2.4.3. Effects of freeze-thaw cycles on fiber reinforced polymers

Cold climate conditions, such as freeze-thaw action, exposure to deicing salts, and low temperature, are the main reasons for these severe environmental conditions (Green et al. 2000). Therefore, the environmental durability of the method and materials that are being used for rehabilitation is very important, especially in these harsh environmental conditions. Nonetheless, a very few number of studies have been performed relating to the environmental durability of FRP materials in these harsh environments. A number of F-T tests on beams plated with carbon fiber reinforced polymer sheets were performed by Kaiser (1989). He found that 100 cycles from +25°C to -25°C did not cause any harmful effects on the structural performance of the beams. In 2000, Green et al. (2000) evaluated the structural performance of beams strengthened using FRP under severe cold environments. He found that the temperature variation of –27°C to +21°C the CFRP reinforced beams did not show any detrimental effects on the beams when subjected to static loads. Also, Mostofinejad and Mohammadi (2020) performed a series of tests on strengthened beams with CFRP to evaluate the F-T durability. The temperature varied between 15°C to -18°C, and the number of F-T cycles was 50. This research also showed that F-T cycles did not cause any negative effects on the concrete beams' strength. The F-T durability of CFRP-strengthened RC beams affected by surface delamination was studied by Markiv et al. (2016). It was found that partial surface delamination and F-T cycles did not have any harmful effects on the load deflection behavior of beams. Hancox (1996) showed that the matrix-dominated characteristics such as in-

plane shear, compressive strength, and transverse tensile, are being more affected by the environmental changes because the fibers are the least sensitive materials in FRPs. Temperature changes did not have significant effects on the longitudinal tensile strength. The tensile strength of epoxy-glass FRP was lowered by 10% when subjected to F-T cycles in research conducted by Dutta and Hui (1996). On the other hand, F-T cycles did not have any significant effects on the elastic modulus or tensile strength of carbon-epoxy FRPs.

Many studies have evaluated the effects of adverse environments on the behavior of FRP reinforced concrete. It has been concluded that the potential risks of premature debonding and failure of the debonding interface are high. To be more specific, freeze-thaw cycles may cause negative effects on FRP and FRP-concrete structures. There are three main reasons that can cause deterioration of FRP-concrete systems due to F-T cycles (Bank 2007): (a) Microcracking of the resin matrix, (b) Debonding between the matrix and fibers, and (c) Degradation of the adhesion of FRPs to the concrete. The current study focuses on the first issue. (Dutta and Hui 1996) used two types of GFRPs for their study and subjected them to -60 to 50°C. They saw cracks after only 100 cycles. As suspected, the usage of -60°C pushed the resin matrix to its tensile strength, which produced microcracks. (Karbhari 2001) evaluated the mechanical properties of CFRP under F-T cycles at temperatures ranging from -18 to 20°C. The results indicated a decrease in the strength of CFRP plates after 450 cycles. This decrease in strength was attributed to the debonding between the matrix and fibers. Therefore, there is a need to evaluate various approaches to face these three causes. Among these approaches, carbon nanotubes show promise.

2.4.4. Overview of Carbon nanotubes in fiber reinforced polymers

Carbon nanotubes (CNTs) were discovered by Sumio Iijima in 1991 (Iijima 1991). CNTs are classified as one-dimensional nanomaterials with an axial dimension being micrometers and a radial dimension being nanometers. The density of CNTs is 1/6 to 1/7 of steel; however, their tensile strength can be up to 50-200 GPa, which is 100 times more than steel. The elastic modulus of CNTs is 5 times that of steel and equal to diamond, which is around 1TPa (Han et al. 2013). SWCNTs are more flexible and have fewer defects compared to MWCNTs. By rolling the concentric graphene sheets, MWCNTs can be made from SWCNTs. It means that, based on the area of application, the choice of MWCNTs and SWCNTs should be made (Li et al. 2015b). The capability of recovering to the original status after large deformations is extraordinary in CNTs. Because of having a great performance in different aspects such as chemistry, mechanics, heat conductivity, and electrical conductivity, the usage of CNTs has involved chemical sensors, composite materials, biomedicine products, and electrical components (Erol et al. 2018; Li et al. 2023; Norizan et al. 2020). CNTs can improve the thermal conductivity, electrical conductivity, and tribological and mechanical properties of metal matrix composites, such as titanium, nickel, copper, aluminum, magnesium, and iron matrix nanocomposites (Dadkhah et al. 2019; Saboori et al. 2018). In many fields such as sports equipment, marine engineering, automotive engineering, and aerospace, CNT-reinforced FRPs have been used recently (Khanna et al. 2021; Okoro et al. 2019; Zhao et al. 2023).

With the advancement of new and intelligent materials in recent years, CNTs, because of having high rigidity and strength, can be used as high-quality reinforcement and hugely enhance the bonding force between layers of FRP. As a result, multiscale demanding functional composite materials can be made using CNTs, while adding functions of nanomaterials. Since it is going to

increase the interlayer bonding force of FRP materials, it will make the material suitable for complex load environments such as F-T cycles (Zakaria et al. 2019). Directly dispersing CNTs in the resin matrix is the earliest method to introduce this material to reinforced FRPs. When CNTs have been dispersed in a resin matrix, they will act as a bridge in the resin-fiber interface, which can efficiently prevent microcracking in the resin matrix. (Ovali 2018) added 0.5, 1, and 2 wt.% of MWCNTs to glass/epoxy and indicated that the wear resistance of this material increased, which is mostly related to the adhesion between fibers and matrix. Moreover, to improve the tensile strength of carbon/epoxy composites. (Roy et al. 2018) utilized various types of functionalized CNTs. Compressive strength and interfacial strength of aramid FRPs increased by 82 and 131% when CNTs were introduced into the system. As mentioned earlier, the debonding between the matrix and fibers was the second reason for failure, so CNT usage can be effective in addressing this reason for failure.

2.4.5. Research Gap and Proposed Investigation

By exploring the response of FRP laminates nanomodified with several types and concentrations of CNTs exposed to freeze-thaw conditions, the effect of this harsh environmental phenomenon was investigated, and steps can be made to improve FRP laminates for use in durable and lasting infrastructure. The hypothesis of this study is that as the expansive forces during freezing push the layers of FRP apart and cause failure along laminate planes or matrix cracking, CNTs hold them together, bridging the gaps across cracks and improving bond strengths. With the addition of CNTs to the FRP used to reinforce structures, material deterioration from harsh environmental conditions could be significantly reduced.

2.5. 3D-Printed CFRP Lattice as Internal Reinforcement

2.5.1. Infrastructure Resilience Imperatives and the Case for FRP Composites

As discussed in Chapter 1, much of the U.S. transportation infrastructure is aging and needs more attention (ASCE 2025). Improving resilience requires materials and systems that can resist harsh environments, carry loads efficiently, and reduce long-term maintenance needs, while still fitting within practical construction methods and costs.

One group of materials that can help meet these goals is FRP composites. FRP consists of high-strength fibers, such as glass or carbon fibers, embedded in a polymer matrix. The fibers carry most of the load and provide strength and stiffness, while the matrix holds the fibers together, transfers stresses, and protects them from damage (Bank 2006). FRP systems are lightweight, corrosion-resistant, and have a high strength-to-weight ratio compared with steel. Glass FRP (GFRP) is widely used because it is inexpensive and chemically resistant, but it has a lower modulus of elasticity and poorer fatigue and alkali resistance than carbon FRP (CFRP). CFRP offers higher stiffness and better long-term performance, which makes it an attractive option for resilient infrastructure applications.

2.5.2. FRP Manufacturing Methods and Woven Architectures

There are multiple ways to prepare FRP. However, traditional methods for preparing FRP composites include wet layup, spray layup, and filament winding (Abanilla et al. 2006). New, modern techniques like Pultrusion, Resin Transfer Modeling (RTM), injection molding, and additive manufacturing have also emerged (Davalos et al. 1996). Of particular interest are woven FRP composites due to their applicability in construction and infrastructure strengthening. Woven composites refer to interlacing two sets of fibers at right angles to each other, so that the bond

strength between them will be robust in both orientations due to interlocking, and to provide good drapability for any other complex shapes (Lee et al. 1998).

2.5.3. Thermoplastic Woven/Lattice CFRP for Construction: Geometric Flexibility and Process Sensitivities

Thermoplastic-based woven composites are newly emerging, and the information about their behavior as reinforcement in concrete is underexplored. Thermoplastic-based woven composites present a wide range of applications in the present context, as they possess superior geometrical flexibility compared to thermosetting fiber composites (Pascault and Williams 2013). Also, thermoplastic-based woven composites show different properties when some manufacturing parameters like nozzle speed, layer thickness, and nozzle temperature vary.

2.5.4. Thermoplastic vs. Thermoset FRP

The two unique types of plastic materials used for FRP are thermoplastic and thermosetting plastics (Grigore 2017). Thermosetting plastic, or simply thermosets, contains a cross-linked network, whereas thermoplastics have simple linear or branched linkages. The characteristic that sets them apart is that thermosets cannot be reverted to their original form when heated; in contrast, thermoplastics can. This indicates that thermosets are stronger mechanically but are brittle. So, when used with FRP, thermoset-based FRP composites can work very differently compared to thermoplastic FRP composites in concrete (Xue et al. 2022). However, thermoplastic-based FRP composites have their own set of advantages, such as the ability for re-shaping, recyclability, and environmental friendliness over thermoset ones. It is also applicable where cost is a primary concern; therefore, it is currently manufactured for use in complex structures at a minimal cost (Reis et al. 2020). If behavior is known, thermoplastic-based FRP composites could potentially be

used as a reinforcing element for concrete structural systems with improved mechanical flexibility, greater design feasibility, and a structure having higher geometrical complexities than the scenario compared to a few years back (Schinner et al. 1996).

2.5.5. Research Gap and Proposed Investigation

The scope of the paper is confined to the performance of flexural beams reinforced with 3D printed thermoplastic-based CFRP woven composites in the form of cage and flat lattices, evaluated within three types of concrete: portland cement concrete (PCC), polymer concrete (PolC), and Ultra High-Performance concrete (UHPC). The study encompasses the preparation of these concrete types, each one for its unique properties: PCC as a benchmark for the structural concrete, UHPC for its exceptional strength and durability, and PolC for its rapid curing time and its rapid strength development phenomena. Use of 3D printed thermoplastic-based CFRP woven composite as reinforcement aids the necessary strength and ductility, and the improved durability helps control the crack propagation and enhances bonding with the concrete matrix. Also, comparing the reinforced beams with unreinforced ones can provide the necessary clarification regarding the merits of using thermoplastic CFRP reinforcement. The standardized casting and testing of the beams, along with their flexural strength, load-deflection behavior, and failure modes, provide insights for the practical implications and recommendations for the use of these innovative reinforcement techniques. The data from this study can be vital for upgrading the design, construction, and maintenance of reinforced concrete structures, leading to more sturdy, durable, and efficient infrastructure solutions.

3. CHAPTER 3: Motivation, Objectives, and Goals

3.1. Motivation

3.1.1. Rehabilitation Drivers and Required Outcomes

The state of U.S. civil infrastructure presents a critical national challenge. Decades of service life, coupled with underinvestment in maintenance and rehabilitation, have led to widespread deterioration, reflected in the ASCE's persistent 'C' grade infrastructure rating. The economic consequences of inaction are severe, potentially exceeding $10 trillion in lost GDP and impacting millions of jobs by 2039. This situation necessitates a paradigm shift towards innovative, durable, and cost-effective materials and methods for infrastructure repair and strengthening. Key factors motivating this specific research program include:

3.1.1.1. Corrosion

The electrochemical corrosion of steel reinforcement in RC structures (bridges, buildings) and metallic components (like CMP culverts) remains a primary driver of structural deficiency. It leads to reduced cross-sections, loss of bond, cracking, and ultimately, diminished load-carrying capacity and potential failure, perpetuating a costly cycle of repair and replacement.

3.1.1.2. Chemical Attack

Concrete infrastructure is vulnerable to aggressive chemical environments. Sulfate attack, prevalent in certain soils and groundwater, induces internal expansion and cracking through deleterious chemical reactions with cement hydration products, significantly reducing material strength and durability and compromising the substrate for effective repairs.

3.1.1.3. Freeze-Thaw Cycles

In cold regions, repeated freeze–thaw cycling drives moisture- and temperature-induced distress that accumulates microcracking in concrete and degrades polymer matrices and fiber–matrix interfaces in FRP systems. The result is progressive loss of stiffness, strength, and adhesion that shortens service life even without obvious visible damage. As FRP use in strengthening and repair expands, it is essential to ensure composite systems retain their matrix-dominated properties and interfacial integrity under prolonged cycling, motivating evaluation of material selections and nanomodification strategies that can maintain performance in these environments.

3.2. Limitations and Gaps in Current Rehabilitation Practices:

3.2.1. Combined Flexural and Shear Strengthening of RC Beams using FRPs:

While CFRP is effective for strengthening RC beams, combining different techniques (e.g., Near-Surface Mounted (NSM) bars for flexure and U-wraps for shear/confinement) introduces complex interactions. There is a knowledge gap regarding how these combined systems influence the overall structural response, particularly concerning failure modes. Optimizing these combinations to enhance strength without inducing premature, brittle failure requires a deeper understanding of their synergistic effects and bond behavior.

3.2.2. Polymer Concrete Overlays:

PC offers rapid, durable repairs, but its long-term success hinges on achieving a robust bond with the underlying concrete substrate. This bond is particularly challenged when the substrate is deteriorated, for instance, by sulfate attack. Current methods may not guarantee sufficient bond strength in such compromised conditions. Enhancing the interfacial properties of PC, potentially

through nanomodification, without negatively impacting workability or significantly increasing cost, represents a critical research need.

3.2.3. GFRP Slip-Lining:

Slip-lining with GFRP offers a corrosion-resistant solution for CMP rehabilitation. However, the structural contribution of the system relies heavily on the composite action achieved via the grout filling the annular space. There is insufficient data and a lack of standardized design guidelines quantifying the influence of different grout types (e.g., high-strength polymeric vs. lower-strength cementitious) on the circumferential stiffness and load capacity of the rehabilitated, often corroded, CMP structure.

3.2.4. Freeze–Thaw Durability of FRP Systems

Current rehabilitation guidance emphasizes fiber-dominated properties and short-term performance, offering limited direction on matrix- and interface-dominated behavior of CFRP under prolonged freeze–thaw cycling. Qualification tests rarely require off-axis tensile assessment that is sensitive to hydrothermal damage, and there is no practical specification for nanomodification (e.g., CNT functionalization, dose, and dispersion controls) tied to durability outcomes. As a result, owners lack criteria to select FRP systems that retain stiffness, strength, and strain capacity in cold climates.

3.2.5. 3D-Printed CFRP Lattice as Internal Reinforcement

Design provisions and construction practices are largely written for steel or thermoset FRP bars and fabrics, with no clear framework for thermoplastic CFRP lattice reinforcement used as internal primary reinforcement. Bond and placement stability (floating/tilt), junction quality, and matrix-

specific modeling (PCC vs. UHPC vs. polymer concrete) are not covered, and stress-block assumptions calibrated to PCC can misrepresent capacity and ductility in nontraditional matrices. This leaves uncertainty in predicted vs. observed flexural behavior and in quality assurance requirements during casting.

3.3. Need for Validated Advanced Solutions

The inherent limitations of conventional materials and repair methods necessitate the exploration and validation of advanced composite systems. FRPs (CFRP, GFRP) and advanced polymer systems (nanomodified PC) offer potential advantages in terms of durability, strength-to-weight ratio, and tailored properties. However, their effective implementation requires comprehensive experimental data, a thorough understanding of their behavior under realistic conditions (including deterioration), and the development of reliable design parameters to ensure safe, efficient, and long-lasting infrastructure rehabilitation. This research directly addresses these needs by investigating specific, promising applications of these advanced materials. The interconnected nature of the research presented in this dissertation, addressing distinct yet related challenges in infrastructure rehabilitation through the application of advanced polymer composite materials, is schematically summarized in Figure 1.

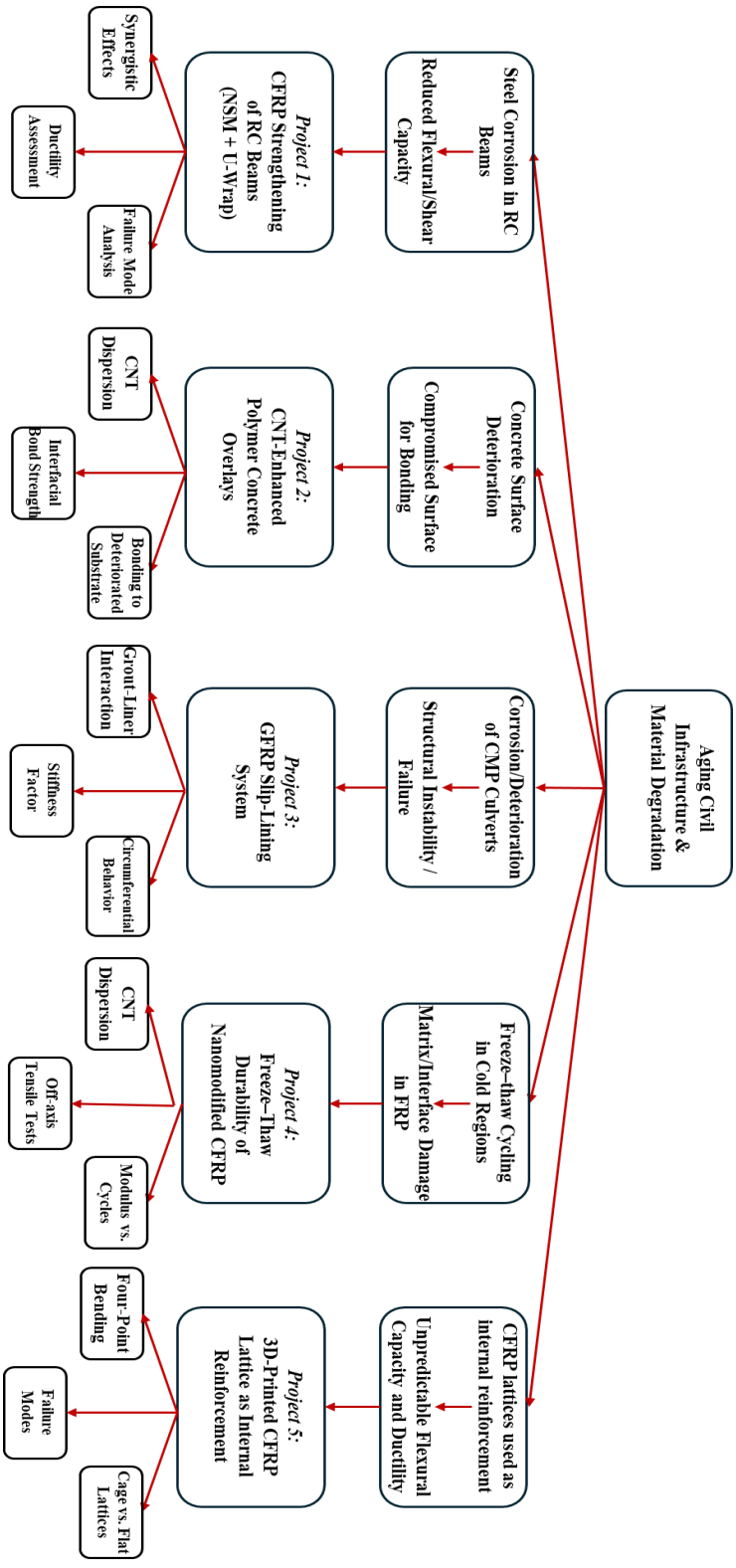

Figure 1: Schematic overview illustrating the integrated research approach

3.4. Goals

The overarching goal of this dissertation is to advance the fundamental understanding and practical application of innovative FRP and polymer-based composite systems for the effective and durable rehabilitation of critical civil infrastructure components susceptible to common degradation mechanisms. This research aims to achieve the following primary goals:

1. Elucidate the synergistic behavior and failure mechanisms of reinforced concrete beams strengthened with combined CFRP systems (NSM bars and U-wraps) to optimize flexural performance and provide data supporting ductile design approaches.

2. Evaluate the efficacy of nanomodification, specifically using functionalized CNTs, in enhancing the interfacial bond strength and performance of PC overlays, particularly when applied to concrete substrates compromised by sulfate attack.

3. Characterize the composite circumferential structural behavior and establish key design parameters (stiffness factor, load capacity) for corroded CMP culverts rehabilitated using GFRP slip liners interfaced with distinct grout systems (polymeric vs. cementitious).

4. Establish freeze–thaw durability benchmarks for CFRP laminates and determine the efficacy of CNT nanomodification (functionalization and dosage) in sustaining or improving off-axis tensile properties and interfacial integrity after prolonged cycling (up to ~250 cycles), yielding material-selection guidance for cold-region applications.

5. Validate 3D-printed thermoplastic CFRP lattices as internal reinforcement by quantifying flexural capacity and displacement/ductility in PCC, UHPC, and polymer concrete beams; examine bond/placement effects and failure modes; and establish practical installation notes and

matrix-appropriate modeling adjustments (e.g., stress-block parameters) to support design and specification.

3.5. Objectives

To achieve the stated goals, the following specific, measurable objectives have been pursued through systematic experimental investigation and analysis:

3.5.1.1. CFRP-Strengthened RC Beams:

Objective 1.1: To experimentally quantify the flexural load capacity, stiffness, and load-displacement characteristics of laboratory-scale RC beams under various strengthening configurations: (a) Control (no strengthening), (b) NSM-CFRP bars only, (c) Full CFRP U-wrap only, (d) NSM-CFRP combined with full U-wrap, and (e) NSM-CFRP combined with partial (shear zone) U-wrap.

Objective 1.2: To instrument beams with strain gauges (on concrete, steel, and CFRP) and meticulously document failure progression through visual inspection and data analysis, identifying the governing failure modes (e.g., concrete crushing, steel yielding, FRP debonding, FRP rupture) for each configuration.

Objective 1.3: To analyze the strain data to assess the influence of U-wrap confinement (full vs. partial) on the stress/strain distribution, the bond performance, and strain development in the NSM-CFRP bars, and the overall ductility of the strengthened system.

Objective 1.4: To synthesize the experimental findings to provide specific recommendations regarding the design implications of combining NSM and U-wrap CFRP strengthening, focusing on predicting performance enhancements and avoiding undesirable brittle failure modes.

3.5.1.2. CNT-Enhanced Polymer Concrete Overlays:

Objective 2.1: To formulate and prepare PC mixes incorporating varying weight percentages (0%, 0.25%, 0.5%) of different MWCNTs – pristine, COOH-functionalized, and NH2-functionalized – relative to the polymer binder, ensuring effective dispersion through magnetic stirring and ultrasonication.

Objective 2.2: To characterize the baseline mechanical properties (compressive strength via ASTM C579, modulus of rupture via ASTM C580) of the neat and MWCNT-modified PC mixes.

Objective 2.3: To prepare PCC substrate specimens cured under two distinct conditions: (a) standard moist curing (healthy substrate) and (b) prolonged immersion in a controlled sulfate solution (deteriorated substrate).

Objective 2.4: To measure and compare the direct pull-off tensile bond strength (per ASTM C1583) between the various PC overlays (neat and MWCNT-modified) and both the healthy and sulfate-exposed PCC substrates.

Objective 2.5: To utilize optical microscopy to analyze the failure surfaces post-testing, assessing the quality of MWCNT dispersion within the PC matrix and identifying the locus of failure (e.g., adhesive failure at interface, cohesive failure within PC or PCC).

Objective 2.6: To investigate potential chemical interaction mechanisms between functionalized MWCNTs and the components of the sulfate-attacked concrete substrate (e.g., ettringite, gypsum) that could explain observed differences in bond strength.

3.5.1.3. GFRP Slip-Lined Culverts:

Objective 3.1: To characterize the key mechanical properties, particularly compressive strength (via ASTM C109/C1107 for cementitious, ASTM C579 for polymeric), of the selected high-strength polymeric grout and lower-strength cementitious grout.

Objective 3.2: To implement a controlled accelerated corrosion procedure on designated CMP sections to achieve a degree of corrosion representative of field conditions.

Objective 3.3: To fabricate composite ring specimens by slip-lining both uncorroded and corroded CMP sections with GFRP pipes and meticulously filling the annular space with either the polymeric or the cementitious grout.

Objective 3.4: To conduct two-point circumferential bending tests on the fabricated composite rings, systematically measuring the applied load versus vertical and horizontal diametrical deformations using load cells and LVDTs integrated with a data acquisition system.

Objective 3.5: To analyze the recorded load-displacement data to determine and compare the peak load capacities and composite ring stiffness factors for all four configurations (uncorroded/corroded x polymeric/cementitious).

Objective 3.6: To evaluate the influence of grout type (polymeric vs. cementitious) and the initial condition of the host CMP (uncorroded vs. corroded) on the overall structural performance, degree of composite action achieved, and observed failure modes of the rehabilitated culvert system.

Objective 3.7: The experimentally determined load capacities and stiffness factors can provide benchmark data for validating predictive models and refining design parameters for GFRP slip-lined culverts.

3.5.1.4. Freeze–Thaw Durability of Nanomodified CFRP (Off-Axis):

Objective 4.1: Fabricate CFRP laminates with neat epoxy (control) and MWCNT modifications (pristine and –COOH at 0.5, 1.0, 1.5 wt% of resin), using heated magnetic stirring and bath ultrasonication to promote dispersion.

Objective 4.2: Expose specimens to immersed freeze–thaw cycling from 0 to 250 cycles with withdrawals at 0/50/100/150/200/250, recording mass change and conditioning history.

Objective 4.3: Measure off-axis tensile properties per ASTM D3039 (strength, modulus, ultimate strain) with video extensometry; construct evolution curves vs. cycle count for each mix.

Objective 4.4: Perform SEM on fracture surfaces to assess dispersion quality, crack-bridging, pull-out, and interfacial failure features, and correlate microstructural observations with mechanical trends.

Objective 4.5: Identify the CNT functionalization/dosage that best sustains or improves off-axis properties after cycling and formulate processing/QC recommendations for cold-region applications

3.5.1.5. 3D-Printed CFRP Lattice as Internal Reinforcement:

Objective 5.1: Manufacture beam specimens (PCC, UHPC, and polymer concrete) reinforced with thermoplastic CFRP lattices in two layouts (cage and flat) plus unreinforced controls, keeping geometry and curing consistent.

Objective 5.2: Conduct four-point bending under displacement control; record load–displacement response and document cracking, failure sequence, and CFRP rupture/crushing interactions.

Objective 5.3: Quantify lattice placement effects (cover, vertical/lateral drift) and evaluate simple fixation methods (chairs/ties) to maintain alignment; relate placement variability to capacity and ductility.

Objective 5.4: Compare observed ultimate moments and displacements with ACI-style FRP flexural predictions; propose matrix-specific modeling adjustments (e.g., stress-block parameters) for UHPC and polymer concrete.

Objective 5.5: Examine lattice junctions via optical/microscopy to identify defects and fiber orientation issues that influence failure, and compile installation/QA notes to support specification and design.

4. CHAPTER 4: Methods, Approach, and Scope of Work

This research employs primarily experimental methodologies across five distinct but related projects focused on advanced materials and techniques for infrastructure rehabilitation. The overarching approach involves laboratory-scale fabrication, standardized material characterization, structural or interfacial testing under controlled conditions, and analysis of performance metrics and failure mechanisms. The scope covers strengthening reinforced concrete beams with CFRP, enhancing polymer concrete overlays with carbon nanotubes for improved bonding, evaluating the circumferential behavior of CMPs rehabilitated using GFRP slip liners, assessing the freeze–thaw durability of CFRP laminates (neat and MWCNT-modified) through off-axis tensile testing with SEM to link matrix/interface response over 0–250 cycles, and investigating thermoplastic CFRP lattices (cage and flat) as internal reinforcement in PCC, UHPC, and polymer concrete beams using four-point bending with placement/QA controls and comparisons to ACI-style flexural predictions. While distinct, these projects share common themes of utilizing advanced composite materials, understanding material/structural interactions at critical interfaces (FRP–concrete, PC–concrete, Grout–Liner–Host Pipe), and addressing infrastructure deterioration caused by factors like corrosion, chemical attack, and cyclic environmental exposure.

4.1. Project 1: CFRP Strengthening of RC Beams using NSM and U-Wraps

4.1.1. Scope of Work:

This project experimentally investigates the flexural behavior and failure modes of reinforced concrete beams strengthened using NSM-CFRP bars combined with CFRP U-wraps. The scope includes fabricating control and strengthened beam specimens, applying different strengthening configurations, conducting four-point bending tests, and analyzing the structural response.

4.1.2. Tasks Grouped by Method:

4.1.2.1. Specimen Fabrication and Strengthening:

Task 1: Cast 20 laboratory-scale RC beams (152.4 mm square cross-section) with identical internal steel reinforcement (4x No. 3 bars, No. 3 stirrups @ 76 mm) according to standard concrete practices.

Task 2: Divide beams into five groups (4 beams each): Control (C), U-wrap only (U), NSM only (N), NSM + full U-wrap (NU), and NSM + shear zone U-wrap (NSU)

Task 3: For N, NU, and NSU groups, prepare grooves (25.4 mm x 25.4 mm) on the tension face during casting using removable plastic forms. Prepare groove surfaces (grinding, cleaning) and install No. 3 NSM-CFRP bars using specialized epoxy gel according to manufacturer specifications and best practices

Task 4: For U, NU, NSU groups, prepare concrete surfaces (grinding to ICRI profile, cleaning, priming). Apply unidirectional CFRP fabric using a wet layup technique with epoxy resin, ensuring proper saturation and compaction. Apply full-span U-wraps for U and NU groups, and shear-zone-only U-wraps for NSU group. Allow adequate curing time for epoxy systems.

4.1.2.2. Material Characterization:

Task 5: Determine concrete properties (compressive strength via ASTM C39, split tensile strength via ASTM C496, elastic modulus via ASTM C469) using standard cylinder tests. Obtain manufacturer data for CFRP bars, fabric, and epoxy resins.

4.1.2.3. Structural Testing and Data Acquisition:

Task 6: Instrument beams with electrical resistance strain gauges at key locations (concrete compression surface, compression steel, tension steel, NSM-CFRP bar surface) using meticulous surface preparation and attachment procedures.

Task 7: Conduct static four-point bending tests on all beam specimens until failure using an MTS testing machine under displacement control.

Task 8: Utilize a data acquisition system (DAQ) to continuously record applied load (from load cell), machine displacement, and strain gauge readings throughout the test.

4.1.2.4. Analysis and Reporting:

Task 9: Process recorded data to generate load-displacement curves and strain distribution diagrams for each beam configuration.

Task 10: Determine peak load capacities and corresponding deflections for each group; perform comparative analysis to quantify the strengthening effectiveness of each configuration relative to the control

Task 11: Visually inspect and document the failure modes for each specimen (e.g., concrete crushing, NSM debonding, epoxy cover splitting, CFRP rupture). Correlate failure modes with strengthening configuration and load-deformation behavior.

Task 12: Analyze strain gauge data to understand stress distribution, steel yielding, and CFRP strain levels achieved at different load stages and failure. Assess the degree of composite action and the efficiency of the strengthening systems.

4.1.3. End Products:

This effort will produce: (1) Quantitative data comparing the flexural load capacity, stiffness, and deformation behavior of RC beams strengthened with NSM-CFRP only, U-wrap only, and combined NSM + U-wrap systems (full and partial). (2) Detailed analysis and documentation of the governing failure modes for each strengthening configuration, highlighting the shift from debonding (NSM-only) to rupture/splitting (combined). (3) Assessment of strain distributions and material utilization. (4) Recommendations regarding the design implications of using combined NSM and U-wrap strengthening, particularly concerning the observed trade-off between enhanced capacity and potentially reduced ductility/warning before failure.

4.2. Project 2: Nanomodification of Polymer Concrete for Enhanced Bonding

4.2.1. Scope of Work:

This project experimentally investigates the effect of incorporating MWCNTs, both pristine and functionalized, on the bond strength of a PC overlay system applied to both healthy and sulfate-deteriorated PCC substrates. The scope includes preparing nano-modified PC mixtures, characterizing PC properties, preparing substrates, conducting pull-off bond tests, and performing microscopic analysis.

4.2.2. Tasks Grouped by Method:

4.2.2.1. Material Preparation and Characterization:

Task 1: Prepare PCC substrate specimens (20 cm x 20 cm x 9 cm) using a standard mix design. Cure specimens under standard conditions

Task 2: Subject a subset of PCC specimens to accelerated sulfate exposure (6% Na_2SO_4 solution, pH 3, for 210 days) to induce controlled surface deterioration. Monitor visual signs of deterioration.

Task 3: Prepare the PC system using a commercial MMA-based binder (Transpo T-17)

Task 4: Prepare nano-modified PC binders by dispersing pristine MWCNTs, COOH-functionalized MWCNTs, and NH_2-functionalized MWCNTs at concentrations of 0.25 wt.% and 0.5 wt.% (by binder weight) into the MMA resin. Utilize a combination of magnetic stirring (800 rpm, 110°C oil bath, 2 hrs) and ultrasonication (60°C water bath, 2 hrs) for dispersion.

Task 5: Prepare PC mixtures (Neat, PC-P25, PC-P50, PC-FC25, PC-FC50, PC-FN25, PC-FN50) by combining the prepared binders with the PC powder component using a high-shear mixer.

Task 6: Characterize baseline mechanical properties of the neat PC and PCC: compressive strength (ASTM C39/C579) and modulus of rupture (ASTM C78/C580).

4.2.2.2. Bond Strength Testing:

Task 7: Prepare surfaces of both healthy and sulfate-exposed PCC substrates according to ICRI guidelines for PC overlays

Task 8: Apply the different PC formulations (neat and nano-modified) as overlays (approx. 2 cm thick) onto the prepared substrates and cure under ambient conditions

Task 9: Perform direct pull-off tensile strength tests according to ASTM C1583. Drill 50 mm diameter cores through the overlay into the substrate. Bond metal loading fixtures to the core surface. Apply tensile load using a calibrated device (Hydrajaws 2000) until failure. Record failure load and meticulously document the failure mode (substrate, interface, overlay, or adhesive)

4.2.2.3. Microscopic Analysis:

Task 10: Utilize optical microscopy (Keyence VHX-7000) to examine the fracture surfaces after pull-off testing, assessing failure location and morphology

Task 11: Use microscopy to qualitatively assess the dispersion state of MWCNTs within the hardened PC matrix samples

4.2.2.4. Analysis and Reporting:

Task 12: Calculate pull-off strength values based on failure load and core area. Statistically analyze bond strength results, comparing different CNT types, concentrations, and substrate conditions (healthy vs. sulfate-exposed). Apply data filtering criteria (e.g., minimum strength threshold, interface failure focus) as appropriate.

Task 13: Correlate bond strength performance and failure modes with CNT type (pristine vs. functionalized), concentration, and substrate condition.

Task 14: Interpret microscopic observations regarding CNT dispersion and failure surface morphology to provide mechanistic insights. Discuss the potential role of chemical interactions between functionalized CNTs and deteriorated substrate components

4.2.3. End Products:

This research will yield: (1) Baseline mechanical properties of the specific PC and PCC used. (2) Quantitative pull-off bond strength data comparing neat PC and various MWCNT-modified PC overlays on both healthy and sulfate-deteriorated concrete substrates. (3) Analysis of failure modes and locations, identifying the influence of CNTs and substrate condition. (4) Microscopic evidence regarding CNT dispersion and interfacial behavior. (5) Assessment of the effectiveness of

MWCNT functionalization (COOH, NH_2) versus pristine MWCNTs for enhancing bond strength, particularly to compromised concrete surfaces. (6) Insights into potential chemical bonding mechanisms between functionalized CNTs and sulfate attack products.

4.3. Project 3: Role of Grout and GFRP Slip Liner on Circumferential Behavior of Retrofitted Corroded Metal Culverts

4.3.1. Scope of Work:

This project experimentally investigates the circumferential structural behavior of Corrugated Metal Pipes, both uncorroded and corroded, rehabilitated using Glass Fiber-Reinforced Polymer GFRP slip liners with two different grout types (cementitious vs. polymeric). The scope includes inducing accelerated corrosion, fabricating composite pipe specimens, conducting circumferential two-point bending tests, and analyzing load-deformation data to determine load capacities and stiffness factors.

4.3.2. Tasks Grouped by Method:

4.3.2.1. Material Procurement and Preparation:

Task 1: Procure 36-inch diameter CMP sections and 28-inch diameter GFRP pipe sections; cut into 12-inch lengths. Procure cementitious (Euclid Hi-Flow) and polymeric (Euclid E3-Flowable) grout materials.

Task 2: For designated CMP specimens, mechanically remove galvanized coating and induce accelerated corrosion over three months via controlled exposure to air/moisture with daily rotation.

4.3.2.2. Grout Characterization:

Task 3: Prepare grout mixtures according to manufacturer's specifications for flowable consistency.

Task 4: Cast 2-inch cube specimens of each grout type and determine compressive strength according to relevant ASTM standards (modified C109 for cementitious, C579 for polymeric)

4.3.2.3. Specimen Fabrication:

Task 5: Fabricate four composite ring specimens: Uncorroded CMP + Cementitious Grout + GFRP; Corroded CMP + Cementitious Grout + GFRP; Uncorroded CMP + Polymeric Grout + GFRP; Corroded CMP + Polymeric Grout + GFRP.

Task 6: Assemble specimens by carefully centering the GFRP liner within the CMP section on a prepared base plate, using wooden spacers to maintain a uniform annular gap, and sealing the base perimeters with silicone.

Task 7: Cast the appropriate grout (cementitious or polymeric) into the annular space, ensuring complete fill.

Task 8: Cure specimens appropriately (moist cure for cementitious grout for 72 hrs.; ambient cure for polymeric)

4.3.2.4. Structural Testing and Data Acquisition:

Task 9: Prepare specimens for testing by applying high-strength gypsum cement (Hydrostone) to the top and bottom corrugations to ensure uniform load application.

Task 10: Instrument specimens with LVDTs positioned to measure vertical diametrical deflection (at crown) and horizontal diametrical change (at mid-height).

Task 11: Conduct circumferential two-point bending tests using a hydraulic jack and load cell, applying load incrementally until failure or significant deformation.

Task 12: Utilize a DAQ system to continuously record applied load and LVDT displacements.

4.3.2.5. Analysis and Reporting:

Task 13: Process load-displacement data for each specimen, plotting vertical and horizontal deformation against applied load.

Task 14: Determine the peak load capacity and corresponding displacements for each configuration.

Task 15: Analyze failure modes and deformation patterns, comparing behavior between grout types and corrosion states. Assess evidence of composite action or debonding.

Task 16: Calculate the circumferential stiffness factor for each specimen.

Task 17: Perform comparative analysis of load capacities and stiffness factors to quantify the influence of grout type and host pipe corrosion on the retrofitted system's circumferential performance.

4.3.3. End Products:

This project will deliver: (1) Compressive strength data for the cementitious and polymeric grouts used. (2) Experimental load vs. diametrical deformation curves characterizing the circumferential behavior of GFRP slip-lined CMPs under different conditions. (3) Quantitative values for peak

load capacity and circumferential stiffness factors for uncorroded and corroded CMPs retrofitted with GFRP liners using both cementitious and polymeric grouts. (4) A comparative assessment highlighting the structural performance differences imparted by grout type and the impact of host pipe corrosion.

4.4. Project 4: Freeze–Thaw Durability of Nanomodified CFRP (Off-Axis Tensile)

4.4.1. Scope of Work:

Establish freeze–thaw durability benchmarks for CFRP laminates by comparing neat epoxy against MWCNT-modified matrices (pristine and –COOH functionalized at 0.5, 1.0, 1.5 wt.% of resin). Specimens are conditioned under immersed freeze–thaw cycling up to 250 cycles with withdrawals at 0, 50, 100, 150, 200, and 250. Off-axis tensile properties (strength, modulus, ultimate strain) are measured per ASTM D3039 using video extensometry, and fracture surfaces are examined via SEM to relate dispersion/interface features to mechanical trends. The outcome is a material-selection and processing recommendation set for cold-region applications.

4.4.2. Tasks Grouped by Method:

4.4.2.1. Materials and Dispersion

Task 1: Prepare seven laminate types: neat, and MWCNT-modified (pristine and –COOH at 0.5, 1.0, 1.5 wt.%). Disperse nanotubes in low-viscosity epoxy via ultrasonic bath (40 kHz, 40 °C) and heated magnetic stirring (≈80 °C, ≈800 rpm), with short degassing prior to sonication; allow resin to cool to ~30 °C before adding hardener.

4.4.2.2. Laminate Fabrication using Vacuum-Assisted Hand Lay-up Technique (VAHT)

Task 2: Cast CFRP plates using vacuum-assisted hand lay-up per ASTM D5687 on a 61 cm × 61 cm base, producing 50.8 cm × 50.8 cm laminates; employ the listed layup stack (release films, breather, peel ply, biaxial textile), vacuum assist to control resin content, and room-temperature cure sequence as previously documented.

4.4.2.3. Specimen Preparation & Conditioning

Task 3: Cut off-axis tensile coupons; condition in water-immersed freeze–thaw chamber with freeze at ~0 °C and thaw at ~40 °C; withdraw at 50-cycle intervals up to 250 cycles; dry at room temperature prior to testing.

4.4.2.4. Mechanical Testing and Data Collection

Task 4: Conduct ASTM D3039 tests on an Instron 5967 with AVE-2 video extensometer; use standard coupon geometry and tabbing procedure; compute ultimate tensile strength using the standard relation and construct property-evolution curves vs. cycle count.

4.4.2.5. Microscopy and Interpretation

Task 5: Perform SEM on fracture surfaces to assess CNT dispersion, crack bridging, pull-out, and interfacial failure features; correlate microstructural observations with measured off-axis performance.

4.4.3. End Products:

This work will produce a curated database of off-axis tensile strength, modulus, and ultimate strain versus freeze–thaw cycle count (0–250) for neat epoxy, pristine MWCNT, and –COOH MWCNT matrices, organized for direct use in figures and tables. A companion SEM atlas will document dispersion quality, crack-bridging, pull-out, and interfacial failure features to support interpretation of the mechanical trends. The project will also provide a concise set of processing and QC recommendations (functionalization, dosage, and two-stage dispersion) for cold-region applications

4.5. Project 5: 3D-Printed CFRP Lattice as Internal Reinforcement

4.5.1. Scope of Work:

Validate thermoplastic CFRP lattices (WEAV3D) as internal reinforcement in PCC, UHPC, and polymer concrete beams, using two layouts (cage and flat) and unreinforced controls. Execute four-point bending under displacement control, document load–displacement behavior, cracking, and CFRP rupture/crushing, quantify placement effects (cover, floating/tilt) and simple fixation (chairs/ties), compare observed ultimate moments/displacements with ACI FRP flexural predictions, and examine lattice junctions via microscopy to identify defects and fiber-orientation issues.

4.5.2. Tasks Grouped by Method:

4.5.2.1. Materials & Documentation

Task 1: Record WEAV3D CFRP tape properties (e.g., PETG-C ~0.21 mm thickness, ~22 mm width, ~1450 MPa tensile resistance, ~101 GPa modulus; mesh ~200×100 mm) and compile material data sheets.

4.5.2.2. Concrete Mix

Task 2: Produce PCC, UHPC, and polymer concrete per documented mix designs and procedures (rotating drum for PCC; high-shear mixing for UHPC per prior protocol; manufacturer-guided rapid-set for polymer concrete); archive mix proportions.

4.5.2.3. Beam Fabrication and Reinforcement Placement

Task 3: Cast beams with cage/flat lattice placement; control cover and mitigate vertical/lateral drift (floating/tilt) using simple fixation.

4.5.2.4. Mechanical Characterization and Testing

Task 4: Conduct four-point bending under displacement control; record load-displacement response and failure mode; identify CFRP rupture/crushing interactions and crack evolution.

4.5.2.5. Microscopy and Analytical Comparisons

Task 5: Examine lattice junctions (optical/microscopy) for defects and fiber-orientation issues; compare ultimate moments/displacements with ACI predictions and note matrix-specific stress-block adjustments for UHPC and polymer concrete.

4.5.3. End Products:

This work will provide a load-displacement database for PCC, UHPC, and polymer concrete beams (control, cage lattice, and flat lattice), annotated with placement sensitivities (cover, vertical/lateral drift) and junction observations to support repeatable fabrication. It will also deliver practical installation and notes (fixation, cover control, junction quality) and a set of matrix-appropriate modeling adjustments (including stress-block considerations) suitable for design and specification

5. CHAPTER 5: An Experimental Study Incorporating Carbon Fiber Composite Bars and Wraps for Concrete Performance and Failure Insight

5.1. Literature Review

5.1.1. Overview

The rehabilitation and strengthening of existing reinforced concrete (RC) structures have become increasingly vital in civil infrastructure management. Reinforced and prestressed concrete infrastructure built in the 60s and 70s is now experiencing severe deterioration, and action is needed to ensure the structural performance is adequate for the demands imposed. Bridges built between 1955 and 1975 are now past their nominal 50-year design life. Corrosion of conventional steel reinforcement is a primary driver of this deterioration and is responsible for numerous structurally deficient bridges, a multi-billion-dollar challenge creating a cycle of maintenance, repair, and replacement. Corrosion undermines structural integrity by degrading the reinforcing steel's physical and mechanical characteristics (e.g., diminishing its cross-sectional area), weakening the crucial bond between steel and concrete, and inducing concrete cover cracking due to expanding rust products (Rodrigues et al. 2021).

For instance, analysis of the 2023 FHWA National Bridge Inventory reveals that 58% of bridges built between 1955 and 1975 now require major rehabilitation or load posting, primarily because corrosion has reduced reinforcing steel cross-sections and induced concrete cover cracking. This deterioration presents a high risk for future closures or weight restrictions and requires substantial

investment. Furthermore, a recent life-cycle assessment demonstrated that failing to intervene early can raise total agency costs by approximately 12% over a 75-year horizon (Lee et al. 2025).

While conventional methods exist to mitigate corrosion (e.g., cathodic protection, inhibitors, coatings, stainless steel rebar (Yan et al. 2016)) or repair compromised structures (e.g., section enlargement, external post-tensioning, epoxy injection, externally bonded steel plates (Al-Mahaidi and Kalfat 2018), these can have limitations in terms of cost, durability, or installation disruption. Therefore, cost-effective and durable repair and strengthening techniques are essential to extend the service lives of structures like bridges safely and efficiently, especially to accommodate rising traffic volumes and comply with contemporary design standards (Sharaky et al. 2018; Wang et al. 2021). Given these challenges, advanced materials like Fiber-Reinforced Polymers (FRPs) have emerged as a promising alternative for structural strengthening, the background and properties of which are discussed next.

5.1.2. Fiber-Reinforced Polymers (FRP) – historical background

The emergence of FRP composites dates back to the 1930s, when Owens Glass Company, having partnered with the Corning company, manufactured the initial patented version of fiberglass (Marsh 2006). Following this, the FRP sector achieved substantial development during World War II, a growth trend that carried on for the subsequent two decades, with implementations mainly found in the aerospace and military sectors (Lubin 1982). Recognizing the potential demonstrated in demanding aerospace applications (Van Den Einde et al. 2003), significant research has since explored FRP composites for the structural engineering field. FRPs have become a major focus for the engineering community, leading to widespread adoption by the construction industry for the repair and strengthening of infrastructure (Vedernikov et al. 2021). Their use spans diverse

geographic regions and climates, highlighting their versatility (Bakis et al. 2003). Economically, while initial material costs can be higher than traditional materials, FRPs offer potential long-term benefits through reduced maintenance needs and extended service life, contributing to their cost-effectiveness in many scenarios (Bakis et al. 2003).

For concrete structures, these FRP applications generally fall into two classifications: internal applications using components like tendons, bars, or rods, and external applications that employ plates, fabrics, or wraps. Typically, internal applications relate to new construction projects (like concrete structures reinforced or prestressed with FRP), whereas external techniques are connected with the rehabilitation, upgrading, and mending of already existing structures, which are usually steel-reinforced concrete, though FRP-reinforced concrete structures themselves might require future strengthening (Ortiz et al. 2023). FRP composites fundamentally consist of reinforcing fibers embedded within a polymer matrix. Understanding the properties of these constituents is key to selecting and designing effective strengthening systems.

5.1.2.1. Reinforcing Fibers: The Load-Bearing Element

Fibers act as the primary load-bearing constituent in FRP composites, necessitating properties like considerable strength, significant stiffness (high elastic modulus), and adequate elongation before fracture. They also need suitable durability for the specific environmental conditions where the structure will be utilized. A fiber's effectiveness is influenced by its length, chemical structure, and cross-sectional geometry, with fibers being available in multiple shapes and sizes. Depending on the specific fiber, diameters typically range from 5 to 25 microns (Budelmann and Rostasy 1993). Carbon, Glass, and Aramid represent the most frequent fiber types for FRPs, yielding the

corresponding composite materials commonly known as CFRP, GFRP, and AFRP. Understanding their distinct properties is crucial for material selection:

4. **Carbon Fibers:** Carbon fibers possess desirable qualities such as significant stiffness (elastic modulus between 200-800 GPa), advantageous ratios of strength and stiffness relative to weight, minimal susceptibility to fatigue damage, and exceptional durability against moisture and chemical exposure. However, their limited ultimate strain results in lower resistance to impacts and limited ductility. Carbon fibers also feature high thermal and electrical conductivity, which presents either an asset or a liability depending on the specific design context. According to (Malik and Foster 2010), these fibers are classified into four categories using their elastic modulus: low modulus (230-250 GPa), intermediate modulus (290-300 GPa), high modulus (350-380 GPa), and ultrahigh modulus types (480-760 GPa). Typically, the low-modulus carbon fibers exhibit lower density, reduced cost, greater strength in tension and compression, and higher ultimate tensile strain compared to their high-modulus counterparts.
5. **Glass Fibers:** As the most widely utilized reinforcement type within FRP composites, glass fibers offer affordability combined with high tensile strength and excellent insulation characteristics. Their disadvantages include limited stiffness (low tensile modulus), high density, and vulnerability to abrasion damage and alkaline conditions; they also exhibit comparatively weaker performance when exposed to moisture, sustained loading (creep), or cyclic stresses (fatigue). Glass fibers are generally classified into three varieties: C-glass, S-glass, and E-glass. C-glass is noted for its high chemical durability, making it suitable for diverse applications. E-glass represents a low-cost, versatile fiber providing good strength, electrical resistivity, and acid resistance. While S-glass fibers deliver superior

strength, stiffness, and ultimate elongation compared to E-glass, they carry a higher price tag and show greater susceptibility to degradation from environmental factors.

6. **Aramid Fibers:** Aramid, a contraction of aromatic polyamide, originates from para-type fibers characterized by straight-chain benzene structures. These fibers exhibit a highly crystalline nature, resulting in significant strength along the fiber's length but comparatively reduced bond strength transversely. Three specific Kevlar® aramid fiber types are employed in FRP fabrication—Kevlar 149, Kevlar 49, and Kevlar 29—possessing elastic moduli of 179 GPa, 131 GPa, and 82 GPa, respectively. Key advantages of aramid fibers include outstanding impact toughness, considerable stiffness, high thermal stability, and lower density relative to other fibers. Conversely, aramids are susceptible to degradation from ultraviolet light, and exposure to moisture can induce creep. In terms of cost, aramid fibers are priced higher than glass fibers but lower than carbon fibers (Ishtiaq et al. 2024; Jambhulkar and Sahu 2024; Nanni 1993).

5.1.2.2. Polymer Matrix (Resins): The Binding Agent

The polymer matrix, or resin, plays several critical roles within the composite: it encases the fibers to shield them from physical abrasion, enables the transfer of shear stresses both between layers (inter-laminar) and within a layer (in-plane), and provides lateral bracing to fibers resisting buckling under compressive forces. Resins are typically rigid or semi-rigid polymers at room temperature. Additionally, the resin's own physical and thermal characteristics substantially impact the final mechanical performance achieved by the composite product. Thermosetting and thermoplastic materials represent the two principal polymer types employed in FRP composites.

3. **Thermosetting Resins:** These are more commonly used in structural FRPs. They begin as low-viscosity liquids composed of small molecules. Upon curing, these molecules chemically cross-link to establish a rigid three-dimensional network; this transformation is permanent, meaning the material cannot be subsequently reformed using heat or pressure. Common examples utilized in composites include polyesters, vinyl esters, and epoxies. Generally, these thermosets demonstrate good resistance to heat and chemicals, along with minimal creep and stress relaxation tendencies. Their primary disadvantages typically include limited strain capacity before failure (brittleness), constrained storage durations prior to use (shelf life), and relatively lengthy manufacturing cycles (Bank 2006).
4. **Thermoplastic Resins:** Polymers used in thermoplastic matrices are composed of molecules arranged in linear chains. These chains are connected by comparatively weak secondary forces (intermolecular bonds), which thermal energy or pressure can disrupt. Consequently, the material softens or melts upon heating and resolidifies when cooled. This behavior allows thermoplastic polymers to be repeatedly softened and reshaped through heating, though doing so might diminish their mechanical performance over time. Their use in externally bonded structural strengthening is less common than thermosets (Bank 2006).

Following the examination of constituent materials, the discussion proceeds to the practical applications and principal properties of the FRP systems most widely employed for structural strengthening.

5.1.3. FRPs in Construction: Properties and Applications

Building on the properties of these constituent materials, specific FRP composites, particularly carbon-fiber-reinforced polymers (CFRP) and glass-fiber-reinforced polymers (GFRP), have found significant application in construction strengthening due to their advantageous characteristics (M. A. Kadhim et al. 2023; Sokairge et al. 2022).

Material Comparison (CFRP vs. GFRP): CFRP and GFRP differ significantly in mechanical properties. CFRP typically exhibits tensile strengths of 3.5–6 GPa and an elastic modulus of 230–250 GPa (for standard modulus fibers), while GFRP offers tensile strengths of 1.5–2.5 GPa and an elastic modulus of 70–90 GPa (Kabashi et al. 2020). This approximately three-fold stiffness advantage means CFRP is highly effective in controlling deflections; for instance, in flexure-critical members, a CFRP retrofit can potentially halve the mid-span deflection compared to an equivalent GFRP retrofit (Qureshi and Sheikh 2023). CFRP's superior tensile strength and stiffness make it particularly effective for enhancing the shear and flexural capacity of RC beams (Zhang et al. 2017).

Material Comparison (CFRP vs. Steel): Compared to traditional steel reinforcement, CFRP exhibits a significantly higher tensile strength-to-weight ratio, potentially offering several times the strength for the same weight. This lighter weight facilitates handling and installation and reduces the dead load added to the structure. Although CFRP's initial material costs are typically higher than steel, its excellent corrosion resistance eliminates a primary deterioration mechanism seen in steel-RC structures, leading to reduced long-term maintenance and potentially lower life-cycle costs, making it a valuable alternative depending on project needs (Bakis et al. 2003).

Corrosion Resistance: FRP's inherent resistance to electrochemical corrosion is a major advantage, significantly contributing to enhanced durability, especially in aggressive environments (Tharmarajah et al. 2015). This property is critical for prolonging the life of structures affected by steel corrosion, making FRP invaluable in rehabilitating aging infrastructure (Liu et al. 2018).

Limitations: A key limitation, particularly for building applications, is the vulnerability of the polymer matrix (especially epoxy) to degradation at elevated temperatures, potentially reducing the effectiveness of FRP strengthening in fire scenarios unless appropriate fire protection measures are implemented.

5.1.4. Flexural Strengthening of RC Beams using the Near-Surface-Mounted (NSM) Method

In the flexural strengthening of RC beams with the usage of FRP, two approaches are suggested by the American Concrete Institute (ACI) 440-2R: near-surface-mounted (NSM) FRP and externally bonded (EB) FRP (Nanni, A., Alkhrdaji, T., Chen, G., Barker, M., Xinbao, Y., and Mayo 1999; Toufigh et al. 2013). EB-FRP involves attaching an FRP laminate to the beam's tension side using epoxy, allowing the laminate to serve as extra reinforcement and boost the beam's flexural strength (Saadatmanesh and Ehsani 1990). NSM-FRP entails creating a groove on the beam's tension side, partially filling it with epoxy, inserting an FRP bar or strips, and then completely sealing it with epoxy (Nanni, A., Alkhrdaji, T., Chen, G., Barker, M., Xinbao, Y., and Mayo 1999). The primary benefit of the NSM-FRP method is its bonding efficiency with the concrete (De Lorenzis and Teng 2007).

For NSM flexural strengthening, CFRP is often preferred over GFRP due to its superior axial stiffness and tensile strength (Van Cao and Pham 2019). The high stiffness allows CFRP to

effectively contribute to the beam's capacity at small strains, and its high strength provides significant reinforcement potential. This efficiency can also allow for optimization of groove sizes (Zhang et al. 2013). Common failure modes observed in tests of NSM-FRP strengthened beams include concrete crushing, yielding of internal steel reinforcement followed by FRP rupture or debonding, or premature debonding of the NSM FRP element (Aljidda et al. 2023; ChennaReddy 2016; M. A. Kadhim et al. 2023). Debonding failure often initiates near cracks or at the end of the NSM strip/bar, potentially due to high interfacial stress concentrations, and is frequently the governing failure mode, especially if the FRP is not sufficiently anchored. Research suggests that with adequate anchorage length, FRP rupture might be less common, as the FRP may only reach 60–70% of its ultimate tensile capacity before other failure modes occur (Hassan and Rizkalla 2003).

5.1.5. Shear Strengthening of RC Beams using the FRP U-Wrap Method

RC beams requiring flexural strengthening (e.g., with NSM FRP) often also need shear strengthening to accommodate increased loads or address existing shear deficiencies. Externally bonded FRP wraps are commonly used for this purpose. The U-wrapping method (wrapping the sides and bottom soffit of the beam) using a wet layup process is frequent. This involves saturating FRP fabric (often CFRP or GFRP) with epoxy resin and applying it to the prepared concrete surfaces, typically with fibers oriented perpendicular to the beam axis or vertically to effectively resist shear cracks (Chennareddy and Taha 2017). Variations include fully wrapping the section (if possible), three-sided U-wraps, or applying discrete strips on the two sides only (Murad and Abu-AlHaj 2021). Extensive research has examined the effectiveness of different wrapping schemes and configurations (Chajes et al. 1995; Kachlakev and McCurry 2000; Taerwe 2020).

Typical failure modes for FRP shear strengthening include debonding of the FRP (often initiating at corners or free edges) or rupture of the FRP fibers. While epoxy-based FRP systems are common, it is worth noting that alternative systems using inorganic matrices, such as fabric-reinforced cementitious matrix (FRCM) composites, are also being investigated, offering potential advantages like better performance at elevated temperatures (Ombres and Mazzuca 2024).

5.1.6. Research Gap and Proposed Investigation

The preceding review establishes the effectiveness of Near-Surface Mounted (NSM) CFRP bars for flexural strengthening and externally bonded CFRP U-wraps for shear strengthening of RC beams. Previous research indicated that combining these techniques could significantly enhance load capacity compared to using NSM reinforcement alone. However, while the strength benefits were recognized, a detailed understanding of the interaction between the NSM bar and the U-wrap confinement, particularly concerning the resulting failure mechanisms and overall structural behavior, remained less explored. NSM-only strengthened beams often exhibit failure due to debonding of the FRP bar from the concrete substrate before the bar's full tensile capacity is utilized. Adding U-wrap confinement was expected to improve this bond, but the precise manner in which this confinement alters the governing failure mode (from debonding to potentially more brittle modes like bar rupture) and influences the overall ductility of the system required further experimental clarification. Specifically, there was a need to investigate how different U-wrap configurations (e.g., full vs. partial span) interact with NSM bars, observe the resulting failure modes directly, and assess the trade-offs between increased capacity and potential changes in failure abruptness.

This research is aimed at addressing this gap by experimentally investigating the flexural behavior and failure modes of RC beams strengthened with NSM-CFRP bars, CFRP U-wraps, and, critically, combinations of both (full-span U-wrap and shear-span-only U-wrap).

5.2. Materials and Methods

This study utilized 20 RC beams divided into five groups to evaluate the impact of different FRP strengthening systems: control group ('C'), U-wrap group ('U'), NSM group ('N'), NSM and U-wrap group ('NU') and NSM and shear zone U-wrap group ('NSU'). C beams were used to establish a baseline performance. To isolate the effects of U-wrap and NSM, U and NU groups were used. For the combination of NSM and U-wrap, full U-wrap and shear zone U-wrap were considered to obtain two types of confinement effects.

5.2.1. Materials

The concrete employed featured a maximum nominal aggregate size of 12.7 mm, with an observed slump measuring 10 ± 1.2 cm. The slump test was performed using the ASTM C143 (ASTM/C143M-15a 2009). The chosen maximum nominal aggregate size of 12.7 mm improves the concrete mix by enhancing workability, reducing shrinkage, and optimizing mechanical strength. Larger aggregates help achieve a better void ratio, decrease cement paste use, and consequently enhance the structural and economic efficiency of the concrete. To assess the mechanical characteristics of the selected mix design, three distinct experimental tests were conducted. The unconfined compression tests were carried out in accordance with ASTM C39 (ASTM 2001) on samples after 7 and 28 days of curing. Furthermore, for a comparative analysis, the compressive strength of samples subjected to heat curing was evaluated at the age of 7 days. Also, the split tensile strength of specimens was evaluated at the age of 28 days based on ASTM

C496 (ASTM 2022). Moreover, the elastic modulus of the specimens was assessed following the ASTM 469 (ASTM C469/C469M − 14l 2014). At 28 days, the average compressive strength of the concrete was 53.09 MPa with a standard deviation of 1.78 MPa. The split tensile strength recorded was 3.49 MPa with a standard deviation of 0.16 MPa. Additionally, the elastic modulus was determined to be 27,636 MPa. Each test result is the mean value of three tested specimens. Figure 2 shows specimens during each test.



Figure 2: Testing of concrete cylinder for (a) Modulus of Elasticity ASTM C469 (b) Split tensile strength ASTM C496 and (c) compressive strength ASTM C39. 6 cylinders tests per batch of concrete mixed.

No. 3 (10 mm) NSM bars were acquired from the RenewWrap company, as shown in Figure 3. The NSM strengthening systems involved using a specialized 2-part epoxy resin NSM gel, produced by the Milliken Infrastructure Company. The guaranteed tensile strength provided by the manufacturer was 2171.85 MPa, and the tensile modulus of elasticity was 124.11 GPa with 1.75% ultimate strain. The U-wrap strengthening system technique was carried out using a unidirectional CFRP fabric, which was 1 mm thick, applied via a wet-layup method. Both the epoxy and the CFRP fabric used in this method were supplied by Fyfe Chemicals. Specifically, unidirectional carbon fabric with the Tyfo S-330 epoxy was used in this study, as shown in Figure 3(a). After 3

days of curing, the epoxy material properties as listed by the manufacturer had a tensile strength of 72.39 MPa, a tensile modulus of 3178 MPa, elongation of 5% and a minimum adhesion strength to concrete of 2.76 MPa. The composite's gross laminate properties as provided by the manufacturer included an ultimate tensile strength of 965.27 MPa, a tensile modulus of 93.08 GPa, and elongation at break of 1%.



Figure 3: (a) Tyfo unidirectional CFRP fabric (b) No. 3 RenewWrap CFRP bar.

5.2.2. Methods

The beam groups were subjected to a displacement-controlled static four-point bending test (2 loading points and 2 supports) until failure at a rate of 1 mm/min. The test was conducted using an MTS 810 actuator equipped with a 50-kip (222 kN) load cell and a data acquisition system. The load cell captured the resistance from the beams, and the machine displacement was recorded. Failure was defined when the load dropped by more than 30% from the peak load.. The loading points were located 152.4 mm apart and 660.4 mm between supports. In this study, flexural load capacity reported is defined as the maximum load a beam can support before failure when subjected to bending. The beams had a square cross-section, each with a depth of 152.4 mm. The beams were reinforced with four No. 3 (10 mm diameter) steel bars. Within these, two bars were

allocated for compression reinforcement, while the remaining two were used for tension reinforcement. The top cover was maintained at 29.5 mm and the bottom cover at 25.4 mm. This configuration was integral to the structural setup of each beam. For shear reinforcement, No. 3 stirrups, also 10 mm in nominal diameter, were spaced at intervals of 76 mm. After the concrete beams were cast, they were placed in heat curing for 7 days. Figure 4 and Figure 5 show the schematic view and the cross section of the beams.

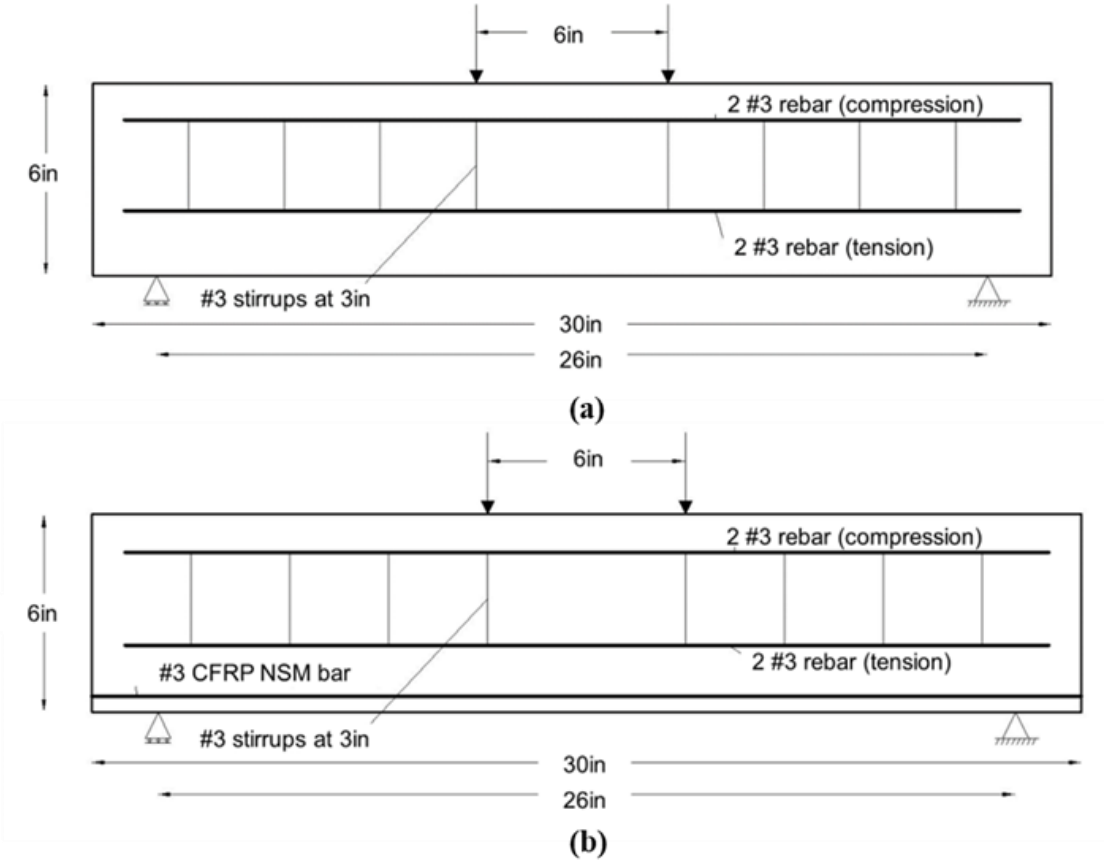

Figure 4: (a) Schematic of RC beam dimensions (b) NSM bar included for types N, NU and NSU not included for C and U types.

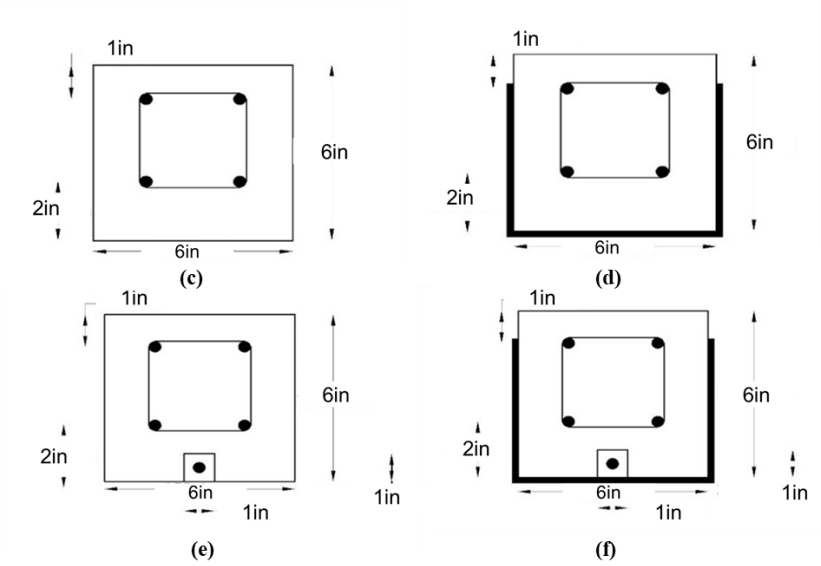

Figure 5: Cross section of RC beams for (c) C (d) U (e) N and (f) NU and NSU. Groove for NSM and U-Wrap dimensions indicated.

To facilitate strain readings, strain gauges were installed at midspan at four locations: on the concrete compression surface, on one of the top compression steel bars, on one of the bottom tension steel bars, and on the surface of the CFRP NSM bar. To ensure the strain gauges were well attached, steps were adopted sequentially (1). Surface preparation: Initially, the surface underwent grinding using various grinders, selected based on the material. Subsequently, the surface was thoroughly cleaned, rendering it prepared for the subsequent steps. (2). Surface cleaning: to eliminate any dust and oily residues from the specimens' surfaces, a combination of three cleaning agents—acetone, a water-based acidic surface cleaner, and a water-based alkaline surface cleaner—was employed. (3). Strain gauge attachment: following the meticulous cleaning and preparation of the material surfaces, strain gauges were affixed using either super glue or epoxy. (4). Surface finishing: To safeguard the strain gauges during the concrete casting process and subsequent phases, a protective surface finishing was implemented. Super 88 Scotch tape was applied to shield the wires, Silicone RTV adhesive sealant was utilized to guard against water exposure, and Nashua 367-17 foil mastic sealant was employed for protection against aggregates.

Figure 3 shows the strain gauges attached to different materials. Figure 6 to Figure 9 show different stages in strain gauges attachment.



Figure 6: Materials used for Strain Gauge Application



Figure 7: Beam molds and strain gauges attached steel cages prepared for fabrication

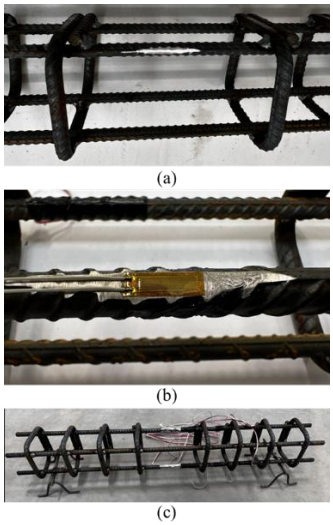

Figure 8: Steel reinforcement cages prepared with strain gauge application (a) Surface grinding (b) Strain gauge adhered to steel (c) Completed strain gauge application on tension and compression surfaces.

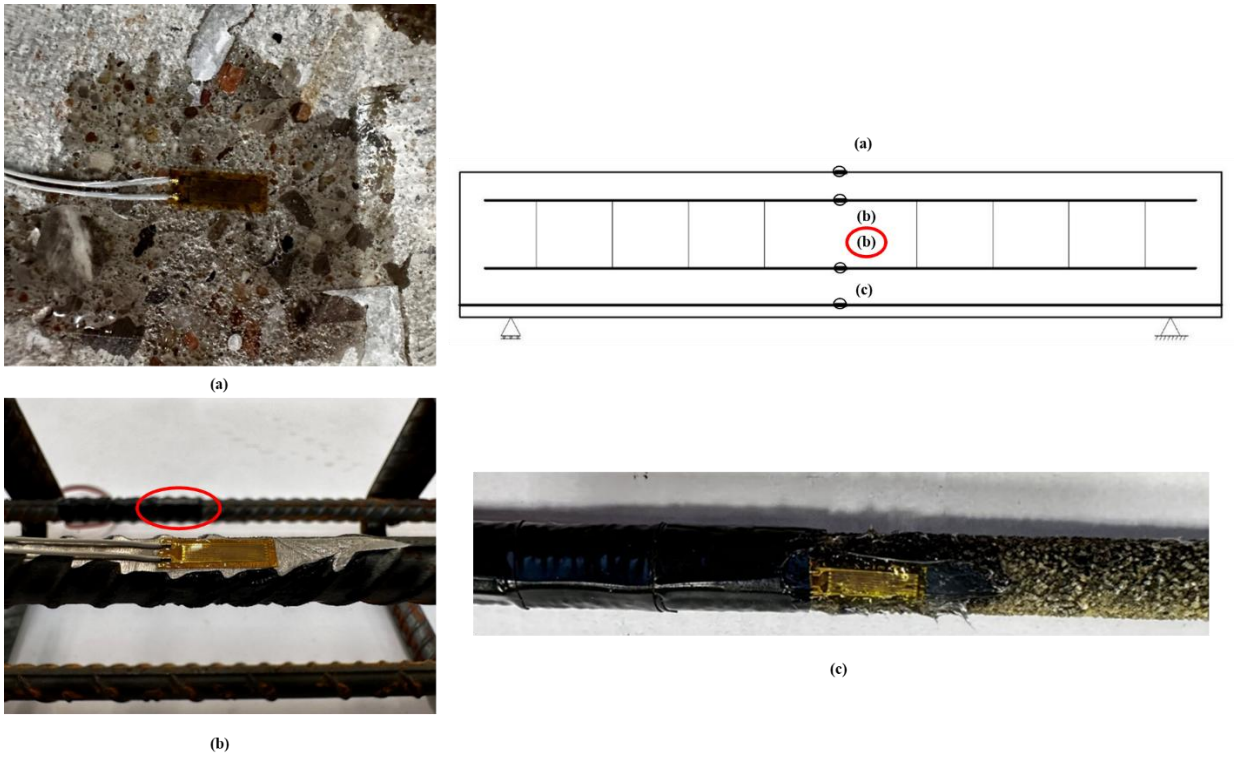

Figure 9: Strain gauge application (a) on concrete compression (b) compression and tension (indicated in red) steel (c) NSM FRP.

5.2.2.1. U-Wrap Shear Strengthening (U Type)

Three side U-wrapping is a technique employed for shear strengthening of concrete beams. Beams U, NU and NSU were strengthened using this CFRP wrapping technique. The concrete surface was prepared to a minimum concrete surface profile as defined by the CFRP fabric manufacturer's guidelines, ACI 440-2R and ICRI surface profile. Abrasive grinding was performed on flat concrete surfaces and for wrapping around edges using a 1.2 cm radius rounded grinder. The prepared surface was cleaned using a water jet and compressed air. The beams were allowed to air dry for twenty-four hours to remove moisture on the surface of the beams. Surface preparation is shown in .

Part A and Part B mixed resin was initially applied as a prime coat on the concrete surface using a soft roller. Mix ratio of Tyfo S-330 according to the manufacturer was 100A:34.5B by weight. For

U and NU beams, the CFRP fabric was cut to specified dimensions: 406 mm along the two sides and the bottom of the beam in the direction of the fibers, and a length of 660 mm opposite to the fiber direction, equal to the length between the two supports for the beam. For the NSU beams, the U-wrap was only applied in the shear area. After cutting the fabric, the CFRP fabric was saturated in epoxy. Saturated fabric was wrapped around the beam and a hard roller was employed to eliminate any trapped air and ensure even layup as illustrated in the figures below. Wrapped beams were allowed to cure for 14 days at room temperature to enable complete hardening of the wrapping and have composite action with the beams. to Figure 13 show the steps of the U-wrapping technique.

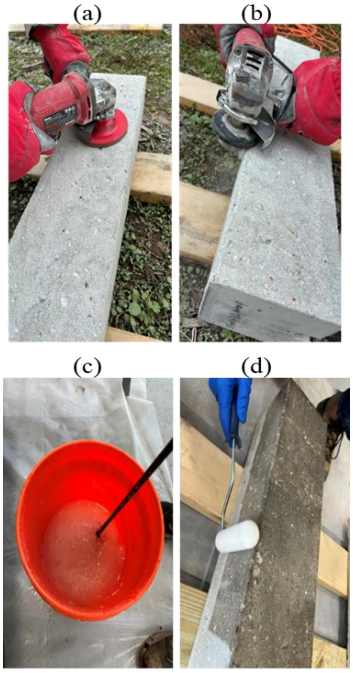

Figure 10: Surface preparation steps for U-wrap to ensure adequate bond. (a) surface grinding, (b) edge grinding, (c) mixing Part A and Part B of epoxy, and (d) applying prime coat on the beam



Figure 11: (a) Carbon fiber fabric wetting process for U-wrap. (b) Rolling wet fabric onto plastic pipe for layup on beam.



Figure 12: Rolling wet fabric onto pre-marked beam covering three sides for U-wrap.



Figure 13: Wet layup process (a) Layup with soft roller, (b) Layup with hard roller, and (c) Finished beam after U-wrap.

5.2.2.2. NSM Flexural Strengthening (N Type)

In the beam series labeled 'N', NU', and 'NSU', which underwent NSM-CFRP flexural reinforcement, each was constructed with an integrated groove on the tension face. To facilitate the creation of the groove on the tension side of the beam, a plastic piece, measuring 25.4 mm in width and depth, was affixed to the concrete form using a double-sided adhesive tape. Twenty-four hours after casting, specimens were demold-ed and the plastic piece was removed, and they were subjected to heat curing for a period of 7 days. Following a 7-day heat curing process, the surface underwent a grinding process using a wire brush, followed by cleaning with a water jet, as shown in Figure 14. The prepared surface was then left to air dry for a day to eliminate any lingering moisture from the surface of the groove. To ensure the NSM groove was devoid of dust and unwanted materials, compressed air was used to remove any remaining particles. These meticulous steps were taken to guarantee the cleanliness of the NSM groove, free from dust, moisture, and unwanted substances. Special attention was given to surface preparation to achieve a rough surface, ensuring a strong mechanical bond between the NSM gel and the concrete, thereby preventing any potential failure between the two materials.



Figure 14: Grinding process for the NSM groove to ensure adequate bond between resin and concrete. (a) Use of a wire brush for grinding inside the groove, (b) Closer look at grind surface.

NSM-CFRP flexural strengthening was performed utilizing carbon CFRP No. 3 bars with a nominal diameter of 10 mm and NSM gel. Figure 15 illustrates the different steps of flexural strengthening of the beams using the NSM-CFRP technique.



Figure 15: Steps of NSM-CFRP strengthening: (a) plastic form used at the bottom of the beam to create a groove before casting, (b) beam after fabrication and hardening, (c) beam after removing plastic form, (d) dispensing NSM gel in the groove, and (e) beam after performing surface preparation and NSM-CFRP flexural strengthening.

5.2.2.3. Combination of Shear and Flexural Strengthening Methods (NU and NSU Type)

NSM-strengthened beams for NU and NSU types were allowed to cure for 3 days for hardening of epoxy gel. The process described for U-wrap was adopted for the NSM-strengthened beams for NU and NSU types. Wrapped beams were allowed to cure for 14 days at room temperature to enable complete hardening of wrapping and composite action with the beams. Therefore, combination beams were cured after strengthening for a total of 17 days before testing. Figure 16 and Figure 17show the process of U-wrapping for NU and NSU beams.

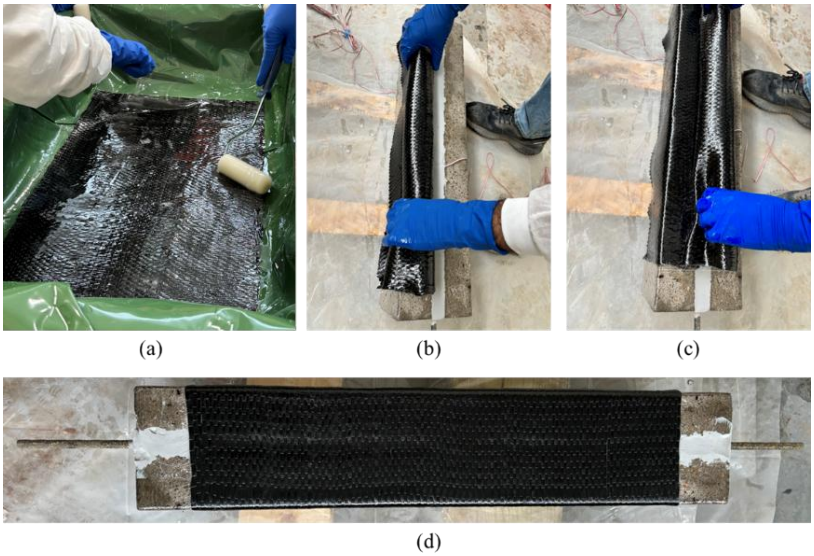

Figure 16: Combination strengthening NSM + complete U-wrap. (a) Wetting process of carbon fiber fabric, (b,c) wet-layup on NSM strengthened beams, (d) completed U-wrap strengthening on NSM-strengthened beam.

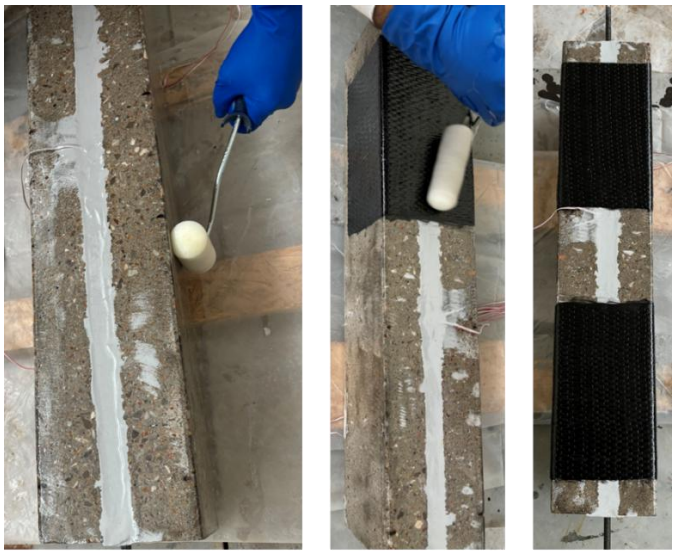

Figure 17: Combination strengthening NSM + shear only U-wrap (a) prime coat on NSM-strengthened beams for wet layup, (b) wet layup in shear only zones, (c) finished wet layup for U-wrap strengthening in shear-only zones for NSM-strengthened beams.

5.3. Results and Discussion

The comprehensive experimental findings for all types of beams are systematically detailed in Table 1. The load-deflection data for a representative beam from each group is depicted in Figure 18. For the control group of RC beams, labeled C1 to C4, the average peak load at failure was found to be 79.19 kN, with a standard deviation of 2.99 kN. The mean deflection associated with this load was 8.70 mm, with a standard deviation of 0.46 mm. The load–deflection pattern of these beams exhibited typical RC beam characteristics, with linear elastic behavior observed up to approximately 50.5 kN, beyond which nonlinear behavior was noted up to the point of failure. For RC beams U1 to U4, reinforced with a CFRP U-wrap, the average peak load at failure was recorded as 94.42 kN, with a standard deviation of 7.19. The mean deflection measured for these beams was 9.73 mm, with a variation of ±0.84 mm. The “U” series beams showed a conventional RC beam load–deflection profile, exhibiting linear elasticity up to an average load of 57.1 kN, after which nonlinear behavior was demonstrated up to the failure load. The RC beams N1 to N4, reinforced

with NSM-FRP, showed an average ultimate load at failure of 144.60 kN, with a standard deviation of 18.39 kN. The corresponding average deflection was 9.60 mm, with a variation of ±0.91 mm. The load–deflection characteristics of these "N" series beams differed notably from both the control "C" beams and the "U" series beams. In the "N" series beams reinforced with NSM-FRP, the load–deflection diagram exhibits linear elasticity up to an average load of 110 kN. Beyond this point, a slope change is noted, maintaining relatively linear behavior up to the maximum load. Nonlinearity then becomes obvious, and the load gradually decreases as the CFRP begins to slip, continuing until failure occurs. The RC beams designated as NU1 to NU4, which were reinforced with both NSM-FRP bars and U-wrap shear strengthening along their entire span, exhibited an average peak load at failure of 157.95 kN, with a standard deviation of 4.57 kN. The average deflection for these beams was measured at 12.86 mm, with a variation of ±2.01 mm. Their load–deflection behavior maintains a linear behavior up the peak load. Beyond the linear elastic portion, NU-type beams demonstrated a slight change in slope in the load displacement behavior but continued to be linear until the first load drop, demonstrating a bilinear behavior.

Table 1: Load and deflection results upon test completion

Beam Type	Load (kN)	Deflection (mm)	Failure Mode	Increase (%)
Control	79.19 ± 2.99	8.70 ± 0.46	CC	
U-wrap only	94.42 ± 7.19	9.73 ± 0.84	CC	19
NSM only	144.60 ± 18.39	9.60 ± 0.91	DB	83
NSM + U-wrap	157.95 ± 4.57	12.86 ± 2.01	R	99
NSM + shear U-wrap	162.17 ± 6.65	14.28 ± 2.23	R/SE	105

Notes: SE is the splitting of the epoxy cover, R is the strength rupture of the CFRP bar, DB is the debonding of the NSM-FRP bar with surrounding epoxy, and CC is concrete crushing after yielding of steel.

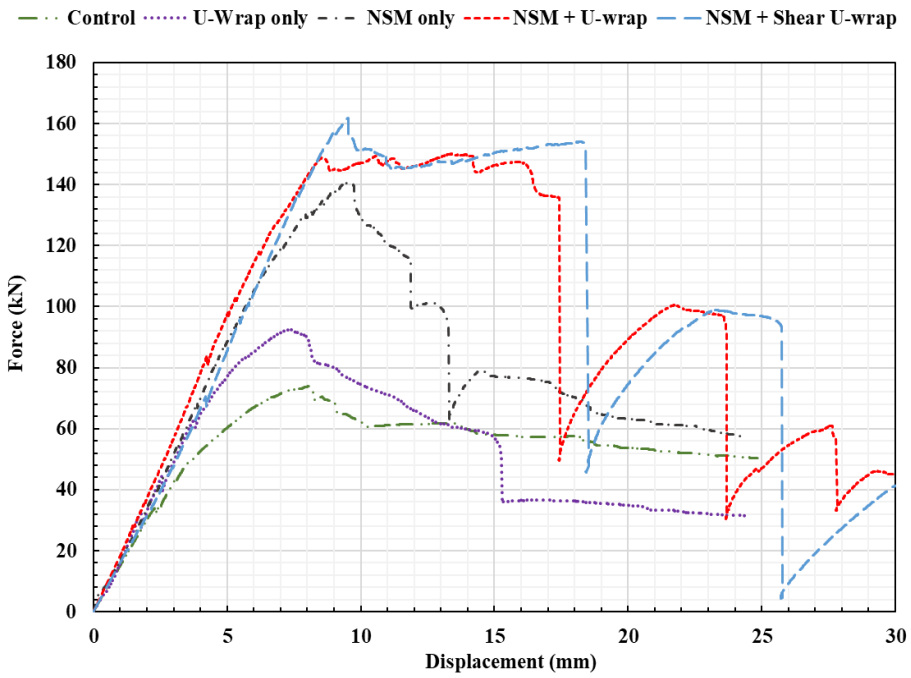

Figure 18: Load-displacement behavior of the median of all tested beams.

From observation of the load displacement graphs, large load drops are evident after some ductile behavior. Almost all beams had a large load drop of around 18 mm displacement with a load drop rate of 78 kN/mm. There is a noticeable stiffness change between beams, which could be attributed to the change in the effect of confinement due to the wrapping, or also due to the change in the bond developed between the NSM bar and the surrounding epoxy. Beyond the load drop, the beams continued to support the load and observed a decrease in load of more than 50% of the peak. At this point, the test was stopped as the test setup would not allow for any more beam deflection. The "NSU" series beams, incorporating U-wrap in the shear span and NSM-FRP for flexural strengthening, displayed an average ultimate load at failure of 162.17 with a variation of ±6.65 kN. The mean deflection was 14.28 mm, with a standard deviation of 2.23 mm. Their load–deflection pattern was largely akin to that observed in the "NU" series, but in some of the specimens, the failure mode was different. Two of the beams experienced a sudden failure due to

the tension rupture of the CFRP. In contrast, the other two showed a progressive failure characterized by continuous CFRP slipping and epoxy splitting until eventual failure occurred. Two of the beams had a large load drop around an 18 mm displacement with a load drop rate of 90 kN/mm. Large drops were not observed in the other two beams, where a gradual load decrease was seen. There was a noticeable stiffness change between one of the beams and the rest, which could be attributed to the change in effect of confinement due to the wrapping, or also due to the change in bond developed between the NSM bar and the surrounding epoxy.

The data in Figure 19 clearly show that combining U-wrap shear and NSM-FRP flexural strengthening significantly alters beam behavior. It is evident that the control beams have the lowest peak load when compared to the N, U, NU, and NSU types. It is evident from this comparison that incorporating NSM flexural strengthening for the control RC beams improves their flexural strength. It can be clearly observed that the NSM-FRP has a significant strength increase in control specimens, as also observed in previous studies (Nanni, A., Alkhrdaji, T., Chen, G., Barker, M., Xinbao, Y., and Mayo 1999; Saadatmanesh and Ehsani 1990; Sbahieh et al. 2023; Soudki and Alkhrdaji 2005; Zhang et al. 2017). The flexural strength is even more dominant because of the high-strength materials, such as the CFRP, which was used to strengthen these beams. Also, it is worth mentioning that the change in slope beyond the linear elastic portion is marginal for N, NU, and NSU beam types, which continue in a linear fashion when compared to the C- and U-type beams. This is attributed to the NSM CFRP bar, which is highly linear to failure. None of the beams, except the combination types (NU and NSU), had significant load drops in the load displacement graphs. Figure 19 provides a summary of these variations in load-carrying capacity across the five beam groups. Performing an analysis to compare the peak load of control beams to other types of beams, it was observed that there was a 19% increase for U-type beams

compared to the control beams. This increase in flexural performance for U-wrap beams can be attributed to the confinement effect. An 83% increase in N-type beams, a 99% increase in NU-type beams, and a 105% increase in NSU-type beams were observed, indicating that the incorporation of the CFRP bar as NSM improves flexural strength and even more so in combined beams. This marks a drastic increase in flexural performance in the NSM-only and combination-strengthened beams compared to control beams. The combination-strengthened beams were 9% and 12% higher in flexural performance compared to N-type beams, indicating that confining the NSM-only beams with the U-wrap improves confinement and bond, thus increasing the flexural strength. In previous work (ChennaReddy 2016), using GFRP NSM, the improvement in flexural performance compared to RC beams was 47%, which is less than the improvement seen in this study, as the type of NSM used was CFRP.

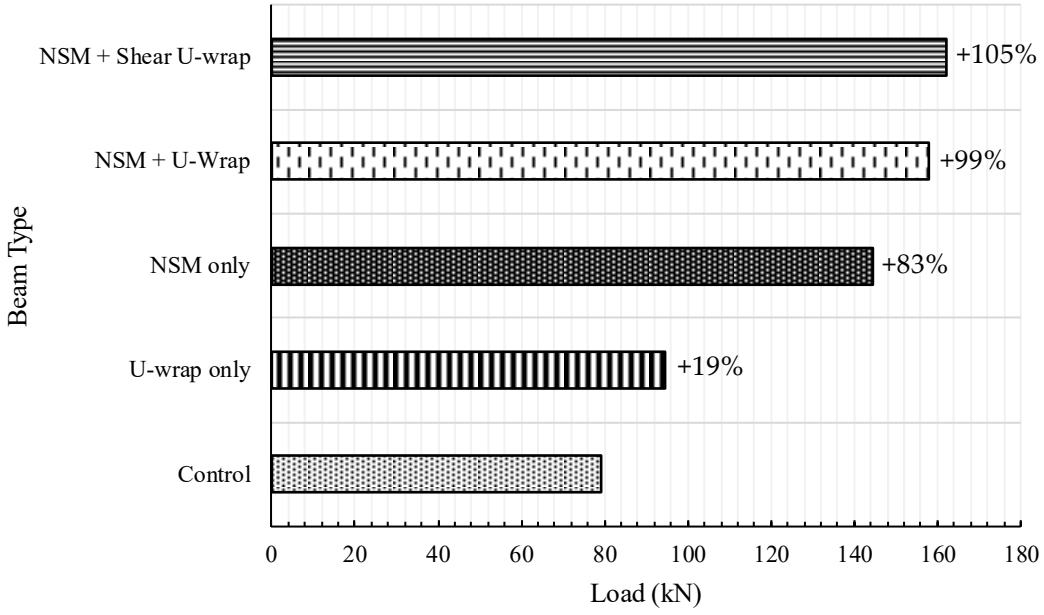

Figure 19: Mean flexural load capacity of tested beams. The percentage increase compared to control beams is shown on each bar.

Figure 20 illustrates the failure modes for each group of beams. It shows significant debonding in NSM-FRP beams and abrupt CFRP rupture in beams where NSM-FRP is used alongside U-wrap shear reinforcement. The control groups, “C” and “U”, mirrored typical RC beam behavior, failing due to concrete crushing following steel yield. The “N” group experienced CFRP bar and epoxy debonding from the concrete. The “NU” group, showing improved bond strength, failed due to CFRP bar rupture. The “NSU” group exhibited two failure patterns: either sudden epoxy cover splitting or CFRP bar rupture, depending on the epoxy cover’s efficacy in strain transfer. In cases where the epoxy effectively transferred strain, CFRP bar rupture occurred. Otherwise, the failure was marked by epoxy cover splitting. The CFRP bars in “NU” and “NSU” reached strains up to near their ultimate capacity before failure, indicating that U-wrap confinement helps prevent debonding and allows the bars to achieve higher strain levels. In the experimental findings, it was noted that in the “N” group, the CFRP bar and epoxy started to slip at maximum load due to debonding from the surrounding concrete. Nonetheless, this slippage was not observed in the “NU” group, where CFRP U-wrap was applied along the entire span.



(a) (b)



(c) (d)



(e) (f)

Figure 20: Different failure modes of the tested beams. (a) Control beam before performing the test, (b) control beam after performing the test, (c) only U-wrap beam, (d) NSM only beam, (e) NSM + full U-wrap beam, (f) NSM + shear U-wrap beam.

For the "C" control beam group, specifically beam C3, the tension steel reached a yield strain of 0.0021 at a load of 49.3 kN, with a midspan deflection of 4.1 mm. The strain gauge readings ceased at a strain of 0.0052, corresponding to a load of 56.9 kN. Simultaneously, the strain in the top compression fibers of the beam reached 0.003. At this level of strain, the beam experienced failure

due to crushing of the concrete. The load at the 0.003 strain level was 74.05 kN, with a midspan deflection of 8.11 mm. In the “N” beam group, for the beam N3, the tension steel reached a strain of 0.0021, while the corresponding CFRP bar strain was 0.0055 at a load of 102.8 kN and a mid-span deflection of 5.45 mm. The highest strain recorded in the tension steel was 0.0026 at 149.88 kN load. The CFRP bar’s maximum strain recorded was 0.013 at a load of 153.14 kN, and after that, the beam ultimately failed at a load of 165.51 kN. In the “NU” beam group, specifically at beam NU2, the strain in the tension steel reached 0.0021, with the CFRP bar strain at 0.0025 under a load of 80.94 kN and a midspan de-flection of 5.45 mm. The maximum strain in tension steel was 0.004 at a 91.19 kN load. The beam ultimately failed at 150 kN. The failure was abrupt due to CFRP bar rupture, with the bar’s maximum strain reaching 0.0125, which is 70% of the bar’s ultimate tensile strain. In the “NSU” beam group, specifically for NSU4, the tension steel reached a strain of 0.0021, with the CFRP bar strain at 0.0032 under a load of 79.3 kN and a midspan deflection of 5.14 mm. The maximum strain in the tension steel was 0.0044 at a 162.22 kN load, and the beam failed at 163.68 kN. The highest recorded concrete compression strain was 0.00386 at 161.59 kN. Also, the peak strain in the CFRP bar was 0.0119. It is noteworthy that in the “NSU” group of beams, two out of the four experienced failures due to CFRP bar rupture. The strain distribution of type N, NU, and NSU beams is depicted in Figure 21.

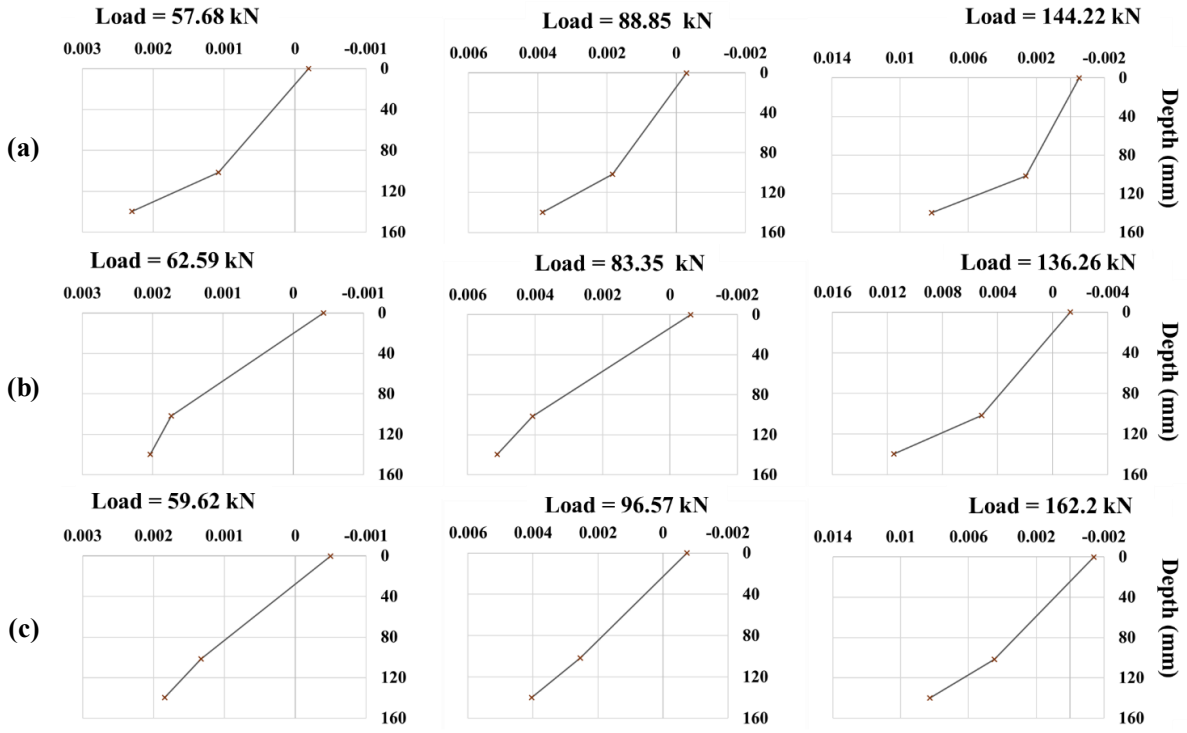

Figure 21: Strain distribution diagrams at various loads for type (a) N, (b) NU, (c) NSU beams.

The failure mode of each beam group is shown in Figure 22. As noted in previous research (Nanni, A., Alkhrdaji, T., Chen, G., Barker, M., Xinbao, Y., and Mayo 1999), the integration of NSM-FRP flexural strengthening with U-wrap shear strengthening not only enhances the bonding in RC beams but also maintains their deformability up to the point of failure. This combination effectively improves the overall structural performance without compromising the beam's ability to deform under load. However, it should be noted that the failure mode for beams strengthened with both U-wrap and NSM-FRP can be quite sudden and abrupt. This highlights a critical aspect to consider in the combined application of these strengthening techniques. The investigation reveals that combining NSM-FRP and U-wrap shear strengthening in RC beams enhances their load-bearing capacity. However, this comes with a trade-off: the strengthened beams are prone to sudden and abrupt failures, along with a rapid loss in capacity, primarily due to the tension rupture of the FRP. As mentioned earlier, 50% of the tested NSU beams did not experience sudden failure. So, the

investigation interestingly suggests that using U-wrap in the shear span leads to an improved bond in FRP, which effectively enhances the beam's strength. This method manages to increase the bond without the associated risk of sudden failure, a notable benefit in structural engineering applications.



Figure 22: Various failure modes of RC beams strengthened with NSM-CFRP, (a) type NU beams, failed by the CFRP bar rupture, (b) type NSU beams, failed by the CFRP bar rupture, (c) type NSU beams, failed by sudden spilling of the epoxy cover.

5.4. Key Discussion

Based on the strain data of the NSM-CFRP bar, a 33.3% increase was observed for the NU beam series (b) over N beam series (a), showing the improvement in bond between the NSM-CFRP bar

and the surrounding epoxy as a result of U-wraps. However, they were accompanied by a bar rupture. The aforementioned investigations show the need for imposing limits in ACI guidelines, combining the two commonly used strengthening techniques to limit strain in NSM-FRP. U-wrap FRP provides significant external confinement to the concrete, which helps in uniformly distributing the stresses across the concrete section. This confinement effect is particularly beneficial in regions susceptible to high shear stresses and where bending moments induce tensile stresses at the concrete surface. By doing so, U-wrap effectively delays the initiation and propagation of cracks. From this study, it is evident that special care should be taken in designing RC strengthening combining NSM and U-wrap FRP strengthening. The investigations show the need for imposing limits in ACI guidelines, combining the two commonly used strengthening techniques to limit strain in NSM-FRP.

5.5. Conclusions

In this study, a total of 20 RC beams were organized into five groups, with each group consisting of four beams. These beams were all subjected to static load testing. The aim of this study was to thoroughly assess the effects of employing NSM-FRP for flexural strengthening, along with U-wrap FRP for shear strengthening in concrete structures. This evaluation sought to understand how these combined methods impact the structural performance and integrity of concrete beams. Here are some significant conclusions.

1. The obtained results indicated that RC beams reinforced with NSM-FRP exhibited a significant increase in strength, showing an 82% enhancement compared to the control beams. This improvement was achieved through the application of the NSM-FRP flexural

strengthening technique. The primary mode of failure observed in these beams was the debonding of the FRP bar and epoxy from the surrounding concrete.

2. The research demonstrated that integrating NSM-FRP for flexural enhancement with full-span U-wrap in RC beams led to an increase in flexural load capacity by approximately 9% compared to beams reinforced only with NSM-FRP. The U-wrap effectively prevented crack growth in the epoxy, improving the bond between NSM-FRP and concrete. This combination altered the failure mode from debonding of the CFRP bar to its rupture at peak tensile strength.
3. The research revealed that applying U-wrap shear strengthening in combination with NSM-FRP flexural strengthening solely in the shear area led to a 12.1% increase in flexural load capacity, compared to beams with NSM-FRP. Among the four beams tested, two failed due to CFRP bar rupture, while the other two experienced sudden epoxy cover splitting. Despite these varying failure modes, strain measurements confirmed that the CFRP bars reached their full tensile capacity, indicating improved bond performance. Both observed failure modes (CFRP rupture and epoxy splitting) were abrupt, impacting the beams' ductility.
4. The integration of U-wrap shear strengthening with NSM-FRP flexural strengthening has shown a marked enhancement in bond performance, positively impacting the overall flexural load capacity of RC beams. Nevertheless, this combination also led to a shift in failure modes. While NSM-FRP flexural-strengthened beams alone exhibited relatively ductile failure, the addition of full U-wraps, which enhances bond performance through confinement, resulted in more sudden and less ductile failure modes, primarily through bar rupture.

5. The structural design of components is based on a ‘fail-safe’ concept, which requires elements to give a warning prior to failure to prevent catastrophes. In infrastructure applications, the nonlinear behavior of structural components is important to avoid brittle (catastrophic) failure, which is required by most design codes worldwide. From this study, it is evident that special care should be taken in designing RC strengthening combining NSM and U-wrap FRP strengthening. The investigations show the need for imposing limits in ACI guidelines, combining the two commonly used strengthening techniques to limit strain in NSM-FRP.
6. Future work can be performed with a larger matrix and large-scale beams for further understanding. Positioning LVDTs for the NSM bars can provide information on slippage during testing.

6. CHAPTER 6: The Influence of Multi-Walled Carbon Nanotubes on the Pull-off Strength of Polymer Concrete Overlays on Concrete Substrates with Sulfate Exposure

6.1. Literature Review

6.1.1. Polymer Concrete Overlays

The deterioration of civil infrastructure, particularly concrete bridge decks, necessitates rapid and durable repair solutions. Overlays are a common strategy, and Polymer Concrete (PC) represents a class of composite materials where the traditional cementitious binder found in portland cement concrete (PCC) is entirely replaced by a synthetic organic polymer, making it a viable selection for infrastructure maintenance, rehabilitation, and preservation (Dikeou 2003; Pratap 2002). This fundamental difference distinguishes PC, sometimes known as synthetic resin or resin concrete, from polymer-modified concrete (PMC) or polymer-impregnated concrete (PIC). PC is generally lightweight, offers high wear and skid resistance, is relatively impermeable to water and chlorides, and cures rapidly (often within hours) – characteristics highly suitable for accelerated construction (Dang et al. 2024; Laredo Dos Reis 2005; Wheat et al. 1993).

Polymer concrete overlays are frequently employed for bridge decks, typically applied in thin layers ranging from 1/2 to 3/4 inch (12.7 to 19 mm). Their primary functions include extending service life, providing a durable/impermeable wearing surface, protecting the underlying substrate and reinforcement from water and chlorides, and restoring friction. The rapid curing nature allows for quick application and return to service, significantly minimizing traffic disruption – often enabling overnight installation and reopening the bridge the following day, making PC overlays

highly suitable for accelerated bridge construction (ABC) projects (Dang et al. 2024; Laredo Dos Reis 2005; Wheat et al. 1993). Different types exist, including Thin Polymer Overlays (TPOs) and Slurry Overlays. While general performance is favorable, success hinges critically on proper installation, especially substrate preparation, as localized failures are often linked to inadequate preparation or mixing.

Similar to the use of advanced FRP composites for strengthening deteriorated beams, PC overlays represent another application of polymer-based materials aimed at restoring or enhancing the performance and durability of existing concrete infrastructure, addressing challenges like rapid repair needs and protection against environmental degradation.

6.1.2. Polymer Concrete Formulation and Binders

Typically, a polymer concrete is comprised of fine and coarse aggregates, a catalyst, and a binder. The defining characteristic of PC is this polymer binder system, usually involving a thermosetting resin (monomer or prepolymer) combined with a catalyst or hardener to initiate polymerization, creating a cross-linked polymer network that binds the aggregates. PC formulations do not contain portland cement or water as part of the binder system (Stansbury and Idacavage 2016). The selection and proportioning of aggregates and fillers (like fly ash, silica fume, slag) are crucial for performance and economy, often used to reduce expensive resin volume and potentially enhance properties. For instance, specific fillers can improve strength, while others might enhance insulation but reduce strength, requiring careful selection (Hong et al. 2017).

The choice of binder for bridge deck overlays is an important factor in achieving several characteristics. The most commonly used binder systems are based on methyl methacrylate (MMA), unsaturated polyester resins, epoxy resins, and vinyl ester resins (Nodehi 2022). Each

offers distinct advantages and disadvantages. Epoxies generally provide excellent adhesion, low shrinkage, and superior chemical resistance, but are relatively expensive and have slower curing. Unsaturated Polyesters are the lowest cost option but suffer from high shrinkage and potentially higher water absorption. MMAs offer very rapid curing even at low temperatures, require less surface preparation, and exhibit good weathering and friction retention, making them ideal for rapid construction, but the monomer is flammable with a strong odor. Vinyl esters present a compromise with low cost, low viscosity (aiding penetration), and good chemical resistance, but also have high shrinkage and potential exothermic reaction issues during cure (Nodehi 2022). The selection involves balancing project needs like speed, budget, environmental exposure, and desired performance. The binder's chemical nature also critically influences interaction with nanomaterials like CNTs.

The suggested ratio of binder to aggregate (filler and coarse) for the design of the PC mix is usually around 1:3.7 by weight (Hong et al. 2017). Studies have also shown that maintaining a weight ratio between filler and coarse aggregate of around 7:3 can enhance the performance of PC. Optimal resin content often falls between 10-20 wt.%, varying with binder and aggregate characteristics. Optimization is key, as resin is the most expensive component (Hong et al. 2017; Manawadu et al. 2023).

6.1.3. Polymer Concrete Properties and Interfacial Bonding

PC has great crack resistance and durability. It generally possesses significantly higher compressive, flexural, and tensile strength than conventional concrete, with rapid strength development being a key advantage (Byron et al. 2021). Its low permeability provides waterproofing and excellent resistance to freeze-thaw cycles and chemical attack (Toufigh et al.

2017). PC overlays offer good abrasion/wear resistance and skid resistance. Also, in order to decrease the galvanic corrosion, it acts as an effective barrier between different substances (Sun and Lee 2023; Yeon et al. 2014). However, properties like shrinkage vary significantly with binder type, and workability depends on resin viscosity and fillers.

A solid adhesion to the concrete substrate is necessary when considering bridge deck overlays. The bond between the overlay and substrate is frequently identified as the main factor concerning serviceability and durability. A strong bond ensures monolithic action for stress transfer and is crucial for the overlay to function effectively and protect the substrate. The interface is often the weakest link, and bond failure (delamination) compromises performance. The ability of the bonded joint to withstand all anticipated in-service loads (traffic, fatigue) and internal stresses from differential volume changes (shrinkage, thermal cycles) is crucial (Manawadu et al. 2023). Given the thinness of overlays, their reliance on the substrate makes bond integrity paramount.

Adhesion relies on a combination of mechanical interlocking and chemical/physical adhesion (Ganguli et al. 2006). Mechanical interlocking occurs as the liquid binder penetrates substrate pores and roughness, forming physical anchors upon hardening. Its effectiveness depends heavily on substrate roughness (CSP). Physical adhesion involves intermolecular forces (van der Waals, hydrogen bonding) requiring intimate molecular contact. Chemical bonding involves primary bonds forming between reactive groups in the binder and on the concrete surface, potentially enhanced by coupling agents like silanes (Gorninski et al. 2004).

Achieving a strong bond is influenced by many factors. Substrate preparation is consistently highlighted as most critical, requiring removal of all unsound material and contaminants to achieve a clean, sound surface with adequate roughness (Wang et al. 2019). Substrate condition (moisture content, strength) also plays a role. PC properties like binder type, shrinkage, and viscosity affect

bond development. Application conditions (temperature, humidity) influence curing and bonding. Environmental factors (temperature cycles, moisture, loading) challenge the bond long-term (Wang et al. 2019). Enhancing the bond strength of PC with the concrete substrate is therefore of great importance and needs to be explored.

6.1.4. Limitations of Conventional Microfiber Reinforcement in PC

Previous studies added carbon fibers and synthetic chopped glass to PC in weight-based amounts ranging from 0.3% to 7.5% to improve toughness, but the mechanical characteristics of PC were often only slightly improved (Shokrieh et al. 2011). Nevertheless, the fiber addition limits the use of PC and decreases its workability (Toufigh et al. 2017). This problem stems from the fact that using chopped fibers makes it harder to achieve an ideal finish, in addition to the lower flowability. While PC generally exhibits high strength, some binders can be inherently brittle with low fracture toughness. Although ductility can be improved by raising the ratio of resin to filler, compressive strength can be reduced by up to 26% and flexural strength by up to 70% (Byron et al. 2021). This suggests a scale mismatch where microfibers struggle to effectively modify matrix behavior without causing processing issues. These limitations highlight the need for innovative approaches, such as nanomaterial incorporation, to improve PC performance, particularly toughness and bond strength, without sacrificing its benefits.

6.1.5. Carbon Nanotubes (CNTs) as Potential Additives for PC

Within the last decade, research studies have evaluated the potential of using nanomaterials to change the performance of materials. The motivation stems from the limitations of micro-scale additives. Whereas the much greater surface area of nanomaterials, relative to microfibers, enables interactions at multiple levels (molecular, nano/meso-structural) and therefore promotes a more

significant impact on the mesoscale, often at very low loading fractions (Ganguli et al. 2006). The role of the PC binder's chemical composition is critical for the efficiency of nano-materials (Theodore et al. 2011). Nanomaterials are more efficient in performance when they are in close contact with the host matrix and a chemical binder because they enhance chemical interactions throughout the polymerization process (Chuah et al. 2014a; David et al. 2014a).

One of the nanomaterials that has been widely utilized is carbon nanotubes (CNTs). Since carbon nanotubes (CNTs) were first discovered (Iijima 1991), their unique structural, chemical, and physical characteristics have drawn considerable interest. Structurally visualized as rolled graphene sheets, CNTs feature a high aspect ratio, with diameters on the nanometer scale and lengths on the micrometer scale, coupled with low densities (Yu et al. 2008). They possess remarkable properties due to strong sp^2 bonds: extreme stiffness (Young's Modulus ~1 TPa for SWCNTs), high strength (>100 GPa possible), high thermal conductivity, and metallic or semiconducting electrical behavior (Popov et al. 2016). These exceptional characteristics make CNTs a highly regarded potential filler material for polymeric nanocomposites (Yu et al. 2016). Researchers have aimed to harness these remarkable traits for various types of applications, such as field emission displays, electronic devices, hydrogen storage, and polymer composites (Avouris 2002).

CNTs are broadly divided into multi-walled carbon nanotubes (MWCNTs) and single-walled carbon nanotubes (SWCNTs). SWCNTs consist of a single graphene cylinder (1-2 nm diameter), while MWCNTs comprise multiple concentric cylinders (5-100+ nm diameter). SWCNTs generally have higher aspect ratios, superior intrinsic mechanical properties (strength, stiffness), are more flexible, and have fewer defects compared to MWCNTs (Thakre et al. 2011). By rolling concentric graphene sheets, MWCNTs can be conceptually derived from SWCNTs. However,

SWCNTs are exponentially more expensive to produce. Consequently, MWCNTs are more commonly used in practical research for composites like PC due to their affordability and availability, despite potentially lower intrinsic properties and higher defect density. The choice depends on balancing performance and cost. Regarding mechanical properties, a single-walled carbon nanotube (SWCNT) is significantly stiffer than steel (Park et al. 2003). For multi-walled nano-tubes (MWCNT), the modulus can range from 200 to 4,000 GPa. MWCNTs offer outstanding mechanical characteristics and have been linked to enhancements in polymer durability, fatigue resistance, glass transition temperature, strength, fracture toughness, and controlled viscoelastic properties (Tang et al. 2013; Yu et al. 2008).

6.1.6. Dispersion and Reinforcement Mechanisms of CNTs in Polymers

The effectiveness of CNTs hinges on overcoming their strong tendency to agglomerate due to van der Waals forces, particularly for high aspect ratio MWCNTs (Chuah et al. 2014a). Achieving uniform dispersion is crucial but challenging. The most widely used dispersion methods include stirring, shear mixing, ball milling, ultrasonication, chemical functionalization, and extrusion (Chuah et al. 2014a). Mechanical methods like high-shear mixing or three-roll milling (calendering) apply physical forces to break agglomerates, with milling being effective for viscous systems and generally non-damaging. Functionalization (chemically modifying the CNT surface) is often critical to improve compatibility, reduce attraction, and enhance interfacial bonding. Covalent functionalization (e.g., acid oxidation creating -COOH groups) forms strong bonds but can alter CNT structure and properties. Non-covalent functionalization uses weaker interactions (e.g., surfactants, polymer wrapping) to preserve CNT structure but may yield weaker adhesion (Hirsch and Vostrowsky 2005). Often, a combination of functionalization and mechanical mixing is needed.

Well-dispersed CNTs reinforce polymers via several nanoscale mechanisms: 1) Load Transfer: Transferring stress from the matrix to the stiff CNTs via the interface, crucial for strength/stiffness improvements and dependent on interfacial adhesion. 2) Crack Bridging: CNTs spanning nano/microcracks resist their opening and propagation, enhancing fracture toughness. 3) Crack Deflection: Forcing cracks along more tortuous paths increases fracture energy. Other mechanisms include energy dissipation through nanotube pull-out or fracture. The success of these mechanisms relies entirely on good dispersion and a strong interface.

6.1.7. Impact of Substrate Deterioration on Overlay Bonding

In addition to bonding with regular concrete, bonds that PC can develop with concrete exposed to extreme, harsh climatic conditions need to be strong. Such conditions cause degradation and negatively impact the performance of concrete infrastructure (Al-samawi et al. 2023; Tang et al. 2013). One of the main negative influences on concrete performance, particularly in unfavorable climatic environments, is sulfate attack (Al-samawi and Zhu 2022; Ikumi et al. 2018).

Sulfate attack is a major concern in sulfate-rich soils, groundwater, or seawater. It involves chemical reactions between sulfate ions and cement hydrates (like $Ca(OH)_2$ and C_3A), forming expansive products like gypsum and ettringite (Akbarpour et al. 2022b; a). The significant volume increase associated with ettringite formation generates internal stresses leading to expansion, cracking, and spalling (Neville 2004). Physical salt crystallization within pores under wet-dry cycles can also exert damaging pressure. Magnesium sulfate attack is particularly aggressive as it can also decompose the C-S-H binder (Rodriguez-Camacho and Uribe-Afif 2002). The sources of sulfate attack can be external or internal; external sources include soil, groundwater, seawater, and

acid rain (Ikumi et al. 2019; Ouyang et al. 1988). This degradation results in reduced strength and integrity, particularly at the concrete surface.

6.1.8. Influence of CNTs on Durability and Bonding

Studies on cementitious materials suggest CNTs can enhance durability. (Han et al. 2013) discovered that MWCNTs can reduce gas and water permeability. (Li et al. 2015a) found that CNTs refine the pore structure. (Bheel et al. 2023) reported improved compressive strength, reduced expansion due to sulfate attack, minimized acid attack effects, and lower chloride permeability with 0.05% CNTs. However, (Camacho et al. 2014)observed increased porosity and accelerated deterioration under carbonation/chloride ingress with CNTs, highlighting the critical importance of dispersion and potential variability.

While previous studies highlighted potential durability benefits of CNTs against chemical attacks, the specific impact of sulfate-induced deterioration on the bond strength of polymer concrete overlays remains underexplored. As noted earlier, the interaction mechanisms of CNTs differ significantly between cement and polymer matrices. Therefore, direct investigation within the PC system is required to understand CNT effects on PC bond performance, especially on deteriorated substrates.

Evidence from related systems suggests CNTs can enhance polymer adhesion. Studies on CNT-modified epoxy adhesives bonding FRP to concrete consistently show improved bond performance, increased load capacity, mitigation of debonding, and enhanced adhesion, often attributed to matrix toughening near the interface and interfacial crack bridging (Li et al. 2021). Enhanced fatigue resistance and fracture toughness reported for CNT-PC (Douba et al. 2019) are highly relevant, as bond failure often involves crack propagation near the interface. Functionalized

CNTs also offer potential for direct chemical bonding across the interface. It is hypothesized that these mechanisms could be particularly beneficial when bonding to flawed, deteriorated substrates where crack initiation resistance is critical.

6.1.9. Research Gap and Proposed Investigation

The main goal of this research is to investigate the effect of incorporating carbon nanotubes on the pull-off strength of polymer concrete with healthy and unhealthy (sulfate-deteriorated) concrete substrates. While the potential benefits are suggested by related literature, direct experimental data quantifying the influence of CNTs on the bond between PC overlays and sulfate-damaged concrete are lacking. Understanding this interaction is crucial for developing materials suitable for harsh environmental conditions and reliable rehabilitation measures.

In order to ascertain these objectives, a wide range of tests is proposed, ranging from the preparation and characterization of polymer concrete with various MWCNT concentrations (using functionalized and pristine MWCNTs) to mechanical property tests such as modulus of rupture (ASTM C580/C78) and compressive strength (ASTM C579). Concrete specimens will be subjected to controlled sulfate-exposed environments to induce deterioration. Polymer concrete with and without nanomodification will be used to bond with both healthy and deteriorated concrete substrates. The bond strength will be evaluated using ASTM C1583 pull-off tests. Microscopy analysis will be performed to evaluate the dispersion of MWCNTs in PC and the failure surfaces of specimens after the pull-off test to understand failure mechanisms. The findings of these tests aim to provide insight into the effect of nanomaterials on polymer concrete bonds with unhealthy and deteriorated concrete, thus enabling the realization of more long-lasting and efficient rehabilitation measures for degraded bridge decks.

6.2. Materials and Methods

Portland cementitious concrete (PCC) mix was used in this study to fabricate the concrete substrate to perform pull-off test methods. The PCC in this study contains superplasticizer, natural river sand fine aggregate, water, and type I/II portland cement. Table 2 presents its properties. In this investigation, 738 cc of MasterGlenium 7920 superplasticizer per 100 kg was utilized, which is in the range of the recommended dosage of 130 cc to 780 cc per 100 kg for cementitious materials. The fine aggregate used in this mix has a nominal maximum size of 2.36 mm. T-17 Polymer Concrete Powder Component and T-17 Polymer Concrete Liquid Component were the two main PC components that were utilized as the overlay material for the concrete substrate (Transpo Industries). In this study, the selection of the binder material and the design of the polymer concrete mix were governed not only by the mechanical properties but, importantly, the effectiveness of dispersion of nanomaterials in the resin for a homogeneous product.

Table 2: Portland cement, concrete, and polymer concrete mix designs.

Materials	PCC (kg/m^3)	PC (kg/m^3)
Superplasticizer	3.5	-
Water	136.6	-
portland cement	455.3	-
Aggregate	910.6	-
T-17 Polymer Concrete Resin	-	250
T-17 Polymer Concrete Powder	-	2000

6.2.1. Mix Design Properties

Cylinders and beams were fabricated and tested according to ASTM C39, ASTM C579, ASTM C78, and ASTM C580 using this mix design for establishing the baseline properties of the two concrete materials. Twelve cylinders in total—six PCC and six PC—were tested to ascertain the two distinct varieties of compressive strengths of concrete in accordance with ASTM C579 and ASTM C39, respectively. A four-point bending test was used to test three beams per type in order

to estimate the modulus of rupture. Forney machines were employed in the two assessments. A Forney machine was used for both tests.

6.2.2. Preparation of Nanomodified Polymer Concrete

Pristine MWCNTs and the two most suitable functionalizations of carboxyl group (COOH) and ammonia group (NH3) MWCNTs with respect to binder weight, using weight contents of 0.25 wt.% and 0.5 wt.%, were chosen to be added to polymer concrete and compared with neat (0 wt.%) polymer concrete. The chosen MWCNT concentrations of 0.25% and 0.5% align with findings from previous studies (David et al. 2014b; Konsta-Gdoutos et al. 2010; Okoro et al. 2019) where optimal mechanical improvements were observed within this range for nano-modified composites. Pristine MWCNTs are unmodified carbon nanotubes with their original surface chemistry. On the other hand, functionalized types of CNTs, such as COOH-functionalized MWCNTs, have carboxyl groups (-COOH) attached to their surface. This functionalization enhances their dispersibility in the polymer matrix and can improve interfacial bonding between the MWCNTs and the polymer. The COOH functionalization can lead to better load transfer and potentially improved mechanical properties compared to pristine MWCNTs (Ferreira et al. 2023). This is especially true during the elastic and plastic stress transfer stage, from concrete to the MWCNT, and during the fracture stage, as the MWCNTs attempt to bridge cracks in the concrete, according to the principles of stress transfer and fracture mechanics in discontinuous fiber systems (Goh 2017). A content of 0 wt.% MWCNTs indicated no incorporation of MWCNTs to establish a baseline database. MWCNTs were acquired from Cheap Tubes, Inc. Two phases were used to disperse the carbon nanotubes into the resin: magnetic stirring and ultrasonication. The strong van der Waals forces among MWCNTs pose dispersion challenges, leading to agglomeration. As shown by (Chuah et al. 2014b), employing a combination of ultrasonication and magnetic stirring minimizes

agglomerates, thereby ensuring uniform distribution and improved mechanical performance. So, before adding the nanomaterials to the methyl methacrylate (MMA) resin, the precise amount of each material was weighed with a precision of 0.01 g. After that, the resin containing MWCNTs was heated to 110 °C in an oil bath while being stirred magnetically at 800 rpm. To trap heat and keep the resin sealed at a fast-stirring rate, the resin container was sealed with aluminum foil. The resin nanocomposite was placed in an ultrasonication bath after two hours of magnetic stirring. Degassed distilled water heated to 60 °C was pre-sent in the bath. After that, ultrasonic waves were used for two more hours. Before being used, the resin nanocomposite was removed from the bath and left to cool to room temperature for almost two hours. The chosen temperatures, stirring rate, and time, and ultrasonication time were intended to minimize the viscosity of the resins during dispersion without causing any molecular polymer damage. The use of ultrasonication enhances dispersion by creating microscopic bubbles inside the resin that release energy and prevent particle agglomeration, resulting in a more even distribution of the particles. The resin container was kept at a constant temperature by the use of the oil and water baths. The purpose of using distilled water is to limit the quantity of particles, such as minerals and salts, that would otherwise reduce the effectiveness of the ultrasonication bath. Degassing removes extra air bubbles from the distilled water solution to guarantee that ultrasonic waves are used to their full potential (Douba et al. 2019). This pre-pared mixture with each MWCNT concentration was added to the T17 powder component and mixed using a high-shear tabletop mixer. The T-17 Polymer Concrete was selected for its excellent inherent workability (e.g., low resin viscosity: 10–12 cPs; good mortar pot life: 8–15 min), which readily accommodated the low concentrations of MWCNTs (0.25–0.5 wt.%) used without unmanageably altering the observed workability or finish ability. Also, the PCC substrate

was designed for suitable casting consistency. Figure 23 and Figure 24 represent the stages of MWCNT dispersion in the MMA and the preparation of the mixture.

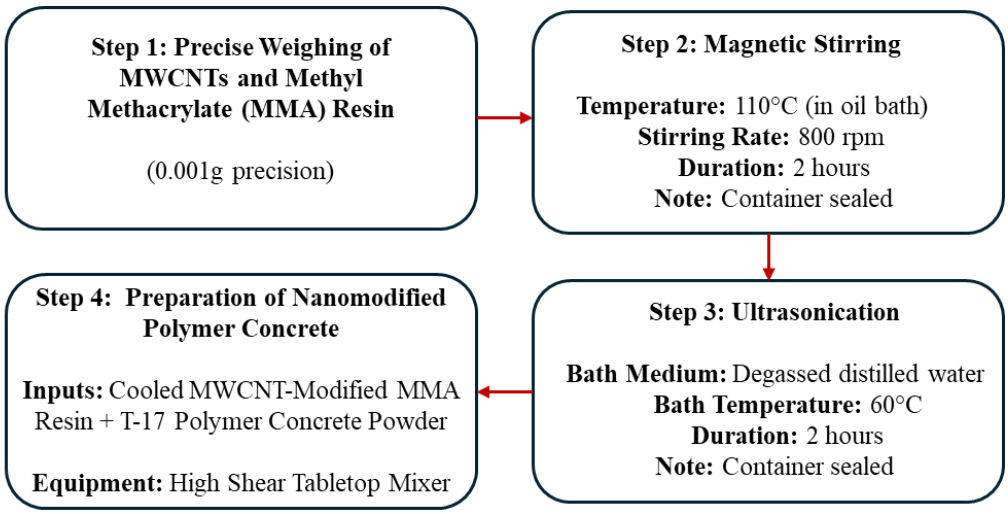

Figure 23: Schematic flowchart illustrating the preparation process of nanomodified polymer concrete.

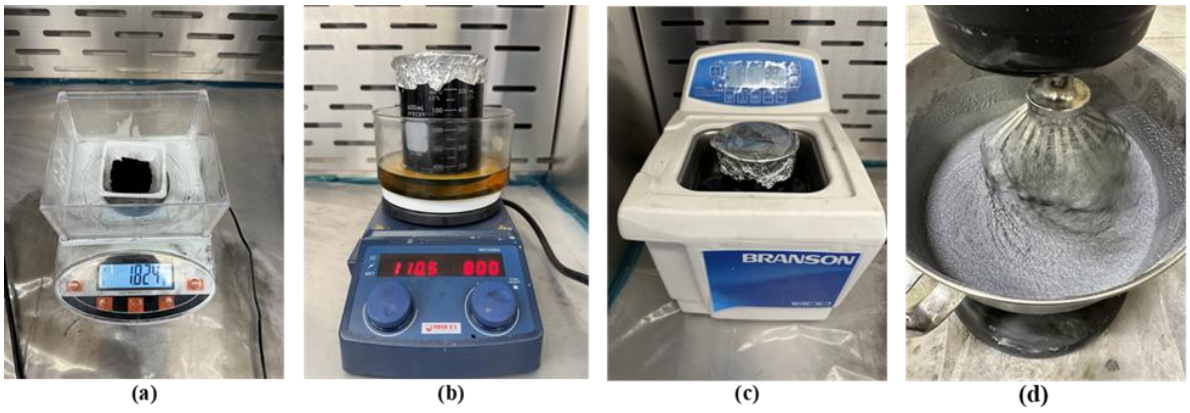

Figure 24: Carbon nanotube dispersion stages in resin: (a) weight of resin and MWCNTs, (b) magnetic stirring, (c) ultrasonication, (d) mixing of PC liquid component incorporating MWCNTs and powder component.

6.2.3. Preparation of Sulfate Exposure Environment

To understand the effect of sulfate attack on the bond strength between the nanomodified PC and concrete substrate, a sulfate solution container was prepared. An artificial sulfate solution was prepared using Na_2SO_4 (Na^+ cation). The sodium sulfate solution's mass fraction was 6%. Because acid attacks are more destructive at lower pH values, sulfuric acid was used to maintain the pH of

the fluid in the container at 3. The specimens were cured in the sulfate container for 210 days. Sulfate exposure was performed for 210 days, upon stage-wise observation for deterioration before PC overlays were applied. Visual observations were conducted regularly for signs of deterioration. Visible and extreme signs were observed after 7 months of exposure, and the specimens were removed. Figure 25 depicts the progress of sulfate attack on the specimens.



Figure 25: Specimens being in contact with sulfate ions after (a) 28 days, (b) 140 days, and (c) 210 days, and (d) shows the production of ettringite after 210 days.

6.2.4. Preparation of Specimens for ASTM C1583 Test

To evaluate the bond strength between the PC overlays and the PCC substrates, the test specimens were meticulously prepared in accordance with ASTM C1583. The preparation involved several distinct stages, from substrate preparation through to the final pull-off test configuration.

Initially, portland cement concrete (PCC) substrate blocks were cast in molds with internal dimensions of 20 cm × 20 cm × 8.89 cm. In the first step, the molds were filled to a depth of 6.35 cm with PCC, thus creating a substrate layer with dimensions of 20 cm × 20 cm × 6.35 cm. These substrates were cured for 28 days under 100% relative humidity. Following this initial curing period, the PCC specimens were divided into two groups for different environmental conditioning:

1. Healthy Substrates: these specimens were kept under normal laboratory conditions for surface treatment and PC overlay application without induced deterioration.

2. Deteriorated Substrates: These specimens were subjected to sulfate exposure for 210 days to induce chemical deterioration.

For both groups, the surface of the PCC substrates designated for overlay was prepared according to the International Concrete Repair Institute (ICRI) guidelines for polymer concrete overlays. Figure 26 shows representative PCC specimens from both conditioning groups after the completion of the surface preparation.

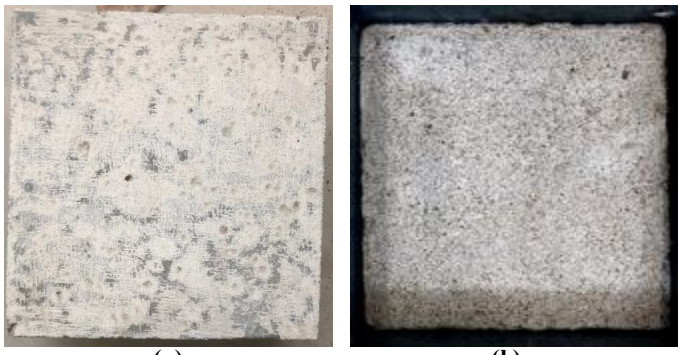

Figure 26: The PCC specimens after performing the surface preparation. (a) cured in normal conditions and (b) cured in the presence of sulfate ions.

After surface preparation, the PCC blocks were placed back into the original 20 cm × 20 cm × 8.89 cm molds. The prepared polymer concrete (PC) overlay material was then cast on top of the prepared PCC substrate, filling the remaining depth of the molds. This resulted in a PC overlay thickness of approximately 2.54 cm. These composite specimens were then allowed to cure for 7 days under ambient laboratory conditions (approximately 23 ± 2 °C and 50 ± 5% RH), forming monolithic test units composed of the PCC substrate and the integrally bonded PC overlay.

These monolithic units were then prepared for the direct tensile pull-off test. Using a universal coring machine equipped with a diamond-bit core drill, 5 cm diameter cores were drilled to a depth of 5.08 cm. This depth ensured that each core passed completely through the PC overlay and extended slightly into the PCC substrate. Steel tensile loading dollies, also 5 cm in diameter, were

then bonded to the top surface of the PC cores using a high-strength, two-part epoxy adhesive. The epoxy was allowed to cure fully according to the manufacturer's specifications, ensuring a strong bond between the dolly and the PC overlay. Figure 27 and Figure 28 illustrate the core drilling process, the attachment of the tensile loading dollies, and the Hydrajaws 2000 pull-off test apparatus employed for applying the tensile load.



Figure 27: Preparation of the test specimens for the pull-off method (left–right), drilling cores, and the attachment of tensile loading devices.



Figure 28: Pull-off test setup.

The pull-off tests were conducted using the Hydrajaws 2000 portable adhesion tester, which applied a continually increasing uniaxial tensile load perpendicular to the plane of the overlay

until failure occurred. The maximum tensile load at failure (P, in Newtons) was recorded. The bond strength, or the tensile strength of the material at the point of failure, was then calculated using equation below:

$$Bond\ or\ Tensile\ Strength\ (MPa) = \frac{P}{A}$$

where A is the cross-sectional area of the cored test specimen (mm^2).

According to ASTM C1583/C1583M-20, several failure modes are possible: (i) cohesive failure within the substrate (PCC), indicating the tensile strength in PCC and overlay are stronger than the substrate; (ii) cohesive failure within the overlay material (PC), indicating the tensile strength in PC and substrate are stronger than the over-lay; (iii) adhesive failure at the bond interface between the overlay and the substrate, representing the true bond strength as this is the weakest plane; or (iv) failure at the interface between the loading dolly and the overlay. For this study, adhesive failure at the PC/PCC interface (iii) was considered valid for assessing bond performance between the PCC and PC. Results from tests where failure occurred primarily at the dolly/overlay interface (iv) were disregarded as per the ASTM guidelines, as these do not reflect the properties of the overlay system itself. The location of failure for each test was carefully recorded.

6.2.5. Microscopic Analysis

Advanced light microscopy was performed using a Keyence VHX-7000 ultramicroscope at the University of Oklahoma's Samuel Roberts Noble Microscopy Lab (SRMNL) to obtain an understanding of failure surfaces. Information on the homogeneity and distribution of

nanomaterials was obtained from microscopic images. The microscope is fully automated and has the ability to capture images at a high magnification of up to 6500x.

6.3. Results and Discussion

6.3.1. Normal Condition

Twelve cylinders in total—six PCC and six PC—were tested to ascertain the two distinct varieties of concrete's compressive strengths in accordance with ASTM C579 and ASTM C39, respectively. The results obtained are shown in Table 3. With a two percent coefficient of variation, the average compressive strengths of PC and PCC were 59.9 and 67.4 MPa, respectively. This shows how consistently the results were obtained for both PCC and PC. A prior investigation examined the compressive strengths of five cylinders measuring 50.8 mm by 101.6 mm for PC and PCC, concluding that the respective mean compressive strengths were 68.9 ± 5.1 MPa and 53.9 ± 5.8 MPa (Murcia et al. 2022). As a result, the compressive strength found during the initial PC compressive strength testing is within the range of values reported in the literature. For PC and PCC, the average modulus of rupture was 23.7 MPa and 7.8 MPa, respectively. The consistency of the tests was shown by the coefficient of variance, which was 3% for PC and 1% for PCC. Two concrete mixes with comparable compressive strengths were produced, based on the findings of the modulus of rupture and compressive strength tests. According to the literature, the tensile strength of PC, as determined by the modulus of rupture, is approximately three times higher than that of PCC, indicating a suitable mix design.

Table 3: Unconfined compression and modulus of rupture test results of PCC and PC.

Property	PCC	PC

Compressive Strength (MPa)	67.4 ± 1.1	59.9 ± 0.9
Modulus of Rupture (MPa)	7.8 ± 0.1	23.7 ± 0.7

Following the 48-h dispersion process, visual observation of the polymer liquid component, as depicted in Figure 29, demonstrated the stabilization of MWCNTs in the resin, indicating efficient dispersion. Subsequent microscopic observations of the cured PC specimens (Figure 30) revealed the presence of small, dark particles, inferred to be MWCNTs or small agglomerates, distributed homogeneously within the nanomodified polymer concrete (e.g., PC-FC50, Figure 30a). These were absent in the non-modified polymer concrete (PC-Neat, Figure 30b). This homogeneous distribution may also be attributed to the surface coating of aggregate particles by the carbon nanotubes due to cohesive forces.

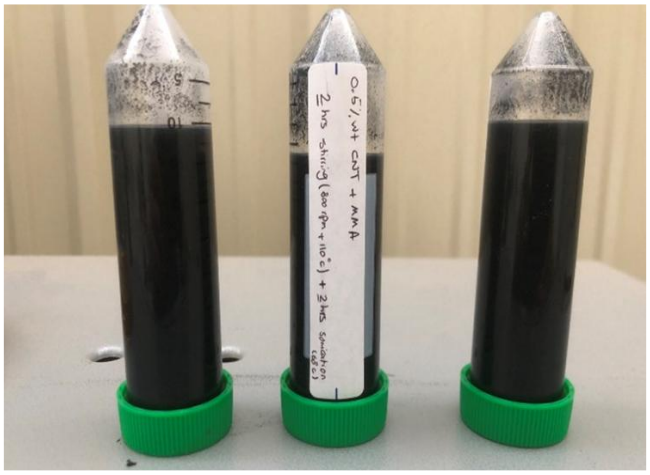

Figure 29: Dispersion stabilization of MWCNT-modified resin after 48 h.

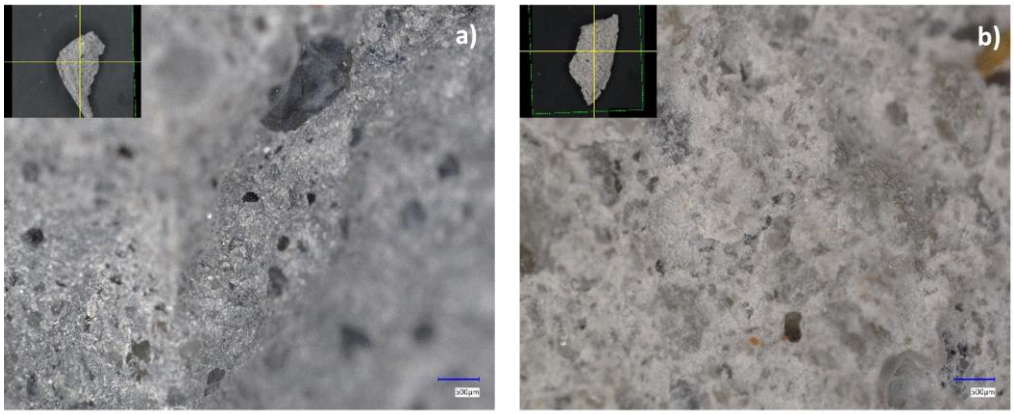

Figure 30: Microscopic images of the neat and nanomodified PC specimens: (a) PC-FC50, (b) PC-Neat.

The pull-off strength of various polymer concrete (PC) compositions with PCC substrates was evaluated according to ASTM 1583 standards. Figure 31 presents the results obtained. For each overlay mix type, the bar on the left shows the average pull-off strength of all tested cores, whereas the bar on the right shows the average strength of only those cores that failed at the polymer-concrete/concrete interface and had bond strengths greater than 1.72 MPa. This threshold of 1.72 MPa (250 psi) was used because test series were considered valid only when at least two pull-off strengths exceeded 1.72 MPa, following Transpo Inc. guidelines.

The neat polymer concrete (PC-Neat) exhibited a high and consistent average pull-off strength of 2.82 MPa with a standard deviation of 0.30 MPa. In contrast, the polymer concrete with 0.25% pristine MWCNTs (PC-P25) showed a significantly lower average pull-off strength of 0.039 MPa. It can be concluded that at 0.25%, the concentration of MWCNT inside the resin was not enough to make changes in better bonding between the resin and aggregates. Despite considering only specimens with at least two pull-off strengths over 1.72 MPa, the average considered strength increased to 0.099 MPa, but the overall performance remained poor. The polymer concrete with 0.5% pristine MWCNTs (PC-P50) demonstrated no measurable pull-off strength, as all tested samples failed to meet the minimum criteria. The 0.25% COOH-functionalized MWCNTs (PC-

FC25) mix showed an average pull-off strength of 2.29 MPa and a standard deviation of 0.79 MPa, indicating reliable performance with a considered strength of 2.32 MPa. Similarly, the 0.5% COOH-functionalized MWCNTs (PC-FC50) composition had an average pull-off strength of 2.22 MPa and a standard deviation of 1.26 MPa, with a considered strength of 2.71 MPa, demonstrating consistent bond strength. The polymer concrete with 0.25% NH2-functionalized MWCNTs (PC-FN25) had an average pull-off strength of 2.75 MPa and a standard deviation of 0.31 MPa, showing reliable performance with a considered strength of 2.54 MPa. However, the 0.5% NH2-functionalized MWCNTs (PC-FN50) mix exhibited an average pull-off strength of 1.81 MPa, with higher variability indicated by a standard deviation of 1.03 MPa and a considered strength of 2.26 MPa. It can be concluded that the reduction in pull-off strength of the nanomodified specimens happened because the dispersion of CNTs inside the resin did not cause an improvement in bonding between the MMA resin and aggregates.

Overall, the results indicate that incorporating functionalized MWCNTs into polymer concrete can induce a similar pull-off strength compared to neat polymer concrete while giving rise to a wide range of other chemical improvements, such as improvements in ductility and fracture toughness. Notably, the polymer concrete with 0.25% and 0.5% COOH-functionalized MWCNTs (PC-FC25) demonstrated the highest and most consistent average pull-off strengths of the PCC containing carbon nanotubes. In contrast, the polymer concrete with 0.25% pristine MWCNTs (PC-P25) showed minimal pull-off strength, highlighting the importance of the type and functionalization of MWCNTs in achieving the desired bond strength. These findings suggest that functionalized MWCNTs, particularly COOH-functionalized ones, are more effective in improving the bond strength of PCC than PC. Figure 32 illustrates the specimens after failure.

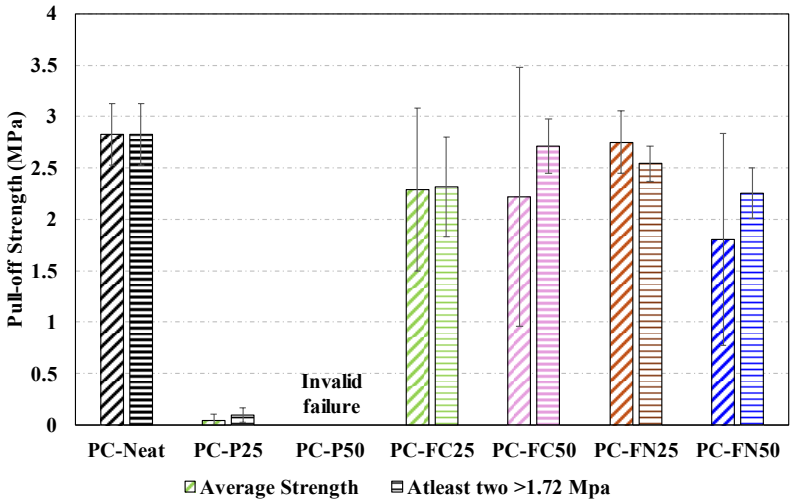

Figure 31: Pull-off strength results of specimens which were cured in normal conditions.

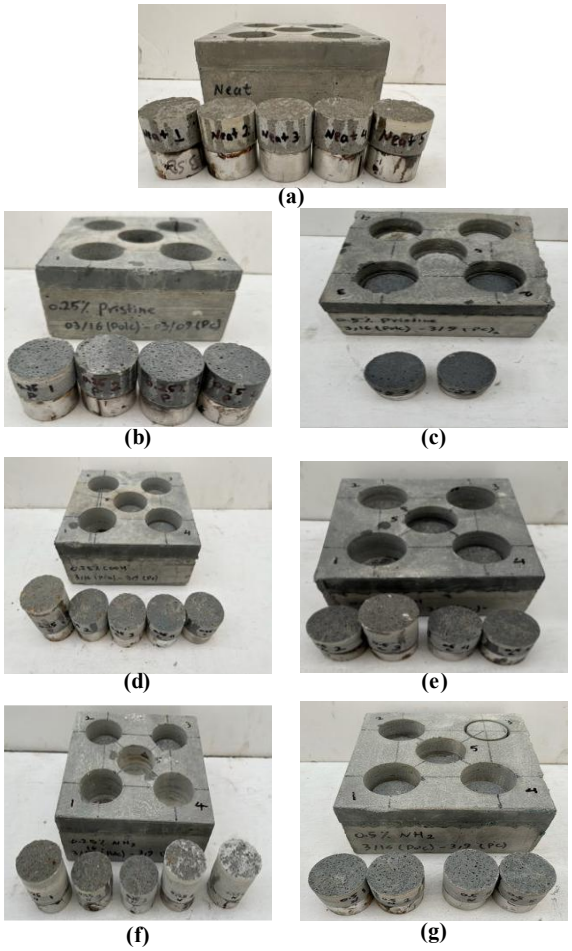

Figure 32: Specimens which were cured in normal conditions after performing the pull-off test: (a) PC-Neat, (b) PC-P25, (c) PC-P50, (d) PC-FC25, (e) PC-FC50, (f) PC-FN25, (g) PC-FN50.

6.3.2. Sulfate Conditions

In normal conditions, functionalized MWCNTs, particularly COOH-functionalized ones, showed better results in terms of the adhesion and durability of the polymer concrete overlays. However, pristine MWCNTs did not provide any significant results. Under sulfate conditions, the performance generally declined, but the 0.5% COOH-functionalized MWCNTs (PC-FC50) still provided a measurable improvement. This improvement highlights their potential in environments subjected to aggressive chemical attacks, such as coastal regions and industrial zones (Camacho et al. 2014). Furthermore, this highlights the importance of selecting appropriate functionalized MWCNTs for maintaining the performance of polymer concrete overlays in harsh environments, which is crucial for developing robust and long-lasting solutions for bridge deck maintenance and repair. The specimens after failure are depicted in Figure 33.

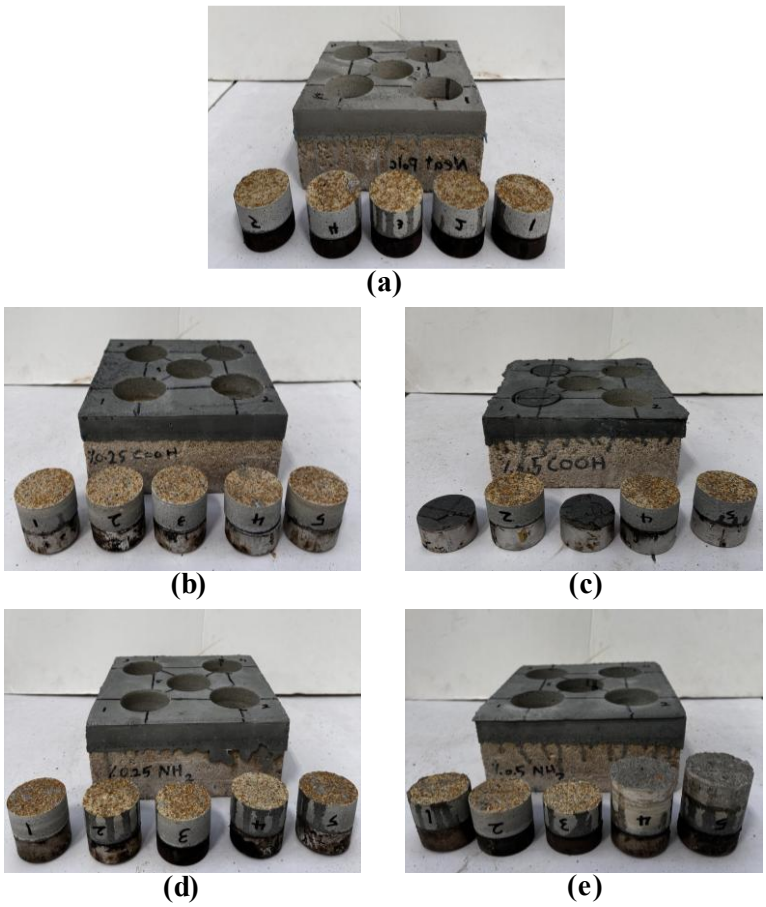

Figure 33: Specimens which were cured in sulfate conditions after performing the pull-off test: (a) PC-Neat, (b) PC-FC25, (c) PC-FC50, (d) PC-FN25, (e) PC-FN50.

Figure 34 compares the pull-off strength of PC-Neat and PC-FC50 in normal and sulfate environments. As one can see, in normal conditions, the bond strength between the neat polymer concrete and healthy substrate was higher than the polymer concrete containing 0.5% COOH. However, it should be mentioned that in deteriorated conditions, when the substrate had experienced damage due to sulfate attack, the bond strength of the polymer concrete containing 0.5% COOH was 15% higher than the neat polymer concrete.

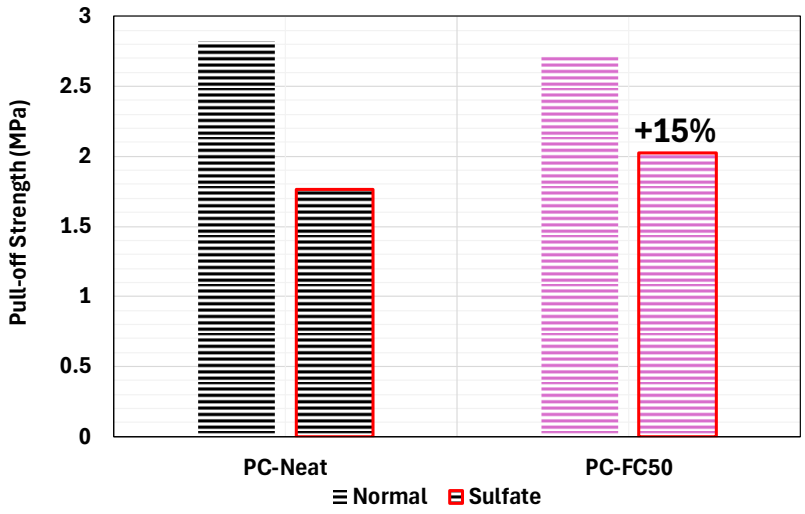

Figure 34: Comparison between PC-Neat and PC-FC50 in healthy and sulfate conditions, considering one or two of the assumptions.

Sulfate attack typically leads to the formation of ettringite ($Ca_6Al_2(SO_4)_3(OH)_{12}\cdot 26H2O$) and gypsum ($CaSO_4\cdot 2H_2O$) in a concrete substrate. The chemical structures of these produced materials are presented in Figure 35. These secondary products weaken the microstructure of the concrete, creating a more reactive surface with higher surface energy (Akbarpour et al. 2022c). The chemical reactions are represented in Equations (1) and (2):

$$Ca(OH)_2 + SO_4^{-2} + 2H_2O \rightarrow Ca(SO)_4 \cdot 2H_2O(Gypsum) \quad (2)$$

$$C_3A + 3CaSO_4^{-2} \cdot 2H_2O + 26H_2O \rightarrow Ca_6Al_2(SO_4)_3(OH)_{12} \cdot 26H_2O(Ettringite) \quad (3)$$

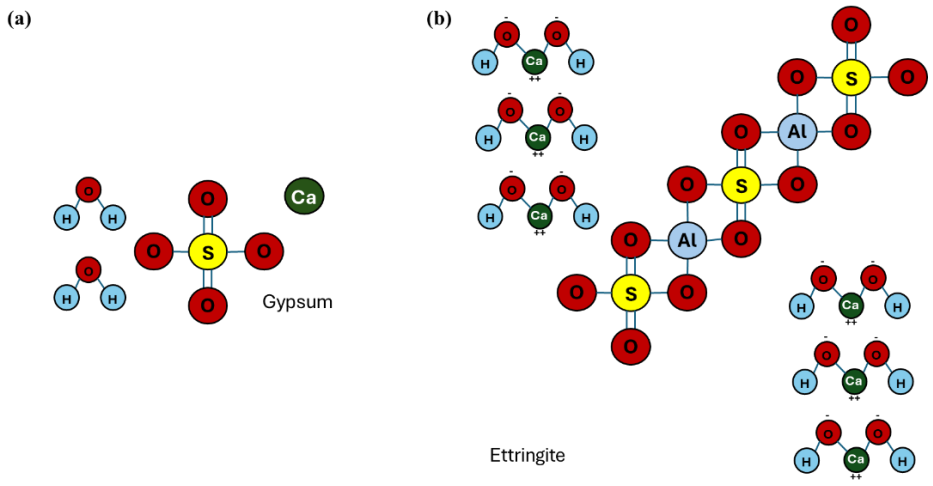

Figure 35: The chemical structures of (a) gypsum and (b) ettringite.

The COOH functionalization facilitates stronger interfacial bonding in harsh environments by introducing polar groups that interact with the polymer matrix and substrate, as observed in (Theodore et al. n.d.). This interaction leads to improved load transfer and mechanical properties. This is key to ensuring that the shear lag mechanism can take place during elastic stress transfer, via the strong bonds between the MWCNTs and polymer concrete (Goh 2017). Moreover, functionalized MWCNTs, such as COOH-MWCNTs, promote better chemical bonding with the sulfate-attacked substrate. The polar groups in functionalized MWCNTs can interact with these secondary products, forming stronger interfacial bonds (Li et al. 2015a). Hydrogen bonding and ionic interactions occur between the -COOH groups of the MWCNTs and the calcium ions or sulfate ions in gypsum and ettringite. In sulfate conditions, the microcracks and weakened substrate create a more reactive surface. The chemical reactions are presented below. Also, a schematic of chemical reactions is presented in Figure 36.

$$-COOH + Ca^{2+} \rightarrow COO - Ca \; ionic \; bonds \quad (4)$$

$$-COOH + SO_4^{-2} + H_2O \rightarrow H - bonding(via\ H\ from\ COOH\ and\ O\ from\ SO_4^{-2}) \quad (5)$$

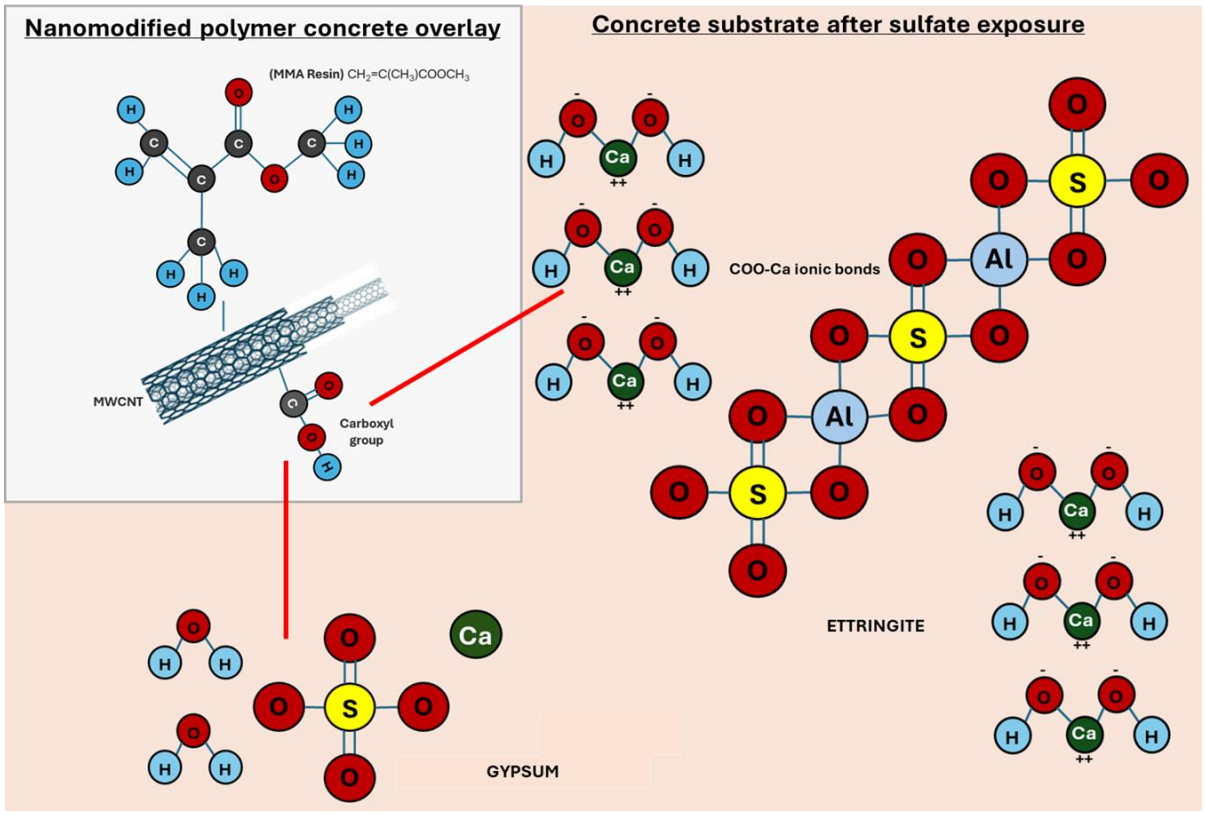

Figure 36: A schematic overview of the chemical reactions between nanomodified polymer concrete and concrete after sulfate exposure.

On the other hand, MWCNTs serve as a physical reinforcement, bridging microcracks and providing mechanical interlocking that is less significant in normal conditions (Li et al. 2019). Therefore, this dual mechanism—chemical bonding and mechanical bridging—leads to improved load transfer and bond strength. Chemical bonding is key to ensuring that the shear lag mechanism can take place during elastic stress transfer, via the strong bonds between the MWCNTs and polymer concrete; mechanical bridging is key to ensuring that the MWCNTs have the capacity to bridge cracks, after which the shear-sliding mechanism occurs and chemical bonds are disrupted, and then frictional loading takes over (Li et al. 2019). In normal conditions, however, the substrate is less reactive, and the functionalized MWCNTs do not have the same opportunity to enhance

chemical or mechanical interlocking. Consequently, neat polymer concrete, with its intrinsically high bond strength, performs better in non-degraded substrates compared to MWCNT-modified polymer concrete. This leads to the conclusion that, in deteriorated conditions, incorporating functionalized COOH can improve the bond strength between a polymer concrete overlay and concrete substrate.

6.3.3. Microscopic Analysis

Various evaluations were performed to evaluate the MWCNTs' dispersion in the resin and PC. A visual inspection was performed to evaluate the dispersion stabilization of the MWCNTs in the resin. Figure 29 depicts the resins incorporating MWCNTs after 48 h. When the dispersion in the resin was satisfactory, the process was continued via addition of the mix to the PC in order to produce nanomodified PC. The macro dispersion states of carbon fillers in the unmodified and nanomodified polymer concrete specimens were evaluated using optical microscopy (OM). A KEYENCE VHX-7000 microscope was utilized to study the macro dispersion of the carbon nano-tubes. The images clearly show shared morphological characteristics as well as notable variances in the materials under investigation. The MWCNT agglomerates had a characteristic spherical shape with diameters up to 600 μm. Also, it is acceptable to see CNT agglomerates in a matrix if there are few and they are not large (Rubel et al. 2019). Figure 30 illustrates the microscopic images of PC-Neat and PC-FC50. The microscopic images reveal a homogeneous distribution of MWCNTs in PC-FC50, corresponding to its superior bond strength. Similar observations were reported in Rubel et al. (2019), where smaller agglomerates improved interfacial adhesion. As one can see in Figure 37, there are more PC particles attached to the PCC after failure in sulfate conditions, which shows that the tensile strength of the PC decreased after 210 days of exposure to the sulfate environment.

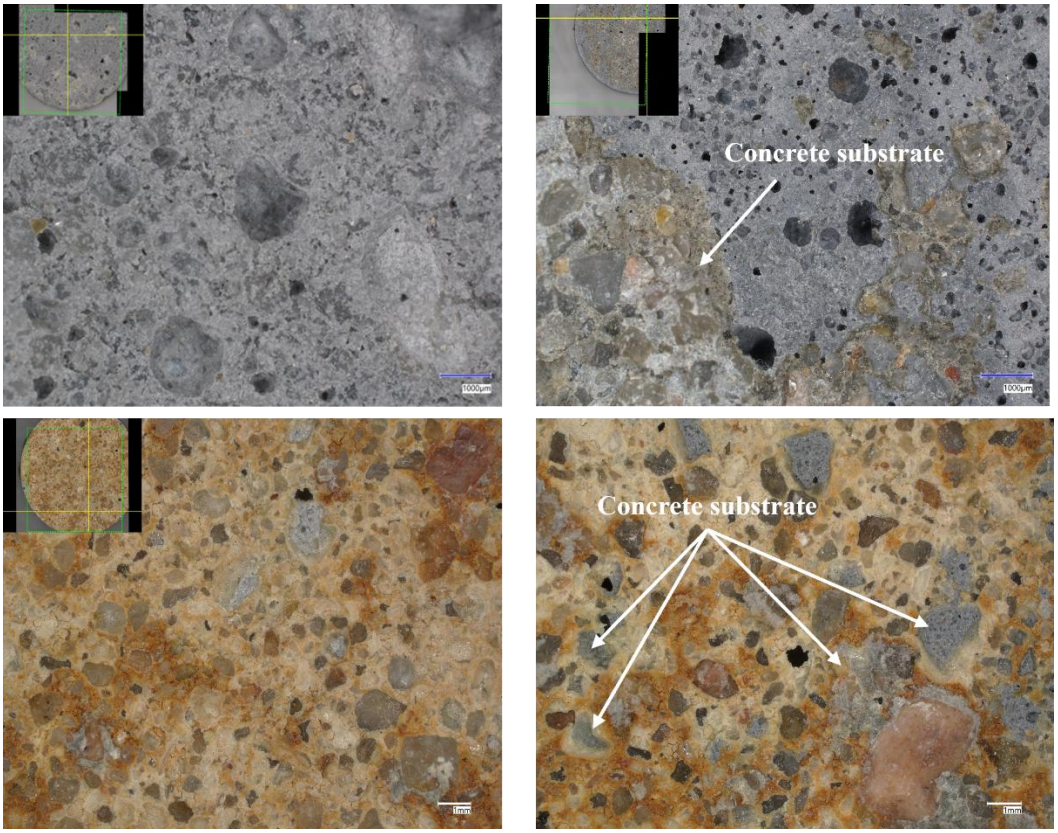

Figure 37: Microscopic images of the surface of the interface of PCC and PC after performing the pull-off test: (top) healthy conditions and (bottom) after sulfate attack.

6.4. Discussion

The findings of this study indicate that MWCNTs interact more effectively with concrete substrates exposed to sulfate environments. As previously noted, polymer concrete modified with MWCNTs exhibited a 15% increase in pull-off strength compared to unmodified (neat) polymer concrete when bonded to sulfate-exposed substrates. However, in normal curing conditions, neat polymer concrete showed the highest pull-off strength compared to all MWCNT-modified mixes. These observations suggest that while MWCNTs may reduce bond strength under standard conditions, their benefits become more pronounced in chemically aggressive environments. Similar improvements in the performance of cementitious materials exposed to sulfate ions through the

use of CNTs have been reported in previous studies (Bheel et al. 2023; Camacho et al. 2014; Li et al. 2015b).

Comparing the different MWCNT types, it was evident that functionalization played a crucial role. Pristine MWCNTs (PC-P25 and PC-P50) generally resulted in a significant degradation of bond strength compared to neat PC under normal conditions, likely due to agglomeration and poor interfacial bonding. In contrast, both COOH-functionalized (PC-FC25, PC-FC50) and NH2-functionalized (PC-FN25, PC-FN50) MWCNTs demonstrated performance closer to, albeit generally not exceeding, that of neat PC in normal conditions. However, the key benefit of functionalized MWCNTs, particularly PC-FC50, emerged under sulfate exposure, where they helped retain or even enhance bond strength relative to neat PC under the same deteriorated conditions.

Also, statistical comparisons of mean pull-off strengths (N = 5 per group for the analyzed raw data) were made using independent two-sample t-tests (Welch's). Under healthy conditions, PC-Neat (2.82 MPa) was compared to modified groups: PC-FC25 (2.29 MPa), PC-FC50 (2.22 MPa), PC-FN25 (2.75 MPa), and PC-FN50 (1.81 MPa). For these specific raw datasets, none of the observed differences reached statistical significance (all $p > 0.05$). Under sulfate-exposed conditions, PC-Neat (1.30 MPa) exhibited statistically significantly higher strength than PC-FC25 (0.00 MPa, $p = 0.0073$, as all samples showed no bond). The mean strength of PC-FC50 (1.65 MPa) was numerically higher than PC-Neat, though this difference was not statistically significant ($p = 0.4036$) with the current sample size. Pull-off strengths for PC-FN25 (1.23 MPa) and PC-P50 (0.74 MPa) under sulfate exposure also did not differ significantly from PC-Neat ($p > 0.05$). While these tests provide a rigorous assessment of statistical significance (using $\alpha = 0.05$), it should be

acknowledged that with a sample size of N = 5 per group, the statistical power to detect more subtle, yet potentially real, differences are limited.

6.5. Conclusions

This study examined the influence of multi-walled carbon nanotubes on the bond performance of polymer concrete overlays applied to both sound and deteriorated concrete substrates, particularly under sulfate exposure. The key conclusions are as follows:

1. Enhanced Performance with COOH-functionalized MWCNTs: The PC mix containing 0.5% COOH-functionalized MWCNTs (PC-FC50) achieved high average pull-off strengths of 2.22 MPa under normal conditions and 1.65 MPa under sulfate exposure, demonstrating reliable performance across environments.
2. Superiority of Functionalized MWCNTs: Functionalized MWCNTs outperformed pristine variants in improving the mechanical properties of PC. For example, 0.25% NH2-functionalized MWCNTs (PC-FN25) achieved an average pull-off strength of 2.75 MPa in normal conditions and 1.23 MPa in sulfate-exposed conditions.
3. Limited Effectiveness of Pristine MWCNTs: The incorporation of pristine MWCNTs (PC-P25 and PC-P50) did not lead to significant improvements in bond strength, underscoring the necessity of functionalization for performance enhancement.
4. Durability in Aggressive Environments: Functionalized MWCNTs helped preserve the bond integrity of PC overlays under sulfate exposure. Notably, the 0.5% COOH-functionalized mix achieved a 15% higher pull-off strength compared to neat PC in sulfate conditions, confirming their potential in chemically aggressive environments.

5. Importance of Dispersion Techniques: Effective dispersion methods, such as magnetic stirring and ultrasonication, were critical in achieving uniform MWCNT distribution within the polymer matrix—essential for realizing the mechanical advantages of nanomodified PC overlays.

7. CHAPTER 7: Role of Grout and GFRP Slip Liner on the Circumferential Behavior of Retrofitted Corroded Metal Culverts

7.1. Literature Review

7.1.1. The Challenge of CMP Deterioration

Corrugated metal pipes (CMPs) are fundamental components of transportation and drainage infrastructures, prominently adopted for their low initial costs, ease of fabrication, and straightforward installation (Hoult et al. 2013). These pipes represent a cornerstone, widely utilized due to these initial advantages. Despite these advantages, CMPs face substantial deterioration primarily due to corrosion (Moore 2001). Corrosion involves the electrochemical degradation of the metal (typically galvanized or aluminized steel), leading to material thinning, reduced structural capacity, and eventual perforation. Environmental elements such as water chemistry (pH, dissolved oxygen, aggressive ions like chlorides and sulfates), aggressive soil characteristics (resistivity, pH, moisture, organics), abrasion from sediment load, and galvanic corrosion interactions significantly accelerate their degradation, posing challenges to infrastructure longevity and public safety (Smith et al. 2015). Low pH and low soil resistivity are particularly aggressive factors. This corrosion, particularly in culverts beneath roads, necessitates frequent maintenance and costly rehabilitation or replacement, significantly impacting transportation budgets and public inconvenience. The typical design lifespan of 50 years is often not achieved, with service life potentially reduced to less than 30 years in aggressive environments, highlighting the need for condition-based assessment rather than relying solely on age (Moore 2001). Common defects stemming from deterioration include shape distortion, joint misalignment or separation, and

perforations, which can lead to infiltration of surrounding soil, formation of voids, and potential roadway subsidence (Moore 2001).

Similar to the corrosion issues affecting steel reinforcement in concrete beams (Project 1) and the general degradation impacting concrete substrates needing overlays (Project 2), the corrosion of CMPs represents a major infrastructure durability challenge, motivating the search for advanced, corrosion-resistant rehabilitation materials and techniques.

7.1.2. Slip Lining as a Rehabilitation Solution

In response to deteriorating culverts, trenchless rehabilitation techniques have gained prominence for minimizing surface disruption and costs (McKim 1997). Among available rehabilitation techniques, slip lining emerges prominently as a widely adopted trenchless method that offers cost-effective and minimally disruptive solutions for rehabilitating deteriorated culverts (Moore and Hu 1996; Zhao and Daigle 2001). Slip lining involves inserting a smaller diameter liner pipe within an existing host pipe and typically filling the annular gap between the liner and host with grout (McAlpine 2006). The trenchless nature reduces traffic delays, environmental disturbance, and enhances safety compared to open-cut replacement. Installation can involve discrete pipe segments joined inside or pulling/pushing a continuous liner pipe (Syachrani et al. 2010). It is important to note that the specific liner material, installation method, and the intended role of the grout significantly influence the design and performance, requiring a tailored approach rather than a generalized one. While excavation along the alignment is minimized, preparatory work like cleaning, obstruction removal, flow bypass, and potential insertion/reception pits can still be substantial (Moore and Hu 1996).

7.1.3. Liner Materials: HDPE and the Emergence of GFRP

Various materials are used for slip liners, including thermoplastics (HDPE, PVC), thermosetting composites (GFRP), and traditional materials (steel, concrete). High-density polyethylene (HDPE), noted for corrosion resistance, flexibility, and superior hydraulic properties, is frequently employed for this application (Haghani et al. 2021). Its flexibility aids installation, and smooth surfaces (Manning's n ~0.009-0.012) enhance hydraulics (Haghani et al. 2021). However, HDPE has relatively low stiffness and strength and is susceptible to long-term creep deformation under sustained load, often necessitating reliance on the grout for structural capacity (Moore and Hu 1996). Standards like ASTM F585 and AASHTO M326 govern its use.

Recognizing the limitations of traditional materials such as steel (corrosion susceptibility) and HDPE (lower structural capacity, creep), (Abdellatef et al. 2021) advocated for glass fiber-reinforced polymer (GFRP) slip liners. GFRP is a composite of high-strength glass fibers (providing strength/stiffness) embedded in a polymer resin matrix (polyester, vinyl ester, or epoxy, which binds fibers and provides protection). These liners, characterized by corrosion resistance, reduced weight (high strength-to-weight ratio), and superior hydraulic performance, represent a promising alternative (Liu et al. 2005). GFRP's key advantage is its excellent corrosion resistance, making it highly durable in aggressive environments where CMPs degrade rapidly, leading to projected service lives of 75-100 years. Its hydraulic smoothness (Manning's n ~0.009-0.011) is comparable to HDPE (Yan et al. 2016).

(Haghani et al. 2021) provided an extensive evaluation of fiber-reinforced polymer (FRP) composites, especially glass FRP (GFRP), highlighting their suitability as alternative materials for culvert construction and rehabilitation. Their research emphasized improved lifecycle costs,

exceptional durability, and reduced maintenance demands compared to traditional steel culverts. FRP composites, with their intrinsic corrosion resistance, lightweight properties, and ease of installation, emerged as sustainable and economically viable solutions for new construction and rehabilitation projects alike. Compared directly to HDPE, GFRP offers substantially higher short-term strength (tensile ~550-1380+ MPa) and stiffness (flexural modulus ~20-40+ GPa), potentially allowing thinner liners or greater structural enhancement. However, GFRP is anisotropic, meaning its properties depend on fiber orientation, which must be considered in design (Bank 2007). While expected to have better long-term strength retention than HDPE, GFRP is not immune to time-dependent effects (creep rupture), and determining appropriate long-term reduction factors requires careful consideration and validated data, as standard creep tests can be challenging to apply.

7.1.4. The Critical Role of Grout

The grout filling the annular space is crucial, serving multiple functions: void filling (preventing liner movement/buckling), load transfer between host/liner/soil, structural support, host pipe stabilization (filling cracks/voids), and sealing against infiltration/exfiltration (Das 2021).

Several grout types are used:

Cementitious Grouts: Traditional portland cement-based grouts, often including fly ash or admixtures. Controlled Low Strength Material (CLSM or flowable fill), with high sand content and low specified strength, is common due to flowability and cost, but field issues with incomplete fill exist. Shrinkage must be controlled (Das 2021).

Cellular Grouts: Lightweight cementitious grouts with high air content (30-90%) introduced via foaming agents. Their low density minimizes hydrostatic pressure on the liner during placement,

reducing flotation/collapse risk, especially for large/flexible liners. They are very flowable but typically have lower strength than denser grouts. The trade-off between installability (low density) and structural performance (strength/stiffness) is a key consideration (Alzlfawi 2023).

Polymer and Geopolymer Grouts: Newer options include rapid-setting, high-strength, high-bond polymer grouts (polyurethane, epoxy) and geopolymers. Geopolymers, based on alkali-activated industrial byproducts (fly ash, slag), offer rapid cure, high early strength, excellent bond, superior chemical/sulfate resistance, low shrinkage, and environmental benefits. They appear highly promising for culvert rehabilitation but require more long-term field validation and specialized expertise (Kohankar Kouchesfehani et al. 2021).

Grout selection depends on structural needs (strength/stiffness), flowability, setting time, shrinkage control, density (to manage pressure), durability requirements, cost, and availability.

7.1.5. Structural Behavior and Design Considerations

The effectiveness of the rehabilitation relies heavily on the interaction between the liner, grout, host pipe, and surrounding soil, aiming for composite action where components share load effectively (Smith et al. 2015). This depends critically on the bond at the grout-liner and grout-host interfaces, achieved via mechanical interlock and chemical adhesion. Bond strength is influenced by grout properties (especially shrinkage), liner surface characteristics (roughness, material type), host pipe condition, and installation quality (Smith et al. 2015).

7.1.6. Performance Evaluation: Experimental Findings and Hydraulics

Experimental studies provide crucial insights. (Simpson et al. 2016) investigated HDPE slip liners with high-density grout, showing significant stiffness improvements and >90% deflection

reductions compared to unlined culverts, attributing stiffness mainly to the grout. Investigations by (Tetreault et al. 2020) compared grout types under severe loading: high-density grout resulted in a rigid, fully composite system with minimal deformation, while low-density grout allowed greater liner flexibility, significant deformation, and grout failure, highlighting grout quality's critical role. Complementary laboratory studies (Tetreault et al. 2020) reinforced this, showing ~10x load capacity and ~50x stiffness increases with high-strength grout compared to unrehabilitated pipes, with modest gains from low-strength grout. These studies collectively underscore the substantial impact of grout selection on rehabilitation efficacy and the importance of achieving composite action.

Advocating for GFRP, (Abdellatef et al. 2021) used FE modeling to show GFRP liners effectively withstand traffic stresses, enhancing structural reliability. Furthermore, (ChennaReddy 2016) identified critical design factors for GFRP liners (wall thrust, bending, buckling, deflection) and used FEA to confirm their stress resistance under traffic loads, validating their suitability. (Tetreault et al. 2020) emphasized the mechanics of liner-grout interaction, clarifying that fully bonded composite behavior enhances performance, while compromised bonding reduces effectiveness.

Hydraulic performance is another key consideration. While slip lining reduces diameter, the smoother surfaces of HDPE and GFRP liners (Manning's n ~0.009-0.012) compared to deteriorated CMPs (n ~0.022+) often maintain or even improve flow capacity. This hydraulic efficiency is essential for effective drainage and flood management.

7.1.7. Research Gap and Proposed Investigation

While the potential of Glass Fiber-Reinforced Polymer (GFRP) slip liners for rehabilitating corroded corrugated metal pipes (CMPs) is recognized, and some longitudinal testing data exists,

a critical knowledge gap persists regarding their circumferential structural behavior under realistic loading conditions. Specifically, there is a lack of experimental data quantifying how different grout types (e.g., cementitious vs. polymeric) interact with the GFRP liner and influence the composite ring stiffness and load capacity, particularly when rehabilitating CMPs that have undergone corrosion. This deficiency is compounded by the absence of standardized testing protocols specifically for GFRP slip-lined CMPs, hindering the development of reliable design parameters, such as the stiffness factor, needed for safe and efficient field implementation. This research directly addresses this gap by undertaking circumferential two-point bending tests on both uncorroded and corroded CMP specimens rehabilitated with GFRP liners using different grout systems, aiming to provide the necessary experimental data to characterize circumferential performance and derive key design parameters.

7.2. Materials and Methods

Corrugated metal pipes (CMPs) utilized in this research were procured by Dub Ross Company in Oklahoma. The obtained pipes had a nominal diameter of 36 inches and were subsequently cut to 12-inch lengths to create uniform test specimens, as illustrated in Figure 38. Among the four acquired CMP sections, two were designated for testing in an uncorroded state, while the remaining two underwent controlled corrosion. Since all CMPs initially featured galvanized surfaces, galvanization was systematically removed using a grinder to facilitate uniform corrosion testing conditions. The process is depicted in Figure 38.

Glass Fiber-Reinforced Polymer (GFRP) pipes with a nominal diameter of 28 inches were also procured for the slip-lining process and were similarly cut into 12-inch segments to match the CMP specimens. Additionally, cementitious and polymeric grouts required for filling the annular

spaces between CMP and GFRP liners were obtained from Euclid Chemical. Figure 39 shows the GFRP pipes used in this study. represents the schematic view of the pipes tested.



Figure 38: Corrugated steel pipes used in this study



Figure 39: GFRP pipes used in this study.

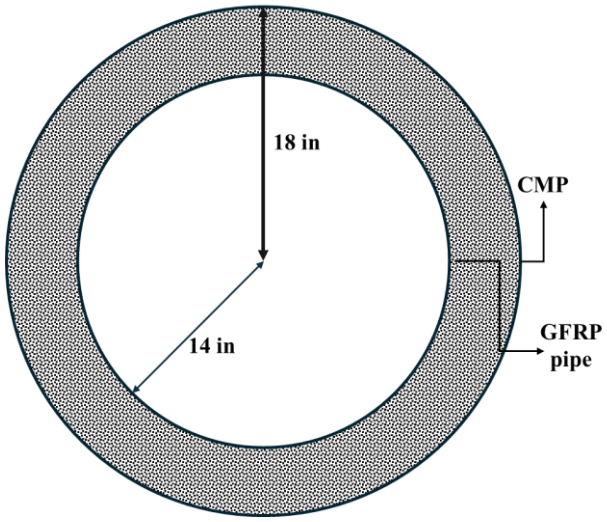

Figure 40: Schematic view of composite pipe dimensions

7.2.1. Accelerated Corrosion Procedure

To simulate and expedite the corrosion process of corrugated metal pipes (CMPs) under controlled laboratory conditions, an accelerated corrosion procedure was implemented. This method aimed to replicate the environmental factors contributing to corrosion, thereby facilitating the assessment of material degradation over a condensed timeframe.

Two CMP sections, each measuring 36 inches in diameter and 12 inches in length, were prepared for evaluating the effect of corrosion. To induce corrosion at the crown, the galvanized coating on the outer top (crown) region of each CMP section was mechanically removed using a grinder, exposing the bare steel in that region to the environment, while the rest of the pipe remained galvanized. This step is crucial, as the zinc coating in galvanized steel serves as a protective barrier against corrosion; its removal accelerates the onset of rusting by exposing the underlying steel to oxidative elements. Figure 41 shows specimens before and after three months of corrosion.



Figure 41: CMP specimens before and after three months of accelerated corrosion, showing the initial uncorroded sections in the tank, the corrosion setup with anode and cathode connections, and the resulting heavy rust concentrated at the crown region..

7.2.2. Mix design and compressive testing of grouts:

For this research project, two types of grouts were selected: a cementitious grout (Hi-Flow Grout) and a polymeric grout (E3-Flowable). The grout materials and their mix designs were obtained by thoroughly reviewing their technical data sheets and application guidelines provided by Euclid Chemical.

7.2.2.1. Cementitious Grout (Hi-Flow Grout):

Hi-Flow Grout is specifically designed to meet high strength, fluidity, and non-shrink criteria essential for structural grouting. It is a natural aggregate system incorporating a shrinkage-compensating binder. Its formulation ensures minimal positive expansion and non-segregating fluidity, which is ideal for high-tolerance applications. For the purposes of this project, a flowable consistency mix design was adopted. According to the manufacturer's specifications, a flowable consistency mix requires approximately 0.9 to 1.0 gallons (3.4 to 3.8 liters) of potable water per 50 lb (22.7 kg) grout bag. The mix design is also represented in Table 4. Mixing was performed for a minimum of 5 minutes to achieve uniform consistency without bleeding or segregation using a standard laboratory mixer. Following the recommended mixing water content, potable water was first added to the mixer, followed by the grout, which was mixed continuously for at least three minutes to achieve a homogeneous mixture. The grout was then placed immediately into the molds to ensure optimal performance.

Table 4: Mix design of cementitious grout

Material	Proportions (Kg/m3)
Cement	1746.15
Water	276.92

7.2.2.2. Polymeric Grout (E3-Flowable):

The E3-Flowable grout used in this project is an expansive epoxy grout system designed for critical applications requiring high flowability and strength. It comprises a three-component system: resin (Part A), hardener (Part B), and DL Technology™ aggregate (Part C). This grout is known for its dust-reduction technology, high chemical resistance, rapid strength gain, and exceptional bearing properties. The high-flow mix design adopted for this project involved one pail of resin and hardener combined with four 30 lb (13.6 kg) bags of aggregate, producing approximately 1.35 cubic feet (0.038 m^3) of grout per kit. Parts A and B were mixed separately first, then combined and mixed thoroughly for an additional two to three minutes using a standard laboratory mixer. The aggregate (Part C) was subsequently added incrementally, ensuring complete wetting of the aggregate particles before immediate placement. The grout was placed in molds, ensuring it met the required minimum thickness and avoiding excessive buildup that could induce cracking from exothermic reactions. The mix design is also represented in Table 5.

Table 5: Mix design of polymeric grout

Material	Proportions
Aggregates	1581.4 (Kg/m3)
Resin	202.3 (L/m3)
Hardener	60.46 (L/m3)

7.2.2.3. Compressive Testing:

To determine the mechanical performance of both grout types, compressive strength tests were performed using 2-inch by 2-inch (50mm x 50mm) cube specimens. The preparation and testing adhered strictly to ASTM standards. For the cementitious grout cubes, the ASTM C1107/C1107M modifications to ASTM C109 were adopted. Specimens were cast, consolidated using finger

consolidation techniques, covered with a non-reactive rigid plate, and cured under controlled moist conditions for 72 hours. Compressive strength testing was conducted at multiple curing ages, following the ASTM C109 method. The results obtained for all the tested specimens for cementitious grout is represented in Table 6. Also, Figure 42 depicts specimens before and after failure.

Table 6: Uniaxial compression test results for cementitious grout specimens

Cementitious Grout	**Load**	**Area**	**Stress**
	lbf	sq in	psi
Sample 1	37964	4	9491
Sample 2	33404	4	8351
Sample 3	29935	4	7483.75
Sample 4	43637	4	10909.25
Sample 5	34605	4	8651.25
Average	35909	4	8977.25
STD	5186.741		1296.685
COV	14%		14%



Figure 42: Cementitious grout specimens before and after failure.

For the polymeric grout, ASTM C579 Method B was employed. The cube specimens were carefully prepared, ensuring complete consolidation and proper curing at room temperature. The loading rate was precisely controlled, reflecting the differences required by the epoxy grout testing methodology. The results obtained for all the tested specimens for polymeric grout are represented in Table 7. Also, Figure 43 depicts specimens before and after failure.

Results from these tests provide essential data to verify that the grout mixes meet the structural performance requirements of the project, ensuring reliable and durable grout performance in the rehabilitated corrugated metal pipe system.

Table 7: Uniaxial compression test results for polymeric grout specimens

Polymeric Grout	**Load**	**Area**	**Stress**
	lbf	sq in	psi
Sample 1	46859	4	11714.75
Sample 2	33153	4	8288.25
Sample 3	42222	4	10555.5
Sample 4	37082	4	9270.5
Sample 5	30936	4	7734
Average	38050.4	4	9512.6
STD	6529.37		1632.343
COV	17%		17%



Figure 43: Polymeric grout specimens before and after failure.

7.2.3. Fabrication of test specimens:

The fabrication of the test specimens involved a detailed and methodical procedure designed to ensure accuracy, repeatability, and consistency across all specimens. This comprehensive process was carefully executed for both cementitious and polymeric grout specimens, initially using uncorroded pipes, and subsequently, after completing the corrosion procedure, using corroded pipes.

7.2.3.1. Initial Preparation:

The fabrication process commenced with the selection of a flat, rigid base plate, upon which a release film was applied. This release film served to facilitate easy removal of the specimens after curing, preventing any bonding between the grout and the base plate.

7.2.3.2. Positioning Pipes:

After preparing the base plate, the exact center of the plate was determined and marked to ensure symmetrical alignment of the test specimen. The corrugated steel pipe was then carefully placed

at the center of the plate, ensuring it was precisely aligned with the marked center. Once properly positioned, the GFRP pipe was inserted centrally within the steel pipe. It was crucial to maintain a consistent annular gap between the steel and GFRP pipes. To achieve uniform spacing, precise measurements were taken at multiple points along the circumference to confirm that the GFRP pipe was perfectly centered within the steel pipe, achieving an equal distance throughout the entire perimeter. Pipe placement is represented in Figure 44.



Figure 44: Placement of the pipe on a plate covered by release film

To securely hold both pipes in the correct position during the grouting process, wooden spacers were strategically placed outside the steel pipes and inside the GFRP pipe. These wooden pieces were evenly spaced around the circumference, ensuring the uniformity of the annular gap was

maintained throughout the casting and curing phases. Figure 45 shows wood spacers and how they kept the pipes in place.



Figure 45: Connecting wood pieces outside the steel pipe and inside the GFRP pipe to hold them in place during casting

7.2.3.3. Sealing Procedure:

To prevent any potential grout leakage during casting, high-quality adhesive silicone was meticulously applied around the outer base perimeter of the steel pipe and the inner base perimeter of the GFRP pipe. This sealing was crucial in maintaining the integrity of the specimen during the casting process and ensuring a clean and precise specimen boundary. Figure 46 illustrates the pipes after silicone addition.



Figure 46: Using GE advanced silicone to seal the inside of the GFRP pipe and outside of the steel pipe

7.2.3.4. Grout Casting:

Cementitious Grout:

Following proper pipe placement and sealing, grout casting commenced. The cementitious grout was prepared by adhering strictly to the manufacturer's guidelines, achieving the recommended flowable consistency. Figure 47 represents the cementitious grout casting.

Similarly, polymeric grout was mixed according to the manufacturer's high-flow specifications. The grout was carefully poured into the annular gap between the steel and GFRP pipes, ensuring a continuous and homogeneous fill to avoid any voids or air entrapment. Grout placement was

conducted from one side to the opposite, allowing uniform and controlled distribution of the grout. Figure 48 shows polymeric grout casting.



Figure 47: Uncorroded CMP with cementitious grout



Figure 48: Polymer grout mixing and curing setup, showing prepared grout batches in buckets with the mixer (top) and the slip-lined specimens immediately after polymer grout placement while curing on the support plates (bottom).

7.2.3.5. Curing Procedure:

Immediately following casting, the cementitious specimens underwent a controlled curing process to ensure optimal strength development and prevent shrinkage cracks. The specimens were covered first with damp burlap to maintain moisture conditions, then sealed with polyethylene sheeting to retain humidity. This moisture-controlled curing environment was maintained consistently for the recommended duration of 72 hours. Figure 49 represents the curing conditions of cementitious grout.



Figure 49: Curing cementitious specimens after casting

7.2.3.6. Post-corrosion Specimen Fabrication:

Once the corrosion procedure for the designated pipes was completed, these corroded pipes underwent the same meticulous fabrication process described above, maintaining strict adherence to the guidelines to ensure comparability between the uncorroded and corroded specimens.

Through these detailed and systematic procedures, consistency and precision were achieved across all fabricated specimens, facilitating accurate subsequent analysis and reliable comparisons between the performance of different grout materials and pipe conditions. Figure 50 represents the corroded specimen with polymeric grout.



Figure 50: Corroded CMP with polymeric grout

7.2.4. Preparation of the test setup:

The experimental setup preparation for performing the two-point loading tests involved several meticulous steps to ensure accuracy, repeatability, and reliability of results. The test setup included essential components such as a hydraulic jack, a 200 kips load cell, linear variable differential transformers (LVDTs), and a data acquisition system (DAQ).

Initially, the fabricated pipe specimens were carefully positioned into the loading frame. Before initiating the loading test, it was crucial to create uniform loading conditions by filling the corrugations present on the top and bottom surfaces of the pipes with a specialized high-strength gypsum cement, known commercially as Hydrostone. A uniform load transfer during the loading test is critical to accurately assessing pipe performance. Thus, the application of Hydrostone ensures a level and even surface for load distribution, preventing localized stress concentrations that could lead to premature specimen failure or inconsistent results.

To achieve optimal results, Hydrostone was carefully cast into the corrugations at both the crown and the invert of the pipes approximately 24 hours before testing commenced. This timeframe provided sufficient curing and hardening, ensuring full load-bearing capacity during testing. represents the Hydrostone, which was cast on the top and bottom of the pipes.

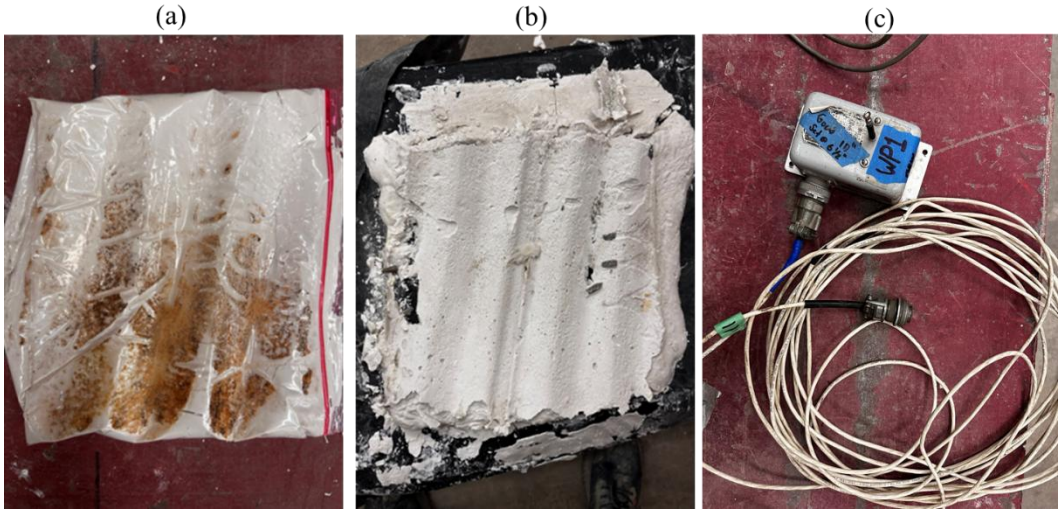

Figure 51: Hydrostone capping and instrumentation: (a) Hydrostone cast on the top of the specimen to fill the corrugations, (b) Hydrostone layer on the bottom surface after demolding, providing a flat bearing surface, and (c) string potentiometer (wire pods) used to record machine displacement during testing.

Following the Hydrostone casting and curing, instrumentation was precisely installed on each specimen. Two LVDTs were strategically positioned to measure deformation accurately during loading: one LVDT was placed vertically at the crown to capture vertical deflections, and another

was positioned horizontally at the mid-height level of the pipe to monitor lateral deformations. Figure 52 shows the LVDTs' support system, which was used to precisely place the LVDTs in the middle of the pipes. The precise placement of these LVDTs is critical, since accurate measurement of both vertical and horizontal deformations is necessary to thoroughly understand structural behavior and deformation patterns under applied loads. The test setup is depicted in Figure 53.



Figure 52: LVDT support system

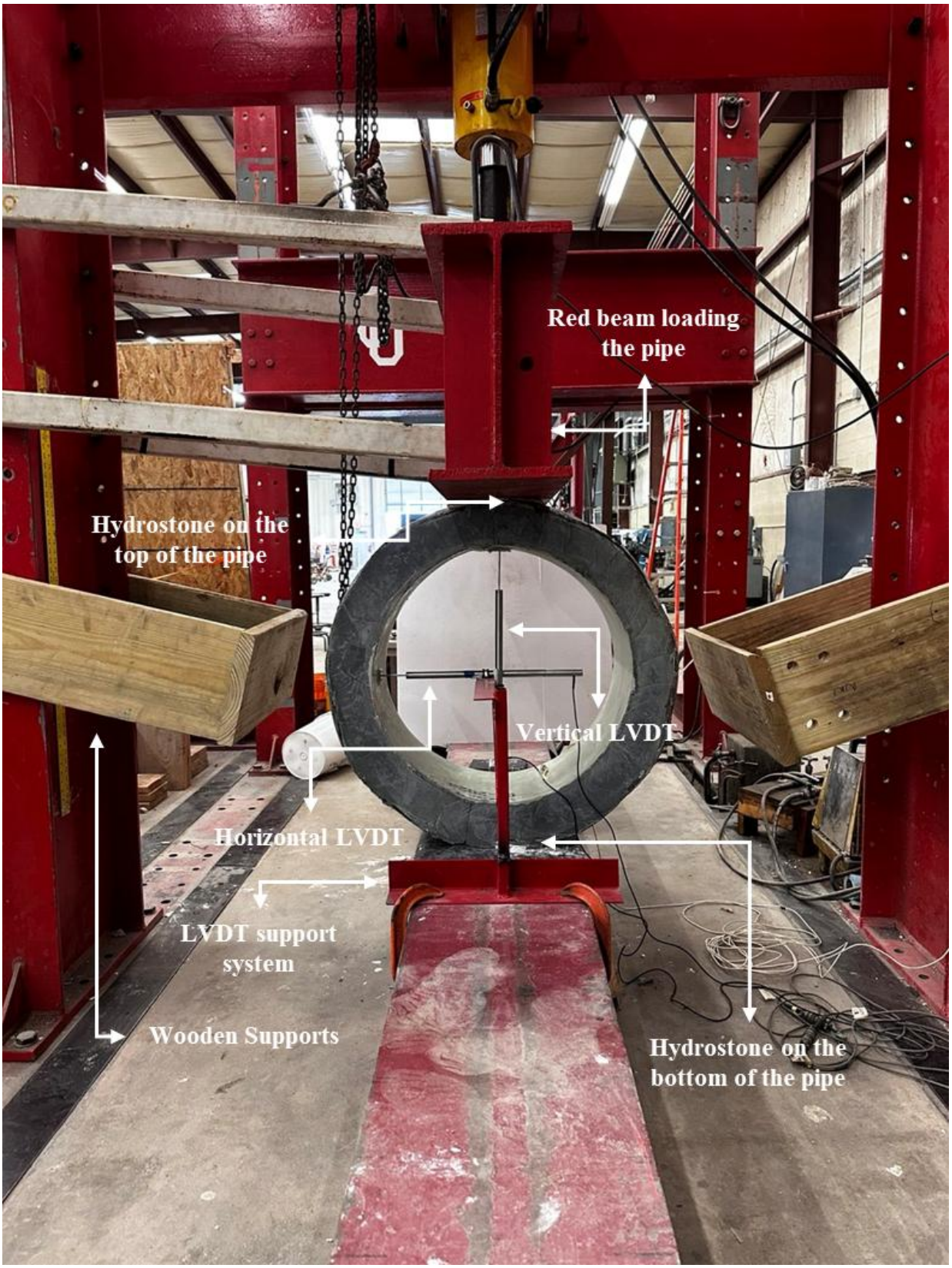

Figure 53: Two-point loading test setup used in this study

Once the instrumentation was securely mounted, the specimen was ready for testing. A robust hydraulic jack integrated with a 200 kips load cell was used to apply the load in a controlled and incremental manner. The load cell ensured precise measurement and monitoring of the applied forces throughout the experiment. This setup, consistent with (Smith et al. 2015) methodology, provided controlled loading conditions essential for evaluating the specimen's structural integrity and accurately assessing its load-bearing and deformation characteristics.

Data from the LVDTs and load cell were continuously collected via a sophisticated DAQ system, enabling real-time monitoring and recording of load versus deformation responses. This comprehensive preparation and instrumentation allowed detailed analyses of the performance characteristics of both cementitious and polymeric grout rehabilitated pipes under various loading conditions, facilitating comparisons and structural evaluations of rehabilitated and corroded pipe systems. Figure 54 shows all the specimens before the test.



Figure 54: Pipes before testing. (a) Uncorroded pipe with cementitious grout, (b) Corroded pipe with cementitious grout, (c) Uncorroded pipe with polymeric grout, (d) Corroded pipe with polymeric grout

7.3. Results and Discussion:

7.3.1. Load-Displacement of LVDTs:

7.3.1.1. Polymeric Grout

The four specimens tested, comprising both corroded and uncorroded steel pipes, each slip-lined with GFRP and grouted with either polymeric or cementitious mixes, demonstrated important structural distinctions in terms of load-displacement response, ultimate strength, and stiffness. The data consistently reveal how corrosion degrades capacity, while also showing how grout type (polymeric versus cementitious) and steel condition (corroded versus uncorroded) interact to shape overall ring behavior. A more thorough discussion of these findings, building upon the trends and numerical comparisons, is presented below.

First key observation concerns the degree of ring "compositeness" that emerges in each specimen. Where polymeric grout was used in uncorroded steel pipes, the high initial slope in the load-displacement curves and the correspondingly higher peak loads indicate that the steel, grout, and GFRP formed a nearly rigid ring at moderate deformations. This is particularly evident in the uncorroded pipe with polymeric grout (Figure 55), which reached a maximum load of about 289.66 kN—higher by approximately 22.8 % compared to its corroded counterpart at 236.17 kN (Figure 56). Notably, this specimen not only displayed a substantial capacity but also sustained moderate vertical and horizontal displacements (6.35 mm and 3.56 mm, respectively) at peak load, underscoring that polymeric grout effectively bonded to the steel pipe and GFRP, even around the corrugations. The polymer matrix also mitigates shrinkage-induced debonding–a frequent concern in cementitious systems—ensuring that steel section, grout, and liner move together under load.

By contrast, corrosion inevitably reduces the available cross-section in the steel, contributing to more localized yielding or buckling in severely thinned areas. This is evident in the corroded pipe with polymeric grout (Figure 56), which reached a maximum load of 236.17 kN. Although polymeric grout still promoted decent bonds, the roughly 22.8 % drop in peak load from the uncorroded condition highlights how steel section loss can trigger earlier failure under high ring compression and bending. In practice, pitting or partial thinning in the invert, crown, or haunches can concentrate strains and initiate microcracking in the grout or local yielding in the steel. Interestingly, the vertical displacement in the corroded sample (6.60 mm) was comparable to the uncorroded one (6.35 mm), but the horizontal displacement (1.78 mm for corroded versus 3.55 in for uncorroded) suggests the corroded ring more readily "pinched in" horizontally. This phenomenon typically arises if local thinning in the steel ring reduces its ability to carry hoop tension.

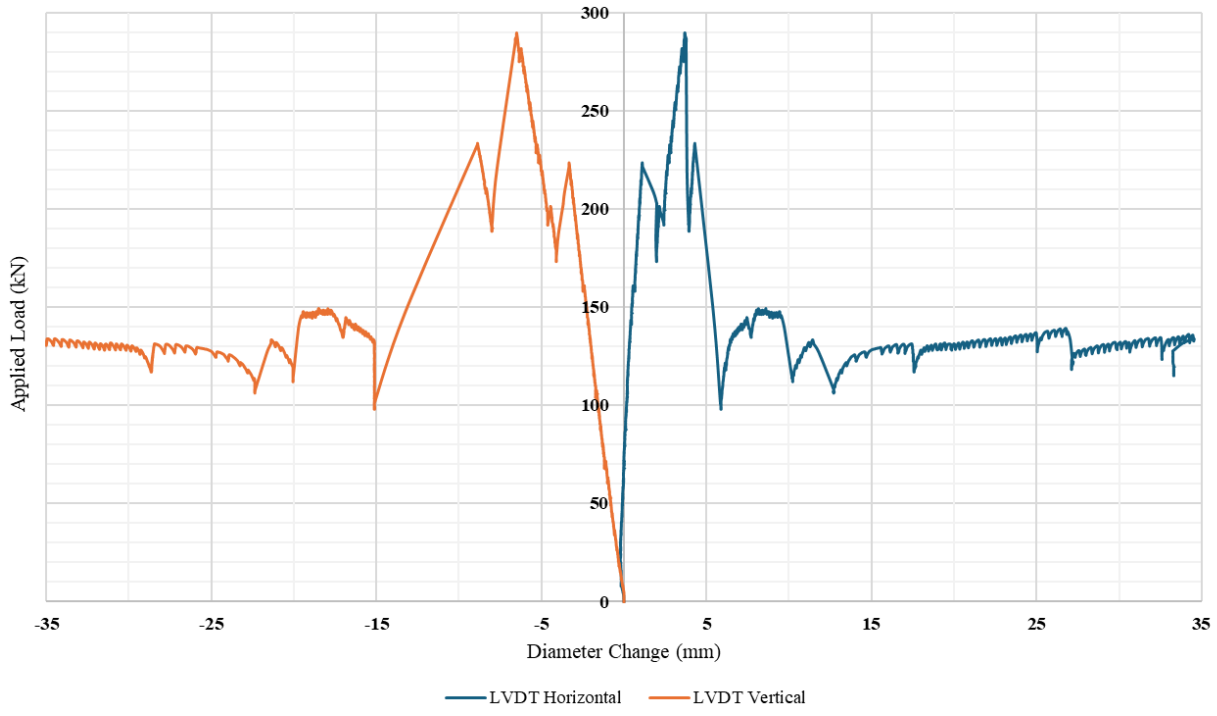

Figure 55: Load-displacement behavior of uncorroded CMP with polymeric grout

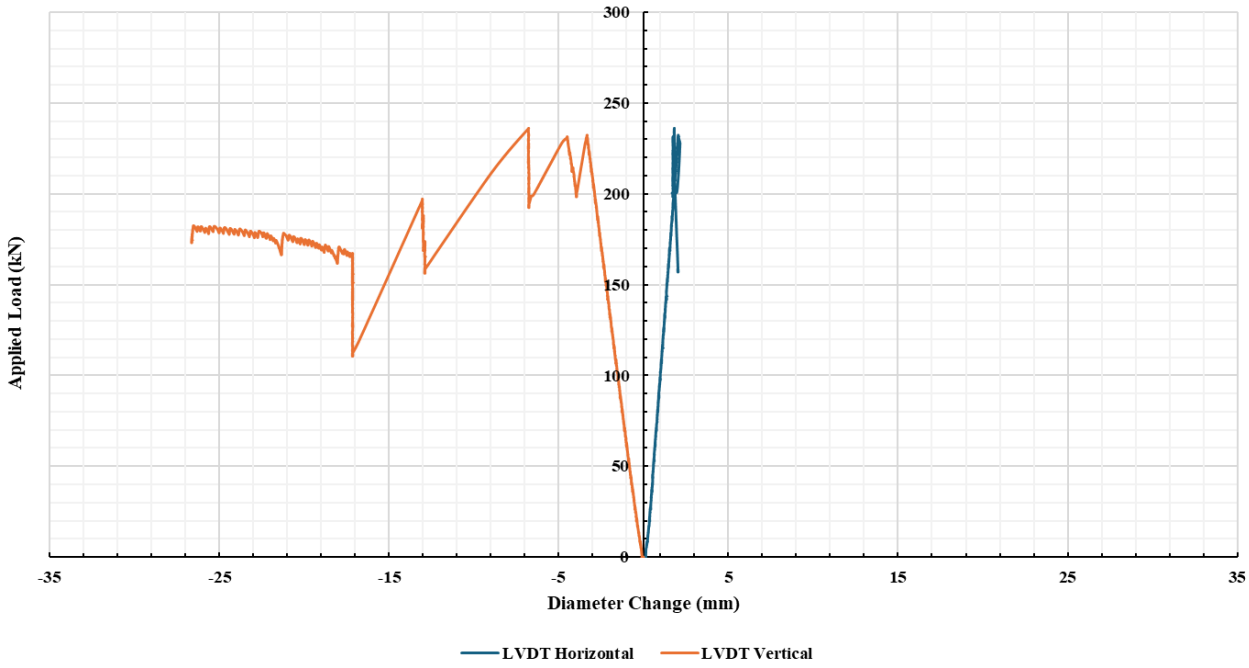

Figure 56: Load-displacement behavior of corroded CMP with polymeric grout

Under vertical loading, a circular pipe typically deforms such that the top and bottom move closer together while the sides (or springlines) tend to move outward, increasing the horizontal diameter. This outward movement is driven by the development of hoop tension in the pipe wall—a force that resists deformation by "pulling" the material around the circumference. In a pipe with intact steel, the full thickness allows it to generate substantial hoop tension, resulting in a larger horizontal expansion. In contrast, when the steel is corroded, local thinning reduces the material's ability to develop hoop tension. Consequently, the horizontal expansion is smaller, which is often described as the pipe "pinching in" horizontally. Although both pipes experience similar vertical displacements under load (6.60 mm and 6.35 mm), the corroded pipe's reduced capacity to generate hoop tension leads to a lower horizontal diameter increase (1.78 mm versus 3.55 mm in the uncorroded case), highlighting the impact of corrosion on the pipe's overall structural performance. Figure 57 depicts the uncorroded CMP with polymeric grout before and after failure. The same behavior was observed in pipes with cementitious grouts as well. Moreover, Figure 58

illustrates the bridging effect between the GFRP pipe and the rest of the composite pipe. This figure highlights how the polymeric grout has penetrated into or around the exposed GFRP fibers near the interface, forming a tight “bridge” between the liner and the grout. In other words, instead of a clean separation or gap at the pipe–grout boundary, you can see strands of GFRP that remain encased in the hardened grout. This indicates good mechanical interlock and adhesion between the liner and the grout, so that when local cracking or damage did occur, fragments of fibers and grout were still attached to one another. Such bridging generally points to strong bond development, which helps transfer load more effectively between the GFRP liner and the grout and contributes to the composite action you see at higher overall loads.



Figure 57: Uncorroded CMP with polymeric grout; (a) at the beginning of the test, (b) after failure; (c) and (d) symmetry of failure which happened in the pipes



Figure 58: Bridging between GFRP pipe and polymeric grout

7.3.1.2. Cementitious grout:

Figure 59 and Figure 60 illustrate the load-displacement behavior of uncorroded and corroded CMP with cementitious grout. The uncorroded steel pipe with cementitious grout reached about 128.58 kN in peak load—6.2 % higher than the 121 kN measured for the corroded pipe. This smaller gap could reflect multiple factors. First, unlike polymeric mixes, cementitious grouts can exhibit microcracking or partial debonding as they cure, especially near steel surfaces or in corrugation troughs. Second, while corrosion still thins the steel cross-section, the cementitious annulus may also begin to crack at lower loads if shrinkage or micro voids pre-exist, limiting the role of steel deterioration. Consequently, both uncorroded and corroded cementitious specimens displayed lower top-end loads compared to their polymeric counterparts. Furthermore, shrinkage in cement-based materials can lessen the uniformity of the bond, preventing the ring from acting as rigidly once higher stresses develop.

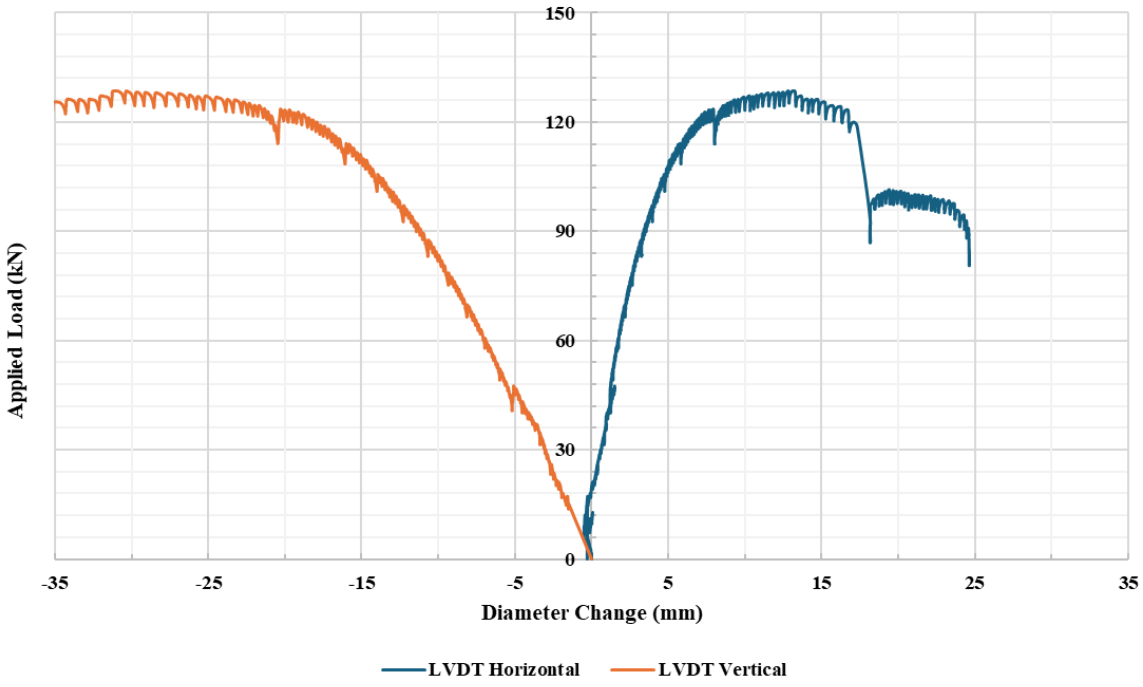

Figure 59: Load-displacement behavior of uncorroded CMP with cementitious grout

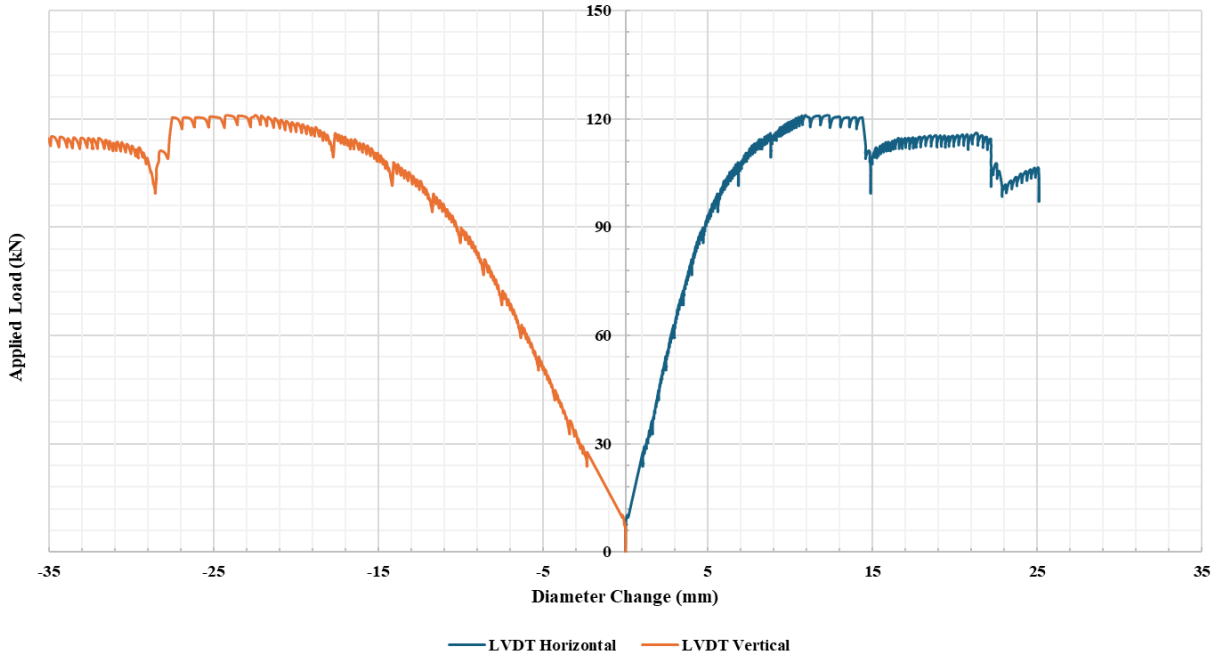

Figure 60: Load-displacement behavior of corroded CMP with cementitious grout

Another noteworthy difference is the magnitude of displacements at peak load. In uncorroded pipes with cementitious grout, vertical and horizontal deformations reached 30.99 mm and 12.95 mm,

respectively. Relative to the polymeric-grout tests, these are significantly larger, indicating that the cementitious system underwent more pronounced deflections before reaching final failure. Once the grout in tension cracks, the effective ring stiffness diminishes; however, if the steel pipe (particularly in an uncorroded condition) remains robust and the overall ring does not catastrophically lose bond, the system can continue carrying load at higher strains. For the corroded pipe, vertical and horizontal displacements dropped to 22.35 mm and 10.92 mm at peak load, reflecting how steel section loss and potentially earlier grout cracking collectively reduce ductility and ultimate capacity. Also, the bridging that happened between the GFRP pipe and polymeric grout was not observed in cementitious grout. It can be seen in Figure 62.



Figure 61: Uncorroded CMP with cementitious grout; (a) at the beginning of the test, (b) after failure



Figure 62: Pipes with cementitious grout after failure; (a) and (b) no bridging was observed between cementitious grout and GFRP pipe, (c) symmetry of failure

7.3.2. Load-Displacement Results of the Machine

The experimental results obtained from two-point loading tests are summarized numerically and visually in the provided Table 8 and Figure 63 to Figure 66, offering detailed insights into the behavior of corrugated metal pipes (CMP) rehabilitated using polymeric and cementitious grouts, under both corroded and uncorroded conditions. Precise examination of these results shows that the highest peak load was recorded for the uncorroded CMP rehabilitated with polymeric grout, reaching a maximum load of 289.66 kN at a displacement of 6.3 mm. This specimen established the benchmark for evaluating performance, exhibiting significantly superior load-bearing capacity and stiffness compared to other configurations.

When comparing the uncorroded polymeric grout specimen with the uncorroded cementitious grout specimen, which recorded a peak load of 128.58 kN at a significantly larger displacement of 22.53 mm, it becomes clear that polymeric grout provided a marked increase of approximately 125% in peak load capacity. This substantial difference indicates superior stiffness, mechanical bonding, and structural integrity of polymeric grout compared to cementitious grout. Moreover, the lower displacement at peak load (72.1% reduction) in polymeric grout highlights its greater rigidity and enhanced ability to resist deformation under loading conditions.

Evaluating the impact of corrosion, the corroded CMP specimen rehabilitated with polymeric grout exhibited a maximum load of 236.17 kN at a displacement of 6.70 mm. Compared to its uncorroded counterpart, this represents an 18.5% reduction in peak load capacity. The displacement increased by approximately 6.7%, suggesting slightly reduced stiffness and diminished load transfer capability due to corrosion-induced deterioration at the grout-pipe interface. Despite these reductions, the polymeric grout continued to exhibit robust performance,

maintaining substantial load-carrying capacity and structural resilience under deteriorated conditions.

In comparison, the corroded CMP specimen rehabilitated with cementitious grout achieved a maximum load of 121.01 kN at a displacement of 18.67 mm. This performance reflects a modest reduction of approximately 5.9% in peak load relative to the uncorroded cementitious grout specimen, which again emphasizes that cementitious grout systems inherently possess limited stiffness and bonding capacity, even before corrosion impacts their performance. However, the displacement at peak load was reduced by about 17.1%, indicating a somewhat less ductile response under corroded conditions due to early cracking or bond degradation induced by corrosion.

A direct comparison between corroded polymeric and cementitious grout systems highlights polymeric grout's pronounced advantage, with polymeric grout providing approximately 95.2% higher peak load capacity than cementitious grout under similar corroded conditions. The much smaller displacement at peak load isn polymeric grout (64% lower) further underscores its superior structural.

Table 8: Peak load and displacement at peak load of tested specimens

Specimen	Peak load (kN)	Machine displacement at peak load (mm)	Stiffness Factor (kN/mm)
Uncorroded CMP with polymeric grout	289.66	6.299	72.07
Corroded CMP with polymeric grout	236.17	6.706	56.83

Uncorroded CMP with cementitious grout	128.58	22.530	9.56
Corroded CMP with Cementitious grout	121.01	18.669	8.29

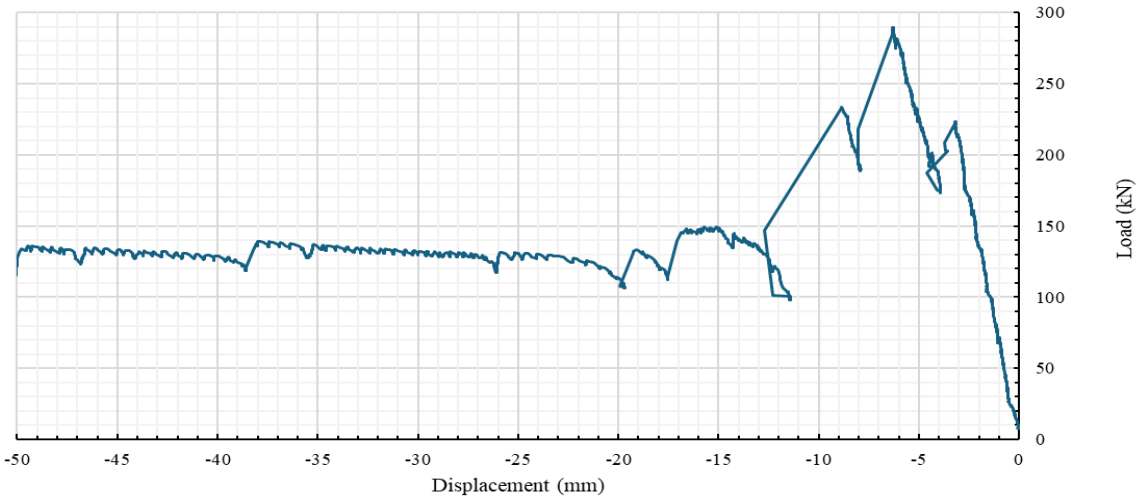

Figure 63: Load-displacement of uncorroded CMP with polymeric grout

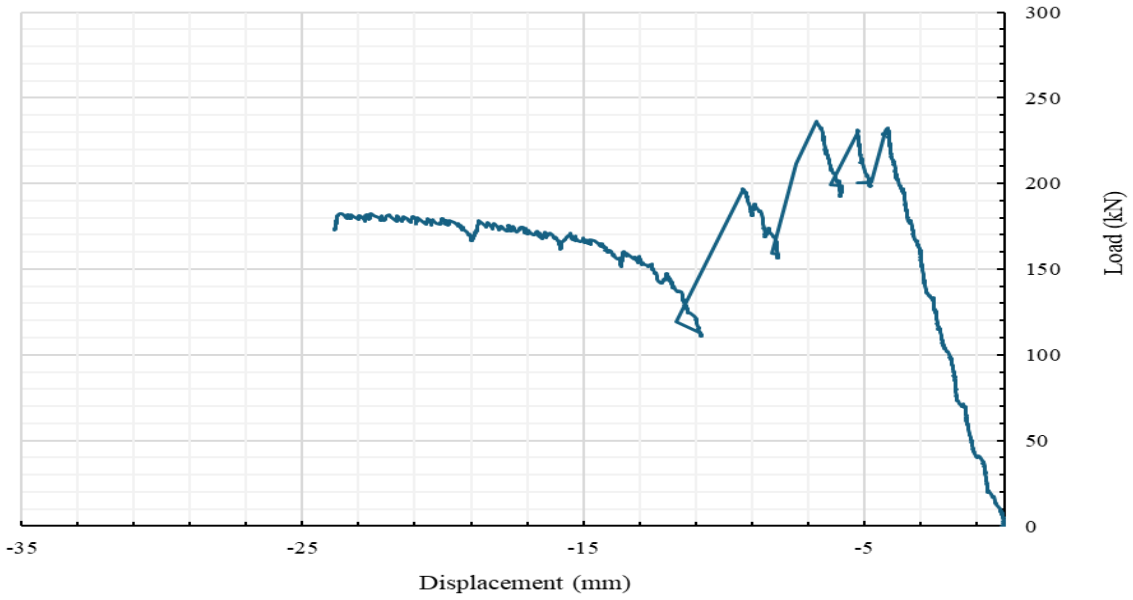

Figure 64: Load-displacement of corroded CMP with polymeric grout

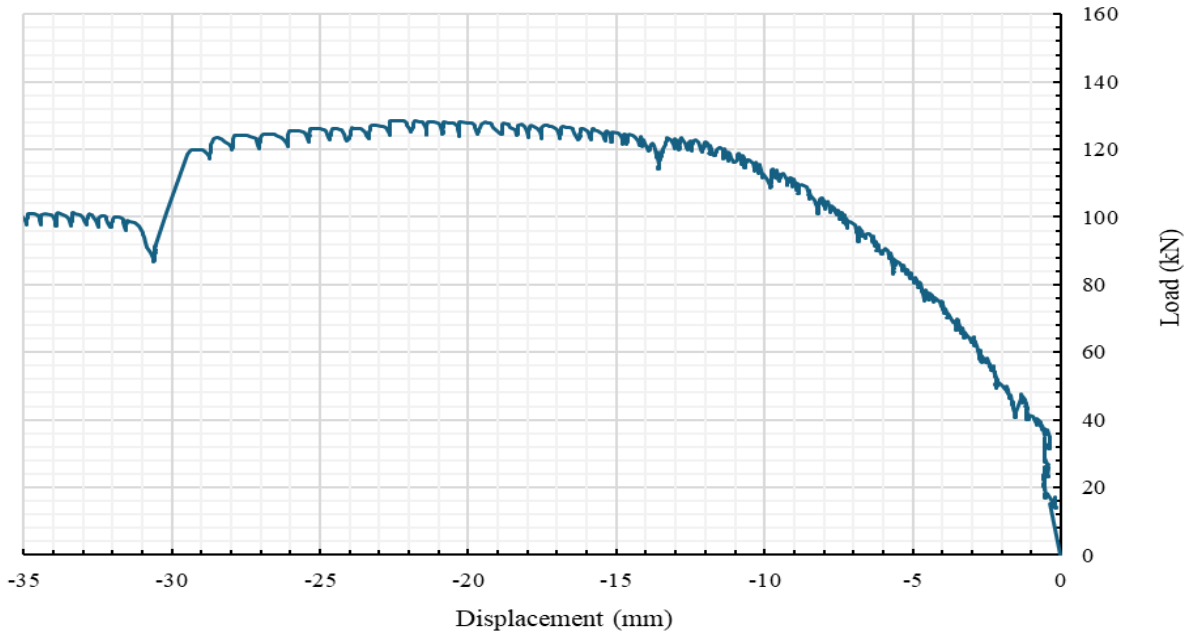

Figure 65: Load-displacement of uncorroded CMP with cementitious grout

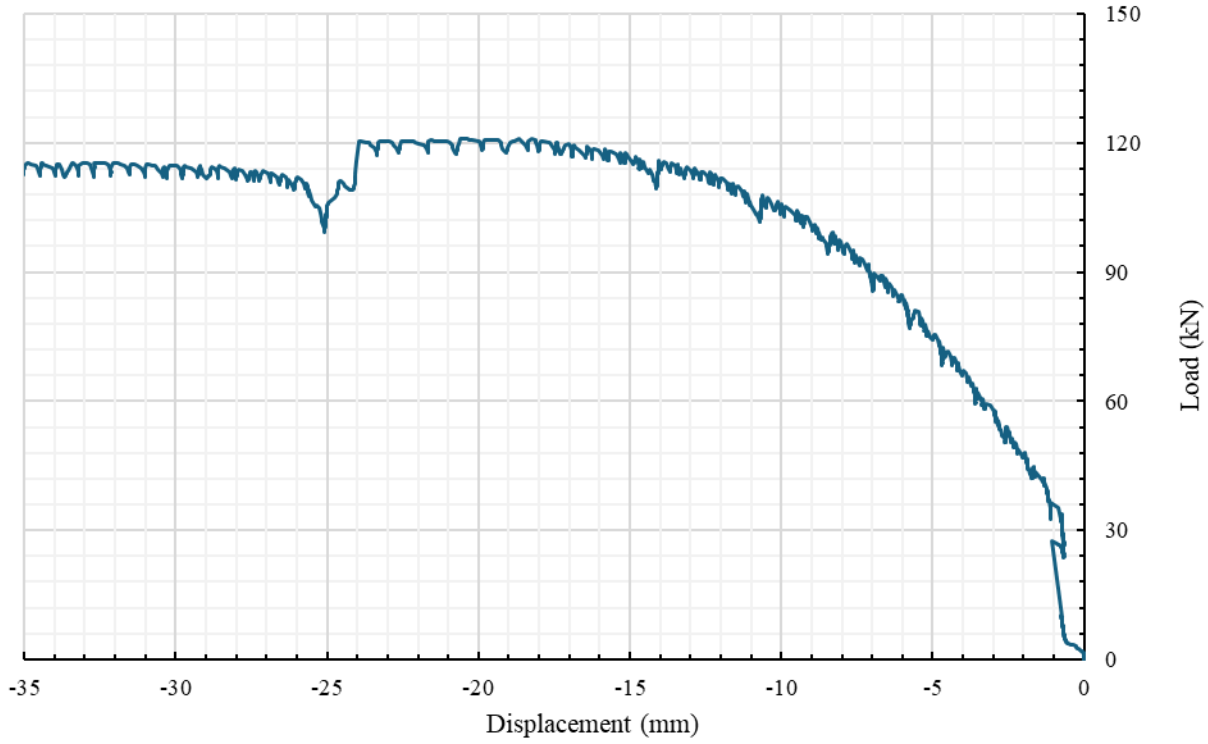

Figure 66: Load-displacement of corroded CMP with cementitious grout

7.3.3. Stiffness Factor:

The stiffness factor, reflecting the structural rigidity of the tested CMP specimens, was calculated using the ratio of the maximum load to the corresponding machine-measured displacement at peak load. It should be mentioned that wire pods have been used to record the machine displacement. Mathematically, stiffness (K) is represented by the equation:

$$K = \frac{P_{max}}{\delta_{max}}$$

here $P_{\max}$ is the peak load in pounds (lbs.), and $\delta_{\max}$ is the corresponding displacement in inches (in). The results indicate a significant variation in stiffness factors across the different tested conditions, based on Table 8. The uncorroded CMP specimen rehabilitated with polymeric grout exhibited the highest stiffness factor, with a value of approximately 72.07 kN/mm. In contrast, the corroded specimen rehabilitated with polymeric grout showed a reduced stiffness factor of about 56.83 kN/mm, indicating an approximate 21.1% reduction in stiffness due to corrosion. This reduction is attributed primarily to the corrosion-induced weakening of the steel-grout interface, which results in decreased composite action and, consequently, lower overall rigidity.

Specimens rehabilitated with cementitious grout showed substantially lower stiffness compared to their polymeric counterparts. Specifically, the uncorroded CMP with cementitious grout recorded a stiffness factor of approximately 9.56 kN/mm, representing a drastic reduction of roughly 86.7% compared to the uncorroded polymeric grout specimen. This substantial decrease highlights the inherently lower mechanical properties, weaker adhesion, and higher susceptibility to cracking of cementitious grouts. The corroded cementitious grout specimen recorded a stiffness factor of approximately 8.29 kN/mm, which is a 13.3% decrease in the stiffness factor compared to the uncorroded specimen.

The comparative assessment clearly demonstrates the superior performance of polymeric grout systems. The uncorroded polymeric grout specimen had a stiffness factor approximately 654% greater than the uncorroded cementitious grout specimen. Under corroded conditions, polymeric grout exhibited a stiffness approximately 586% greater than the cementitious grout specimen. These differences underscore polymeric grout's superior structural integrity, mechanical bonding, and resistance to deformation and deterioration under both ideal and compromised conditions.

In conclusion, polymeric grout significantly outperforms cementitious grout in enhancing the structural stiffness of rehabilitated CMP specimens, both under corroded and uncorroded conditions. The observed stiffness variations align with established literature and underscore the critical importance of grout selection in structural rehabilitation projects, emphasizing polymeric grout's enhanced durability, higher load-bearing capacity, and superior resilience against corrosion-induced deterioration.

7.4. Conclusions:

1. As expected, thinning or pitting of the steel wall reduces both the load-carrying capacity and stiffness. In polymeric-grout systems, the capacity reduction was around 22.8 %, whereas in cementitious-grout systems it was only 5.9 %. This difference in "corrosion penalty" underscores that if a pipe is already stiffly supported by a high-bond polymeric grout, losing steel cross-section becomes more critical than in a cementitious system that might already rely on less uniform bond.
2. Polymeric grout consistently led to higher peak loads under two-point bending, in part because of the grout's strong adhesive interface, negligible shrinkage, and higher post-crack toughness relative to cementitious mixes. The uncorroded polymeric specimen far

exceeded its cementitious counterpart by a margin of load (289.66 kN vs. 128.58 kN). Even the corroded polymeric ring carried 236.17 kN.

3. The differences between vertical and horizontal displacements illustrate the varied ways each ring distorts under two-point bending. In polymeric systems, we typically see a more uniform ratio of vertical to horizontal movement, whereas in cementitious systems—especially corroded—there may be more localized crack planes or hinge formation that changes how the ring flattens.
4. In a real culvert under shallow soil cover plus traffic loads, a more rigid, higher-bond system (e.g., polymeric grout + uncorroded steel) would attract larger loads but also be less tolerant of local flaws if steel were severely corroded. Meanwhile, a less uniform but thicker cementitious annulus could still carry load through broader cracking, albeit at lower ultimate capacity. The present tests suggest that, under field conditions, polymeric grout can deliver significantly higher peak strength—an advantage for pipes expected to carry traffic or surcharges. That said, corrosion undermines the steel's role in all slip-lined systems and underscores the need for close inspection of pitting depth or galvanic loss prior to rehabilitation.
5. Polymeric grout significantly enhances the structural performance of rehabilitated CMPs compared to cementitious grout, providing notably higher stiffness and superior load-carrying capacity. Specifically, the stiffness factor of the uncorroded CMP with polymeric grout exceeded that of the cementitious grout specimen by approximately 654.1%, emphasizing polymeric grout's superior rigidity and mechanical bonding properties.

In summary, these four tests confirm that polymeric grout in uncorroded pipes yields the strongest performance, with stiff and high-capacity ring action. Corrosion in polymeric specimens remains

impactful (over a 20 % drop) but not catastrophic, thanks to the ongoing robust bond. For cementitious grout, overall capacities are lower, large deflections develop before failure, and corrosion's impact is smaller in absolute terms but still important. Such insights align with earlier literature findings—for instance, (Smith et al. 2015), who reported significant gains in load capacity (by factors of three to ten) once grouts are used, along with a strong emphasis on the synergy between steel ring, grout, and liner. These results confirm that even in corroded pipes, slip-lining with GFRP plus a suitably chosen grout (particularly polymeric) substantially extends structural service life, improves ring stiffness, and offers a compelling, trenchless rehabilitation path for aging CMP infrastructure.

8. CHAPTER 8: Effects of Freeze-Thaw Environments on Nanomodified Carbon Fiber Reinforced Polymer Composites

8.1. Literature Review

8.1.1. Freeze-Thaw Mechanism

Freeze-thaw (F–T) durability of concrete is highly important in cold areas. Pore structure has close relations to F-T durability (Kong et al. 2005). The amount of ice formed in pores and the freezing point of pore solution are decided by the size, radius, and volume of the pores (Cai and Liu 1998). In general, in a specific range of temperature intervals, a bigger internal hydraulic pressure will be caused by frozen concrete pore solution, and as a result, more destructive frost damage will happen (Pinandita Faiz 1998). F–T can generate surface spalling, which will lead to mass loss of concrete; also, the developed internal cracking will cause strength deterioration of the concrete (Guo et al. 2018). Under F–T cycles, the coefficient of thermal expansion and thermal conductivity will increase, while the specific heat capacity of concrete will decrease. Because of the coarsening effect, the porosity of concrete will increase, which is one of the outcomes of F–T cycles (Luo et al. 2022). The F-T deterioration is a complicated chemical and physical phenomenon that starts at the internal microstructure of concrete. For instance, the permeability of concrete increases when F-T happens because the pore structure of concrete deteriorates, and the F-T damage accelerates the entry of erosion medium and external water (Qiu et al. 2020). After the cracks form in concrete due to the F-T, it facilitates the penetration of carbon dioxide, salt, moisture, and other agents into the concrete pore structure. This penetration will cause deterioration of the reinforcement materials. For instance, steel reinforcement corrosion (SRC) will happen inside the concrete as a result of an increase in permeability (Kim and Kim 2013).

8.1.2. Bonding Importance

The basis of the capacity of concrete and steel to coordinate deformation and work together is their sufficient bonding force (Zhang et al. 2022). This bonding force is hugely important when using fiber-reinforced polymers (FRPs) as a reinforcement material in concrete structures as well. This bonding force can be affected by harsh environments since the coefficients of expansion and contraction in these two materials are different. Hugely effective alternatives to steel are fiber-reinforced polymer sheets and plates, which are being used as internal and external reinforcement materials for strengthening and rehabilitation (Zaman et al. 2013). FRPs are comprised of a polymer matrix, which has been strengthened using different types of fibers, such as carbon fibers or glass fibers (Barkoula et al. 2008). A huge range of materials that have a good resistance against corrosion and adverse environments, possess good mechanical properties, and are lightweight can be produced by combining these two types of fibers with a polymer-based matrix. The fiber fraction that is being mostly used is between 30 to 60 percent and primarily rests on the type of composite that is being used. Among the most common materials that are being used for reinforcement of polymer matrix, glass is the most used one, which comprises 90% of manufacturing exercises (Vaidya 2015). There are three types of glass fibers: C-glass, S-glass, and E-glass. E-glass is the most used one, and S-glass is the strongest. The number of different oxides such as iron, aluminum, calcium, boron, and sodium, along with silica oxide, defines the type of glass (Hwang and Han 1986). On the other hand, carbon fibers are being used mostly too. Polyacrylonitrile is the main component of 90% of carbon fibers; others are made of rayon and petroleum pitch. Compared to glass fibers, these fibers possess a low coefficient of thermal expansion, high thermal conductivity, dimensional accuracy at higher temperatures, and excellent strength and modulus (Hosford 2013).

8.1.3. Effects of freeze-thaw cycles on fiber reinforced polymers

Cold climate conditions, such as freeze-thaw action, exposure to deicing salts, and low temperature, are the main reasons for these severe environmental conditions (Green et al. 2000). Therefore, the environmental durability of the method and materials that are being used for rehabilitation is very important, especially in these harsh environmental conditions. Nonetheless, a very few number of studies have been performed relating to the environmental durability of FRP materials in these harsh environments. A number of F-T tests on beams plated with carbon fiber reinforced polymer sheets were performed by (Kaiser 1989). He found that 100 cycles from +25°C to -25°C did not cause any harmful effects on the structural performance of the beams. In 2000, (Green et al. 2000) evaluated the structural performance of beams strengthened using FRP under severe cold environments. He found that the temperature variation of –27°C to +21°C the CFRP reinforced beams did not show any detrimental effects on the beams when subjected to static loads. Also, (Mostofinejad and Mohammadi 2020) performed a series of tests on strengthened beams with CFRP to evaluate the F-T durability. The temperature varied between 15°C to -18°C, and the number of F-T cycles was 50. This research also showed that F-T cycles did not cause any negative effects on the concrete beams' strength. The F-T durability of CFRP-strengthened RC beams affected by surface delamination was studied by (Markiv et al. 2016). It was found that partial surface delamination and F-T cycles did not have any harmful effects on the load deflection behavior of beams. (Hancox 1996) showed that the matrix-dominated characteristics such as in-plane shear, compressive strength, and transverse tensile, are being more affected by the environmental changes because the fibers are the least sensitive materials in FRPs. Temperature changes did not have significant effects on the longitudinal tensile strength. The tensile strength of epoxy-glass FRP was lowered by 10% when subjected to F-T cycles in research conducted by

(Dutta and Hui 1996). On the other hand, F-T cycles did not have any significant effects on the elastic modulus or tensile strength of carbon-epoxy FRPs.

Many studies have evaluated the effects of adverse environments on the behavior of FRP reinforced concrete. It has been concluded that the potential risks of premature debonding and failure of the debonding interface are high. To be more specific, freeze-thaw cycles may cause negative effects on FRP and FRP-concrete structures. There are three main reasons that can cause deterioration of FRP-concrete systems due to F-T cycles (Bank 2007). (a) Microcracking of the resin matrix (b) Debonding between the matrix and fibers and (c) Degradation of the adhesion of FRPs to the concrete. The current study focuses on the first issue. (Dutta and Hui 1996) used two types of GFRPs for their study and subjected them to -60 to 50°C. They saw cracks after only 100 cycles. As suspected, the usage of -60°C pushed the resin matrix to its tensile strength, which produced microcracks. (Karbhari 2001) evaluated the mechanical properties of CFRP under F-T cycles at temperatures ranging from -18 to 20°C. The results indicated a decrease in the strength of CFRP plates after 450 cycles. This decrease in strength was attributed to the debonding between the matrix and fibers. Therefore, there is a need to evaluate various approaches to face these three causes. Among these approaches, carbon nanotubes show promise.

8.1.4. Overview of Carbon nanotubes in fiber reinforced polymers

Carbon nanotubes (CNTs) were discovered by Sumio Iijima in 1991 (Iijima 1991). CNTs are classified as one-dimensional nanomaterials with an axial dimension being micrometers and a radial dimension being nanometers. The density of CNTs is 1/6 to 1/7 of steel; however, its tensile strength can be up to 50-200 GPa, which is 100 times more than steel. The elastic modulus of CNTs is 5 times that of steel and equal to diamond, which is around 1TPa (Han et al. 2013). CNTs

are divided into multi-walled carbon nanotubes (MWCNTs) and single-walled carbon nanotubes (SWCNTs). SWCNTs are more flexible and have fewer defects compared to MWCNTs. By rolling the concentric graphene sheets, MWCNTs can be made from SWCNTs. It means that, based on the area of application, the choice of MWCNTs and SWCNTs should be made (Li et al. 2015b). The capability of recovering to the original status after large deformations is extraordinary in CNTs. Because of having a great performance in different aspects such as chemistry, mechanics, heat conductivity, and electrical conductivity, the usage of CNTs has involved chemical sensors, composite materials, biomedicine products, and electrical components (Erol et al. 2018; Li et al. 2023; Norizan et al. 2020). CNTs can improve the thermal conductivity, electrical conductivity, and tribological and mechanical properties of metal matrix composites, such as titanium, nickel, copper, aluminum, magnesium, and iron matrix nanocomposites (Dadkhah et al. 2019; Saboori et al. 2018). In many fields such as sports equipment, marine engineering, automotive engineering, and aerospace, CNT-reinforced FRPs have been used recently (Khanna et al. 2021; Okoro et al. 2019; Zhao et al. 2023).

With the advancement of new and intelligent materials in recent years, CNTs, because of having high rigidity and strength, can be used as high-quality reinforcement and hugely enhance the bonding force between layers of FRP. As a result, multiscale demanding functional composite materials can be made using CNTs, while adding functions of nanomaterials. Since it is going to increase the interlayer bonding force of FRP materials, it will make the material suitable for complex load environments such as F-T cycles (Zakaria et al. 2019). Directly dispersing CNTs in the resin matrix is the earliest method to introduce this material to reinforced FRPs. When CNTs have been dispersed in a resin matrix, they will act as a bridge in the resin-fiber interface, which can efficiently prevent microcracking in the resin matrix. (Ovali 2018) added 0.5, 1, and 2 wt.%

of MWCNTs to glass/epoxy and indicated that the wear resistance of this material increased, which is mostly related to the adhesion between fibers and matrix. Moreover, to improve the tensile strength of carbon/epoxy composites. (Roy et al. 2018) utilized various types of functionalized CNTs. Compressive strength and interfacial strength of aramid FRPs increased by 82 and 131% when CNTs were introduced into the system. As mentioned earlier, the debonding between the matrix and fibers was the second reason for failure, so CNT usage can be effective in addressing this reason for failure.

8.1.5. Research Gap and Proposed Investigation

By exploring the response of FRP laminates nanomodified with several types and concentrations of CNTs exposed to freeze-thaw conditions, the effect of this harsh environmental phenomenon was investigated, and steps can be made to improve FRP laminates for use in durable and lasting infrastructure. The hypothesis of this study is that as the expansive forces during freezing push the layers of FRP apart and cause failure along laminate planes or matrix cracking, CNTs hold them together, bridging the gaps across cracks and improving bond strengths. With the addition of CNTs to the FRP used to reinforce structures, material deterioration from harsh environmental conditions could be significantly reduced.

8.2. Materials and Methods

To evaluate the effects of F-T cycles on nanomodified CFRP specimens, seven types of CFRP plates were cast: neat (no nanotubes), nanomodified with pristine MWCNTs (0.5%, 1.0%, and 1.5% by weight pristine nanotubes), and nanomodified with functionalized MWCNTs (0.5%, 1.0%, 1.5% wt. functionalized-COOH nanotubes). The matrix of nanomodified CFRP specimens is represented in Figure 67.

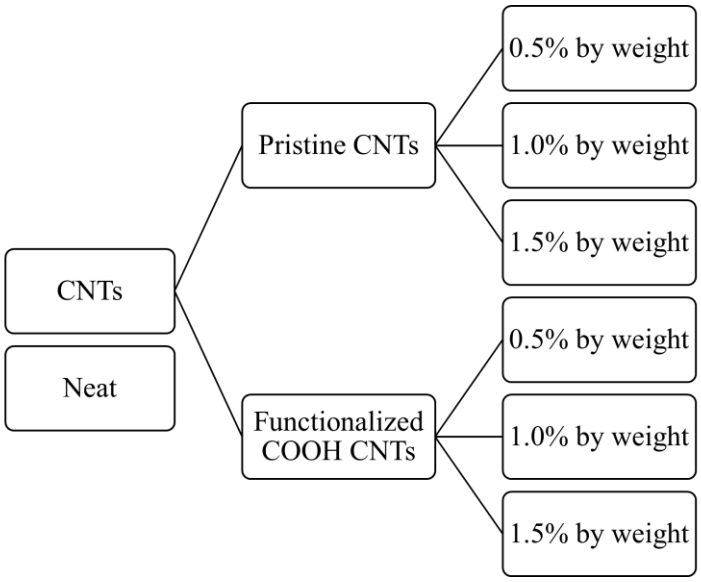

Figure 67: Matrix of CFRP types manufactured for freeze-thaw cycling.

8.2.1. CNT Dispersion in Epoxy Resin

MWCNTs were dispersed in low viscosity 635 Thin Epoxy Resin from US Composites. The procedure was identical for functionalized and pristine nanotubes. The MWCNTs were from Cheap Tubes, Inc., with a 20-30 nm outer diameter, 5-10 nm inner diameter, and 10-30 μm length. All handling of unsuspended CNTs was under a fume hood to avoid airborne CNT contamination. The amount of CNTs added to the epoxy was based on the weight percentage of the epoxy. The CNT-epoxy mixture was mechanically stirred by hand for approximately 30 seconds. The beaker was then covered with a glass plate and placed in an ultrasonic water bath (Branson 1800) at 40 kHz and degassed for five minutes. The setting was then switched to sonic with a bath temperature of 40 °C (104 °F) for one hour. The beaker was then stirred on an 80 °C (176 °F) magnetic stirrer (Four E's Scientific 5-inch) with a 2-inch magnetic bar at 800 rpm for two hours. After stirring, the epoxy resin was left to cool to room temperature, approximately 30 °C (86 °F), before adding any hardener. Figure 68 represents the CNT dispersion equipment.

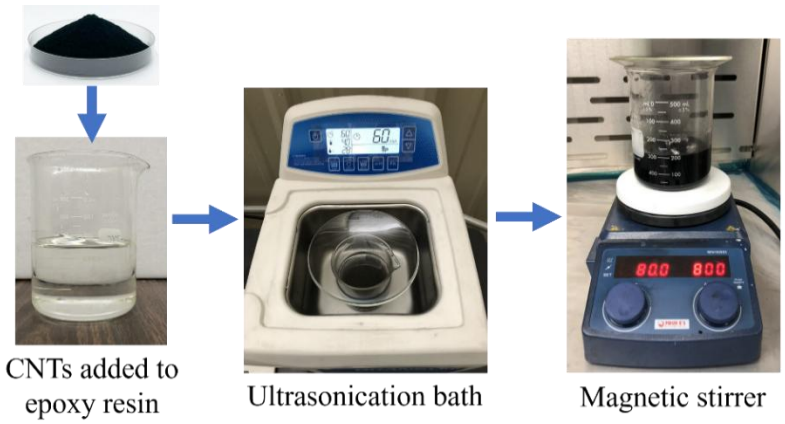

Figure 68: CNT Dispersion Equipment.

8.2.2. Vacuum-Assisted Hand Lay-up Technique (VAHT)

All CFRP composite laminates for tensile specimens were cast using the vacuum-assisted hand lay-up technique (VAHT) in compliance with ASTM D5687. Before casting a nanomodified CFRP plate, nanotubes were already dispersed in the thin epoxy resin and cooled to room temperature. A 61 cm by 61 cm flat steel plate was secured to a stable and level surface as a base layer. Table 9 specifies materials sourced from US Composites that were cut to size to cast a 50.8 cm by 50.8 cm plate of CFRP.

Table 9: VAHT Layer Dimensions and Quantities

Material	Size of Layer	Quantity of Layers
Nylon Release Film	58 cm by 58 cm	2
Breather Cloth	53 cm by 53 cm	1
Perforated Release Film	53 cm by 53 cm	1
Peel Ply	53 cm by 53 cm	2
Biaxial Plain Weave Carbon Fiber Textile	50.8 cm by 50.8 cm	6 for Tensile Specimens 4 for Specimen Tabs

The nanomodified (or neat for control specimens) epoxy resin is mixed into epoxy hardener (556 2:1 Slow Epoxy Hardener) in a 2:1 ratio. The mixture was stirred by hand with a non-absorbent utensil for 30 seconds, or until mix was homogeneous. The carbon fiber textile was placed with fiber weave aligned at 0° and 90°. A dense foam roller was used to fully saturate the material layers by spreading and rolling the epoxy in between each peel ply and carbon fiber layer. The remaining layers were not rolled. Airtight tape was applied to the edges of the steel plate, and the release film was placed on top by pressing the edges firmly on the tape to seal the edges. Failure to fully saturate the materials with the epoxy will result in damage to the composite's mechanical properties. To avoid oversaturation, which also hinders performance, a vacuum pump (Edwards, 1.5 x 10-3 Torr) was attached just beneath the top release film layer to create suction that will pull the epoxy towards the breather cloth, which absorbed any excess epoxy. For room-temperature curing, the approximate temperature of the laboratory was 30 °C throughout the casting process. The vacuum pump remained running for six hours and was then turned off. The FRP plate was left in place for 24 hours. After 24 hours, all layers were peeled from the carbon fiber plate, and the plate was left at room temperature to cure for an additional 24 hours. The outside 25.4 mm perimeter of the plate, as well as the immediate area where the vacuum hose was placed, was not used for specimens to avoid material inconsistencies.

8.2.3. Testing Overview

Seven types of CFRP plates were cast with the VAHT procedure: neat, nanomodified with pristine CNTs (0.5%, 1.0%, and 1.5% by weight pristine nanotubes), and nanomodified with functionalized CNTs (0.5%, 1.0%, 1.5% wt. functionalized-COOH nanotubes). For 0, 50, 100, 150, 200, and 250 freeze-thaw cycles, ten CFRP tensile specimens of each CNT type were made. CFRP tensile specimens were placed in an environmental chamber submerged in water for 250 freeze-thaw

cycles. For every 50 cycles, one set of ten specimens was removed from the chamber and evaluated through a series of destructive tensile tests. Before tensile testing, GFRP end tabs were bonded to both ends of each CFRP coupon to prevent grip damage and promote uniform load transfer. The tabs, cut to 25.4 mm in length and matching the specimen width, were attached using a two-part epoxy after removal from the environmental chamber and drying at room temperature for 24 hours.

8.2.4. Freeze-Thaw Cycling

Ten CFRP tensile specimens of each type of chosen nanotube and cycle designation were submerged in water inside an environmental chamber. The freeze-thaw chamber freeze phase occurred at 0 °C, and the thawing occurred at 40 °C. Thermocouples were placed inside the controlled operation of the chamber to most accurately measure the temperature of the specimens in the chamber and ensure complete freeze-thaw cycles. Specimens were removed approximately every 50 cycles up to 250 cycles. After removal from the environmental chamber, specimens were left at room temperature to dry for 24 hours before adhering tabs. Figure 69 represents the process of freeze-thaw in the environmental chamber.

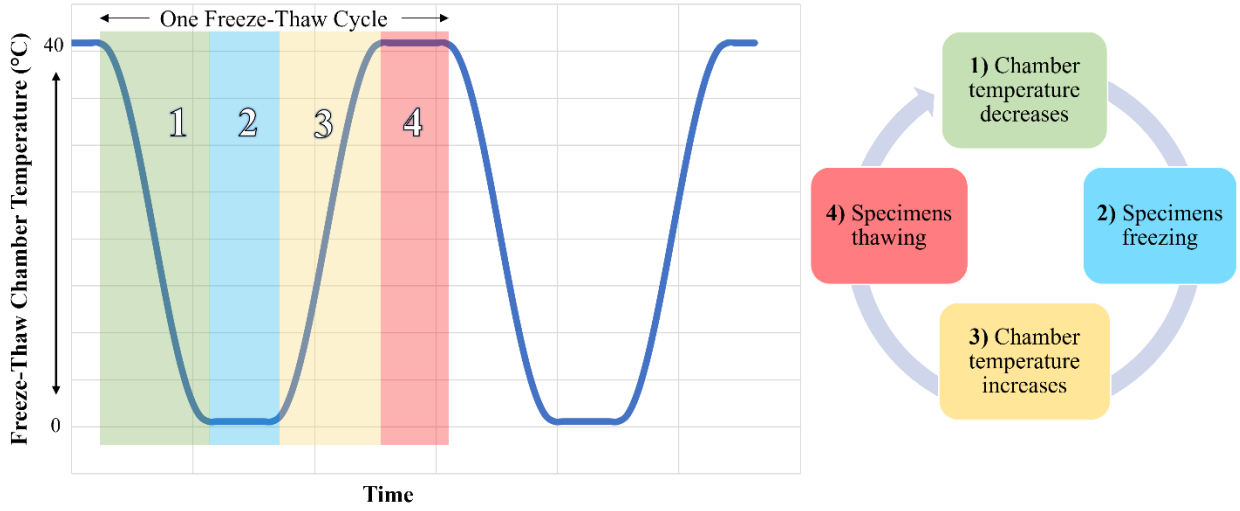

Figure 69: Freeze-thaw cycling in environmental chamber.

8.2.5. Static Tensile Testing of CFRP

Static tensile testing was done in compliance with ASTM D3039-17. All tensile testing was performed on an Instron 5967 Universal Testing Frame with an Instron AVE 2 Non-Contacting Video Extensometer. Tensile specimens were 127 mm by 15 mm. 18 mm by 15 mm tabs for the tensile specimens were four-layer off-axis carbon fiber cast with VAHT at the same curing temperature as the respective specimen and adhered to specimens with high-viscosity TYFO Saturant Epoxy (FYFE Co.). Flat-faced clamps were placed over the tabs for 48 hours at room temperature for curing. A gauge length of 50.8 mm was marked for all specimens with a white paint marker to create a high-contrast image for the video extensometer. Specimens were aligned with the direction of loading, and grips were tightened approximately 3 mm away from the edge of the specimen tabs. Testing of five specimens per type was done at a displacement rate of 1 mm per minute until failure. Ultimate tensile strength was calculated per ASTM D3039. Figure 70 illustrates the equipment and setup used in this study.

$$F^{tu} = P^{max}/A$$

Where:

Ftu = ultimate tensile strength

Pmax = maximum force before failure

A = Average cross-sectional area

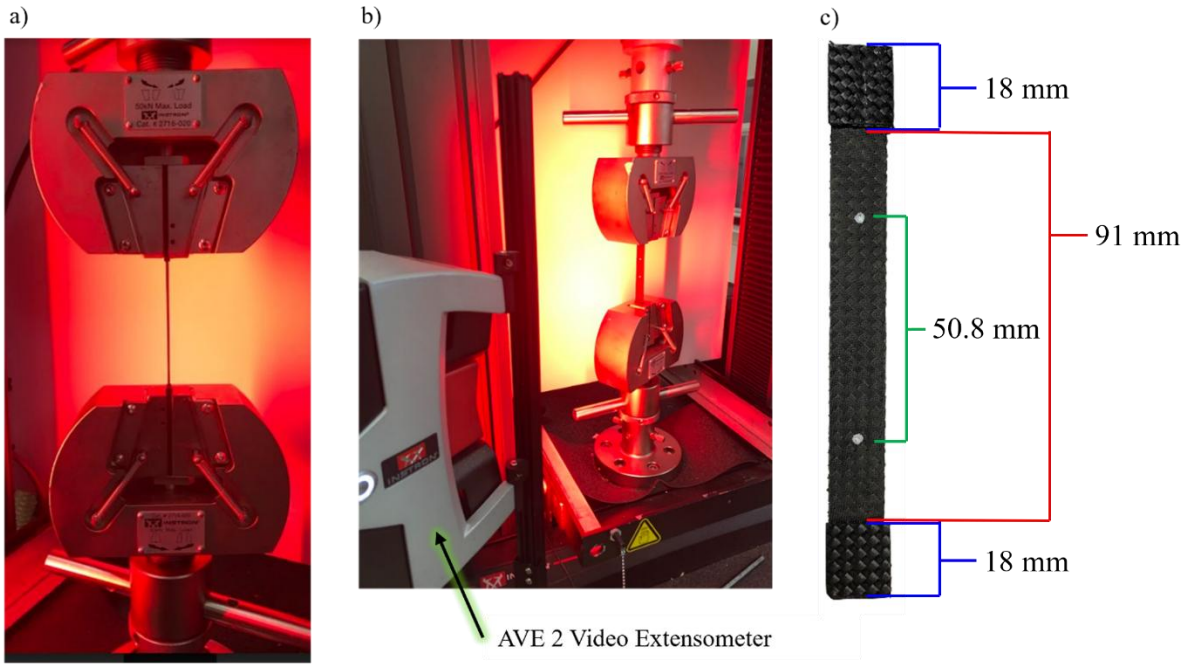

Figure 70: Tensile testing setup (a) Instron 5967 Universal Testing Frame tensile grips with specimen loaded; (b) Instron AVE 2 Non-Contacting Video Extensometer with tensile test setup; (c) CFRP tabbed tensile specimen.

Since interlaminar bonding of the epoxy between fibers is a critical property that controls much of the FRP laminate behavior, this study focused on revealing the interlaminar response of the FRP controlled in large part by the epoxy matrix. Testing of the biaxial FRP at a 45° angle from the direction of loading (i.e., off-axis, Figure 71(a)) is a more effective method than loading at 0° (i.e., on-axis, Figure 71(b)) to reveal the response of the epoxy matrix in the FRP (Soliman et al. 2012).

By testing the fibers in their "weak" axis with less resistance to deformation, the epoxy matrix is forced to engage more to sustain loading, and specimens ultimately fail in fiber pullout (Figure 71(c)) instead of fiber fracture (Figure 71(d)). Because the interlaminar bond strength of the FRP relies significantly on the matrix properties, this method of testing is an effective way to monitor the differences that nanomodification of the epoxy matrix presents. After curing, each CFRP plate was cut into tensile coupons so that the long axis of each coupon was oriented at 45° to the principal fiber direction, producing off-axis (45°) specimens for testing.

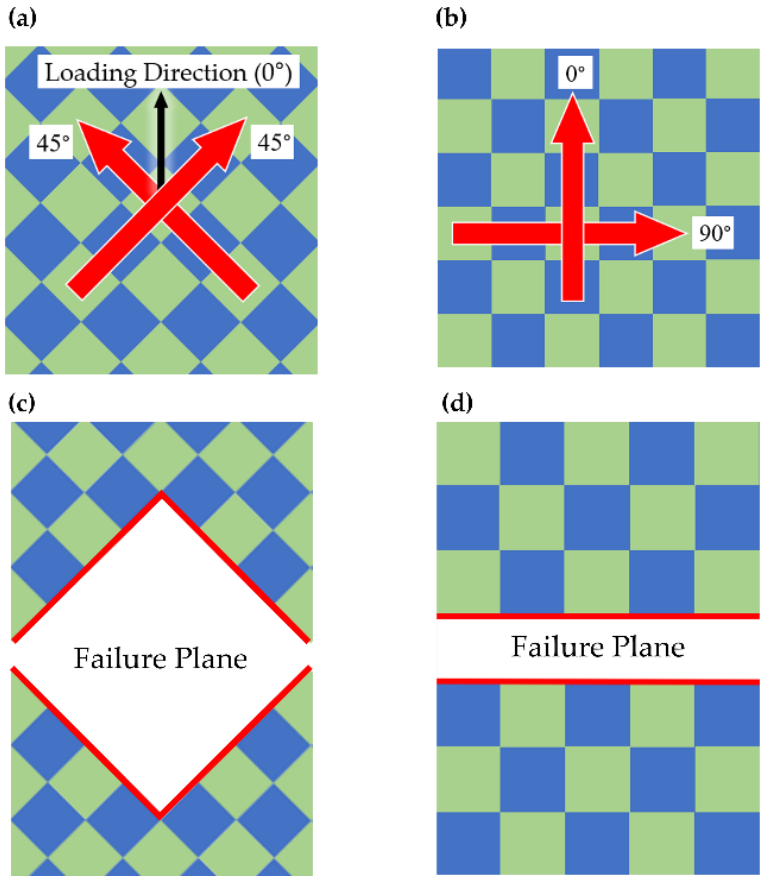

Figure 71: Schematic of off-axis versus on-axis loading: (a) Off-axis fiber orientation; (b) On-axis Fiber Orientation (c) Off-axis failure mode in tension, loaded at 0°; (d) On-axis failure mode in tension, loaded at 0°.

8.2.6. Scanning Electron Microscopy (SEM) Imaging

Scanning Electron Microscope (SEM) imaging is a common method to look at the quality of CNT dispersal in the cured matrix. Individual nanotubes are too small to be seen with optical lens microscopes. SEM uses an electron gun pointed towards a conductive specimen to create images based on reflected electron signals. Since epoxy is not conductive enough for this purpose, a thin coat of conductive metal is layered (called sputtering) onto the surface of the sample by electric charge. A Zeiss Neon FE-SEM was used to capture images of room-temperature cured epoxy samples to evaluate the microstructure and distribution of CNTs. Specimens of isolated epoxy were fractured with a chisel to create a fracture plane where CNTs would be visible. An iridium sputter-coat was applied to all samples to enhance conductivity for image quality.

8.3. Results and Discussion

8.3.1. Mechanical properties

Figure 72 shows the evolution of (a) tensile strength, (b) tensile strain, and (c) Young's modulus on CFRP specimens at different numbers of F-T cycles. Six types of nanomodified CFRP specimens and their results are compared to the neat specimen. As mentioned earlier, to evaluate the effects of different types of CNTs on the aforementioned mechanical properties, two types of CNTs have been used: pristine and functionalized CNTs. Also, to evaluate the effect of the amount of CNT on the mechanical properties, three different percentages of 0.5%, 1%, and 1.5% wt. of pristine and functionalized types of CNTs were used. Moreover, specimens were tested at 0, 50, 100, 150, 200, and 250 F-T cycles to evaluate the effect of freeze-thaw.

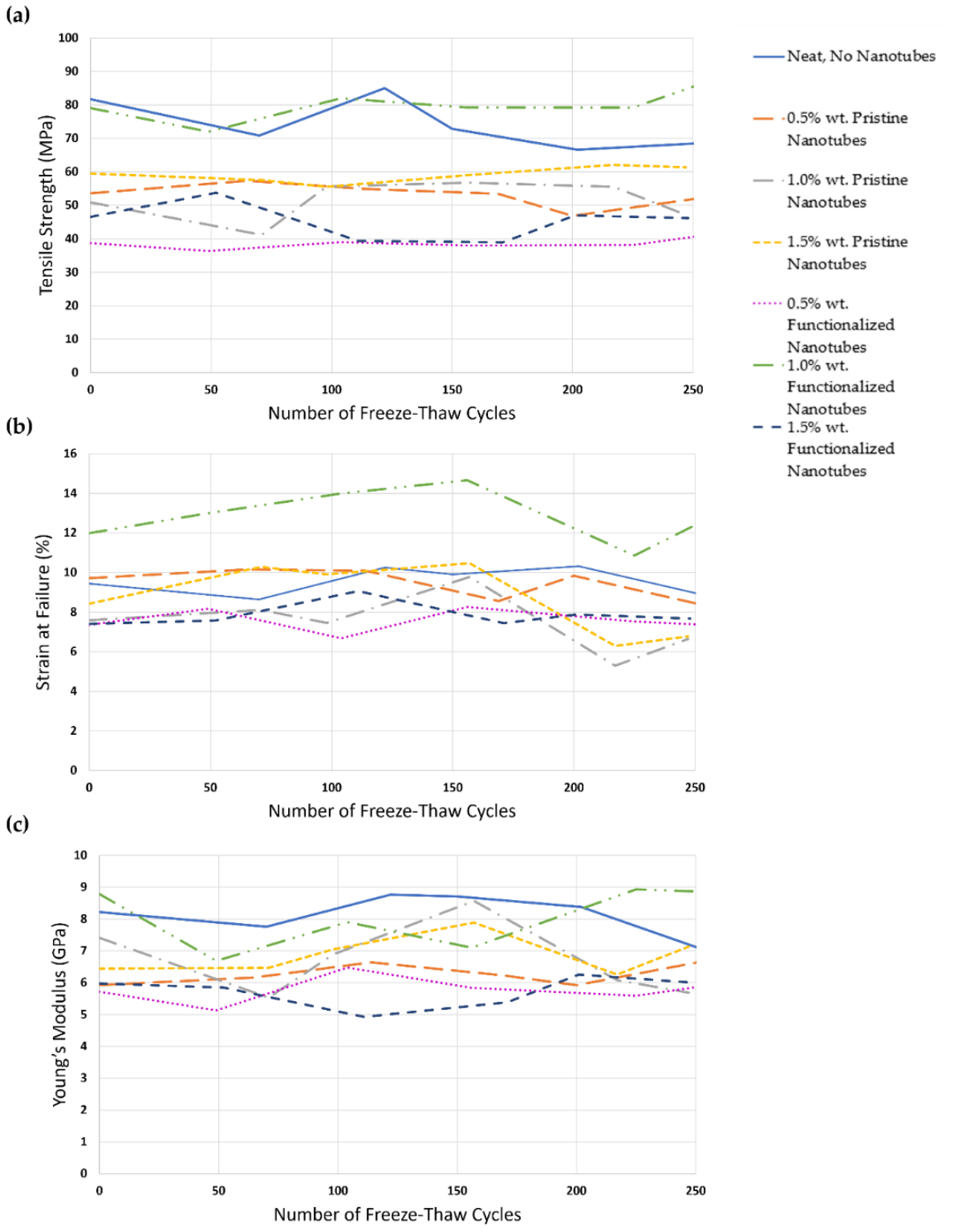

Figure 72: Evolution of (a) strength, (b) strain, and (c) modulus of elasticity of CFRP tensile specimens over 250 freeze-thaw cycles.

First, in order to understand the effect of CNT incorporation on the tensile strength, Figure 72(a) should be evaluated. As can be seen in the figure, specimens without CNT incorporation and specimens containing 1% functionalized CNTs demonstrated the highest values for tensile strength. The higher tensile strength of the 1% functionalized specimens is related to the ability of functionalized CNTs to improve the link between fiber and resin or improve the tensile strength of the resin itself. On the other hand, since the improvement in the tensile strength only happened at 1% functionalized ones, it can be concluded that at 0.5% the concentration of CNT inside the resin was not enough to make changes in interlaminar engagement. On the other hand, at 1.5% the concentration of CNT inside the resin was high, which caused agglomeration inside the resin. When that happens, the CNTs cannot bond properly with the matrix. Also, when CNTs are introduced inside the resin, the curing kinetics of the resin will change, so it can be another reason for having lower tensile strength in these specimens.

As in all the diagrams in Figure 72, the values for nanomodified specimens at 0 cycles are approximately equal to the values after 250 cycles. The detailed results of Figure 72 are represented in Table 10. For instance, the tensile strength of 0.5% pristine CNT at 0 cycles is around 53.6 MPa, and after 250 cycles is around 52.9 MPa. This value was 50.9, 59.5, 38.8, and 46.5 at 0 cycles for 1% pristine, 1.5% pristine, 0.5% functionalized, and 1.5% functionalized, respectively. These values after 250 cycles are approximately the same. So, it can be concluded that F-T cycles did not have any detrimental effects on the behavior of nano-modified FRP material after 250 cycles. As can be seen in Figure 72(a), the tensile strength of neat specimens dropped after 250 cycles, but 1% functionalized specimens indicated higher amounts of tensile strength after cycles. Since the neat specimens are the only specimens that have experienced a drop in the tensile strength after cycles, it can be concluded that CNT incorporation has improved the F-T behavior of CFRP

material by not letting deterioration happens after being affected by freeze-thaw. This improvement can be a result of better bonding between the resin matrix and fibers or higher tensile strength of the resin matrix.

Table 10: Results of CFRP specimens

		Tensile Strength (MPa)	Strain (%)	Modulus of Elasticity (GPa)
after 0 cycles				
Neat	Mean	81.72	9.44	8.22
	Standard Deviation	4.27	1.15	0.8524
	COV (%)	5.23	12.22	10.38
P 0.5%	Mean (%)	53.57 (-34%)*	9.72 (3%)*	5.92 (-28%)*
	Standard Deviation	4.66	0.56	0.60
	COV (%)	8.70	5.77	10.14
P 1.0%	Mean (%)	50.88 (-38%)*	7.58 (-20%)*	7.41 (-10%)*
	Standard Deviation	3.4529	1.13	0.78
	COV (%)	0.0679	14.93	10.47
P 1.5%	Mean (%)	59.45 (-27%)*	8.43 (-11%)*	6.44 (-22%)*
	Standard Deviation	3.67	0.94	0.38
	COV (%)	6.18	11.10	5.83
F 0.5%	Mean (%)	38.75 (-53%)*	7.36 (-22%)*	5.72 (-31%)*
	Standard Deviation	1.67	0.24	0.44
	COV (%)	4.31	3.23	7.69
F 1.0%	Mean (%)	79.03 (-3%)*	11.99 (27%)*	8.79 (7%)*
	Standard Deviation	2.51	1.39	1.27
	COV (%)	3.18	11.58	14.46
F 1.5%	Mean (%)	46.54 (-43%)*	7.40 (-22%)*	5.98 (-27%)*
	Standard Deviation	4.00	0.82	1.34
	COV (%)	8.60	11.06	22.36
after 250 cycles				

Neat	Mean	69.25 (-15%)*	8.37 (-11%)*	6.57 (-20%)*
	Standard Deviation	2.54	0.92	0.64
	COV (%)	3.67	10.96	9.77
P 0.5%	Mean (%)	52.86 (-35%)*	8.18 (-13%)*	6.77 (-18%)*
	Standard Deviation	4.39	0.68	0.70
	COV (%)	8.31	8.27	10.40
P 1.0%	Mean (%)	47.20 (-42%)*	6.64 (-30%)*	5.69 (-31%)*
	Standard Deviation	3.15	0.71	0.92
	COV (%)	6.68	10.66	16.12
P 1.5%	Mean (%)	61.38 (-25%)*	6.77 (-28%)*	7.13 (-13%)*
	Standard Deviation	5.26	0.30	0.87
	COV (%)	8.56	4.37	12.22
F 0.5%	Mean (%)	42.25 (-48%)*	7.28 (-23%)*	6.05 (-26%)*
	Standard Deviation	2.63	0.50	0.51
	COV (%)	6.23	6.94	8.41
F 1.0%	Mean (%)	89.67 (10%)*	13.43 (42%)*	8.83 (7%)*
	Standard Deviation	5.51	0.83	0.69
	COV (%)	6.14	6.14	7.87
F 1.5%	Mean (%)	46.20 (-43%)*	7.67 (-19%)*	6.01 (-27%)*
	Standard Deviation	1.56	0.32	0.94
	COV (%)	3.37	4.11	15.64

*Compared to neat CFRP for zero freeze-thaw cycles

Median stress-strain behavior at 0 and 250 freeze-thaw cycles can be seen in Figure 73. Specimens display yielding behavior, unlike typical brittle linear elastic behavior seen in CFRP loaded on-axis. As you can see in Figure 73(a), neat specimens show higher peak stress at 0 cycles. Adding CNTs to CFRP decreased the peak stress of all specimens at zero cycles. Also, it should be noted that the decrease in peak stress is lower for 1% functionalized carbon nanotubes compared to other nanomodified specimens. As you can see in Figure 73(a), specimens

containing 1.5% pristine and 1% functionalized CNTs indicated higher peak stress values in comparison to other percentages. It can be concluded that for pristine type of CNTs, 1.5% is the optimal value, and for functionalized type of CNTs, 1% is the optimal value.

Figure 73(b) represents the effect of CNTs on stress-strain behavior after 250 F-T cycles. As you can see, except 1% functionalized CNT, all the other specimens containing CNT indicated lower peak stress values than neat specimens, which can be related to the change of curing kinetics inside the resin, which decreased the bond strength between the matrix and fibers. Specimens containing 1% CNT indicated the highest peak stress values, which is an indication of improvement in bonding between resin and fibers. Also, like Figure 73(a), the optimal percentage of pristine type of CNT was 1.5% which shows the higher peak compared to other percentages of pristine type. It can be concluded that 1.5% pristine is the optimal value of pristine type of carbon nanotubes for the conditions of this study.

In order to evaluate the effect of F-T cycles, Figure 73(a) and Figure 73(b) should be compared. The strength of neat specimens decreased after 250 F-T cycles, which could be an indication of the detrimental effects of F-T cycles on the mechanical behavior of CFRP. As mentioned earlier, this could be related to the deterioration inside the resin matrix after F-T cycles or the debonding between resin and fibers. On the other hand, all the specimens containing CNTs did not experience obvious negative effects after 250 F-T cycles. More interestingly, the peak stress of specimens containing 1% CFRP showed higher peak stress after 250 F-T cycles. Enhanced performance of the functionalized-COOH 1% CFRP specimens is attributed to the ability of carboxyl-functionalized CNTs to bond better with the epoxy matrix.

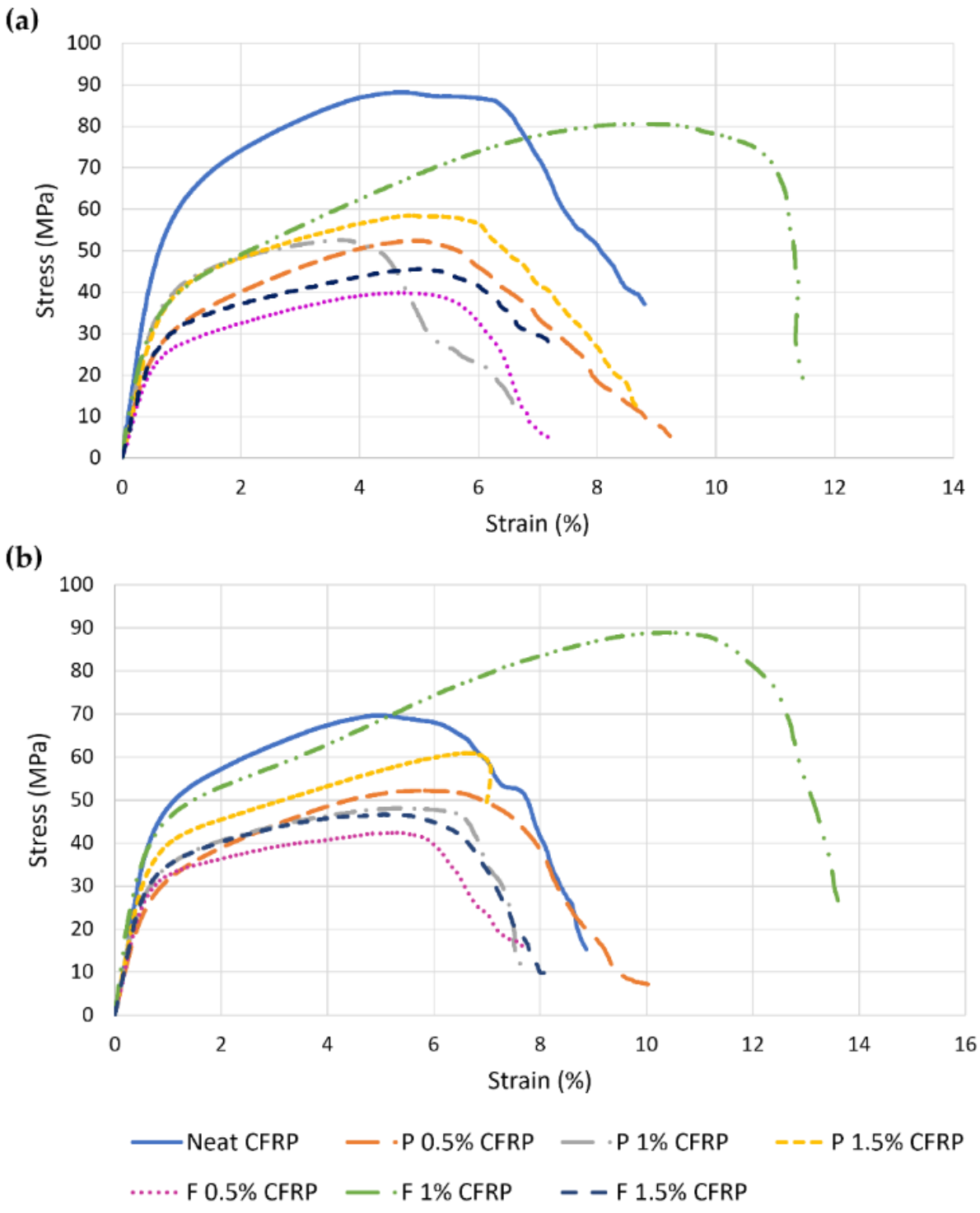

Figure 73: Stress-strain relationship for CFRP after (a) 0 freeze-thaw cycles and (b) 250 freeze-thaw cycles.

8.3.2. CNT Dispersion Quality and SEM

SEM imaging of room temperature cured epoxy was used to check CNT dispersion quality and identify any damage to the CNTs, and results are shown in Figure 74. Images of the neat epoxy are shown in Figure 74(a) and (b). Figure 74(c) shows one of the CNT agglomerations throughout the epoxy samples, and Figure 74(d) shows a higher magnification view of this agglomeration. However, all agglomerations were similar to sizes found acceptable in other existing literature (Rubel et al. 2019). It is acceptable to see CNT agglomerates in a matrix as long as there are few and they are not large. Overall, dispersion of CNTs in both types of nanomodified epoxy appears acceptable.

Single MWCNTs can be seen protruding from the epoxy. The aspect ratio of the CNT appears undamaged, confirming that the ultrasonication procedure did not damage the CNTs during dispersion. In Figure 74(h), CNTs can be seen bridging a cavity in the epoxy. The ability of the CNTs to reach across small cracks or pores like this one is what allows the increase in tensile and interfacial adhesion strength if properly engaged within the matrix. Additionally, Figure 74(f) and (g) show that some of the functionalized-COOH CNTs sticking out of the matrix appear broken off. This is an indication that matrix-CNT interfacial bonding was strong and did not allow the CNTs to pull out of the matrix during rupture. Conversely, in Figure 74(e) showing pristine CNTs, there are fewer broken CNTs, a sign that the pristine CNTs may not have bonded as well in the epoxy matrix.

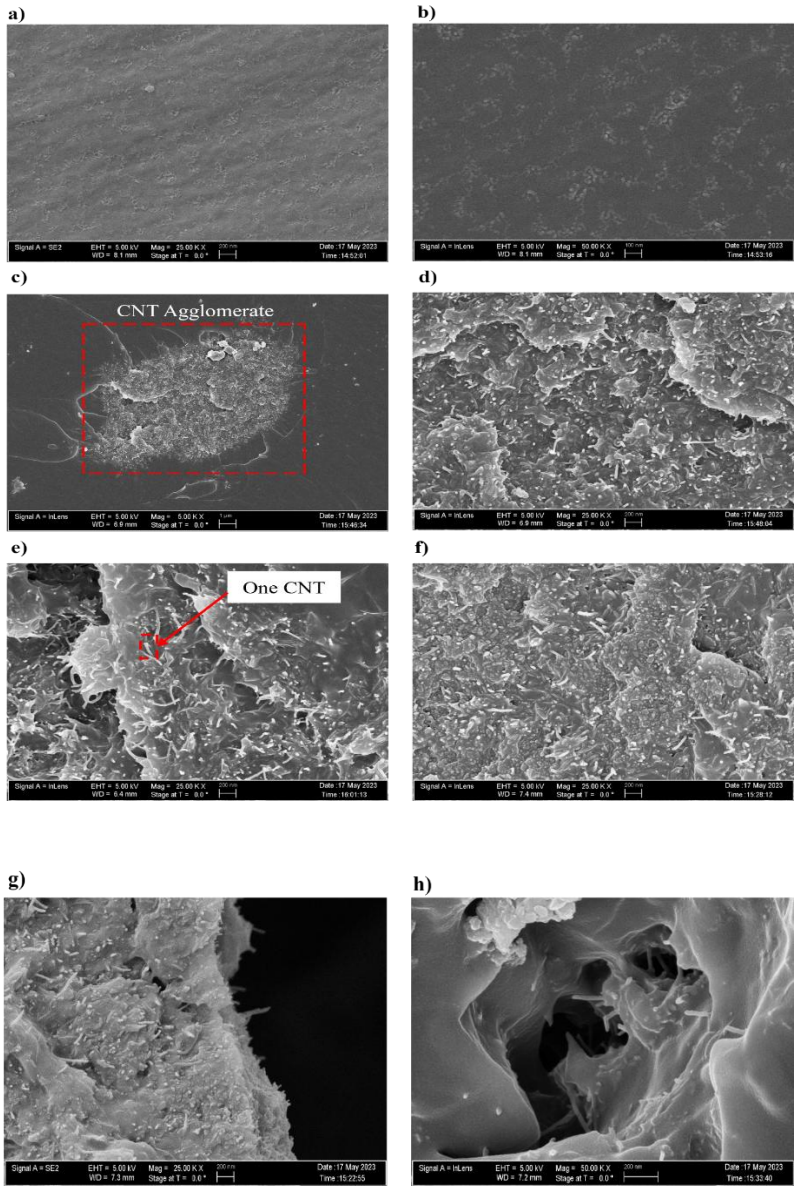

Figure 74: SEM images of (a) neat 25K X, (b) neat 50K X, (c) pristine CNT 5K X, (d) pristine CNT 25K X, (e) pristine CNT 25K X, (f) functionalized-COOH CNT 25K X, (g) functionalized-COOH CNT 25K X, (h) functionalized-COOH CNT 50K X epoxy cured at room temperature.

8.4. Conclusions

This study investigates the effects of freeze-thaw cycles on carbon fiber reinforced polymer specimens which have been nanomodified using different proportions and types of carbon nanotubes. A total of 6 types of nano modified specimens, using pristine and functionalized CNTs with varying percentages of 0.5%, 1%, and 1.5% by weight, was evaluated alongside a neat (non-

modified) specimen. These specimens were subjected to tensile tests after 0, 50, 100, 150, 200, and 250 F-T cycles. The purpose of this study was to evaluate the freeze thaw resistance of CFRP specimens and how the usage of carbon nanotubes can change the behavior. Based on the findings of this research, the following conclusions can be made:

1. Among all CNT-modified specimens, those with 1% functionalized CNTs showed the highest tensile strength, attributed to improved bonding between fibers and resin. The functionalized CNTs at 1% provided an effective reinforcement, while 0.5% did not yield sufficient CNT dispersion, and 1.5% showed signs of agglomeration, negatively impacting performance.
2. All CNT-modified specimens retained mechanical properties after 250 F-T cycles, showing minimal reduction in tensile strength, strain, and Young's modulus. In contrast, the neat specimens experienced significant declines in these properties, demonstrating that CNT incorporation enhances F-T durability.
3. While neat specimens exhibited higher peak stress at 0 cycles, CNT-modified specimens, particularly those with 1.5% pristine and 1% functionalized CNTs, displayed optimal stress-strain behavior. The peak stress values for the 1% functionalized specimens were highest post-250 F-T cycles, indicating improved resin-fiber bonding.
4. The 1% functionalized CNT specimens displayed superior performance after F-T cycles, maintaining or improving peak stress levels. This indicates that functionalized CNTs can mitigate F-T-induced debonding between the matrix and fibers, likely due to enhanced compatibility between the carboxyl-functionalized CNTs and epoxy matrix.
5. Based on tensile strength retention, durability, and optimal stress-strain behavior, functionalized CNTs at 1% and pristine CNTs at 1.5% appear to be the most effective for

enhancing CFRP performance under F-T conditions, with 1% functionalized CNTs providing the most consistent improvement across all measured parameters.

9. CHAPTER 9: Thermoplastic Carbon Fiber Reinforced Polymer Tapes in Cementitious and Polymer Concretes

9.1. Literature Review

9.1.1. Infrastructure Resilience Imperatives and the Case for FRP Composites

The field of construction and infrastructure needs continuous reforms. The infrastructure report from the ASCE 2025 rates America's infrastructure an overall C, indicating that the built structures are in fair condition but require significant upkeep (Infrastructure Report CARD 2025). Resilience and innovation are two of the main elements that govern the provided grade. The current technology cannot keep up with innovation in the industry. As a result, considering innovation and resilience a key component influencing infrastructure, essential procedure improvements as well as the replacement of outdated conventional material with new, modern materials are key to keeping America’s infrastructure up and running (Engineers 2018). An example of such a material is Fiber Reinforced Polymer (FRP). FRP is a composite material made of fibers embedded in a polymer matrix. The fibers primarily help to take load and provide the necessary stability, stiffness, and strength, and the polymer matrix holds the fibers in place, transfers load, and acts as a shield for the fibers during the manufacturing process (Gowayed 2013). Hence, the final product FRP is extremely adaptive to its intended applications, lightweight, corrosion-resistant, and has a high strength-to-weight ratio (Bank 2007). The widely used FRP composites include Glass fiber reinforced polymer (GFRP) and Carbon fiber reinforced polymer (CFRP). Glass fibers are inexpensive and have high tensile strength and high chemical resistance (Zheng et al. 2022). However, they have a low modulus of elasticity and low resistance to cyclic loads and can corrode

in an alkali environment. Hence, CFRP is an ideal material compared to GFRP in terms of its material properties (Cousin et al. 2019).

9.1.2. FRP Manufacturing Methods and Woven Architectures

There are multiple ways to prepare FRP. However, traditional methods for preparing FRP composites include wet layup, spray layup, and filament winding (Abanilla et al. 2006). New, modern techniques like Pultrusion, Resin Transfer Modeling (RTM), injection molding, and additive manufacturing have also emerged (Davalos et al. 1996). Of particular interest are woven FRP composites due to their applicability in construction and infrastructure strengthening. Woven composites refer to interlacing two sets of fibers at right angles to each other, so that the bond strength between them will be robust in both orientations due to interlocking, and to provide good drapability for any other complex shapes (Lee et al. 1998).

9.1.3. Thermoplastic Woven/Lattice CFRP for Construction: Geometric Flexibility and Process Sensitivities

Thermoplastic-based woven composites are newly emerging, and the information about their behavior as reinforcement in concrete is underexplored. Thermoplastic-based woven composites present a wide range of applications in the present context, as they possess superior geometrical flexibility compared to thermosetting fiber composites (Pascault and Williams 2013). Also, thermoplastic-based woven composites show different properties when some manufacturing parameters like nozzle speed, layer thickness, and nozzle temperature vary.

9.1.4. Thermoplastic vs. Thermoset FRP

The two unique types of plastic materials used for FRP are thermoplastic and thermosetting plastics (Grigore 2017). Thermosetting plastic, or simply thermosets, contains a cross-linked network, whereas thermoplastics have simple linear or branched linkages. The characteristic that sets them apart is that thermosets cannot be reverted to their original form when heated; in contrast, thermoplastics can. This indicates that thermosets are stronger mechanically but are brittle. So, when used with FRP, thermoset-based FRP composites can work very differently compared to thermoplastic FRP composites in concrete (Xue et al. 2022). However, thermoplastic-based FRP composites have their own set of advantages, such as the ability for re-shaping, recyclability, and environmental friendliness over thermoset ones. It is also applicable where cost is a primary concern; therefore, it is currently manufactured for use in complex structures at a minimal cost (Reis et al. 2020). If behavior is known, thermoplastic-based FRP composites could potentially be used as a reinforcing element for concrete structural systems with improved mechanical flexibility, greater design feasibility, and a structure having higher geometrical complexities than the scenario compared to a few years back (Schinner et al. 1996).

9.1.5. Research Gap and Proposed Investigation

The scope of the paper is confined to the performance of flexural beams reinforced with 3D printed thermoplastic-based CFRP woven composites in the form of cage and flat lattices, evaluated within three types of concrete: portland cement concrete (PCC), polymer concrete (PolC), and Ultra High-Performance concrete (UHPC). The study encompasses the preparation of these concrete types, each one for its unique properties: PCC as a benchmark for the structural concrete, UHPC for its exceptional strength and durability, and PolC for its rapid curing time and its rapid strength

development phenomena. Use of 3D printed thermoplastic-based CFRP woven composite as reinforcement aids the necessary strength and ductility, and the improved durability helps control the crack propagation and enhances bonding with the concrete matrix. Also, comparing the reinforced beams with unreinforced ones can provide the necessary clarification regarding the merits of using thermoplastic CFRP reinforcement. The standardized casting and testing of the beams, along with their flexural strength, load-deflection behavior, and failure modes, provide insights for the practical implications and recommendations for the use of these innovative reinforcement techniques. The data from this study can be vital for upgrading the design, construction, and maintenance of reinforced concrete structures, leading to more sturdy, durable, and efficient infrastructure solutions.

9.2. Materials and Methods

9.2.1. Woven thermoplastic CFRP composite

Woven CFRP composites have 38% higher tensile strength than multidirectional nonwoven composites, and carbon fiber composites have retained over 95% of their tensile strength (Nartam et al. 2024). Woven thermoplastic composites, such as PETG-C, have advantages in terms of manufacturing, flexibility, and recyclability. While thermosetting CFRP meshes, which go through irreversible chemical changes during curing usually have better mechanical properties such as higher strength and better resistance to high temperatures, thermoplastic composites can be remelted and reshaped, making handling easier and production more economical. These material characteristics result in variations in performance, with thermosetting composites typically providing greater strength retention and endurance in harsh environments (Ozkan et al. 2020). The study utilized two designs of woven thermoplastic CFRP composites acquired from WEAV 3D

Inc. referred to as Cage lattice and Flat lattice as in Figure 75. The WEAV3D reinforcement production process integrates thermoplastic pre-impregnated tapes, the width is customized according to the need and then is fed into a composite forming machine, which weaves and consolidates the lattice structure, reducing waste and enabling the cycle time to be within two to five minutes. This structure is then tailored during the molding phase (including continuous lamination and injection molding) to meet the specific requirements, offering a quicker alternative to traditional RTM and hand layup methods (Muzzy and Kays 1984). The CFRP Lattice provided by WEAV3D Inc had a higher tensile strength of 1450 MPa compared to the GFRP which has a range of 750 to 975 MPa. Hence, considering the long-term strength consequences of GFRP, carbon fibers are used as they possess high resistance to tension, compression, and fatigue loads as well as high temperature resistance (San-José et al. 2006).

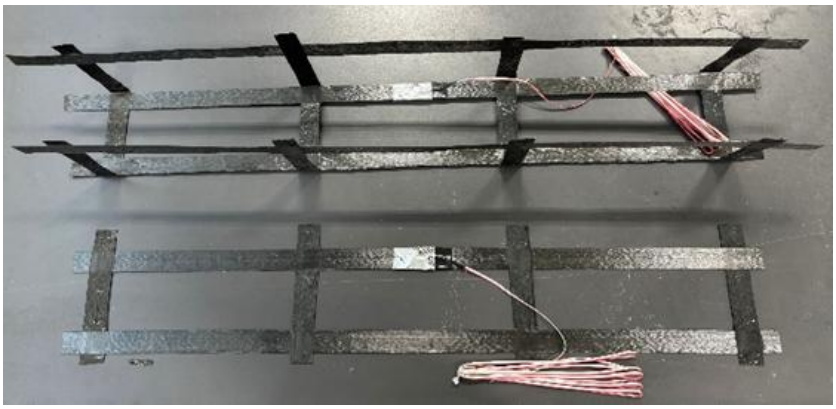

Figure 75: Woven thermoplastic CFRP cage (top) and flat lattices (bottom) composite acquired from WEAV 3D Inc.

The dimensions of different types of tapes, like PA410-C, PETG-G, etc. have an overall average thickness of 0.5mm and an average width of 25mm. However, PETG-C carbon fibers are used for the project, whose specific properties can be seen in Table 11. The longitudinal and cross tape is stuck in such a way that no internal bond failure occurs within the material itself, according to the manufacturer. This material's density varied between 1360 and 1790 kg/m3. The WEAV3D CFRP

tapes have to thickness ratio >100, and the mesh size for the cage and flat lattice is of size 200mmx100mm. The physical material properties of the WEAV3D CFRP tapes are given in Table 11.

Table 11: Data Sheet for CFRP Tape (provided by WEAV3D Inc)

Parameters	PETG-C
Thickness (t) (mm)	0.21
Width (mm)	22
Tensile Resistance (σ_u) (MPa)	1450
Ultimate Strain(ε_u) (%)	1.4
Young's Modulus (ε) (GPa)	101.2
Fiber Content (V/V) (%)	-

9.2.2. Concrete mix designs and process

Three types of concrete are used for this study: portland cement concrete (PCC), ultra high-performance concrete (UHPC), and polymer concrete (PolC). Mix designs were prepared for each concrete mix type. The PCC was developed, and details are given in (Akbarpour et al. 2024). A rotating drum mixer was used to perform the mixing process. The UHPC mix design was a successor of a former mix design conducted at the University of Oklahoma that served as the benchmark for the mix and this study. The UHPC was prepared using a high shear paddle mixer and the process outlined in (Pezeshkian et al. 2020). Dry materials are mixed first for 10 minutes, water and high-range water-reducing admixture are then added over 1–2-minute periods, mixing is continued until the material reaches a fluid state, and then the steel fibers are added. The PolC mix was developed according to the manufacturer's data sheet. The composite was mixed for 3 minutes using a mechanical drill with a mixing paddle and a bucket until a homogenous mixture was obtained. Since polymer concrete is a rapid-setting material, the mixing process was

completed within 5-10 minutes to avoid material setting. Mix designs for each concrete mix type are shown in Table 12.

Table 12: Mix Design constituents for PCC, UHPC and PolC

Constituent	**Mix Proportion** (kg/m^3)
PCC Mix Design	
Cement Type (I)	1
Fine Aggregate	1.975
Coarse Aggregate	2.475
Water/Cement	0.45
High Range Water Reducer	260 ml/100kg of Cement
UHPC Mix Design	
Cement Type (I)	0.6
Silica Fume	0.1
Slag Cement	0.3
Masonry Sand (1:1 agg/cm)	1
Water /Cement	0.2
Steel Fibers	2% by Volume
High Range Water Reducer	120-150 ml/100kg of
PolC Mix Design	
Polymer Powder	8.87
Coarse Aggregate	4.45
Epoxy Resin	1

Studying different types of concrete (PCC, UHPC, and PolC), allows researchers to compare how well each type of concrete performs in comparable circumstances and comprehend how the respective material characteristics interact with the same reinforcing material. The study can highlight the effectiveness of the CFRP reinforcement across diverse materials, revealing any strengths and weaknesses in specific concrete types. This approach offers a more comprehensive

viewpoint, enabling findings to be used in a greater variety of engineering and construction applications. Limiting the test matrix to only one type of concrete may not capture all these variations. Therefore, using PCC, UHPC, and PolC as concrete types in this study enables a wider range of information about CFRP tape interactions. Using fiber-based UHPC, which has different properties compared to PCC, which is also unique in itself, and PolC, being entirely polymer-based and water-free, really enhances the goal of this work and establishes a broader benchmark for further research.

9.2.3. Compressive Strength Test

Three 100-mm x 200-mm cylinders were fabricated and tested for compressive strength according to ASTM C39 and ASTM C579 for PCC and PolC. Three 100-mm x 200-mm compressive strength cylinders were fabricated and tested for UHPC according to ASTM C39 and ASTM C1856. Cylinders were initially cured in their molds and then demolded for the curing process. Curing conditions for the cement-based concrete were maintained at wet room temperature for 28 days at 100% relative humidity. Polymer concrete was dry cured in a curing room at around 25 to 27 degrees Celsius. Cylinders were prepared by first grinding the specimen to remove the peaks, and then ASTM C39 was used as the standard specification for compression testing. Compressive strength testing was performed using a Forney Compression Testing Machine at a load rate of 1 MPa/sec for PCC and UHPC, where compressive load at failure was recorded. Compressive strength for PolC was determined by testing cylinders at a load rate of 0.7 MPa/sec. To ensure equal load distribution, silicon caps are used on the cylinders, and the peak load of each cylinder is recorded. Compressive strength (fc) for any cylinder is calculated from the peak load using the Equation below:

$$\textit{Compressive Strength} \quad f_c = \frac{4\,P_{max}}{\pi D^2}$$

Where fc is the compressive strength (MPa), Pmax is the maximum load (kN), and D is the average diameter of cylinders (mm).

9.2.4. Fabrication of Test Beams

Three beams (150mm x 150mm x 900mm) were fabricated with each concrete type, one having cage lattice, flat lattice, and no reinforcement, for testing under flexure and obtaining the load vs displacement behavior. A total of nine beams were fabricated and tested for this study. The fabrication process involved making wooden molds pre-marked for a 2-inch cover. Once each concrete was mixed, it was added up to the mark. The lattices (cage or flat) were placed on the surface of the concrete, and the remaining concrete was added. A vibratory table was used throughout the process to ensure adequate consolidation with minimal air voids, and for the concrete to accommodate well around the cage lattice. Figure 76 shows the fabrication process for PCC and UHPC concretes. Curing conditions for cement-based concretes were maintained at wet room temperatures for 28 days at 100% relative humidity.



Figure 76: Fabrication of (a) PCC beams and (b) UHPC beams

9.2.5. Flexural Test

Each RC beam was subjected to an increasing static load until failure, following a four-point bending method in an MTS 810 test frame. The loading procedure was controlled at a rate of 1 mm/min until the woven 3D printed WEAV3D reinforcement failed, as the section was tension controlled, and for the no reinforcement section, the concrete crushing point of failure. The testing was conducted using a load frame connected to a data acquisition system, which managed and controlled the testing process. This system was responsible for recording the load and crosshead displacements at a frequency of 1 Hz. The maximum bending moment at a distance a was given by the equation below, where P is the load recorded and a is the distance where the bending moment is calculated. The beam setup is shown in Figure 77. Beams were loaded into the MTS test frame using a forklift.

$$\textit{Maximum Bending Moment} = \frac{P}{2}a = 5P \text{ , where } a = 10\ in$$

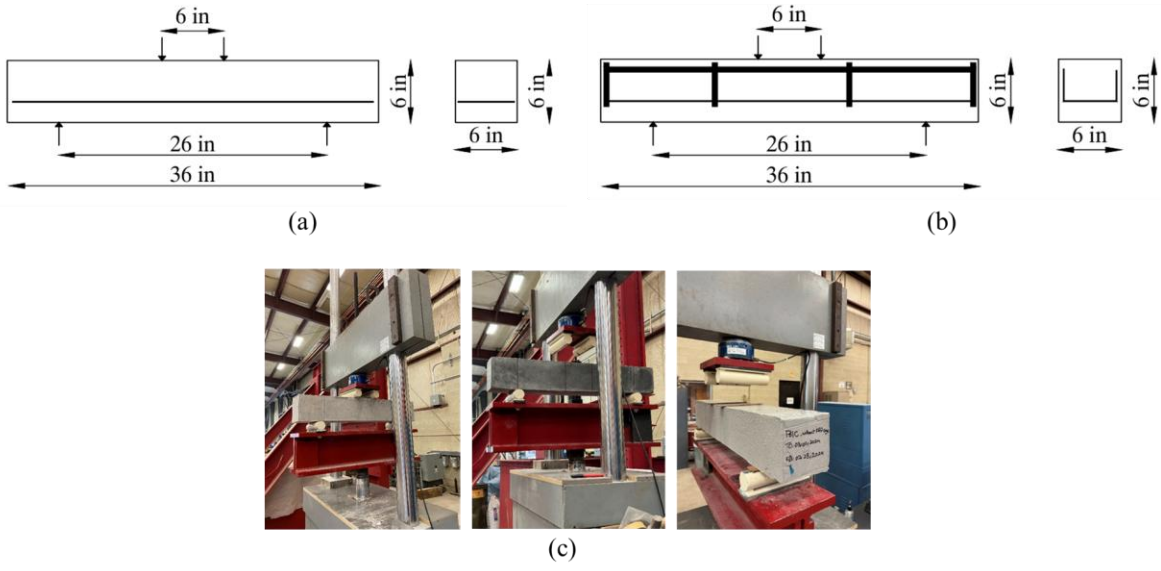

Figure 77: Flexural Bending Setup for (a) flat lattice, (b) cage lattice (not to scale), and (c) concrete beams loaded in the test frame.

9.2.6. Microscopic analysis

Advanced light microscopy was performed on PETG-C WEAV3D reinforcement using Keyence VHX-7000 ultramicroscope at the Samuel Roberts Noble Microscopy Lab (SRMNL) at the University of Oklahoma. The microscope is fully automated and has the ability to capture high magnification of up to 6500x. The precision of fiber orientations and intersections of changing angles obtained using the technology was studied using microscopic images, as shown in Figure 78. In addition, post-testing damage in the flexural test specimens was correlated to these images and results to improve understanding of the flexural behavior of the reinforced concrete beams.

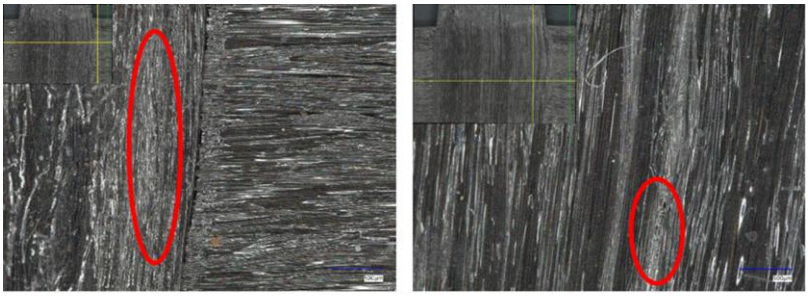

Figure 78: Microscopic images indicating defects in the material (a) long defect (b) small defects

9.2.7. Theoretical calculations

PTC Mathcad 8.0.0.0 was used for theoretical calculations of nominal moment based on beam geometry and reinforcement characteristics. The theoretical moment carrying capacity changes according to the concrete used; however, we have considered the same theoretical equations for all three types of concrete. The calculations are based on ACI 440.1R-15 and utilize the rectangular Whitney Stress Block. The theoretical moment capacity for PolC with a flat lattice is calculated as follows, showing the sample calculation.

$$M_n = A_f . f_{fu} . \left(d - \frac{\beta_{1E} \cdot c_{new}}{2}\right)$$

$c_{new} = A_f \cdot \frac{f_{fu}}{\alpha_{1E} \cdot \beta_{1E} \cdot f'c. \ b}$

Where c_{new} is the new neutral axis depth obtained after multiple iterations, for the under-reinforced section.

Af = Area of FRP reinforcement

f_{fu} = Manufacturer's guaranteed strength after environmental reduction

f'_c = Compressive strength of respective concrete

α_{1E} = Modifier for the magnitude of equivalent uniform compressive stress in concrete for under-reinforced FRP sections

β_{1E} = Modifier for the depth of equivalent rectangular stress block for under-reinforced FRP sections

Compressive strength values for PCC, PolC, and UHPC were obtained from the compression tests of cylinders for each mix design.

9.3. Results and Discussion

The average compressive strength obtained for PCC was 53.1 ±1.2 MPa, for PolC was 46 ± 4.6 MPa, and for UHPC was 126.6 ±19.4 MPa. The graphs for the peak load and displacement of PCC, UHPC, and PolC beams with and without the reinforcement can be seen in Figure 79. The peak load for the PCC control specimen and PCC flat lattice type of reinforcement remained the same at around 18 kN, whereas the PCC cage lattice showed a lesser peak load than the control beam but exhibited almost 5.5mm of displacement before failure. The PCC control beam showed a brittle failure, which was expected as no reinforcement was provided. The PCC flat lattice beam performed almost like the PCC cage lattice beam in terms of ductility, having a maximum

displacement of around 5.4mm. Moreover, the UHPC control beam had a brittle failure once the peak load increased above 20 kN. The UHPC beams with cage lattice and flat lattice had smaller peak loads but had considerable ductility before failure. Both specimens achieved around 24mm of displacement before failure. In the case of the PolC control specimen, the peak load rose to around 80 kN and then failed instantaneously. Though the peak load remained similar for the PolC cage lattice and flat lattice beams, the displacement was larger: 3.5mm for the PolC flat lattice beam and 5mm for the PolC cage lattice beam. Overall, the reinforced beam having flat lattice reinforcement demonstrated better ductility compared to its caged and non-reinforced counterparts.

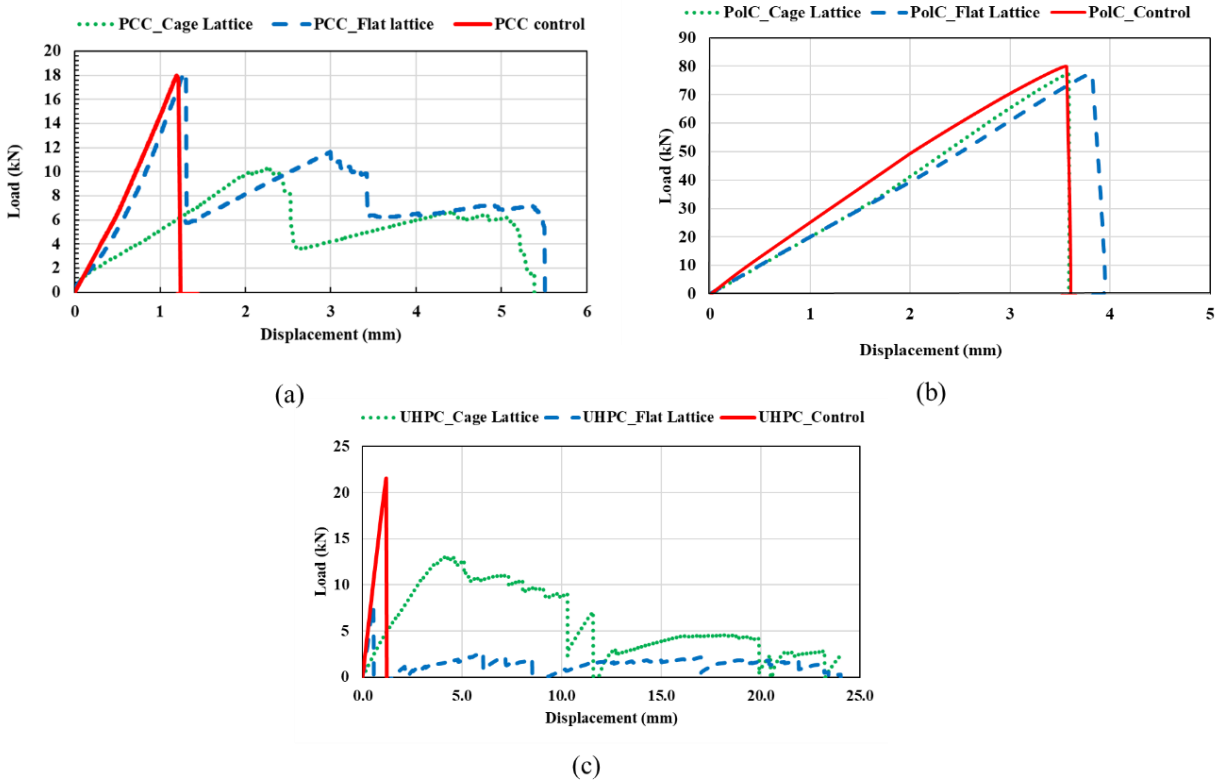

Figure 79: Load vs displacement graphs of (a) PCC, (b) PolC and (c) UHPC beams

The failure pattern of all the UHPC, PCC and PolC beams with and without WEAV3D reinforcement is shown Figure 80, Figure 81, and Figure 82, respectively. The crack pattern

changed according to the concrete used. The PCC, UHPC, and PolC beams showed completely different characteristics when relative to their cracking before failure. The PCC beam with no reinforcement and the one with a flat lattice had a sudden brittle failure. That indicates the flat lattice reinforcement in PCC did not contribute to ductility when the load was applied at the mid span of the beam. The beam showed complete rupture and was split into two pieces at failure. The beam with a cage lattice showed a different pattern. It had considerable ductility, and the beam remained intact without splitting. This indicates that the beam with a cage lattice is sturdier and more resilient than the other tested configurations. UHPC beams behaved similarly to the PCC beams. The ones without reinforcement and with flat lattice reinforcement had splitting failures, whereas the ones with cage lattice remained intact. Moreover, in the PolC beams, all three types of reinforcement were split into two pieces while testing, and showed the brittleness of PolC, but this concrete has a different scenario of the unreinforced beam withstanding slightly greater loads than the reinforced ones, which depicts that the reinforcement used doesn't really make a difference in the PolC.

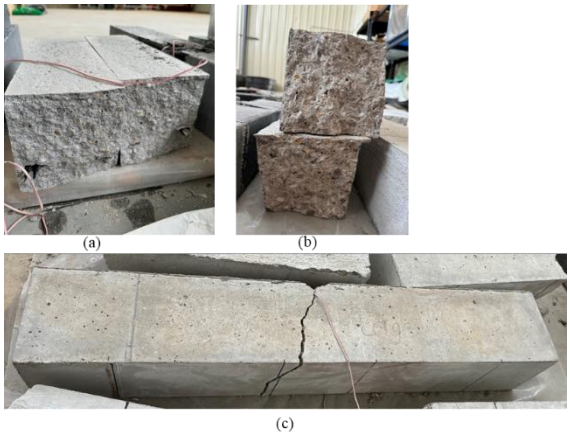

Figure 80: Failure Pattern of PCC beams with (a) Flat lattice, (b) no WEAV3D Reinforcement, and (c) Cage lattice.

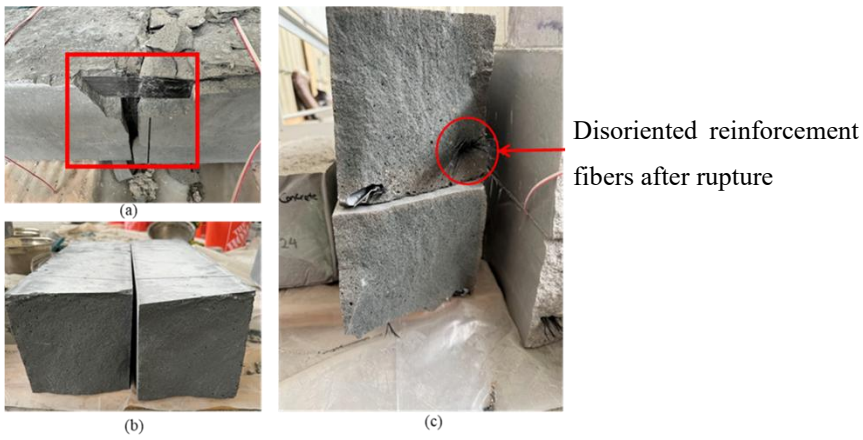

Figure 81: Failure Pattern of UHPC beams with (a) Flat lattice, (b) No WEAV3D reinforcement, and (c) Cage lattice.

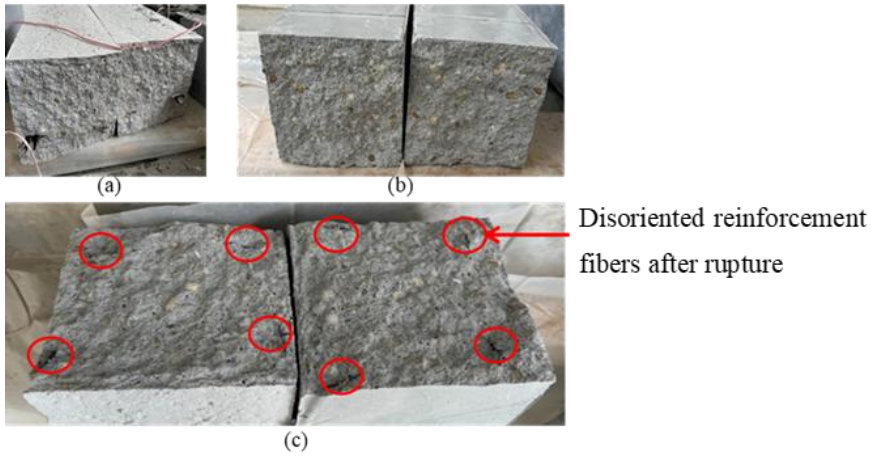

Figure 82: Failure Pattern of PolC beams with (a) Flat lattice, (b) No WEAV3D reinforcement, (c) Cage Lattice

The bar plot in shows that the ultimate moment of the cage lattice and flat lattice beams is the same for a given concrete type. This is because the difference between the cage lattice and flat lattice is the shear reinforcement provided on the cage lattice, which is lacking on the flat lattice, as in flexure, the shear reinforcement does not make any contribution, which showed the same number of predicted moment capacity, but the obtained moment capacity differed. From the data shown, the polymer concrete has the largest moment capacity obtained compared to UHPC and

PCC. Also, the design compressive stress distribution for each type of concrete is different and needs modification accordingly, but here it was assumed the same as conventional concrete which make sense as PolC has excessively high obtained capacity compared to UHPC and PCC which make sense as the stress distribution equation shall vary according to the concrete used or the bond between the PolC and WEAV3D CFRP tapes could have been really strong than PCC and UHPC. Additionally, the defects seen from microscopic images, where the fibers on the bidirectional junction are ripping off, could also have potentially altered the capacity. Moreover, the floating of the cages and flat lattice reinforcement while pouring the concrete into the mold has shifted the designated location for the reinforcement, which also might have altered the obtained capacity to some extent on all three types of concrete. It is extremely lightweight, and while the cover provided was 50 mm each, it can be seen in Figure 81 and Figure 82 that the reinforcement got tilted and slightly bent due to its floatation with the concrete and was not in the planned location.

It was also observed that the predicted capacity is significantly lower compared to the obtained capacity for the PolC. This could be attributed to the calculation using the stress distribution block, which was assumed to be the same for each type of concrete, based on PCC. Therefore, the stress distribution for PolC should be recalculated with proper evaluation, which could result in much higher predicted capacity, aligning better with the obtained values and making the graph more representative of PolC's behavior. However, there are no equations developed for PolC that can benefit this type of calculation, which led to this approximated assumption. The major takeaway is that CFRP tapes exhibit high strength and strong bonding with PolC compared to other types of concrete.

The failure mechanism of beams having flat and cage reinforcements can be attributed to the different ways these reinforcements distribute stress. As cage lattice reinforcements can withstand

cracking and distortion, they increase the ductility of beams by enabling more displacement before failure, as they have the shear withstanding capacity. On the other hand, since flat lattices lack shear reinforcement, they often fail more abruptly under the flexural loads. While they still improve the beam's ductility compared to non-reinforced beams, flat lattices cannot withstand large displacements before failure, compared to robust cage lattice structures. It is highly recommended to fasten the reinforcement to mitigate the movement and floating of the cage and flat lattice during the concrete pouring. It is also suggested to work on the individual design compressive stress distribution for the UHPC and PolC used, so that the predicted moment capacity and the obtained capacity can be more comparable. Most importantly, the former detailed microscopic examination of the FRP lattice is necessary so that the material used does not affect the result obtained. Moreover, the PolC has a very low set time, so it is always suggested to work in small batches so that the PolC can be used on time. The cage and flat lattice's fibers are highly susceptible to damage, so careful handling is recommended.

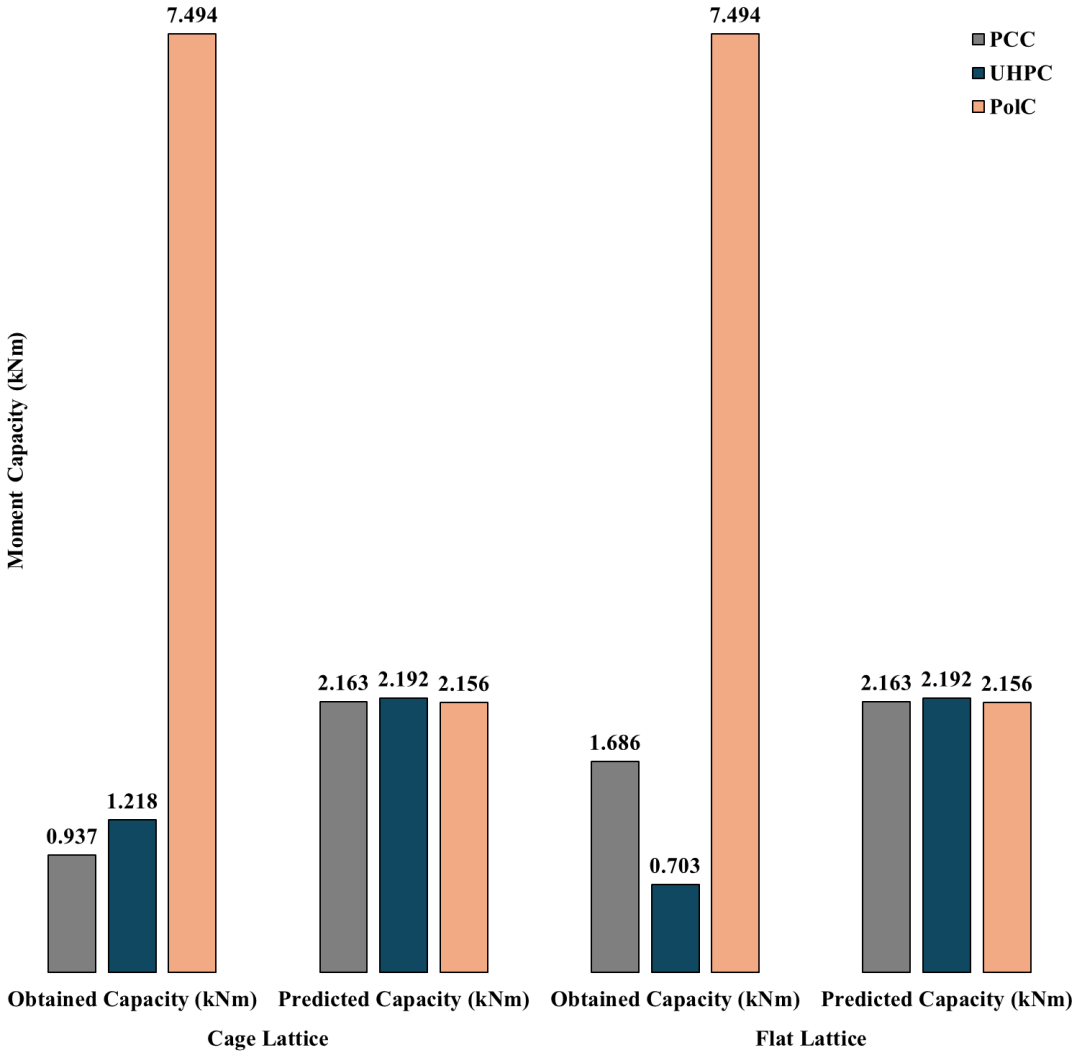

Figure 83: Bar Plot showing theoretical capacity vs observed capacity of PCC, UHPC, and PolC beams with cage and flat lattices

9.4. Conclusions

This study examined the flexural behavior of nine concrete beams reinforced with WEAV3D CFRP under four-point loading. Several key discoveries were made as follows:

1. Beams reinforced with CFRP in cage and flat lattice configurations exhibited higher ductility compared to the brittle failure observed in unreinforced specimens.

2. During casting, the lightweight CFRP reinforcement exhibited floating and lateral displacements of up to 50 mm in some specimens, affecting placement accuracy.
3. Scanning Electron Microscopy (SEM) revealed fiber disorientation and disrupted internal bonding within the CFRP structure, suggesting premature bond deterioration during casting.
4. All beams failed in tension, with CFRP rupture occurring prior to concrete crushing, indicating that the tensile strength of the composite governs the failure mode.

This research contributes valuable data on the mechanical performance and bond characteristics of WEAV3D CFRP reinforcement in three distinct concrete types—polymer concrete (PolC), ultra-high-performance concrete (UHPC), and portland cement concrete (PCC):

5. PolC beams exhibited significantly higher flexural capacities (up to ~80 kN) than theoretical estimates, likely due to strong bonding with the CFRP tapes.
6. UHPC beams reached 55% (cage lattice) and 32% (flat lattice) of their theoretical capacities, reflecting the need for better compatibility and bond optimization.
7. PCC beams demonstrated more balanced stress distribution, with cage and flat lattices achieving 43% and 78% of their theoretical capacities, respectively.
8. These results emphasize the importance of bond quality, reinforcement placement stability, and the mechanical compatibility between reinforcement and matrix material.

This study highlights the potential of WEAV3D CFRP as a lightweight, non-metallic primary reinforcement system:

9. The customized lattice configurations allowed for flexible integration with different concrete types, suggesting adaptability for targeted structural applications.

10. Despite casting challenges, the reinforcement demonstrated capacity enhancement and ductility improvement, particularly in polymer-based matrices.
11. The research adds to the limited experimental data on structural behavior of non-metallic reinforcements, supporting future development of predictive flexural design methods for CFRP-reinforced systems.

10. CHAPTER 10: Conclusions and Recommendations for Future Work

10.1. Conclusions:

10.1.1. Project 1: CFRP-Strengthened RC Beams (NSM Bars + U-Wraps)

This project investigated reinforced concrete beams strengthened with NSM CFRP bars, externally bonded CFRP U-wraps, and their combinations under four-point bending. Groups included Control, U-wrap only, NSM, NSM+full U-wrap, and NSM+shear-span U-wrap. The project quantified nominal moment, strain development, failure mode, and load–deflection, and assessed the effect of confinement and anchorage on ductility and strain-compatibility. The key findings and conclusions from this project are summarized below.

1. NSM bars substantially increased nominal moment; adding U-wrap confinement (full or shear-span) delivered additional strength on the order of 9–12% over NSM alone, with representative peak loads rising from ~145 kN (NSM) to ~158–162 kN (NSM+wrap).
2. The governing limit state shifted from bond-controlled debonding/epoxy splitting (NSM-only) to CFRP bar rupture in many combined cases, consistent with higher FRP strain development (NSM-bar strains on the order of 1.3–1.4%, ~70–80% of ε_u, at peak).
3. Load–deflection histories became bilinear with discrete post-peak drops where rupture governed; partial (shear-span) wrapping achieved most of the bond/strain-utilization benefit while moderating the frequency of rupture-controlled failures.

4. Structural implication: Treat U-wrap extent and anchorage as primary design variables: use wraps to mobilize NSM strain, but pair strength checks with explicit displacement-ductility and strain-compatibility checks so added capacity is not accompanied by brittle response.

10.1.2. Project 2: CNT-Enhanced Polymer Concrete Overlays (Bond on Healthy vs. Sulfate-Damaged Substrates)

This project evaluated polymer concrete overlays with neat and MWCNT-modified mixes (pristine and functionalized) on healthy and sulfate-damaged substrates using ASTM C1583 pull-off testing and microscopy. The project considered dispersion (two-stage mixing) and surface preparation to establish a substrate-conditioned selection that preserves interface tensile capacity. The main outcomes and conclusions derived from this investigation are presented below.

1. Healthy substrates: Neat PC provided the most reliable interface tensile capacity (pull-off ≈2.8 MPa with low scatter). Pristine MWCNTs (0.25%) have collapsed adhesion (~0.04–0.10 MPa on valid tests) and are not recommended where bond governs.
2. Sulfate-damaged substrates: A 0.5% COOH-functionalized MWCNT mix raised pull-off from ~1.30 to ~1.65 MPa on the same deteriorated substrate, demonstrating a practical, condition-based route to preserve interface capacity.
3. Structural implication: Specify neat PC for sound concrete; for sulfate-affected decks, specify ~0.5% COOH-MWCNT PC with verified dispersion (two-stage mixing) and ICRI CSP 5–9 surface prep. Avoid pristine CNTs at 0.25–0.5% when adhesion is critical.

10.1.3. Project 3 — GFRP Slip-Lined CMP Culverts (Role of Annular Grout)

This project examined GFRP slip-lined corrugated metal pipe sections with polymeric and cementitious annular grout by circumferential ring testing on uncorroded and corroded hosts. The project determined peak load, displacement, stiffness factor, and composite ring action, and identified grout modulus and bond as first-order variables for stiffness and service-load deformation. The conclusions are represented below. The major results and corresponding conclusions of this study are outlined below.

1. Annular grout choice controlled the circumferential response. Polymeric grout achieved ~65,100 lbf at ~0.25 in displacement on uncorroded rings versus ~28,900 lbf at ~0.89 in with cementitious grout, yielding a stiffness factor ≈262,600 vs. ≈32,600 lbf/in (≈7× higher). Under corrosion, polymeric systems remained decisively stiffer (≈4.4×).
2. Capacity/stiffness in polymeric systems decreased on the order of 18–23% with corrosion (vs ~6% for cementitious), reflecting higher sensitivity of a stiffer composite to wall-thickness loss.
3. Structural implication: Annular grout selection is first-order. Use polymeric grout when circumferential stiffness and service-load deformation control are critical; account for ≈18–23% capacity sensitivity to corrosion in polymeric systems vs. ≈6% for cementitious.

10.1.4. Project 4 — Freeze–Thaw Durability of Nanomodified CFRP (Off-Axis Tensile)

This project studied freeze–thaw durability of CFRP laminates using off-axis tensile response over 0–250 cycles, comparing neat epoxy and CNT-modified systems. The project related mechanical trends to SEM observations of crack-bridging and fiber–matrix interfacial adhesion to support

durability qualification for cold-region service. The detailed conclusions based on the experimental results are listed below.

1. Neat CFRP: Mean tensile strength decreased from ≈81.7 MPa (0 cycles) to ≈69.3 MPa (250 cycles) (≈−15%); ultimate strain and modulus decreased ≈−11% and ≈−20%, respectively.
2. CNT-modified CFRP: Properties were largely retained across cycle counts; standouts were –COOH 1.0% (≈79.0 MPa at 0 cycles → ≈89.7 MPa at 250 cycles) and pristine 1.5% (most resilient among pristine mixes at 250 cycles).
3. Structural implication: For cold-region service with matrix/interface demands, prefer –COOH ≈1.0% or pristine ≈1.5% (with verified dispersion) and qualify using off-axis metrics, not fiber-dominated tests alone.

10.1.5. Project 5 — 3D-Printed Thermoplastic CFRP Lattice as Internal Reinforcement (PCC, UHPC, PC)

This project investigated thermoplastic CFRP lattice as internal reinforcement in PCC, UHPC, and polymer concrete beams under four-point bending. The project focused on displacement capacity, observed nominal moments versus PCC-based predictions, and sensitivities to placement (cover, floating/tilt) and junction quality, with notes for installation, and stress-block assumptions. The principal observations and conclusions obtained from the experimental program are provided below.

1. Lattices enhanced displacement capacity: UHPC beams reached ~24 mm before failure (vs brittle control just above ~20 kN), and PC beams maintained ~80 kN peak load while achieving larger displacements (≈5.0 mm cage; ≈3.5 mm flat) relative to controls.

2. Observed nominal moments departed from PCC-based predictions, particularly in polymer concrete. Performance was sensitive to placement (cover, floating/tilt) and junction quality, which could localize tensile rupture.
3. Structural implication: Implement positive fixation (chairs/ties) and cover control; adopt matrix-appropriate compressive stress-block assumptions—especially for PC—and use lattice geometry (cage vs. flat) to tune ductility.

10.2. Recommendations for Future Work

1. Test NSM CFRP bars with larger diameters (with bigger grooves and longer bonded lengths) to see how diameter affects bond, FRP strain development, and the shift from debonding to bar rupture when U-wraps are used.
2. Re-run the pull-off program for polymer concrete overlays on substrates damaged by chlorides/deicing, freeze–thaw scaling, ASR, and carbonation, to understand the performance of MWCNTs on other deteriorated substrates.
3. Test GFRP slip-lined CMP rings buried in soil (confined condition) with controlled backfill and compaction to measure circumferential stiffness and deformation under load, and compare the results with the unconfined ring tests for both polymeric and cementitious annular grout.
4. Extend the freeze–thaw study to more extreme temperatures (lower minimums and higher maximums, with moisture exposure and longer cycling) and then repeat the off-axis tensile tests to check if 1.0% COOH and 1.5% pristine mixes still retain their advantage.
5. For the thermoplastic CFRP lattice in PCC/UHPC/PC, run longer-term four-point bending with sustained load and repeated loading, while controlling placement (cover, floating/tilt)

and junction quality, to tighten the stress-block assumptions and set simple installation guidelines.

11. References

Abanilla, M. A., V. M. Karbhari, and Y. Li. 2006. "Interlaminar and intralaminar durability characterization of wet layup carbon/epoxy used in external strengthening." *Compos. Part B Eng.*, 37 (7–8): 650–661. https://doi.org/10.1016/j.compositesb.2006.02.023.

Abdellatef, M., R. Chennareddy, and M. M. R. Taha. 2021. "Design of GFRP slip liner for retrofitting corroded metal culverts." *Tran-SET 2021 - Proc. Tran-SET Conf. 2021*, 332–339. American Society of Civil Engineers (ASCE).

Akbarpour, A., M. Mahdikhani, and R. Z. Moayed. 2022a. "Effects of natural zeolite and sulfate ions on the mechanical properties and microstructure of plastic concrete." *Front. Struct. Civ. Eng.*, 16 (1): 86–98. Higher Education Press Limited Company. https://doi.org/10.1007/s11709-021-0793-x.

Akbarpour, A., M. Mahdikhani, and R. Ziaie Moayed. 2022b. "Mechanical Behavior and Permeability of Plastic Concrete Containing Natural Zeolite under Triaxial and Uniaxial Compression." *J. Mater. Civ. Eng.*, 34 (2). https://doi.org/10.1061/(asce)mt.1943-5533.0004093.

Akbarpour, A., M. Mahdikhani, and R. Ziaie Moayed. 2022c. "Mechanical Behavior and Permeability of Plastic Concrete Containing Natural Zeolite under Triaxial and Uniaxial Compression." *J. Mater. Civ. Eng.*, 34 (2): 04021453. American Society of Civil Engineers. https://doi.org/10.1061/(asce)mt.1943-5533.0004093.

Akbarpour, A., J. Volz, and S. Vemuganti. 2024. "An Experimental Study Incorporating Carbon Fiber Composite Bars and Wraps for Concrete Performance and Failure Insight." *J. Compos.*

Sci., 8 (5). https://doi.org/10.3390/jcs8050174.

Al-Mahaidi, R., and R. Kalfat. 2018. "Methods of Structural Rehabilitation and Strengthening." *Rehabil. Concr. Struct. with Fiber-Reinforced Polym.*, 7–13.

Al-samawi, M., and J. Zhu. 2022. "Evaluation of the corrosion effects on the performance of composite bridge based on cellular automata and finite element method." *Struct. Infrastruct. Eng.*, 18 (5): 630–652. Taylor & Francis. https://doi.org/10.1080/15732479.2020.1860095.

Al-samawi, M., J. Zhu, and W. Rong. 2023. "Application of 3D cellular automata-based analysis to chloride diffusion process in concrete bridges." *Structures*, 47: 500–519. Elsevier. https://doi.org/10.1016/j.istruc.2022.11.071.

Aljidda, O., A. El Refai, and W. Alnahhal. 2023. "Comparative study on the bond performance of near-surface mounted fiber-reinforced polymer bars." *Constr. Build. Mater.*, 364 (November 2022): 129923. Elsevier Ltd. https://doi.org/10.1016/j.conbuildmat.2022.129923.

Alzlfawi, A. 2023. *Investigation of Cellular Grout as an Annulus Void Fill Material for Sliplined Culverts*.

ASTM/C143M-15a. 2009. "Standard Test Method for Slump of Hydraulic Cement Concrete (C 143)." *ASTM Int.*, 99–101.

ASTM C469/C469M − 14l. 2014. "Standard Test Method for Static Modulus of Elasticity and Poisson's Ratio of Concrete in Compression." *Annu. B. ASTM Stand.*, 1–5. https://doi.org/10.1520/C0469.

Avouris, P. 2002. "Molecular electronics with carbon nanotubes." *Acc. Chem. Res.*, 35 (12): 1026–1034. https://doi.org/10.1021/ar010152e.

Bakis, C. E., L. C. Bank, V. L. Brown, E. Cosenza, J. F. Davalos, J. J. Lesko, A. Machida, S. H. Rizkalla, and T. C. Triantafillou. 2003. "Fiber-Reinforced Polymer Composites for Construction - State-of-the-Art Review." *Perspect. Civ. Eng. Commem. 150th Anniv. Am. Soc. Civ. Eng.*, 6 (May): 369–383. https://doi.org/10.1061/(asce)1090-0268(2002)6:2(73).

Bank, L. C. 2006. *Composites for Construction*. *Compos. Constr.*

Bank, L. C. 2007. *Composites for Construction: Structural Design with FRP Materials*. *Compos. Constr. Struct. Des. with FRP Mater.*

Barkoula, N. M., B. Alcock, N. O. Cabrera, and T. Peijs. 2008. "Flame-Retardancy Properties of Intumescent Ammonium Poly(Phosphate) and Mineral Filler Magnesium Hydroxide in Combination with Graphene." *Polym. Polym. Compos.*, 16 (2): 101–113. https://doi.org/10.1002/pc.

Bheel, N., B. S. Mohammed, M. S. Liew, and N. A. W. A. Zawawi. 2023. "Durability Behaviours of Engineered Cementitious Composites Blended with Carbon Nanotubes against Sulphate and Acid Attacks by Applying RSM Modelling and Optimization." *Buildings*, 13 (8). https://doi.org/10.3390/buildings13082032.

Budelmann, H., and F. S. Rostasy. 1993. "Creep rupture behavior of FRP Elements for Prestressed Concrete - Phenomenon, results and forecast models." *Am. Concr. Institute, ACI Spec. Publ.*, 87–100.

Byron, D., A. Pacheli Heitman, J. Neves, P. P. de Souza, and P. S. de Oliveira Patricio. 2021. "Evaluation of properties of polymer concrete based on epoxy resin and functionalized carbon nanotubes." *Constr. Build. Mater.*, 309. https://doi.org/10.1016/j.conbuildmat.2021.125155.

Cai, H., and X. Liu. 1998. “Freeze-thaw durability of concrete: Ice formation process in pores.” *Cem. Concr. Res.*, 28 (9): 1281–1287. https://doi.org/10.1016/S0008-8846(98)00103-3.

Camacho, M. del C., O. Galao, F. J. Baeza, E. Zornoza, and P. Garcés. 2014. “Mechanical properties and durability of CNT cement composites.” *Materials (Basel).*, 7 (3): 1640–1651. https://doi.org/10.3390/ma7031640.

Van Cao, V., and S. Q. Pham. 2019. “Comparison of CFRP and GFRP Wraps on Reducing Seismic Damage of Deficient Reinforced Concrete Structures.” *Int. J. Civ. Eng.*, 17 (11): 1667–1681. Springer International Publishing. https://doi.org/10.1007/s40999-019-00429-y.

Chajes, M. J., T. F. Januszka, D. R. Mertz, T. A. Thomson, and W. W. Finch. 1995. “Shear strengthening of reinforced concrete beams using externally applied composite fabrics.” *ACI Struct. J.*, 92 (3): 295–303. https://doi.org/10.14359/1130.

ChennaReddy, R. 2016. “SIGNIFICANCE OF U-WRAP FRP SHEAR STRENGTHENING ON FLEXURAL BEHAVIOR OF RC BEAMS STRENGTHENED USING NEAR SURFACE MOUNTED FRP BARS(700mm beam).”

Chennareddy, R., and M. M. R. Taha. 2017. “Effect of Combining Near-Surface-Mounted and U-Wrap Fiber-Reinforced Polymer Strengthening Techniques on Behavior of Reinforced Concrete Beams.” *ACI Struct. J.*, 114 (3): 721–730. https://doi.org/10.14359/51689443.

Chuah, S., Z. Pan, J. G. Sanjayan, C. M. Wang, and W. H. Duan. 2014a. “Nano reinforced cement and concrete composites and new perspective from graphene oxide.” *Constr. Build. Mater.*

Chuah, S., Z. Pan, J. G. Sanjayan, C. M. Wang, and W. H. Duan. 2014b. “Nano reinforced cement and concrete composites and new perspective from graphene oxide.” *Constr. Build. Mater.*

Cousin, P., M. Hassan, P. V. Vijay, M. Robert, and B. Benmokrane. 2019. “Chemical resistance of carbon, basalt, and glass fibers used in FRP reinforcing bars.” *J. Compos. Mater.*, 53 (26–27): 3651–3670. SAGE Publications Ltd. https://doi.org/10.1177/0021998319844306.

Dadkhah, M., A. Saboori, and P. Fino. 2019. “An overview of the recent developments in metal matrix nanocomposites reinforced by graphene.” *Materials (Basel).*

Dang, T. K. M., M. Nikzad, R. Arablouei, S. Masood, D. K. Bui, V. K. Truong, and I. Sbarski. 2024. “Experimental study and predictive modelling of damping ratio in hybrid polymer concrete.” *Constr. Build. Mater.*, 411. https://doi.org/10.1016/j.conbuildmat.2023.134541.

Das, S. 2021. “Performance Enhancement Of Controlled Low-Strength Grout Material (CLSM) For Annulus Voids Of Sliplined Culverts.”

Davalos, J. F., H. A. Salim, P. Qiao, R. Lopez-Anido, and E. J. Barbero. 1996. “Analysis and design of pultruded FRP shapes under bending.” *Compos. Part B Eng.*, 27 (3–4): 295–305. https://doi.org/10.1016/1359-8368(95)00015-1.

David, O. Ben, L. Banks-Sills, J. Aboudi, V. Fourman, R. Eliasi, T. Simhi, A. Shlayer, and O. Raz. 2014a. “Evaluation of the Mechanical Properties of PMMA Reinforced with Carbon Nanotubes - Experiments and Modeling.” *Exp. Mech.*, 54 (2): 175–186. https://doi.org/10.1007/s11340-013-9792-8.

David, O. Ben, L. Banks-Sills, J. Aboudi, V. Fourman, R. Eliasi, T. Simhi, A. Shlayer, and O. Raz. 2014b. “Evaluation of the Mechanical Properties of PMMA Reinforced with Carbon Nanotubes - Experiments and Modeling.” *Exp. Mech.*, 54 (2): 175–186. https://doi.org/10.1007/s11340-013-9792-8.

Dikeou, J. T. 2003. “History of ACI committee 548: The past thirty years.” *Am. Concr. Institute, ACI Spec. Publ.*, 1–11.

Douba, A. E., M. Emiroglu, U. F. Kandil, and M. M. Reda Taha. 2019. “Very ductile polymer concrete using carbon nanotubes.” *Constr. Build. Mater.*, 196: 468–477. Elsevier Ltd. https://doi.org/10.1016/j.conbuildmat.2018.11.021.

Dutta, P. K., and D. Hui. 1996. “Low-temperature and freeze-thaw durability of thick composites.” *Compos. Part B Eng.*, 27 (3–4): 371–379. https://doi.org/10.1016/1359-8368(96)00007-8.

Van Den Einde, L., L. Zhao, and F. Seible. 2003. “Use of FRP composites in civil structural applications.” *Constr. Build. Mater.*, 389–403.

Engineers, A. S. of C. 2018. *Failure to Act: Closing the Infrastructure Investment Gap for America’s Economic Future*. *Fail. to Act Closing Infrastruct. Invest. Gap Am. Econ. Futur.* American Society of Civil Engineers (ASCE).

Erol, O., I. Uyan, M. Hatip, C. Yilmaz, A. B. Tekinay, and M. O. Guler. 2018. “Recent advances in bioactive 1D and 2D carbon nanomaterials for biomedical applications.” *Nanomedicine Nanotechnology, Biol. Med.*

Ferreira, P., M. Riscado, S. Bernardo, M. G. Freire, J. L. Faria, A. P. M. Tavares, C. G. Silva, and F. Sousa. 2023. “Pristine Multi-walled carbon nanotubes for a rapid and efficient plasmid DNA clarification.” *Sep. Purif. Technol.*, 320 (January): 124224. Elsevier B.V. https://doi.org/10.1016/j.seppur.2023.124224.

Ganguli, S., H. Aglan, P. Dennig, and G. Irvin. 2006. “Effect of loading and surface modification of MWCNTs on the fracture behavior of epoxy nanocomposites.” *J. Reinf. Plast. Compos.*,

25 (2): 175–188. https://doi.org/10.1177/0731684405056425.

Goh, K. L. 2017. “Discontinuous-Fibre Reinforced Composites.” (1): 21–49. https://doi.org/10.1007/978-1-4471-7305-2.

Gorninski, J. P., D. C. Dal Molin, and C. S. Kazmierczak. 2004. “Study of the modulus of elasticity of polymer concrete compounds and comparative assessment of polymer concrete and portland cement concrete.” *Cem. Concr. Res.*, 34 (11): 2091–2095. https://doi.org/10.1016/j.cemconres.2004.03.012.

Gowayed, Y. 2013. “Types of fiber and fiber arrangement in fiber-reinforced polymer (FRP) composites.” *Dev. Fiber-Reinforced Polym. Compos. Civ. Eng.*, 3–17.

Green, M. F., L. A. Bisby, Y. Beaudoin, and P. Labossière. 2000. “Effect of freeze-thaw cycles on the bond durability between fibre reinforced polymer plate reinforcement and concrete.” *Can. J. Civ. Eng.*, 27 (5): 949–959. https://doi.org/10.1139/l00-031.

Grigore, M. E. 2017. “Methods of recycling, properties and applications of recycled thermoplastic polymers.” *Recycling*.

Guo, Y., R. Zhang, Q. Xiao, H. Guo, Z. Wang, X. Li, J. Chen, and J. Zhu. 2018. “Asynchronous fracture of hierarchical microstructures in hard domain of thermoplastic polyurethane elastomer: Effect of chain extender.” *Polymer (Guildf).*, 138: 242–254. Elsevier Ltd. https://doi.org/10.1016/j.polymer.2018.01.035.

Haghani, R., J. Yang, M. Gutierrez, C. D. Eamon, and J. Volz. 2021. “Fiber reinforced polymer culvert bridges—a feasibility study from structural and lcc points of view.” *Infrastructures*, 6 (9). https://doi.org/10.3390/infrastructures6090128.

Han, B., Z. Yang, X. Shi, and X. Yu. 2013. “Transport properties of carbon-nanotube/cement composites.” *J. Mater. Eng. Perform.*, 22 (1): 184–189. https://doi.org/10.1007/s11665-012-0228-x.

Hancox, N. L. 1996. “Engineering mechanics of composite materials.” *Mater. Des.*, 17 (2): 114. https://doi.org/10.1016/s0261-3069(97)87195-6.

Hassan, T., and S. Rizkalla. 2003. “Investigation of Bond in Concrete Structures Strengthened with Near Surface Mounted Carbon Fiber Reinforced Polymer Strips.” *J. Compos. Constr.*, 7 (3): 248–257. https://doi.org/10.1061/(asce)1090-0268(2003)7:3(248).

Hirsch, A., and O. Vostrowsky. 2005. “Functionalization of carbon nanotubes.” *Top. Curr. Chem.*, 245: 193–237. https://doi.org/10.1007/b98169.

Hong, C. S., C. D. Shackelford, and M. A. Malusis. 2017. “Numerical Evaluation of Vertical Cutoff Walls Comprising Zeolite-Amended Backfills for Enhanced Metals Containment.” *J. Geotech. Geoenvironmental Eng.*, 143 (7): 04017028. https://doi.org/10.1061/(asce)gt.1943-5606.0001699.

Hosford, W. R. 2013. *Elementary Materials Science*. *Elem. Mater. Sci.*

Hoult, N. A., W. Andy Take, C. Lee, and M. Dutton. 2013. “Experimental accuracy of two dimensional strain measurements using Digital Image Correlation.” *Eng. Struct.*, 46: 718–726. https://doi.org/10.1016/j.engstruct.2012.08.018.

Hwang, W., and K. S. Han. 1986. “Fatigue of Composites—Fatigue Modulus Concept and Life Prediction.” *J. Compos. Mater.*, 20 (2): 154–165. https://doi.org/10.1177/002199838602000203.

Iijima, S. 1991. “Helical microtubules of graphitic carbon.” *Nature*, 354 (6348): 56–58. https://doi.org/10.1038/354056a0.

Ikumi, T., S. H. P. Cavalaro, and I. Segura. 2019. “The role of porosity in external sulphate attack.” *Cem. Concr. Compos.*, 97 (January 2018): 1–12. Elsevier. https://doi.org/10.1016/j.cemconcomp.2018.12.016.

Ikumi, T., S. Cavalaro, I. Segura, C. Goodier, and S. Austin. 2018. “Simplified analytical assessment of damaged induced by the external sulphate attack in concrete piles.” *fib Symp.*, 2282–2289. Springer, Cham.

Infrastructure Report CARD. 2025. “A comprehensive assessment of America’s infrastructure.” *Asce*.

Ishtiaq, S., M. Q. Saleem, R. Naveed, M. Harris, and S. A. Khan. 2024. “Glass–Carbon–Kevlar fiber reinforced hybrid polymer composite (HPC): Part (A) mechanical and thermal characterization for high GSM laminates.” *Compos. Part C Open Access*, 14: 100468. Elsevier. https://doi.org/10.1016/j.jcomc.2024.100468.

Jambhulkar, T., and R. K. Sahu. 2024. “Modelling and optimization of hybrid Kevlar/glass fabric reinforced polymer composites for low-velocity impact resistant applications.” *Forces Mech.*, 15: 100267. Elsevier. https://doi.org/10.1016/j.finmec.2024.100267.

Kabashi, N., B. Avdyli, E. Krasniqi, and A. Këpuska. 2020. “Comparative approach to flexural behavior of reinforced beams with GFRP, CFRP, and steel bars.” *Civ. Eng. J.*, 6 (1): 50–59. https://doi.org/10.28991/cej-2020-03091452.

Kachlakev, D., and D. D. McCurry. 2000. “Behavior of full-scale reinforced concrete beams

retrofitted for shear and flexural with FRP laminates." *Compos. Part B Eng.*, 31 (6–7): 445–452. https://doi.org/10.1016/S1359-8368(00)00023-8.

Kaiser, H. 1989. "Bewehren von Stahlbeton mit kohlenstoffaserverstärkten Epoxidharzen."

Karbhari, V. M. 2001. "Materials Considerations in FRP Rehabilitation of Concrete Structures." *J. Mater. Civ. Eng.*, 13 (2): 90–97. American Society of Civil Engineers (ASCE). https://doi.org/10.1061/(asce)0899-1561(2001)13:2(90).

Khanna, V., V. Kumar, and S. A. Bansal. 2021. "Mechanical properties of aluminium-graphene/carbon nanotubes (CNTs) metal matrix composites: Advancement, opportunities and perspective." *Mater. Res. Bull.*

Kim, J.-H., and G.-H. Kim. 2013. "Thermoplastic Polyurethane (TPU)/Ethylene-Propylene-Diene Monomer Rubber (EPDM) and TPU/Polybutadiene Rubber (BR) Blends for the Application of Footwear Outsole Materials." *Elastomers Compos.*, 48 (3): 195–200. https://doi.org/10.7473/ec.2013.48.3.195.

Kohankar Kouchesfehani, Z., A. Darabnoush Tehrani, and M. Najafi. 2021. "Culvert Renewal with Cementitious-Geopolymer Spray–Applied Pipe Lining: Field Data Collection and Assessment." *J. Pipeline Syst. Eng. Pract.*, 12 (3). American Society of Civil Engineers (ASCE). https://doi.org/10.1061/(asce)ps.1949-1204.0000555.

Kong, A., A. Fam, and M. F. Green. 2005. "Freeze-thaw behavior of FRP-confined concrete under sustained load." *Am. Concr. Institute, ACI Spec. Publ.*, SP-230: 705–722. https://doi.org/10.14359/14862.

Konsta-Gdoutos, M. S., Z. S. Metaxa, and S. P. Shah. 2010. "Highly dispersed carbon nanotube

reinforced cement based materials." *Cem. Concr. Res.*, 40 (7): 1052–1059. Elsevier Ltd. https://doi.org/10.1016/j.cemconres.2010.02.015.

Laredo Dos Reis, J. M. 2005. "Mechanical characterization of fiber reinforced Polymer Concrete." *Mater. Res.*, 8 (3): 357–360. https://doi.org/10.1590/s1516-14392005000300023.

Lee, S. B., S. R. Stock, M. D. Butts, T. L. Starr, T. M. Breunig, and J. H. Kinney. 1998. "Pore geometry in woven fiber structures: 0°/90° plain-weave cloth layup preform." *J. Mater. Res.*, 13 (5): 1209–1217. Materials Research Society. https://doi.org/10.1557/JMR.1998.0172.

Lee, S. H., L. S. An, and H. K. Kim. 2025. "Risk-based bridge life cycle cost and environmental impact assessment considering climate change effects." *Sci. Rep.*, 15 (1): 1–18. Nature Research. https://doi.org/10.1038/s41598-024-82568-4.

Li, C., A. Li, J. Tang, X. Yang, J. Li, and J. Jiang. 2023. "Preparation and properties of Portland cement from secondary recycle waste of rare earth tailing." *Constr. Build. Mater.*, 406 (August): 133337. Elsevier Ltd. https://doi.org/10.1016/j.conbuildmat.2023.133337.

Li, F., C. Zhou, P. Yang, B. Wang, J. Hu, J. Wei, and Q. Yu. 2019. "Direct synthesis of carbon nanotubes on fly ash particles to produce carbon nanotubes/fly ash composites." *Front. Struct. Civ. Eng.*, 13 (6): 1405–1414. https://doi.org/10.1007/s11709-019-0564-0.

Li, J., Z. Zhang, J. Fu, Z. Liang, and K. R. Ramakrishnan. 2021. "Mechanical properties and structural health monitoring performance of carbon nanotube-modified FRP composites: A review." *Nanotechnol. Rev.*, 10 (1): 1438–1468. https://doi.org/10.1515/ntrev-2021-0104.

Li, W. W., W. M. Ji, Y. C. Wang, Y. Liu, R. X. Shen, and F. Xing. 2015a. "Investigation on the mechanical properties of a cement-based material containing carbon nanotube under drying

and freeze-thaw conditions." *Materials (Basel).*, 8 (12): 8780–8792. https://doi.org/10.3390/ma8125491.

Li, Y., Z. Zhu, J. Yu, and B. Ding. 2015b. "Carbon Nanotubes Enhanced Fluorinated Polyurethane Macroporous Membranes for Waterproof and Breathable Application." *ACS Appl. Mater. Interfaces*, 7 (24): 13538–13546. American Chemical Society. https://doi.org/10.1021/acsami.5b02848.

Liu, K., D. Sun, A. Wang, G. Zhang, and J. Tang. 2018. "Long-Term Performance of Blended Cement Paste Containing Fly Ash against Sodium Sulfate Attack." *J. Mater. Civ. Eng.*, 30 (12): 04018309. https://doi.org/10.1061/(asce)mt.1943-5533.0002516.

De Lorenzis, L., and J. G. Teng. 2007. "Near-surface mounted FRP reinforcement: An emerging technique for strengthening structures." *Compos. Part B Eng.*, 38 (2): 119–143. https://doi.org/10.1016/j.compositesb.2006.08.003.

Lubin, G. 1982. *Handbook of Composites*. *Handb. Compos.*

Luo, S., T. Bai, M. Guo, Y. Wei, and W. Ma. 2022. "Impact of Freeze–Thaw Cycles on the Long-Term Performance of Concrete Pavement and Related Improvement Measures: A Review." *Materials (Basel).*, 15 (13). https://doi.org/10.3390/ma15134568.

M. A. Kadhim, M., A. Jawdhari, M. M. Altaee, A. Majdi, and A. Fam. 2023. "Parametric investigation of continuous beams strengthened with near surface mounted FRP bars." *Eng. Struct.*, 293 (June): 116619. Elsevier Ltd. https://doi.org/10.1016/j.engstruct.2023.116619.

Malik, A. R., and S. J. Foster. 2010. "Carbon fiber-reinforced polymer confined reactive powder concrete columns-experimental investigation." *ACI Struct. J.*, 107 (3): 263–271.

https://doi.org/10.14359/51663691.

Manawadu, A., P. Qiao, and H. Wen. 2023. “Characterization of Substrate-to-Overlay Interface Bond in Concrete Repairs: A Review.” *Constr. Build. Mater.*

Markiv, T., K. Sobol, M. Franus, and W. Franus. 2016. “Mechanical and durability properties of concretes incorporating natural zeolite.” *Arch. Civ. Mech. Eng.*, 16 (4): 554–562. https://doi.org/10.1016/j.acme.2016.03.013.

Marsh, G. 2006. “50 years of reinforced plastic boats.” *Reinf. Plast.*, 50 (9): 16–19. https://doi.org/10.1016/S0034-3617(06)71125-0.

McAlpine, G. 2006. “Structural rehabilitation of semi elliptical concrete sewers.” *Proc. 2006 Pipeline Div. Spec. Conf. - Pipelines 2006 Serv. to Own.*, 58. American Society of Civil Engineers (ASCE).

McKim, R. A. 1997. “Selection Method for Trenchless Technologies.” *J. Infrastruct. Syst.*, 3 (3): 119–125. American Society of Civil Engineers (ASCE). https://doi.org/10.1061/(asce)1076-0342(1997)3:3(119).

Moore, I. D. 2001. “Buried Pipes and Culverts.” *Geotech. Geoenvironmental Eng. Handb.*, 541–567. Springer US.

Moore, I. D., and F. Hu. 1996. “Linear viscoelastic modelling of profiled high density polyethylene pipe.” *Can. J. Civ. Eng.*, 23 (2): 395–407. https://doi.org/10.1139/l96-044.

Mostofinejad, D., and M. Mohammadi. 2020. “Effect of Freeze–Thaw Cycles on FRP-Concrete Bond Strength in EBR and EBROG Systems.” *J. Compos. Constr.*, 24 (3). American Society of Civil Engineers (ASCE). https://doi.org/10.1061/(asce)cc.1943-5614.0001010.

Murad, Y., and T. Abu-AlHaj. 2021. “Flexural strengthening and repairing of heat damaged RC beams using continuous near-surface mounted CFRP ropes.” *Structures*, 33 (April): 451–462. Elsevier Ltd. https://doi.org/10.1016/j.istruc.2021.04.079.

Murcia, D. H., B. Çomak, E. Soliman, and M. M. Reda Taha. 2022. “Flexural Behavior of a Novel Textile-Reinforced Polymer Concrete.” *Polymers (Basel).*, 14 (1). https://doi.org/10.3390/polym14010176.

Muzzy, J. D., and A. O. Kays. 1984. “Thermoplastic vs. thermosetting structural composites.” *Polym. Compos.*, 5 (3): 169–172. https://doi.org/10.1002/pc.750050302.

Nanni, A., Alkhrdaji, T., Chen, G., Barker, M., Xinbao, Y., and Mayo, R. 1999. “Overview of testing to failure program of a highway bridge strengthened with FRP composites.” *4th Int. Symp. FRP Reinf. Concr. Struct.*, 69–80.

Nanni, A. 1993. “Flexural Behavior and Design of RC Members Using FRP Reinforcement.” *J. Struct. Eng.*, 119 (11): 3344–3359. American Society of Civil Engineers (ASCE). https://doi.org/10.1061/(asce)0733-9445(1993)119:11(3344).

Nartam, S., V. Rautela, S. Budhe, J. Paul, and S. de Barros. 2024. “Strength Retention of Carbon Fiber/Epoxy Vitrimer Composite Material for Primary Structures: Towards Recyclable and Reusable Carbon Fiber Composites †.” *Appl. Mech.*, 5 (4): 804–817. https://doi.org/10.3390/applmech5040045.

Neville, A. 2004. “The confused world of sulfate attack on concrete.” *Cem. Concr. Res.*, 34 (8): 1275–1296. https://doi.org/10.1016/j.cemconres.2004.04.004.

Nodehi, M. 2022. “Epoxy, polyester and vinyl ester based polymer concrete: a review.” *Innov.*

Infrastruct. Solut., 7 (1). Springer Science and Business Media Deutschland GmbH. https://doi.org/10.1007/s41062-021-00661-3.

Norizan, M. N., M. H. Moklis, S. Z. Ngah Demon, N. A. Halim, A. Samsuri, I. S. Mohamad, V. F. Knight, and N. Abdullah. 2020. "Carbon nanotubes: Functionalisation and their application in chemical sensors." *RSC Adv.*, 10 (71): 43704–43732. https://doi.org/10.1039/d0ra09438b.

Okoro, A. M., S. S. Lephuthing, S. R. Oke, O. E. Falodun, M. A. Awotunde, and P. A. Olubambi. 2019. "A Review of Spark Plasma Sintering of Carbon Nanotubes Reinforced Titanium-Based Nanocomposites: Fabrication, Densification, and Mechanical Properties." *JOM*. Minerals, Metals and Materials Society.

Ombres, L., and P. Mazzuca. 2024. "Residual Flexural Behavior of PBO FRCM-Strengthened Reinforced Concrete Beams after Exposure to Elevated Temperatures." *J. Compos. Constr.*, 28 (1): 1–12. https://doi.org/10.1061/jccof2.cceng-4318.

Ortiz, J. D., S. S. Khedmatgozar Dolati, P. Malla, A. Nanni, and A. Mehrabi. 2023. "FRP-Reinforced/Strengthened Concrete: State-of-the-Art Review on Durability and Mechanical Effects." *Materials (Basel).*, 16 (5): 1–30. https://doi.org/10.3390/ma16051990.

Ouyang, C., A. Nanni, and W. F. Chang. 1988. "Internal and external sources of sulfate ions in portland cement mortar: two types of chemical attack." *Cem. Concr. Res.*, 18 (5): 699–709. Pergamon. https://doi.org/10.1016/0008-8846(88)90092-0.

Ovali, I. 2018. "Tribological performance of glass/epoxy composites filled with MWCNTs." *Int. J. Mater. Res.*, 109 (4): 341–349. Carl Hanser Verlag. https://doi.org/10.3139/146.111607.

Ozkan, D., M. S. Gok, and A. C. Karaoglanli. 2020. "Carbon Fiber Reinforced Polymer (CFRP)

Composite Materials, Their Characteristic Properties, Industrial Application Areas and Their Machinability." *Adv. Struct. Mater.*, 235–253. Springer.

Park, S. J., M. S. Cho, S. T. Lim, H. J. Choi, and M. S. Jhon. 2003. "Synthesis and Dispersion Characteristics of Multi-Walled Carbon Nanotube Composites with Poly(methyl methacrylate) Prepared by In-Situ Bulk Polymerization." *Macromol. Rapid Commun.*, 24 (18): 1070–1073. https://doi.org/10.1002/marc.200300089.

Pascault, J. P., and R. J. J. Williams. 2013. "Thermosetting Polymers." *Handb. Polym. Synth. Charact. Process.*, 519–533. John Wiley and Sons.

Pezeshkian, M., A. Delnavaz, and M. Delnavaz. 2020. "Effect of Natural Zeolite on Mechanical Properties and Autogenous Shrinkage of Ultrahigh-Performance Concrete." *J. Mater. Civ. Eng.*, 32 (5): 04020093. https://doi.org/10.1061/(asce)mt.1943-5533.0002968.

Pinandita Faiz, R. 1998. "No Titילle." **ペインクリニック学会治療指針２**, 43 (March): 1–9.

Popov, V. N., S. Kliment, and V. N. Popov. 2016. "Carbon Nanotubes : Properties and Application Carbon nanotubes : properties and application." *Mater. Sci. Engin. R*, 43 (December): 61–102.

Pratap, A. 2002. "Vinyl ester and acrylic based polymer concrete for electrical applications." *Prog. Cryst. Growth Charact. Mater.*, 45 (1–2): 117–125. https://doi.org/10.1016/S0960-8974(02)00036-0.

Qiu, J., Y. Zhou, N. I. Vatin, X. Guan, S. Sultanov, and K. Khemarak. 2020. "Damage constitutive model of coal gangue concrete under freeze-thaw cycles." *Constr. Build. Mater.*, 264: 120720. Elsevier Ltd. https://doi.org/10.1016/j.conbuildmat.2020.120720.

Qureshi, M. F., and S. A. Sheikh. 2023. “Shear behaviour of GFRP strengthened RC beams at elevated temperatures.” *Constr. Build. Mater.*, 368: 130371. Elsevier. https://doi.org/10.1016/j.conbuildmat.2023.130371.

Reis, J. P., M. de Moura, and S. Samborski. 2020. “Thermoplastic composites and their promising applications in joining and repair composites structures: A review.” *Materials (Basel).*

Rodrigues, R., S. Gaboreau, J. Gance, I. Ignatiadis, and S. Betelu. 2021. “Reinforced concrete structures: A review of corrosion mechanisms and advances in electrical methods for corrosion monitoring.” *Constr. Build. Mater.* Elsevier.

Rodriguez-Camacho, R. E., and R. Uribe-Afif. 2002. “Importance of using the natural pozzolans on concrete durability.” *Cem. Concr. Res.*, 32 (42): 1851–1858.

Roy, S., R. S. Petrova, and S. Mitra. 2018. “Effect of carbon nanotube (CNT) functionalization in epoxy-CNT composites.” *Nanotechnol. Rev.*, 7 (6): 475–485. De Gruyter. https://doi.org/10.1515/ntrev-2018-0068.

Rubel, R. I., M. H. Ali, M. A. Jafor, and M. M. Alam. 2019. “Carbon nanotubes agglomeration in reinforced composites: A review.” *AIMS Mater. Sci.*, 6 (5): 756–780. https://doi.org/10.3934/matersci.2019.5.756.

Saadatmanesh, H., and M. R. Ehsani. 1990. “Fiber composite plates can strengthen beams.” *Concr. Int.*, 12 (3): 65–71.

Saboori, A., M. Dadkhah, P. Fino, and M. Pavese. 2018. “An overview of metal matrix nanocomposites reinforced with graphene nanoplatelets; mechanical, electrical and thermophysical properties.” *Metals (Basel).*

San-José, J. T., I. Vegas, and F. Meyer. 2006. “Structural analysis of FRP reinforced polymer concrete material.” *Constr. Build. Mater.*, 20 (10): 971–981. https://doi.org/10.1016/j.conbuildmat.2005.06.012.

Sbahieh, S., G. Mckay, and S. G. Al-Ghamdi. 2023. “A comparative life cycle assessment of fiber-reinforced polymers as a sustainable reinforcement option in concrete beams.” *Front. Built Environ.*, 9: 1194121. Frontiers Media S.A. https://doi.org/10.3389/fbuil.2023.1194121.

Schinner, G., J. Brandt, and H. Richter. 1996. “Recycling carbon-fiber-reinforced thermoplastic composites.” *J. Thermoplast. Compos. Mater.*, 9 (3): 239–245. SAGE Publications Ltd. https://doi.org/10.1177/089270579600900302.

Sharaky, I. A., M. Baena, C. Barris, H. E. M. Sallam, and L. Torres. 2018. “Effect of axial stiffness of NSM FRP reinforcement and concrete cover confinement on flexural behaviour of strengthened RC beams: Experimental and numerical study.” *Eng. Struct.*, 173 (March 2017): 987–1001. https://doi.org/10.1016/j.engstruct.2018.07.062.

Shokrieh, M. M., M. Heidari-Rarani, M. Shakouri, and E. Kashizadeh. 2011. “Effects of thermal cycles on mechanical properties of an optimized polymer concrete.” *Constr. Build. Mater.*, 25 (8): 3540–3549. https://doi.org/10.1016/j.conbuildmat.2011.03.047.

Simpson, B., I. D. Moore, and N. A. Hoult. 2016. “Experimental Investigation of Rehabilitated Steel Culvert Performance under Static Surface Loading.” *J. Geotech. Geoenvironmental Eng.*, 142 (2): 1–12. https://doi.org/10.1061/(asce)gt.1943-5606.0001406.

Smith, T., N. A. Hoult, and I. D. Moore. 2015. “Role of Grout Strength and Liners on the Performance of Slip-Lined Pipes.” *J. Pipeline Syst. Eng. Pract.*, 6 (4): 2–9. https://doi.org/10.1061/(asce)ps.1949-1204.0000203.

Sokairge, H., F. Elgabbas, and H. Elshafie. 2022. “Structural behavior of RC beams strengthened with prestressed near surface mounted technique using basalt FRP bars.” *Eng. Struct.*, 250 (October 2021): 113489. Elsevier Ltd. https://doi.org/10.1016/j.engstruct.2021.113489.

Soliman, E., M. Al-Haik, and M. R. Taha. 2012. “On and off-axis tension behavior of fiber reinforced polymer composites incorporating multi-walled carbon nanotubes.” *J. Compos. Mater.*, 46 (14): 1661–1675. https://doi.org/10.1177/0021998311422456.

Soudki, K., and T. Alkhrdaji. 2005. “Guide for the Design and Construction of Externally Bonded FRP Systems for Strengthening Concrete Structures (ACI 440.2R-02).” *Proc. Struct. Congr. Expo.*, 1627–1633.

Stansbury, J. W., and M. J. Idacavage. 2016. “3D printing with polymers: Challenges among expanding options and opportunities.” *Dent. Mater.*, 54–64.

Sun, Y., and H. S. Lee. 2023. “Using maturity method to predict compressive strength of acrylic polymer concrete containing TMPTMA or silane at sub-zero curing temperatures.” *Compos. Commun.*, 40. https://doi.org/10.1016/j.coco.2023.101597.

Syachrani, S., H. S. Jeong, V. Rai, M. J. Chae, and T. Iseley. 2010. “A risk management approach to safety assessment of trenchless technologies for culvert rehabilitation.” *Tunn. Undergr. Sp. Technol.*, 25 (6): 681–688. https://doi.org/10.1016/j.tust.2010.05.005.

Taerwe, L. 2020. “Rehabilitation of navy pier beams with composite sheets.” *Non-Metallic Reinf. Concr. Struct.*, 551–558.

Tang, L. C., Y. J. Wan, K. Peng, Y. B. Pei, L. Bin Wu, L. M. Chen, L. J. Shu, J. X. Jiang, and G. Q. Lai. 2013. “Fracture toughness and electrical conductivity of epoxy composites filled with

carbon nanotubes and spherical particles." *Compos. Part A Appl. Sci. Manuf.*, 45: 95–101. Elsevier. https://doi.org/10.1016/J.COMPOSITESA.2012.09.012.

Tetreault, J., I. D. Moore, and N. A. Hoult. 2020. "Laboratory Study on Effect of Grout Choice on Culvert Rehabilitation Using Sliplining." *J. Pipeline Syst. Eng. Pract.*, 11 (1): 1–13. https://doi.org/10.1061/(asce)ps.1949-1204.0000420.

Thakre, P. R., D. C. Lagoudas, J. C. Riddick, T. S. Gates, S. J. V. Frankland, J. G. Ratcliffe, Jiang Zhu, and E. V Barrera. 2011. "Investigation of the effect of single wall carbon nanotubes on interlaminar fracture toughness of woven carbon fiber-epoxy composites." *J. Compos. Mater.*, 45 (10): 1091–1107. https://doi.org/10.1177/0021998310389088.

Tharmarajah, G., S. E. Taylor, D. J. Cleland, and D. Robinson. 2015. "Corrosion-resistant FRP reinforcement for bridge deck slabs." *Proc. Inst. Civ. Eng. - Bridg. Eng.*, 168 (3): 208–217. Thomas Telford Ltd. https://doi.org/10.1680/jbren.13.00001.

Theodore, M., M. Hosur, J. Thomas, S. J.-M. S. And, and U. 2011. n.d. "Influence of functionalization on properties of MWCNT–epoxy nanocomposites." *ElsevierM Theodore, M Hosur, J Thomas, S JeelaniMaterials Sci. Eng. A, 2011•Elsevier*.

Theodore, M., M. Hosur, J. Thomas, and S. Jeelani. 2011. "Influence of functionalization on properties of MWCNT-epoxy nanocomposites." *Mater. Sci. Eng. A*, 528 (3): 1192–1200. https://doi.org/10.1016/j.msea.2010.09.095.

Toufigh, V., S. Masoud Shirkhorshidi, and M. Hosseinali. 2017. "Experimental Investigation and Constitutive Modeling of Polymer Concrete and Sand Interface." *Int. J. Geomech.*, 17 (1). American Society of Civil Engineers (ASCE). https://doi.org/10.1061/(asce)gm.1943-5622.0000695.

Toufigh, V., V. Toufigh, H. Saadatmanesh, and S. Ahmari. 2013. "Strength evaluation and energy-dissipation behavior of fiber-reinforced polymer concrete." *asmedigitalcollection.asme.orgV Toufigh, V Toufigh, H Saadatmanesh, S AhmariAdvances Civ. Eng. Mater. 2013•asmedigitalcollection.asme.org*, 2 (1): 622–636. https://doi.org/10.1520/ACEM20130074.

Vaidya, U. 2015. "Thermoplastic composites for aerospace applications." *JEC Compos. Mag.*, 52 (96): 41–44. JEC Composites Magazine. https://doi.org/10.1007/978-3-030-35346-9_4.

Vedernikov, A., F. Tucci, P. Carlone, S. Gusev, S. Konev, D. Firsov, I. Akhatov, and A. Safonov. 2021. "Effects of pulling speed on structural performance of L-shaped pultruded profiles." *Compos. Struct.*, 255 (September 2020): 112967. Elsevier Ltd. https://doi.org/10.1016/j.compstruct.2020.112967.

Wang, C., S. yang Li, X. jia He, Q. Chen, H. Zhang, and X. yu Liu. 2021. "Improved prediction of water retention characteristic based on soil gradation and clay fraction." *Geoderma*, 404 (May): 115293. Elsevier B.V. https://doi.org/10.1016/j.geoderma.2021.115293.

Wang, J., Q. Dai, S. Guo, and R. Si. 2019. "Mechanical and durability performance evaluation of crumb rubber-modified epoxy polymer concrete overlays." *Constr. Build. Mater.*, 203: 469–480. https://doi.org/10.1016/j.conbuildmat.2019.01.085.

Wheat, D. L., D. W. Fowler, and A. I. Al-Negheimish. 1993. "Thermal and Fatigue Behavior of Polymer Concrete Overlaid Beams." *J. Mater. Civ. Eng.*, 5 (4): 460–477. American Society of Civil Engineers (ASCE). https://doi.org/10.1061/(ASCE)0899-1561(1993)5:4(460).

Xue, X., S. Y. Liu, Z. Y. Zhang, Q. Z. Wang, and C. Z. Xiao. 2022. "A technology review of recycling methods for fiber-reinforced thermosets." *J. Reinf. Plast. Compos.*, 41 (11–12):

459–480. SAGE Publications Ltd. https://doi.org/10.1177/07316844211055208.

Yan, F., Z. Lin, and M. Yang. 2016. “Bond mechanism and bond strength of GFRP bars to concrete: A review.” *Compos. Part B Eng.*, 98: 56–69. https://doi.org/10.1016/j.compositesb.2016.04.068.

Yeon, K. S., J. H. Yeon, Y. S. Choi, and S. H. Min. 2014. “Deformation behavior of acrylic polymer concrete: Effects of methacrylic acid and curing temperature.” *Constr. Build. Mater.*, 63: 125–131. https://doi.org/10.1016/j.conbuildmat.2014.04.051.

Yu, F., L. Cao, Z. Meng, N. Lin, and X. Y. Liu. 2016. “Crosslinked waterborne polyurethane with high waterproof performance.” *Polym. Chem.*, 7 (23): 3913–3922. Royal Society of Chemistry. https://doi.org/10.1039/c6py00350h.

Yu, N., Z. H. Zhang, and S. Y. He. 2008. “Fracture toughness and fatigue life of MWCNT/epoxy composites.” *Mater. Sci. Eng. A*, 494 (1–2): 380–384. Elsevier. https://doi.org/10.1016/j.msea.2008.04.051.

Zakaria, M. R., H. Md Akil, M. H. Abdul Kudus, F. Ullah, F. Javed, and N. Nosbi. 2019. “Hybrid carbon fiber-carbon nanotubes reinforced polymer composites: A review.” *Compos. Part B Eng.*

Zaman, A., S. A. Gutub, and M. A. Wafa. 2013. “A review on FRP composites applications and durability concerns in the construction sector.” *J. Reinf. Plast. Compos.*

Zhang, P., Q. Guan, Q. Li, E. Engineering, M. F. Maghrebi, D. Azad, S. H. Mousavi, H. S. Kazeran, M. P. Khiavi, M. A. Ghorbani, and E. Faculty. 2013. “Mechanical Properties of Plastic Concrete Containing Bentonite.” 5 (100): 1317–1322. https://doi.org/10.17265/2161-

6221/2014.12.006.

Zhang, S. S., T. Yu, and G. M. Chen. 2017. “Reinforced concrete beams strengthened in flexure with near-surface mounted (NSM) CFRP strips: Current status and research needs.” *Compos. Part B Eng.*

Zhang, S., B. Tian, B. Chen, X. Lu, B. Xiong, and N. Shuang. 2022. “The Influence of Freeze–Thaw Cycles and Corrosion on Reinforced Concrete and the Relationship between the Evolutions of the Microstructure and Mechanical Properties.” *Materials (Basel).*, 15 (18). https://doi.org/10.3390/ma15186215.

Zhang, Z., J. Zhou, J. Yang, Y. Zou, and Z. Wang. 2020. “Understanding of the deterioration characteristic of concrete exposed to external sulfate attack: Insight into mesoscopic pore structures.” *Constr. Build. Mater.*, 260: 119932. Elsevier Ltd. https://doi.org/10.1016/j.conbuildmat.2020.119932.

Zhao, J., S. Li, and Z. Zhang. 2023. “Integrated composite wall with geopolymer permanent insulation formwork: Interface bonding behavior and mechanism.” *Constr. Build. Mater.*, 403 (August). Elsevier Ltd. https://doi.org/10.1016/j.conbuildmat.2023.133110.

Zhao, J. Q., and L. Daigle. 2001. “Structural performance of sliplined watermain.” *Can. J. Civ. Eng.*, 28 (6): 969–978. National Research Council of Canada. https://doi.org/10.1139/l01-068.

Zheng, H., W. Zhang, B. Li, J. Zhu, C. Wang, G. Song, G. Wu, X. Yang, Y. Huang, and L. Ma. 2022. “Recent advances of interphases in carbon fiber-reinforced polymer composites: A review.” *Compos. Part B Eng.*, 233 (October 2021): 109639. Elsevier Ltd. https://doi.org/10.1016/j.compositesb.2022.109639.

12. Appendix: Publications

List of Published Papers:

1. Akbarpour, A., J. Volz, and S. Vemuganti. 2024. "An Experimental Study Incorporating Carbon Fiber Composite Bars and Wraps for Concrete Performance and Failure Insight." *J. Compos. Sci.*, 8 (5). https://doi.org/10.3390/jcs8050174.
2. Akbarpour, A., J. Volz, and S. Vemuganti. 2025. "The Influence of Multi-Walled Carbon Nanotubes on the Pull-Off Strength of Polymer Concrete Overlays on Concrete Substrates with Sulfate Exposure." *J. Compos. Sci.*, 9 (6): 272. https://doi.org/10.3390/jcs9060272.
3. Adhikari, S., A. Akbarpour, J. Volz, R. W. Floyd, and S. Vemuganti. 2025. "Thermoplastic carbon fiber reinforced polymer tapes in cementitious and polymer concretes." *Funct. Compos. Struct.*, 7 (2). https://doi.org/10.1088/2631-6331/add9e1.

List of in Progress Papers:

4. Akbarpour, A., J. Volz, R. W. Floyd, and S. Vemuganti. "Role of Grout and GFRP Slip Liner on the Circumferential Behavior of Retrofitted Corroded Metal Culverts."
5. Akbarpour, A., A. Liever, and S. Vemuganti. "Effects of Freeze-Thaw Environments on Nanomodified Carbon Fiber Reinforced Polymer Composites."